arXiv:cond-mat/0407333v2 [cond-mat.stat-mech] 31 May 2007

# Experimental X-Ray Studies of Liquid Surfaces

A thesis presented

by

Oleg Grigorievich Shpyrko

to

The Department of Physics

in partial fulfillment of the requirements

for the degree of

Doctor of Philosophy

in the subject of

Physics

Harvard University

Cambridge, Massachusetts

December 2003

© 2003 - Oleg Grigorievich Shpyrko
All rights reserved.

Thesis advisor
**Peter S. Pershan**

Author
**Oleg Grigorievich Shpyrko**

**Experimental X-Ray Studies of Liquid Surfaces**

# Abstract

Over the past two decades synchrotron facilities dedicated to the generation of x-rays for study of atoms, molecules and condensed matter have proliferated in Europe, Asia and the United States. As a result of the special properties of x-rays produced by these machines, there has been an enormous growth in the experimental possibilities. In this work we will demonstrate how these special properties can be used to carry out hitherto impossible measurements of the Ångström level structure of the free surfaces of liquids.

A large part of this thesis is devoted to surface-induced atomic or molecular layering phenomenon in liquids. While the atomic structure of metallic and dielectric liquids is similar in the bulk, the microscopic atomic structure at the liquid-vapor interface of dielectric liquids is believed to be fundamentally different from that of a metal: metallic liquids exhibit an oscillatory density profile extending over a few atomic lengths into the bulk, as opposed to a more simple monotonic density profile that is thought to be characteristic of dielectric liquids formed from atoms or small molecules. Unfortunately, this oscillatory density profile is partially obscured by the surface roughness generated by thermally excited capillary waves. As a result, extraction of the microscopic form of this local density profile requires the special experimental and theoretical methods that are the subject of this thesis. It will be shown that the layering is present in all metallic liquids studied so far. Although there have been x-ray reflectivity studies of other liquids, the only measurement to probe the surface structure for a non-metallic liquid made of small molecules is the one reported here on the surface of water. In view of the fact that the surface tension for liquid K is not very different from that of water these measurements demonstrate

that the appearance of layering in metals is not simply a consequence of higher surface tension. In addition to studies of pure liquids, part of this thesis is devoted to surface of binary metallic alloys. The phenomena we investigated include Gibbs adsorption and the tetra-point wetting transition.

# Table of Contents

Abstract . . . . . iii

**Table of Contents** **v**

**Acknowledgements** **xxx**

**1 Introduction** **1**
1.1 Overview . . . . . 2
1.2 Citations to Previously Published Work . . . . . 7
Bibliography . . . . . 11

**2 Theoretical and Experimental Overview** **21**
2.1 X-rays . . . . . 21
2.2 Index of Reflection . . . . . 21
2.3 Critical Angle of Reflection . . . . . 23
2.4 X-Ray Surface Techniques: Overview . . . . . 23
2.5 Reflectivity . . . . . 24
2.5.1 Kinematics of Reflectivity Measurement . . . . . 24
2.6 Ideal Surface: Fresnel Reflectivity . . . . . 24
2.7 Reflectivity from a Structured Surface . . . . . 26
2.7.1 Born Approximation vs. Dynamic Parratt Formalism . . . . . 26
2.7.2 Master Formula . . . . . 27
2.8 Form Factor: Examples . . . . . 27
2.8.1 Ideally sharp flat surface . . . . . 28
2.8.2 Flat surface with a gradual interfacial profile . . . . . 28
2.8.3 Crystalline and Quasi-Crystalline Model . . . . . 29
2.8.4 High-density surface layer . . . . . 31
2.9 Thermal Capillary Wave Fluctuations . . . . . 33
2.9.1 Solids vs. Liquids . . . . . 33

2.9.2 Off-specular diffuse scattering . . . 33
2.9.3 Specular Reflectivity and Local Density Profile . . . 38
2.9.4 Integration of the Resolution Function . . . 42
2.10 Experimental Details . . . 47
2.10.1 Synchrotron Radiation Sources . . . 47
2.10.2 Liquid Surface Spectrometer . . . 48
2.10.3 Active Vibration Isolation System . . . 52
2.10.4 Ultra High Vacuum Chamber . . . 53
2.10.5 Liquid Metal Sample preparation . . . 54
2.10.6 Surface Cleaning by Ion Sputtering . . . 56
2.10.7 Temperature control . . . 58
2.10.8 Curvature Effects . . . 58
Bibliography . . . 66

**3 Surface-Induced Atomic Layering 70**
3.1 Theoretical predictions . . . 70
3.1.1 Velasco's Theory . . . 70
3.2 Candidates for X-ray Study of Atomic Layering . . . 72
3.3 Distorted Crystal Density Model . . . 74
3.3.1 Model Description . . . 76
3.3.2 An Alternative Density Model . . . 76
3.3.3 Fitting Functions . . . 77
3.4 X-Ray Measurements of Liquid Mercury, Gallium and Indium . . . 80
3.4.1 X-Ray Reflectivity Comparison . . . 80
3.4.2 Temperature-Dependent Reflectivity: Liquid Ga . . . 83
3.4.3 X-Ray Diffuse Scattering Data: Liquid In . . . 85
Bibliography . . . 87

**4 Temperature Dependent Surface Structure of Liquid Mercury 90**
4.1 Abstract . . . 90
4.2 Introduction . . . 90
4.3 Experimental Details . . . 92
4.4 Sample Preparation . . . 93
4.5 X-Ray Reflectivity Measurements . . . 94
4.6 Electron Density Model . . . 94
4.7 Discussion . . . 97
4.8 Summary . . . 101
Bibliography . . . 102

**5 X-ray Studies on Liquid Indium** **104**
5.1 Abstract . . . 104
5.2 Introduction . . . 105
5.3 Experimental Details . . . 108
5.4 Theory . . . 111
5.5 Experimental Results . . . 116
5.6 Discussion . . . 121
5.7 Summary . . . 128
Bibliography . . . 129

**6 Surface Structure of KNa alloy** **134**
6.1 Abstract . . . 134
6.2 Introduction . . . 134
6.3 Sample Preparation . . . 138
6.4 Experimental geometry . . . 139
6.5 X-Ray Diffuse Scattering Measurements . . . 140
6.6 X-Ray Reflectivity Measurements . . . 141
6.7 Capillary Wave Contributions . . . 143
6.8 Oxidation Studies . . . 143
6.9 Summary . . . 145
Bibliography . . . 147

**7 Layering in Alkali Metals: Liquid Potassium** **150**
7.1 Abstract . . . 150
7.2 Introduction . . . 151
7.3 Experimental Details . . . 153
7.4 Measurements . . . 160
7.4.1 Advantages of Linear Detector . . . 160
7.4.2 Diffuse Scattering Data: Eta Effect . . . 162
7.4.3 Resolution Effects . . . 164
7.4.4 Specular Reflectivity Data . . . 164
7.4.5 Surface Structure Factor Data . . . 167
7.5 Summary and Discussion . . . 169
Bibliography . . . 171

**8 Search for Layering in Non-metallic Liquids: Water** **175**
8.1 Abstract . . . 175
8.2 Introduction . . . 175
8.3 Effect of Capillary Waves . . . 179

8.4 Experimental Details . . . 180
8.5 X-ray Diffuse Scattering Data . . . 182
8.6 X-ray Reflectivity Data . . . 185
8.7 Summary . . . 189
Bibliography . . . 191

**9 Surface of Liquid Sn: Anomalous layering 195**
9.1 Abstract . . . 195
9.2 Introduction . . . 195
9.3 Experimental . . . 197
9.4 X-ray reflectivity measurements . . . 198
9.5 The Surface Structure Factor . . . 200
9.6 The Case For Exclusion of Surface Impurities . . . 207
9.6.1 Grazing Incidence Fluorescence Scattering . . . 208
9.6.2 Resonant X-ray Reflectivity . . . 210
9.7 Conclusion . . . 216
Bibliography . . . 218

**10 Surface Phases in Binary Liquid Metal Alloys 221**
10.1 Abstract . . . 221
10.2 Introduction . . . 222
10.3 Surface X-ray Scattering Techniques . . . 224
10.4 Experimental . . . 227
10.5 Results and Discussion . . . 228
10.5.1 Surface Segregation in Ga-In . . . 228
10.5.2 Wetting phase transition in Ga-Bi . . . 229
10.5.3 Pair formation in Hg-Au . . . 237
Bibliography . . . 240

**11 Surface Induced Order in Liquid Metals and Binary Alloys 243**
11.1 Abstract . . . 243
11.2 Liquid Metals and Surface Induced Order . . . 243
11.3 Surface Structure of Binary Liquid Alloys . . . 246
11.3.1 K-Na . . . 247
11.3.2 Bi-In . . . 249
11.3.3 Ga-Bi . . . 249
Bibliography . . . 254

**12 Surface studies of liquid Hg/Au alloys** **256**
12.1 Abstract . . . 256
12.2 Introduction . . . 257
12.3 Experimental Details . . . 260
12.4 X-ray Reflectivity and Modelling . . . 262
12.5 Experimental Results . . . 268
12.6 Analysis and Discussion . . . 274
12.6.1 Dilute Au limit and Capillary Wave Roughness . . . 275
12.6.2 Au-rich limit and Surface Phase Formation . . . 279
Bibliography . . . 286

**13 Resonant x-ray study of liquid Bi-In surface** **290**
13.1 Abstract . . . 290
13.2 Introduction . . . 290
13.3 Experimental Setup . . . 292
13.4 Resonant X-ray Scattering . . . 293
13.5 Sample Preparation . . . 293
13.6 X-Ray Reflectivity Data . . . 295
13.7 Electron Density Model . . . 295
13.8 Data Fitting Analysis . . . 297
13.9 Summary . . . 300
Bibliography . . . 302

**14 Microscopic Structure of the Short-Range Wetting Film at the Surface of Liquid Ga-Bi Alloys** **304**
14.1 Abstract . . . 304
14.2 Introduction . . . 304
14.3 Sample Preparation . . . 307
14.4 Experimental Techniques . . . 307
14.5 Results . . . 309
14.6 Summary . . . 314
Bibliography . . . 316

**15 Wetting film at GaBi surface** **318**
15.1 Abstract . . . 318
15.2 Introduction . . . 318
15.3 Bulk and Surface Structure . . . 319
15.4 Experimental Techniques . . . 321
15.5 Results . . . 323

15.6 Conclusions . . . . . 327
Bibliography . . . . . 329

**16 Short-Range Wetting at Alloy Surfaces: Square Gradient Theory 331**
16.1 Abstract . . . . . 331
16.2 Introduction . . . . . 332
16.3 Bulk & Surface Thermodynamics . . . . . 335
16.4 X-ray reflectivity measurements . . . . . 340
16.4.1 Experiment . . . . . 340
16.4.2 Wetting film structures approaching (l/l/v)-coexistence . . . . 345
16.4.3 Wetting film structures: On (l/l/v)-coexistence . . . . . 348
16.5 Liquid/Liquid Interface . . . . . 351
16.5.1 Square Gradient Theory . . . . . 351
16.5.2 Capillary Wave Excitations on the (l/l) Interface . . . . . 354
16.5.3 Intrinsic Profile and (l/l) interfacial tension of Ga-Bi . . . . . 356
16.5.4 (l/l) interfacial tension of Ga-Pb . . . . . 361
16.6 Wetting Phenomenology at the Free Surface . . . . . 363
16.7 Summary . . . . . 368
16.8 Appendix: Bulk thermodynamics . . . . . 370
Bibliography . . . . . 374

**Index 382**

# List of Figures


2.1 Kinematics of the x-ray measurement. . . . . 25

2.2 Density profiles $\rho(z)/\rho_\infty(z)$ and respective reflectivity curves $R(q_z)/R_F(q_z)$ for a smooth and roughened surfaces (A), crystalline and layering structure (B) and thin/thick high-density layers (C) . . . . . 30

2.3 The difference between intrinsic and thermal profile, an example taken from experimental studies of liquid Gallium at room temperature. . . 41

2.4 The schematic describing the integration of capillary wave contributions over the rectangular resolution function in $q_{xy}$ space, for the case when the singularity O is located *inside* the resolution volume. . . . . 44

2.5 A schematic describing the procedure integration of capillary wave contributions over the rectangular resolution function in $q_{xy}$-space for the case when the singularity O is located *outside* of the resolution volume. 46

2.6 A comparison between synchrotron radiation development (x-ray source brightness, expressed in photons/sec/0.1% bandwidth $/mm^2/mrad^2$ and the growth in leading-edge computing speed (expressed in millions of operations/sec) which occurred over the past 60 years . . . . . 49

2.7 A schematic picture of liquid spectrometer setup. Shown are: the incoming synchrotron beam (a), the steering crystal (b), the liquid sample within the UHV chamber (c), temperature control and the active vibration isolation system (d) and the detector (e) . . . . . 51

2.8 A photo and schematic of a typical UHV chamber setup: Liquid Sample (A) contained in sample holder (B), output Be window (C) (input Be window is located on the other side of the chamber), ion pump (D), turbo pump (E), hose leading to rotary pump (F), ion sputtering gun (G), a hose leading to Ar cylinder (H), viewport for monitoring the sample (I), a bellow (J), vacuum gauge and a port for RGA system (K), linear transfer mechanism (L), bottom flange containing thermocouple, heater and electrical contacts feedthroughs (M) and chamber frame (N). 57

2.9 A schematic picture describing radiation shield setup: radiation shield (A) with Be foil walls (B), liquid sample (C) contained in a Mo sample pan (D), positioned directly on top of a Boralectric resistive heater (E). For the measurement the shield is lowered so that the sample is completely surrounded by the shield and its' walls . . . . . 59

2.10 Illustration of reflection geometry from curved sample. . . . . 61

2.11 Graphical representation of a "walking scan" procedure: a series of detector height scans for various sample height position, taken on a sample of liquid GaBi alloy. Sample height position was changed in increments of 0.2mm, see legend for more details. . . . . 63

2.12 The displacements of the center positions of detective height scans from the walking scan shown in Figure 2.11, adjusted for twice the amount of the sample height displacement to account for a geometrical change in position of the beam for an ideally flat reflecting surface, as a function of sample height position. The derivative of this plot is the effective measure of the local surface curvature, $R^{-1}$. . . . . 64

3.1 Surface-normal average of the density at the surfaces of liquid metal (solid line) and dielectric liquid (broken line). . . . . 71

3.2 The plot showing x-ray reflectivity data taken from liquid Hg (circles), Ga (squares) and In (triangles), along with theoretically predicted Fresnel curves (lines). . . . . 81

3.3 The plot showing Fresnel-normalized x-ray reflectivity data taken from liquid Hg (circles), Ga (squares) and In (triangles). . . . . 82
3.4 Fresnel-normalized x-ray reflectivity data measured for liquid Ga in the temperature range of 22°C to 160°C. . . . . 83
3.5 The temperature-dependent reflectivity datasets pictured in Figure 3.4 normalized to the thermal capillary wave fluctuations. . . . . 84
3.6 Diffuse scattering data for liquid indium (symbols), along with the theoretical simulations which follow from capillary wave theory (lines), taken at 3.0, 3.5, 4.0 and 4.5 degrees, which correspond to $\eta$ values of 0.049, 0.066, 0.087 and 0.110 respectively. . . . . 86

4.1 (a) X-ray reflectivity of liquid Hg. △: $-35$°C; ■: 0°C; ○: $+23$°C; (—): calculated Fresnel reflectivity $R_F$. (b) Room temperature reflectivity normalized by $R_F$ (—) for two Hg samples. ○: glass chamber with $H_2$ gas. ●: UHV chamber. (c) Calculated local layering profiles having $d = 2.72$ Å, $\overline{\sigma} = 0.46$ Å, and $\sigma_T = 1.0$ Å. $(\cdots)$: no surface modification. (—): adlayer model. (- - -): surface depletion model. (d) Best fit profiles for vacuum data. (—): Room temperature ($\sigma_T = 1.0$ Å). (- - -): $T = -36$°C ($\sigma_T = 0.8$ Å). . . . . 95
4.2 (a) $R/R_F$ for different temperatures, from sample measured in $H_2$ atmosphere. Solid lines are fit curves for which $\sigma_T$ has been varied. (b) Temperature dependence of $\sigma_T^2$. △: Measurement in vacuum). ○: Measurement in $H_2$ gas). ●: Second sample measured in $H_2$ gas. ◇: Ga data from Ref. 8. Lines: Capillary wave form $\sigma_{cw}^2(T)$ for Hg (- - -) and Ga (—). (c) Temperature dependence of $(R/R_F)/\exp(-q^2\sigma_{cw}^2)$ at the layering peak, normalized at the melting point, for Ga (◇) and Hg (symbols as in (b)). . . . . 99

5.1 Sketch of the geometry of x-ray scattering from the liquid surface with $\alpha$ and $\beta$ denoting incoming and outgoing angle, the incoming and outgoing wavevector $\vec{k}_{in}$ and $\vec{k}_{out}$ respectively and the azimuthal angle $2\theta$. The momentum transfer $\vec{q}$ has an in-plane component $q_{xy}$ and a surface-normal component $q_z$. . . . . 111

5.2 Specular x-ray reflectivity for liquid Indium at 170 °C taken with vertical detector resolutions of 0.06 $\text{Å}^{-1}$ (scintillation detector; open circles: X22B, closed circles: X25) and 0.32 $\text{Å}^{-1}$ (PSD in single channel mode; squares: X25). The reflectivity is normalized to the Fresnel reflectivity $R_f$ of a flat In surface. Solid lines are fits as described in the text. Data from X22B was not incorporated in any fits. . . . . 117

5.3 Diffuse scattering as a function of scattering angle $\beta$ for different fixed incoming angles $\alpha$. Solid lines: Diffuse scattering calculated from the experimentally determined structure factor with no further adjustable parameters. Inset: linear plot emphasizing the fit near the specular peak for $\alpha = 4.5°$ . . . . . 120

5.4 (a) Comparison of the local real space density profile for liquid Indium (—) with the thermally averaged density profile for the same metal (- - -). The averaged density profile is directly accessible by experiment and has been measured at 170° C. (b) Real space local density profile for liquid Gallium (- - -) and liquid Indium (—) after the removal of thermal broadening. Densities $\tilde{\rho}(z)$ are normalized to the bulk densities $\rho_\infty$ of liquid Gallium and Indium. Inset: Decay of the amplitude of the surface–normal density profile for liquid Ga (open circles) and liquid In (filled circles). The lines represent the fit of this decay of the surface layering to the form $\exp(-z/l)$ for liquid Ga (—) and In (- - -). . . . 123

5.5 (a) Bulk (△) and surface (•) structure factors for liquid In. The bulk structure factor data are taken from Orton et al.[22] The solid line is a fit of the model explained in the text to the experimentally determined surface structure factor. The broken line is a guide for the eye. The inset compares the decay of the longitudinal surface density oscillations (filled circles; solid line represents fit to an exponential) to the decay of the bulk pair correlation function (open triangles; broken line represents fit to exponential). The coordinate $z$ of the x-axis represents the distance from the surface in the case of the decaying surface layering and the radial distance from a reference atom in the bulk liquid in the case of the decaying bulk pair correlation. The data for the bulk pair correlation function are taken from Waseda.[42] (b) Bulk (△) and surface (•) structure factors for liquid Ga. The bulk structure factor data are taken from Narten et al.[15] Solid lines are fits to reflectivity data, broken lines are guides for the eye. The inset compares the decay of the longitudinal surface density oscillations (filled circles; solid line represents fit to exponential) to the decay of the bulk pair correlation function (open triangles; broken line represents fit to exponential). The data for the bulk pair correlation function are taken from Waseda.[42] 125

6.1 Bulk liquid structure factor measured for liquid $K_{67}Na_{33}$ (○) compared to the bulk structure factors of pure liquid K and Na from Ref. 14 (—). Inset: geometry for x-ray reflectivity and off-specular diffuse scattering as described in the text. . . . . 137

6.2 (a) Off-specular diffuse scattering from the surface of liquid $K_{67}Na_{33}$ for different incoming angles $\alpha$: (○): 0.9° (multiplied by 25 for clarity), (■): 1.2° (× 5), (△): 1.77°, (●): 2.1° (× .2), (□): 2.45° (× .1). (b) Extrapolated diffuse scattering (assuming no surface layering) for $\alpha =$ 4.5 °: (—) resolution of the present experiment ($\Delta q_z \approx 0.03$ Å$^{-1}$). ( - - - ) assuming the resolution attainable at a low divergence x-ray source: ($\Delta q_z \approx 3 \times 10^{-4}$ Å$^{-1}$). (intensity × 100). . . . . 142

6.3 X-ray reflectivity from a clean liquid $K_{67}Na_{33}$ surface at room temperature (□) and $K_{67}Na_{33}$ following an exposure to 3000 L of oxygen (●) Also included for reference: (—) calculated Fresnel reflectivity from an ideal $K_{67}Na_{33}$ surface; (- - -) calculated reflectivity $R_{cw}$ from a $K_{67}Na_{33}$ surface roughened by capillary waves at room temperature. Inset: Surface structure factor $|\Phi(q_z)|^2$ of liquid $K_{67}Na_{33}$ at room temperature (□). For comparison the surface structure factors for liquid Ga (closed triangles) and In (closed boxes) are included. $q_z$ is normalized to the position of the first peak in the bulk $S(q)$ . . . . . 144

7.1 Schematic description of the experimental setup. . . . . 154

7.2 Kinematics of the x-ray measurement. . . . . 155

7.3 Comparison of an X-ray diffuse scattering scans taken with point detector - filled squares, and position sensitive detector (PSD) - open circles. The specular condition corresponds to $q_z$=0.3 $\mathring{A}^{-1}$. The resolution of the bicron detector (0.22mm vertically and 2.5mm horizontally) was chosen to match that of a PSD. Also shown is a line which represents theoretical modeling using the capillary-wave theory for given resolution, temperature (70°$C$) and surface tension (110 mN/m). . . . . 161

7.4 X-Ray diffuse scattering scans taken with PSD, as a function of wavevector transfer component $q_{xy}$. Specular condition corresponds to values of $q_z$ (bottom to top): 0.3, 0.4, 0.6, 0.8, 1.0 and 1.1 $\mathring{A}^{-1}$. For comparison, the scans are normalized to unity at $q_{xy}$=0. Lines represent theoretically simulated scans for given values of $q_z$. The inset shows a similar scan taken at 1.2 $\mathring{A}^{-1}$, for which the specular peak is marginally observable. . . . . 163

7.5 Effects of varying the horizontal resolution function on the diffuse scattering data. Diffuse scans taken with PSD, peak position corresponding to $q_z$=0.4 $\mathring{A}^{-1}$, as a function of angular deviation from specular condition ($\alpha - \beta$) with fixed vertical resolution (.22mm), while horizontal resolution was changed (bottom to top: 2mm, 4mm, 8mm). . . . . 165

7.6 Fresnel-normalized reflectivity signal $R/R_f(q_z)$ for liquid K (circles) compared to capillary wave predictions (dashed line). The inset shows the capillary wave factor $\eta$ for liquid K as a function of $q_z$. . . . . 166

7.7 Surface structure factor $\Phi(q_z)$ for liquid Ga (open circles), liquid In (open squares) and liquid K (filled circles) obtained from X-ray reflectivity data by deconvolving resolution, Fresnel reflectivity and capillary wave contributions, shown here as a function of $q_z/q_{peak}$, here $q_{peak}$ is the value of $q_z$ at which the layering peak is observed (2.4 $\mathring{A}^{-1}$ for Ga and 2.2 $\mathring{A}^{-1}$ for In) or is expected to be observed (1.6 $\mathring{A}^{-1}$ for K). The inset shows the same three sets of data extended to a greater range. 168

8.1 X-ray reflectivity from free liquid surfaces of the indicated samples. Points - measured [$R(q_z)$], lines - calculated for an ideally flat and steplike interface [$R_F(q_z)$]. The inset shows the ratio of the two. . . . 178

8.2 Schematic description of the experimental setup. . . . . 181

8.3 Comparison of measured diffuse scattering with capillary wave theory predictions for the angles of incidence $\alpha$ (top to bottom): 2.1°, 2.8°, 3.5°, 4.2°, 5.0°, 5.7°, 6.0°, and 6.4°. The last data set corresponding to 7.1° shown in the inset no longer exhibits a distinguishable specular peak. The $q_z$ values corresponding to the specular condition $q_y = 0$ Å$^{-1}$ are 0.3, 0.4, 0.5, 0.7, 0.8, 0.85, 0.9, and 1.0 $\mathring{A}^{-1}$, respectively. . . . . 183

8.4 Fresnel-normalized X-ray reflectivity from free liquid surfaces water, taken for two different values of resolution with bicron detector (circles) and linear detector (squares). Blue and red lines show theoretical expected values for the two measurements, respectively, assuming no surface structure. . . . . 186

8.5 Comparison of the structure factor squared $\mid \Phi(q_z) \mid^2$ for water (circles), liquid potassium (squares), and liquid gallium (triangles). The wavevector $q_z$ is normalized to the expected position of the layering peak $q_{peak}$ of each sample. The inset shows the data on an extended scale. For discussion see text. . . . . 187

9.1 Kinematics of the x-ray measurement. $k_{in}$ and $k_{out}$ are the wavevectors of the incident and detected x-rays, respectively. . . . . 198

9.2 The measured x-ray specular reflectivity (points) of the surface of liquid Sn. The Fresnel reflectivity (solid line) of an ideally flat and abrupt surface, and the reflectivity of an ideal surface roughened by thermally-excited capillary waves (dashed line) are also shown. . . . . 199

9.3 Diffuse scattering off the liquid Sn surface measured at a fixed grazing angle of incidence $\alpha = 5.05°$ (open circles). The peak corresponds to the specular condition at $q_z = 0.48$ Å$^{-1}$. The line is the capillary wave theory predictions for surface tension $\gamma = 560$ mN/m. . . . . 202

9.4 The structure factor (squared) of the Sn surface as derived from the measured reflectivity $|\Phi(q_z)|^2 = R(q_z)/[R_F(q_z)CW(q_z)]$ (open circles). The dashed line is the theoretically expected $|\Phi(q_z)|^2$ of a simple layered density profile as found previously for Ga and In. The solid line is a fit to a model, discussed in the text, where the distance between the first and second layers is reduced by 10% relative to that of the subsequent layers. . . . . 204

9.5 Models for the intrinsic surface-normal electron density profiles of Sn for a simple, equally-spaced layering model (dashed line), and for a model including a contraction of the spacing between the first and second layers by 10% (solid line). The models yield the reflectivities shown by the same lines in Fig. 9.2. The inset is a blow up of the peak region. . . . . 206

9.6 Experimental setup used in the GI-XRF measurements: the synchrotron beam (a) is Bragg-reflected from a monochromator (b) which directs it downwards at the liquid Sn sample located inside a UHV chamber (c). The specularly-reflected beam (solid line) is blocked by a beam stop on the exit window (d) to minimize the background. The fluorescence from the sample's surface (dotted lines) is detected off-specularly by an energy-dispersive detector (e) located as close to the chamber as possible to maximize its solid angle of acceptance. . . . . 208

9.7 Raw (line) and background-subtracted (open circles) measured fluorescence from the surface of liquid Sn. The sharp lines are due to the K emissions lines[20] of Fe (E=6.4 keV), Nb (E=16.6 keV), Mo (E=17.5 keV) and Sn (E=25.2 keV). . . . . 211

9.8 (Top) Relative energy variation of the reflectivity off the liquid Sn surface at a fixed $q_z = 0.3$ Å$^{-1}$. The line is the theoretical prediction of the change in the reflectivity due to the variation of the dispersion correction $f'(E)$ of the scattering factor near the edge, as calculated by the IFEFFIT[23] program. The open circles are the measured values. (Bottom) Measured energy variation of the intensity transmitted through an Sn foil (points). The K edge of Sn at E=29.20 keV shows up clearly in both measurements. . . . . 213

9.9 The structure factor (squared) of the Sn surface as derived from the measured reflectivity, at (E=29.20 keV, triangles), above ((E=29.22 keV, circles) and below (E=17 keV, squares) the K-edge. The solid line is a fit to the density model featuring reduced interatomic spacing for the top layer by approximately 10 %. The dashed line is calculated for a model with a high-density surface monolayer of an atomic species other than Sn. The inset shows the density profile of such a layer. For a discussion see text. . . . . 215

10.1 Sketch of the geometry of x-ray scattering from the liquid surface with $\alpha$ and $\beta$ denoting incoming and outgoing angle, the incoming and outgoing wavevector $k_{in}$ and $k_{out}$ respectively and the azimuthal angle $2\theta$. The momentum transfer $q$ has an in-plane component $q_{xy}$ and a surface-normal component $q_z$. . . . . 225

10.2 X-ray reflectivity from liquid Ga and liquid Ga-In (16.5% In) at 25° C. The broken line represents the fit of the model described in the text to the measured reflectivity from liquid Ga. The solid line represents the fit of the same model with one additional high density adlayer to the measured reflectivity from the liquid Ga-In eutectic. . . . . 230

10.3 X-ray reflectivity from Ga-Bi for three different temperatures. The solid lines show the fit of the data to a simple surface segregation model with one Bi monolayer on top of the Ga rich bulk phase. The difference between the 35° C and the 95° C data is due to the increased roughness at higher temperatures. The 260° C data cannot be fitted by this model. The inset shows the principal difference in surface structure between the 35° C and the 260° C data, indicating a wetting phase transition. . . . . 232

10.4 Comparison of the intrinsic or local real space density profiles (thermal broadening removed) for Ga-Bi at two different temperatures as well as for elemental Ga. The density is normalized to the bulk density of liquid Ga. The zero position in $z$ is arbitrarily assigned to the center of the first Ga layering peak. . . . . 233

10.5 Grazing Incidence Diffraction from Ga-Bi at 35° C. The solid line shows the in-plane structure averaged over the penetration depth of x-rays away from the critical angle for total external reflection (about 1000 Å). The open triangles show the diffraction peak obtained for $\alpha < \alpha_{crit}$ ($\alpha_{crit} = 0.14°$ for Ga at $\lambda = 0.653$ $\mathring{A}$) thus probing the surface region evanescently. . . . . 236

10.6 (a) X-ray reflectivity of Hg and Hg/0.06at%Au normalized to the Fresnel reflectivity of Hg. (b) Normalized reflectivity of a Hg/0.13% alloy. 238

11.1 (a) X-ray reflectivity geometry for the liquid metal, with layering of ions producing an oscillatory density profile $\rho(z)$. (b) X-ray reflectivity for liquid Hg (−35°C, ∘), Ga (+25°C) and In (+170°C, △). Solid lines: calculated Fresnel reflectivity from a flat surface. Data for Ga and In are shifted for clarity. . . . . 245

11.2 (a) X-ray reflectivity from a $K_{80}Na_{20}$ alloy measured by integrating over a large range of $\alpha$ at fixed $\alpha + \beta$. The normalized reflectivity is shown in the inset. The dotted lines show a capillary wave roughness with no layering with $\sigma = 1.2$ $\mathring{A}$ and 1.5 $\mathring{A}$, respectively. (b) Normalized x-ray reflectivity of liquid In (+170°C, closed circles) and In-22at %Bi (80 °C, open circles). . . . . 248

11.3 (a) Normalized x-ray reflectivity of liquid Ga (+25°C, ∘), and on the Ga-Bi two-phase coexistence curve at 35°C (•) and 228°C. (b)Grazing incidence diffraction from Ga-Bi at 150°C (filled triangles), 205°C (△), 228°C, and 255°C at $\alpha = 0.08°$. The solid line shows corresponding profiles for $\alpha = 0.30°$ where the bulk is predominately sampled. The data was acquired using Soller slits, 0.05 $\mathring{A}^{-1}$ FWHM. Still, it was not possible to reliably subtract the background. . . . . 251

12.1 Geometry for x-ray reflectivity from a layered liquid metal surface. Maxima in the oscillatory surface-normal density profile $\rho(z)$ correspond to layers of atoms parallel to the liquid–vapor interface. . . . 259

12.2 (a) Model density profiles and (b) corresponding Fresnel-normalized reflectivities as described in text. Curves i–iii in both panels are shifted for clarity. . . . . 264

12.3 Surface phase diagram for liquid Hg-Au alloys, with nominal Au concentrations from 0–0.20% and at temperatures between −28 and +25°C indicated by crosses (+). $R/R_F$ curves are shown on semilog scales, all with identical axes as marked for the 0.13%, −18°C alloy. (∘): Reported solubility limit of Au in Hg. The shaded band is a guide for the eye. . . . . 269

12.4 Fresnel-normalized reflectivity of (a) Hg 0.06at% Au and (b) Hg 0.10at% Au at all measured temperatures, and (c) Hg 0.13at% Au at room temperature. The curves for 0.10at% and 0.13at% alloys are shifted for clarity. Solid lines are fits as discussed in text. . . . . 271

12.5 Fresnel-normalized reflectivity of (a) Hg 0.10at% Au at −13°C, (b) Hg 0.13at% Au below room temperature, and (c) Hg 0.20at% Au for the first cooldown from room temperature. The curves for 0.13at% and 0.20at% alloys are shifted by factors of $10^{-2}$ and $10^{-5}$ respectively. Solid lines are fits as discussed in text. . . . . 272

12.6 Fresnel-normalized reflectivity for Hg 0.20 %Au for the second cooldown from room temperature. +4°C (•), −12°C (△), −24°C (■), −31°C (□), −37°C (⋄), (- - -): +25°C experimental data from first cooldown. 273

12.7 Model density profiles calculated from parameters listed in Table 1. Solid lines are from room temperature fits, and shorter dash length corresponds to lower temperatures. (a) Hg (b) Hg 0.06% Au (c) Hg 0.10% Au Inset: temperature dependence of the excess mean-squared surface roughness ($\sigma_T^2 - \sigma_{cw}^2$) for Hg (■), Hg 0.06at% Au (○), and Hg 0.10at% Au (closed triangles). . . . . 276

12.8 Model density profiles. (a) Hg 0.13% Au: +7°C (—), −18°C (- - -), −67°C (· · ·). (b) Hg 0.20% Au: +25°C (— - - —), +16°C (— - —), +8°C (- · - · -), −20°C (— —), −24°C (- - -), −27°C (—). . . . . 281

13.1 (a) Energy scan in transmission through Bi foil. (b) Fresnel-normalized x-ray reflectivity of $Bi_{22}In_{78}$. ○: 12.5 keV (two independent measurements); •: 13.4 keV; (—): 12.5 keV fit; (- - -) 13.4 keV fit. (c) Best fit real space number density profile relative to bulk atomic percent. (—): Total number density; (– –): In density; (- - -): Bi density. (d) Surface energy as a function of surface Bi concentration $x_{0,\mathrm{Bi}}$ for the bulk concentration $x_{\mathrm{Bi}} = 0.22$, according to Eq. 13.3.1. (- - -): $w = 0$ . (—): $w = -10k_BT$. . . . . 294

13.2 (a) Model surface-normal number density profiles, relative to bulk atomic percent. (—): total number density; (– –): In density; (- - -): Bi density. (b) Calculated Fresnel-normalized reflectivity curves. (—): 12.5 keV; (- - -): 13.4 keV. i: Surface layering with uniform composition ($x_{\mathrm{Bi}} = 0.22$). ii: Surface layering, with Bi enhancement in the first atomic layer ($x_{0,\mathrm{Bi}} = 0.35$). . . . . 298

14.1 Phase diagram of Ga-Bi (Ref. 8). Between 29.5° C and 222° C, solid Bi is in equilibrium with a Ga-rich liquid phase. Between 222° C and 262° C, a liquid Bi-rich phase is in coexistence with a liquid Ga-rich phase. The surface structure of this alloy has been measured between 35° C and 258° C at selected points along the coexistence line (■). For $T$ <222° C partial wetting occurs (a), whereas complete wetting is found for $T$ >222° C (b). The inset depicts the geometry for specular x-ray reflectivity. . . . . 306

14.2 (a) Fresnel normalized reflectivity $R/R_F$ from Ga-Bi alloys for $T < T_{mono}$: (■): 100 at% Ga; (△): 99.7 at% Ga (35° C); (×): 98.7% Ga (95° C); (□): 98.4% Ga (110° C ); (○): 96.5% Ga (155° C ); (●): 95.3% Ga (178° C ) and (◇): 93.2% Ga (207° C ). Shaded line: fit to layered density profile of pure Ga (see Ref. 9); solid lines: fit to layered density profile of Ga plus Bi monolayer (see Ref. 10); broken lines: fit to Bi monolayer (this work). (b) Intrinsic density profiles normalized to $\rho_\infty$ for Ga-Bi for 110° C $\leq T \leq$ 207° C using the one-box model described in the text. The profiles essentially fall on top of each other and two representative fits are shown: 110° C (solid line) and 207° C (broken line). (c): Schematic representation of the (two-)box model. (d): CW roughness $\sigma_{cw}$ for Ga-Bi alloys as a function of temperature using $\gamma$ from our fit (■) and from macroscopic surface tension measurements (□, see Ref. 14). . . . . 308

14.3 $R/R_F$ from Ga-Bi alloys for $T > T_w$: (•): 90.6 at% Ga (228° C); (□): 88.8% Ga (238° C); (△): ditto, but after heating to 258 ° C and cooling down; (×): 79.1% Ga (258° C); (for comparison, see:(⋄), 207° C). Solid lines fit to two-box model; broken line: fit to one-box model. Inset: intrinsic density profiles, $\tilde{\rho}(z)$, for Ga-Bi alloys normalized to the bulk density, $\rho_{Ga,bulk} = \rho_\infty$, at $T > T_w$: solid lines ordered in decreasing wetting film density: 228° C, 238° C and 258° C. Compare to the one-box density profile of Ga-Bi at 207° C (shaded line). . . . . 312

15.1 Bulk Phase diagram of Ga-Bi (Ref.[9]). Bold solid line: liquid-liquid coexistence, dashed line: liquid-liquid coexistence metastable, dotted line: liquid-solid coexistence. On the right: Schematic bulk behavior in the different temperature regimes. . . . . 320

15.2 (a) Fresnel normalized x-ray reflectivity $R/R_F$ from the surface of Ga-Bi: (diamonds) $T = 205°C$, (open circles) $T = 220°C$, (solid circles) $T = 222.5°C$. solid lines: fit to $R/R_F$ with density profiles depicted in Fig. 15.2(b). The arrow indicates the $q_z$-position for the temperature-dependent reflectivity measurements at fixed $q_z = 0.8\mathring{A}^{-1}$ (T-scan) shown in Fig. 15.3; (b): Electron density profiles for $T = 205°C$ (dotted line), $T = 220°C$ (dashed line) and $T = 222.5°C$ (solid line), normalized to the bulk electron density of the Ga-rich subphase. . . . 325

15.3 temperature-dependent x-ray reflectivity at $q_z = 0.8\mathring{A}^{-1}$ normalized to $R/R_F$ at $T = 222.5°C$. (squares) decreasing temperature, (triangles) increasing temperature. line: guide for the eye. . . . . 326

16.1 The atomic fraction ($c$)-temperature($T$) bulk phase diagram of Ga-Bi. The symbols indicate coexistence lines of Predel's phase diagram. The lines show the phase boundaries calculated from thermodynamic data. The dashed lines represent the metastable extension of the (l/l) coexistence line below $T_M$. The points are: C-bulk critical point, M-monotectic point, A,B,D,E-points on the experimental path. The insets illustrate the surface and bulk phases. In region II the wetting film is 50 $\mathring{A}$ thick and the Ga-rich fluid is 5 mm thick. The bold circles in the insets symbolize the Bi-monolayer. . . . . 333

16.2 **(a)** The chemical potential ($\mu$)-temperature ($T$) bulk phase diagram of Ga-Bi. The axes are temperature, $T$, the difference ($\mu_{Bi} - \mu_{Ga}$) of the chemical potentials of the single species, and their sum ($\mu_{Bi} + \mu_{Ga}$). The solid symbols indicate the following coexistence lines: (solid circles) liquid/liquid/vapor (l/l/v) triple line, (solid squares) solid/liquid/vapor (s/l/v) triple line, (small triangles) metastable extension of the liquid/liquid/vapor (l/l/v) triple line below $T_M$, (open circles) experimental path B-D probing complete wetting. The points are: C-bulk critical point, M-monotectic point, A,B,D,E-points on the experimental path. To illustrate the 3-dimensional structure of the phase diagram, a projection of the phase boundary lines on the ($\mu_{Bi} - \mu_{Ga}$,$T$) plane is drawn in the plot. The symbols surrounded by a circle show where the aforementioned characteristic points fall on this projection. **(b)**($\Delta\mu_m$,$T$) phase diagram: (A-M) is the (s/l/v), and (M-C) is the (l/l/v) coexistence line. The path B-D is in the single phase region, and M and C are the monotectic and critical points. Inset: effective wetting layer thickness $d$ on A→M (squares) and B→D (open circles). The solid line is a fit to the A→M $d$-values. **(c)** The measured $d$ along the experimental path. . . . . 336

16.3 (a) scattering geometry (b) Sketch of the experimental setup. The arrow close to the mounting indicates the variable position of the thermal shield in respect to the sample surface. . . . . 341

16.4 Illustration of the approximation of the analytic electron density profile (dashed line) by thin slabs in order to apply the Parratt formalism. Here, only the region close to the monolayer feature is depicted. . . . 344

16.5 **(a)** Normalized reflectivities $R/R_F$ for selected points D and B corresponding to $T_D$=255.0°C, $T_B$ = 240.4°C. Dashed lines indicate $R/R_F$ = 1. **(b)** $T$-dependent normalized reflectivities $R/R_F$ while approaching coexistence on path D →B along with fits. Dashed lines indicate $R/R_F = 1$.**(c)** Electron density profiles $\rho/\rho_{sub}$. All regions with $\rho/\rho_{sub} > 1$ indicating Bi-enrichment as compared with the Ga-rich subphase are gray shaded. . . . . 346

16.6 **(a)** T-dependent normalized reflectivities R/$R_F$ while leaving coexistence on path B →D along with fits. Dashed lines indicate $R/R_F = 1$. With increasing $T$, each $R/R_F$ is shifted by 1.2. **(b)** Electron density profiles $\rho/\rho_{sub}$. All regions with $\rho/\rho_{sub} > 1$ indicating Bi-enrichment as compared with the Ga-rich subphase are gray shaded. . . . . 349

16.7 **(a)** Calculated intrinsic profile $c(z)$ $(-)$ for $T = T_E = 225°C$, $t$ = 0.07 in comparison with the erf-function profile (dashed line): $c(z) = \frac{c^I+c^{II}}{2} + \frac{(c^{II}-c^I)}{2}$ erf $\left(\frac{z}{\sqrt{2}\sigma_{intr}(E)}\right)$ with $\sigma_{intr}(E) = 6.35$ $\mathring{A}$. **(b)** Calculated intrinsic concentration profiles $c(z)$ for selected temperatures $T$, reduced temperatures $t$ resp. as indicated in the figure. . . . . 358

16.8 Comparison of temperature dependent, measured interfacial width $\sigma$ (■) with calculated interfacial widths (lines): $\sigma_{calc} = \sqrt{\sigma_{intr}^2 + \sigma_{cap}^2}$ $(-)$ , intrinsic width $\sigma_{intr}$ $(\cdot-)$, and capillary width $\sigma_{cap}$ $(--)$. . . . . 359

16.9 Calculated (l/l) interfacial tension $\gamma_{ll}$ of Ga-Bi as a function of the reduced temperature $t$. The dashed line represents the TSFU prediction for Ga-Bi. The symbol $t_M$ indicates the monotectic temperature at $t_M$(Ga-Bi)= 0.08. . . . . 360

16.10 Calculated (l/l) interfacial tension $\gamma_{ll}$ of Ga-Pb as a function of the reduced temperature $t$. The solid points are our calculated values. The dashed line represents a fit to the measurements by Merkwitz et. al.. The symbol $t_M$ indicates the monotectic temperature at $t_M$(Ga-Pb)= 0.3. . . . . 362

# List of Tables


3.1 Comparison of candidates for Surface-induced layering study.[5,6,7,8,9] . 75

3.2 A listing of typical fitting parameters related to atomic layering model described here. Table (a) contains parameters describing the spectrometer geometry, table (b) lists parameters relevant to the studied material and table (c) includes parameters describing the density profile 78

12.1 Parameters for layered density profiles having the form given in Eq. 12.4.12, where $\sigma_n^2 = n\overline{\sigma}^2 + \sigma_T^2$ and $w_n = 1$ except as indicated in the table. Data for pure Hg, measured in the same UHV chamber, are from Ref. 12. For all fits, $d = 2.72 \pm 0.02$ Å. . . . . 275

13.1 Parameters used to calculate energy dependent x-ray reflectivity. . . 296

13.2 Fit parameters for model profiles, identified by the figure in which they appear. The length scales $d$, $\overline{\sigma}$, and $\sigma_0$ are in units of Å. . . . . 299

16.1 Material parameters of the coexisting liquid phases as calculated from the bulk phase diagram as well as electron density profiles as obtained from our fits to $R/R_F$ for selected temperatures $T$ along the on-coexistence path B→E. The atomic fraction of Ga in the coexisting Ga-rich, Bi-rich liquid phase are $c^I$, $c^I$ resp. The symbols $\rho/\rho_{sub}(calc)$, $\rho/\rho_{sub}(obs)$ denote the calculated, observed electron density ratios resp. 351

16.2 Redlich-Kister polynomials used to model the (l/l) miscibility gap of Ga-Bi. . . . . 372

# Acknowledgements

I would like to thank my thesis advisor, Professor Peter Pershan, for many suggestions and constant support and guidance during this research.

My research was done in collaboration with three postdoctoral fellows who contributed their knowledge and experience as well as provided guidance on many projects - Holger Tostmann, Patrick Huber and Alexei Grigoriev. All of us shared a lot of sleepless synchrotron night shifts together.

I would like to thank my fellow physics graduate student Masa Fukuto for being like a "big brother" to me during all these years. Special thanks go out to other members of our research group for their support and thoughtful discussions regarding our projects and physics in general - Konstantin Penanen, Ralf Heilmann, Oleg Gang, Yohko Yano, Christoph Steimer and Kyle Alvine.

I acknowledge the contributions from our collaborators Ben Ocko and Moshe Deutsch, as well as the beamline support at X22B and X25 beamlines at NSLS in Brookhaven National Lab and CMC-CAT and ChemMatCARS sectors at APS, Argonne National Lab. Specifically, I would like to mention Binhua Lin, Tim Graber, Jeff Gerbhardt, Mati Meron, Thomas Gog and Elaine DiMasi.

Over these years I had received a great deal of encouragement from my family - parents Nina and Grigory, my brother Igor and stepfather Vlad. I would also like to thank my physics schoolteacher Alexey Rozenwayn for igniting my interest in the wonderful world of science.

Cambridge, Massachusetts — Oleg Shpyrko
December, 2003

# Chapter 1

# Introduction

For many centuries metals have played a crucial role in history of civilization - from primitive tools of the Iron Age to the modern wonders of science and technology. With the sizes of high-tech device fabrication technology rapidly approaching the nanometer length scale frontier, the properties of the surface become of a great interest. As such the understanding of surface phenomena and the role surfaces of metals and alloys play in various processes such as mixing, alloying, refining, oxidation and wetting becomes increasingly important. The present thesis is therefore motivated by both the need to understand practical technological issues as well as the fundamental questions related to thermodynamics of the surfaces of liquid metals and their alloys.

For solid surfaces a number of local experimental techniques, such as atomic force microscopy (AFM) and scanning tunneling microscopy (STM) are widely available and can provide an atomic-size resolution information. In the past couple of years it was shown that these microscopy techniques could be applied to liquid systems, namely studies of wetting and capillarity[1,2,3]. However, the spatial resolution achieved in these studies was limited to nanometer length scales, which is not enough to resolve atomic structural features. Optical methods, such as ellipsometry[4], can be used to

obtain some structural data from the free surfaces of liquids, however they cannot provide any information about features much smaller than the wavelength of visible light. Techniques which use X-rays, on the other hand, make it possible to studying structural features of the surface which occur on the length scale of a few $\mathring{A}$. Advances in synchrotron radiation allow for these techniques to be applied to study the structural phenomena at the free surfaces of liquids. Over the past 20 years these methods has been applied to the study of a number of liquid systems, including measurements of the surface structure of liquid metals[5,6,7,8,9,10,11,12,13,14,15,16,17,18,19,20,21,22,23,24,25,26,27,28], superfluid helium[29,30,31,32,33,34], liquid crystals[35,36,37,38,39,40,41,42], water[36,39,43] and various other systems[41,44,45,46,47,48,49,50,51,52,53,54,55,56,57,58,59,60].

This work describes X-ray surface techniques that we have applied to studying surface phenomena such as surface-induced layering in metallic liquids, capillary wave excitations in both metallic and dielectric liquids, as well as critical wetting phenomena in binary metallic alloys.

## 1.1 Overview

This thesis is structured as follows:

Chapter 2 includes a discussion of the scientific background of various x-ray surface techniques used in this work, as well as the practical limitations of these methods as applied to studies of liquids in general and metallic liquids in particular.

Chapter 3 contains a brief review of some of the previous experiments which provide the groundwork for the measurements described in this thesis, mainly the studies of surface-induced layering in liquid Hg[7], Ga[8] and In[16].

Chapter 4 covers the temperature-dependent studies of surface-induced layering phenomena in liquid Hg. Liquid Hg is the first metal for which surface layering has been experimentally confirmed and this is the first experiment where we attempted to study the temperature-dependent behavior of the layering structure.

Chapter 5 reviews experimental studies of liquid In in more details. This is the first study where we have thoroughly examined the off-specular contributions from thermally excited capillary wave excitations and the validity of the capillary wave theory in application to metallic liquid surfaces.

Chapters 6 and 7 include a discussion of x-ray specular reflectivity and diffuse scattering measurements from the surface of liquid alkali metals. Chapter 6 deals with experimental results from binary sodium-potassium alloy, while Chapter 7 deals with studies of surface of pure potassium. These studies resolve a long-standing fundamental question of whether the surface-induced atomic layering is a result of high-surface tension acting as an effective hard wall potential. Unlike most high-surface tension metals studied so far, the relatively low surface tensions of the alkali metals are comparable to water and are not that much larger than some other dielectric liquids. Furthermore since their electronic properties are nearly-free electron like the relation between their structure and their electronic properties is more easily treated than for most other metals.

In view of the relatively low surface tension the surface roughness due to thermally excited capillary waves partially obscures the surface layering in alkali metals. Although this is somewhat similar to the Debye-Waller effect that is common in crystallography, the problem of thermal excitations on a two-dimensional surface is subtler. The procedures for extracting the surface structure from finite temperature

measurements will also be discussed in these Chapters.

Chapter 8 contains a discussion of x-ray specular reflectivity and diffuse scattering measurements from the surface of water. Water is one of the most basic substances known to mankind, and it is commonly used as a substrate in many structural measurements, such as self-assembled monolayers, while at the same time the $\mathring{A}$ level molecular structure of water surface is only partially known[61]. The new generation of synchrotron sources provides an opportunity to significantly improve our knowledge of the surface of water. X-ray surface studies of liquid potassium described in Chapter 7 demonstrated that by combining x-ray specular reflectivity and x-ray diffuse scattering it is possible to obtain structural information on the surface layering of liquids whose low surface tensions limit the reflectivity measurements to values of $q_z$ that are less than $2\pi$/layering distance. The experiments described in this section make use of the method described in Chapter 7 to confirm the absence of molecular layering at the free surface of water.

Chapter 9 deals with experimental studies of liquid Sn. Although liquid Sn does exhibit a strong layering peak that is similar to those observed in all of the other metals that have been studied, there is a secondary maximum in the reflectivity at low angles that was not observed in Ga[8], In[16] or K[27]. A somewhat similar feature was observed for liquid Hg[7]; however, in view of the high vapor pressure for Hg the possibility that this feature might have been due to an impurity was never excluded. In contrast the fact that liquid Sn was studied at a third generation synchrotron (APS) under UHV conditions allowed a combination of resonance scattering and x-ray fluorescence studies that absolutely exclude the possibility that the effect is associated with impurities. This feature is definitely an unexpected intrinsic property of the

surface of liquid Sn. The analysis to be presented in this chapter will demonstrate that the data is consistent with the existence of a high density atomic layer at the surface, which can be attributed to spacing for the uppermost layer at the surface.

Chapter 10 and Chapter 11 reviews x-ray reflectivity and diffuse scattering results for a number of binary alloys: Chapter 10 concentrates on GaBi, GaIn and HgAu, while Chapter 11 covers KNa, BiIn and GaBi alloys. In these chapters we address issues such as Gibbs adsorption, surface segregation, formation of surface phases and surface wetting.

Chapter 12 provides temperature dependent x-ray reflectivity measurements for mercury-gold alloy. Upon approaching the solubility limit of Au in Hg, a new surface phase forms which is 1–2 atomic diameters thick and has a density of about half that of bulk Hg. We present a surface phase diagram, summarizing the evolution of this unexpected surface structure through comparatively small changes in temperature and composition.

Chapter 13 describes resonant x-ray reflectivity measurements from the surface of liquid $Bi_{22}In_{78}$. In contrast to Gibbs adsorption of a complete monolayer observed in all liquid alloys studied to date we find only a modest surface Bi enhancement, with 35 at% Bi in the first atomic layer. This suggests that surface adsorption in Bi-In is dominated by attractive interactions that increase the number of Bi-In neighbors at the surface.

Chapters 14 through 16 contain a discussion of the results of an experimental study of tetra-point wetting on the free surface of binary alloy mixture of gallium and bismuth. Almost all experimental and theoretical studies describing wetting transition published to date address dielectric liquids in which the wetting is dominated by

long-ranged Van der Waals interactions[62]. The single exception is wetting near the bulk liquid/gas critical point for which the vanishingly small difference between the density of the liquid and the gas cause the amplitude of the long-range Van der Waals force to also become vanishingly small. In this case wetting should be dominated by short-range forces.[63,64]. In contrast, wetting in metallic liquids is naturally governed by short-range Coulomb screened potentials.

The measurements described in these chapters determined the microscopic (i.e. Ångström level) compositional gradient of the liquid/liquid interface between the wetting layer and the bulk liquid[65,66]. For this binary system, the wetting transition is pinned to a bulk monotectic temperature, creating a rare case of tetra point wetting, where four phases coexist in the bulk: a Ga-rich liquid, a Bi-rich liquid, a solid Bi, and a vapor[67,68].

In Chapter 16 the compositional gradient at the liquid/liquid interface is interpreted in terms of a mean-field square gradient model that was extended by inclusion of capillary waves as the dominant thermal fluctuations. This theory makes use of the influence parameter, $\kappa$, which governs the contribution of the concentration gradient to the surface energy. With this in hand, the liquid/liquid interfacial energy, which is very difficult to measure directly, was determined. With knowledge of the interfacial energy it was possible to separate the thermal capillary contributions from the intrinsic width of the liquid/liquid interface.

## 1.2 Citations to Previously Published Work

As is customary in physics department,the format of this thesis is introductory chapters followed by reprints of previously published papers. The references to the published materials are listed below: The overview presented in Chapter 3 is based on the following papers:

- H. Tostmann, E. DiMasi, P.S. Pershan, B.M. Ocko, O.G. Shpyrko and M. Deutsch, "Structure of Liquid Metals and the Effect of Capillary Waves: X-Ray Studies on Liquid Indium", *Phys. Rev. B* 59, 783 (1999)

- E. DiMasi, H. Tostmann, O. G. Shpyrko, M. Deutsch, P.S. Pershan and B.M. Ocko, "Surface Induced Order in Liquid Metals and Binary Alloy", *Journal of Physics: Condensed Matter* 12, 209 (2000) and

- E. DiMasi, O. M. Magnussen, B. M. Ocko, M. Deutsch, H. Tostmann, O. G. Shpyrko, M. J. Regan and P. S. Pershan "Temperature Dependent Surface Structure of Liquid Mercury" *Bull. Am. Phys. Soc.* 42, 310 (1997)

Chapter 4 is based on

- E. DiMasi, O. M. Magnussen, B. M. Ocko, M. Deutsch, H. Tostmann, O. G. Shpyrko, M. J. Regan and P. S. Pershan "Temperature Dependent Surface Structure of Liquid Mercury", *Bull. Am. Phys. Soc.* 42, 310 (1997)

Chapter 5 presents results published in

- H. Tostmann, E. DiMasi, P.S. Pershan, B.M. Ocko, O.G. Shpyrko and M. Deutsch, "Structure of Liquid Metals and the Effect of Capillary Waves: X-Ray Studies on Liquid Indium", *Phys. Rev. B* 59, 783 (1999)

Chapter 6 contains the results presented in a publication

- H. Tostmann, E. DiMasi, P.S. Pershan, B.M. Ocko, O.G. Shpyrko and M. Deutsch, "Microscopic Surface Structure of Liquid Alkali Metals", *Phys. Rev. B* 61 (1999) 7284

Chapter 7 is based on

- O.G. Shpyrko, P. Huber, P.S. Pershan, B.M. Ocko, H. Tostmann, A. Grigoriev and M. Deutsch, "X-ray Study of the Liquid Potassium Surface: Structure and Capillary Wave Excitations", *Phys. Rev. B* 67, 115405 (2003).

Chapter 8 is based on

- O.G. Shpyrko, M. Fukuto, P.S. Pershan, B.M. Ocko, I. Kuzmenko and M. Deutsch "Surface Layering of Liquids: The Role of Surface Tension", *Phys. Rev. B* 69 245423, (2004)

Chapter 9 is derived from two papers:

- O.G. Shpyrko, A. Grigoriev , C. Steimer, P.S. Pershan, B. Lin, T. Graber, J. Gerbhardt, M. Meron, B.M. Ocko and M. Deutsch "Anomalous Layering at the Liquid Sn Surface", *Phys. Rev. B*, 70, 224206 (2004)

- A. Grigoriev , O.G. Shpyrko, C. Steimer, P.S. Pershan, B. Lin, T. Graber, J. Gerbhardt, M. Meron, B.M. Ocko and M. Deutsch "Surface Oxidation of Liquid Tin", *Surf. Sci.* 575, 3, 223 (2005).

Chapters 10 and 11 presents reviews from

- H. Tostmann, E. DiMasi, O. G. Shpyrko, P. S. Pershan, B. M. Ocko and M. Deutsch, "Surface Phases in Binary Liquid Metal Alloys: an X-ray Study", *Ber. Bunsenges. Phys. Chem.* 102, 1136-1141 (1998)

and

- E. DiMasi, H. Tostmann, O. G. Shpyrko, M. Deutsch, P.S. Pershan and B.M. Ocko, "Surface Induced Order in Liquid Metals and Binary Alloy", *Journal of Physics: Condensed Matter* 12, 209 (2000)

Chapter 12 presents results from

- E. DiMasi, H. Tostmann, O. G. Shpyrko, M. Deutsch, P.S. Pershan and B.M. Ocko, "Resonant X-Ray Scattering from the Surface of a Dilute Hg-Au Alloy", *Materials Science V* Vol. 590. Eds. Mini, Perry and Stock. Materials Research Society (2000).

Chapter 13 contains measurements previously published in

- E. DiMasi, H. Tostmann, O. G. Shpyrko, M. Deutsch, P.S. Pershan and B.M. Ocko, "Pairing Interactions and Gibbs Adsorption at the Liquid Bi-In Surface: a Resonant X-ray Reflectivity Study", *Phys. Rev. Lett.* 86, 1538 (2001).

Chapters 14 through 16 include the measurements published in the following four papers:

- P. Huber, O.G. Shpyrko, P.S. Pershan, B.M. Ocko, E. DiMasi, M. Deutsch "Short-Range Wetting at Liquid Gallium-Bismuth Alloy Surfaces: X-ray Reflectivity Measurements and Square Gradient Theory", *Phys. Rev. B* 68, 085409 (2003)

- P. Huber, O.G. Shpyrko, P.S. Pershan, E. DiMasi, B.M. Ocko, H. Tostmann and M. Deutsch "Wetting at the Free Surface of a Liquid Gallium-Bismuth Alloy: An X-ray Reflectivity Study Close to the Bulk Monotectic Point", *Colloids & Surfaces A.* 206, 515 (2002)

- H. Tostmann, E. DiMasi, O.G. Shpyrko, P.S. Pershan, B.M. Ocko and M.Deutsch "Microscopic Structure of the Wetting Film at the Surface of Liquid Ga-Bi Alloys", *Phys. Rev. Lett.* 84 (2000) 4385

  and

- P. Huber, O.G. Shpyrko, P.S. Pershan, B.M. Ocko, E. DiMasi, and M. Deutsch "Tetra Point Wetting at the Free Surface of Liquid Ga-Bi", Phys. Rev. Lett. 89, 035502 (2002).

# Bibliography


[1] M. Salmeron. Scanning polarization force microscopy: A technique for studies of wetting phenomena at the nanometer scale. In *International Workshop on Wetting: From Microscopic Origins to Industrial Applications*, volume 56, page 63, Hyeres, France, 2000. Oil and Gas Science and Technology: Revue de l'Institut Francais du Petrole.

[2] M. Salmeron, editor. *Nanoscale wetting and de-wetting of lubricants with scanning polarization force microscopy.* Fundamentals of Tribology and Bridging the Gap Between the Macro- and Micro/Nanoscales, NATO ASI Series E: Applied Sciences. Kluwer Academic Publishers, The Netherlands, 2001.

[3] F. Mugele, T. Becker, R. Nikopoulos, M. Kohonen, and S. Herminghaus. *Journal of Adhesion Science and Technology*, 16:951, 2002.

[4] D. Nattland, S. C. Muller, P. D. Poh, and W. Freyland. Wetting phenomena at the liquid-vapor interface of gallium- bismuth alloys studied by spectroscopic ellipsometry. *J. Non-Cryst. Solids*, 207:772–775, 1996.

[5] E. B. Flom, M. Y. Li, A. Acero, N. Maskil, and S. A. Rice. Inplane structure of the liquid-vapor interface of an alloy - a grazing-incidence x-ray-diffraction study of bismuth gallium. *Science*, 260(5106):332–335, 1993.

[6] D. Sluis, M.P. D'Evelyn, and S.A. Rice. Experimental and theoretical studies of the density profile in the liquid-vapor interface of cs. *Journal of Chemical Physics*, 78(3):1611–13, 1983.

[7] O. M. Magnussen, B. M. Ocko, M. J. Regan, K. Penanen, P. S. Pershan, and M. Deutsch. X-ray reflectivity measurements of surface layering in liquid mercury. *Phys. Rev. Lett.*, 74(22):4444–4447, 1995.

[8] M.J. Regan, E.H. Kawamoto, S. Lee, P.S. Pershan, N. Maskil, M. Deutsch, O.M. Magnussen, B.M. Ocko, and L.E. Berman. Surface layering in liquid gallium: an x-ray reflectivity study. *Phys. Rev. Lett.*, 75(13):2498–501, 1995.

[9] M.J. Regan, O.M. Magnussen, E.H. Kawamoto, P.S. Pershan, B.M. Ocko, N. Maskil, M. Deutsch, S. Lee, K. Penanen, and L.E. Berman. X-ray studies of atomic layering at liquid metal surfaces. *J. Non-Cryst. Solids*, 205-207:762–6, 1996.

[10] N. Lei, Z. Q. Huang, and S. A. Rice. Surface segregation and layering in the liquid-vapor interface of a dilute bismuth:gallium alloy. *Journal of Chemical Physics*, 104(12):4802–4805, 1996.

[11] M.J. Regan, P.S. Pershan, O.M. Magnussen, B.M. Ocko, M. Deutsch, and L.E. Berman. X-ray reflectivity studies of liquid metal and alloy surfaces. *Physical Review B (Condensed Matter)*, 55(23):15874–84, 1997.

[12] M.J. Regan, H. Tostmann, P.S. Pershan, O.M. Magnussen, E. DiMasi, B.M. Ocko, and M. Deutsch. X-ray study of the oxidation of liquid-gallium surfaces. *Physical Review B (Condensed Matter)*, 55(16):10786–90, 1997.

[13] H. Tostmann, E. DiMasi, O. G. Shpyrko, P. S. Pershan, B. M. Ocko, and M. Deutsch. Surface phases in binary liquid metal alloys: An x-ray study. *Ber. Bunsen-Ges. Phys. Chem. Chem. Phys.*, 102(9):1136–1141, 1998.

[14] M. S. Zhao, D. Chekmarev, and S. A. Rice. Quantum monte carlo simulations of the structure in the liquid- vapor interface of BiGa binary alloys. *Journal of Chemical Physics*, 108(12):5055–5067, 1998.

[15] E. DiMasi, H. Tostmann, B. M. Ocko, P. S. Pershan, and M. Deutsch. X-ray reflectivity study of temperature-dependent surface layering in liquid Hg. *Phys. Rev. B*, 58(20):R13419–R13422, 1998.

[16] H. Tostmann, E. DiMasi, P. S. Pershan, B. M. Ocko, O. G. Shpyrko, and M. Deutsch. Surface structure of liquid metals and the effect of capillary waves: X-ray studies on liquid indium. *Phys. Rev. B*, 59(2):783–791, 1999.

[17] H. Tostmann, E. DiMasi, B.M. Ocko, M. Deutsch, and P.S. Pershan. X-ray studies of liquid metal surfaces. *J. Non-Cryst. Solids*, 250-252:182–90, 1999.

[18] E. DiMasi, H. Tostmann, B.M. Ocko, P.S. Pershan, and M. Deutsch. Competition between surface layering and surface phase formation in dilute liquid hg-au alloys. *Journal of Physical Chemistry B*, 103(45):9952–9, 1999.

[19] B. Yang, D. Gidalevitz, D. X. Li, Z. Q. Huang, and S. A. Rice. Two-dimensional freezing in the liquid-vapor interface of a dilute pb : Ga alloy. *Proceedings of the National Academy of Sciences of the United States of America*, 96(23):13009–13011, 1999.

[20] B. Yang, D. X. Li, Z. Q. Huang, and S. A. Rice. Structure of the liquid-vapor interface of a dilute alloy of pb in ga. *Phys. Rev. B*, 62(19):13111–13120, 2000.

[21] E. DiMasi, H. Tostmann, O.G. Shpyrko, M. Deutsch, P.S. Pershan, and B.M. Ocko. Surface-induced order in liquid metals and binary alloys. *Journal of Physics: Condensed Matter*, 12(8A):A209–14, 2000.

[22] H. Tostmann, E. DiMasi, P.S. Pershan, B.M. Ocko, O.G. Shpyrko, and M. Deutsch. Microscopic surface structure of liquid alkali metals. *Physical Review B (Condensed Matter)*, 61(11):7284–7, 2000.

[23] E. DiMasi, H. Tostmann, B.M. Ocko, P. Huber, O.G. Shpyrko, P.S. Pershan, M. Deutsch, and L.E. Berman. Resonant x-ray scattering from the surface of a dilute liquid hg-au alloy. In S.M.; Perry D.L. Stock, S.R.; Mini, editor, *Applications of Synchrotron Radiation Techniques to Materials Science V. Symposium*, pages 183–8, Warrendale, PA, USA Boston, MA, USA, 2000. Mater. Res. Soc.

[24] E. DiMasi, H. Tostmann, O. G. Shpyrko, P. Huber, B. M. Ocko, P. S. Pershan, M. Deutsch, and L. E. Berman. Pairing interactions and gibbs adsorption at the liquid bi-in surface: A resonant x-ray reflectivity study. *Phys. Rev. Lett.*, 86(8):1538–1541, 2001.

[25] P. Huber, O.G. Shpyrko, P.S. Pershan, B.M. Ocko, E. DiMasi, and M. Deutsch. Tetra point wetting at the free surface of liquid Ga-Bi. *Phys. Rev. Lett.*, 89(3):035502/1–4, 2002.

[26] P. Huber, O.G. Shpyrko, P.S. Pershan, H. Tostmann, E. DiMasi, B.M. Ocko, and M. Deutsch. Wetting behavior at the free surface of a liquid gallium-bismuth

alloy: an x-ray reflectivity study close to the bulk monotectic point. *Colloids and Surfaces A (Physicochemical and Engineering Aspects)*, 206(1-3):515–20, 2002.

[27] O. Shpyrko, P. Huber, A. Grigoriev, P. Pershan, B. Ocko, H. Tostmann, and M. Deutsch. X-ray study of the liquid potassium surface: structure and capillary wave excitations. *Physical Review B (Condensed Matter and Materials Physics)*, 67(11):115405–1–7, 2003.

[28] O.G. Shpyrko, A. Grigoriev, P.S. Pershan, C. Steimer, B.M. Ocko, M. Deutsch, B. Lin, M. Meron, T. Graber, and J. Gerbhardt. Surface structure of liquid tin: High-density packing of the top layer. *(in preparation)*, 2003.

[29] L.B. Lurio, T.A. Rabedeau, P.S. Pershan, and I.F. Silvera. X-ray specular reflectivity of the /sup 4/he liquid-vapor interface. *Physica B*, 169:507–8, 1991.

[30] L.B. Lurio, T.A. Rabedeau, P.S. Pershan, I.F. Silvera, M. Deutsch, S.D. Kosowsky, and B.M. Ocko. Liquid-vapor density profile of helium: an x-ray study. *Phys. Rev. Lett.*, 68(17):2628–31, 1992.

[31] L.B. Lurio, T.A. Rabedeau, P.S. Pershan, I.F. Silvera, M. Deutsch, S.D. Kosowsky, and B.M. Ocko. X-ray specular-reflectivity study of the liquid-vapor density profile of /sup 4/he. *Physical Review B (Condensed Matter)*, 48(13):9644–59, 1993.

[32] K. Penanen, P.S. Pershan, M.J. Regan, and I.F. Silvera. X-ray induced electrostatic charging of helium films. *Journal of Low Temperature Physics*, 101(3-4):489–94, 1995.

[33] K. Penanen, M. Fukuto, R.K. Heilmann, I.F. Silvera, and P.S. Pershan. /sup 4/he liquid-vapor interface below 1 k studied using x-ray reflectivity. *Physical Review B (Condensed Matter)*, 62(14):9621–40, 2000.

[34] K. Penanen, M. Fukuto, I.F. Silvera, and P.S. Pershan. X-ray-induced thinning of /sup 3/he and /sup 3/he//sup 4/he mixture films. *Physical Review B (Condensed Matter)*, 62(14):9641–7, 2000.

[35] P.S. Pershan, A. Braslau, A.H. Weiss, and J. Als-Nielsen. Smectic layering at the free surface of liquid crystals in the nematic phase: x-ray reflectivity. *Phys. Rev. A*, 35(4800), 1987.

[36] A. Braslau, M. Deutsch, P.S. Pershan, A.H. Weiss, J. Als-Nielsen, and J. Bohr. Surface roughness of water measured by x-ray reflectivity. *Phys. Rev. Lett.*, 54(2):114–17, 1985.

[37] B.M. Ocko, A. Braslau, P.S. Pershan, J. Als-Nielsen, and M. Deutsch. Quantized layer growth at liquid-crystal surfaces. *Phys. Rev. Lett.*, 57(1):94–7, 1986.

[38] G.J. Kellogg, P.S. Pershan, E.H. Kawamoto, W.F. Foster, M. Deutsch, and B.M. Ocko. X-ray reflectivity measurements and landau theory of smectic wetting in liquid crystal-benzyl alcohol mixtures. *Physical Review E (Statistical Physics, Plasmas, Fluids, and Related Interdisciplinary Topics)*, 51(5):4709–26, 1995.

[39] A. Braslau, P. S. Pershan, G. Swislow, B. M. Ocko, and J. Als-Nielsen. Capillary waves on the surface of simple liquids measured by x- ray reflectivity. *Phys. Rev. A*, 38(5):2457–2470, 1988.

[40] B.M. Ocko, P.S. Pershan, C.R. Safinya, and L.Y. Chiang. Incommensurate smectic order at the free surface in the nematic phase of 4-n-heptylphenyl-4'-(4"-nitrobenzoyloxy)benzoate (db7no/sub 2/). *Physical Review A (General Physics)*, 35(4):1868–72, 1987.

[41] G. Swislow, D. Schwartz, B.M. Ocko, P.S. Pershan, and J.D. Litster. X-ray studies of the surface and bulk structure of the isotropic and nematic phase of a lyotropic liquid crystal. *Physical Review A (Statistical Physics, Plasmas, Fluids, and Related Interdisciplinary Topics)*, 43(12):6815–25, 1991.

[42] R. Lucht, P. Marczuk, C. Bahr, and G. H. Findenegg. X-ray reflectivity study of smectic wetting and prewetting at the free surface of isotropic liquid crystals - art. no. 041704. *Phys. Rev. E*, 6304(4):1704–+, 2001.

[43] O.G. Shpyrko, M. Fukuto, B.M. Ocko, P.S. Pershan, and I. Kuzmenko. The surface of water: Absence of structure. *(in preparation)*, 2003.

[44] D.K. Schwartz, M.L. Schlossman, and P.S. Pershan. Re-entrant appearance of phases in a relaxed langmuir monolayer of tetracosanoic acid as determined by x-ray scattering. *Journal of Chemical Physics*, 96(3):2356–70, 1992.

[45] M.L. Schlossman, D.K. Schwartz, P.S. Pershan, E.H. Kawamoto, G.J. Kellogg, and S. Lee. Relaxation and the reentrant appearance of phases in a molecular monolayer. *Phys. Rev. Lett.*, 66(12):1599–602, 1991.

[46] M.L. Schlossman, D.K. Schwartz, E.H. Kawamoto, G.J. Kellogg, P.S. Pershan, M.W. Kim, and T.C. Chung. X-ray reflectivity of a polymer monolayer at the water/vapor interface. *J. Phys. Chem.*, 95(17):6628–32, 1991.

[47] G.M. Bommarito, W.J. Foster, P.S. Pershan, and M.L. Schlossman. A determination of the phase diagram of relaxed langmuir monolayers of behenic acid. *Journal of Chemical Physics*, 105(12):5265–84, 1996.

[48] M. Fukuto, K. Penanen, R.K. Heilmann, P.S. Pershan, and D. Vaknin. C/sub 60/-propylamine adduct monolayers at the gas/water interface: a brewster angle microscopy and x-ray scattering study. *Journal of Chemical Physics*, 107(14):5531–46, 1997.

[49] M. Fukuto, R.K. Heilmann, P.S. Pershan, J.A. Griffiths, S.M. Yu, and D.A. Tirrell. X-ray measurements of noncapillary spatial fluctuations from a liquid surface. *Phys. Rev. Lett.*, 81(16):3455–8, 1998.

[50] A. K. Doerr, M. Tolan, W. Prange, J. P. Schlomka, T. Seydel, W. Press, D. Smilgies, and B. Struth. Observation of capillary waves on liquid thin films from mesoscopic to atomic length scales. *Phys. Rev. Lett.*, 83(17):3470–3473, 1999.

[51] B. R. McClain, M. Yoon, J. D. Litster, and S. G. J. Mochrie. Interfacial roughness in a near-critical binary fluid mixture: X-ray reflectivity and near-specular diffuse scattering. *Eur. Phys. J. B*, 10(1):45–52, 1999.

[52] M. Fukuto, R.K. Heilmann, P.S. Pershan, S.M. Yu, J.A. Griffiths, and D.A. Tirrell. Structure of poly( gamma -benzyl-l-glutamate) monolayers at the gas-water interface: A brewster angle microscopy and x-ray scattering study. *Journal of Chemical Physics*, 111(21):9761–77, 1999.

[53] R. K. Heilmann, M. Fukuto, and P. S. Pershan. Quenching of capillary waves in

composite wetting films from a binary vapor: An x-ray reflectivity study - art. no. 205405. *Phys. Rev. B*, 6320(20):5405–+, 2001.

[54] R.K. Heilmann, M. Fukuto, and P.S. Pershan. Quenching of capillary waves in composite wetting films from a binary vapor: An x-ray reflectivity study. *Physical Review B (Condensed Matter and Materials Physics)*, 63(20):205405/1–16, 2001.

[55] W. Prange, T. Kurbjuhn, M. Tolan, and W. Press. The structure of hexane/perfluorohexane thin liquid films. *J. Phys.-Condes. Matter*, 13(21):4957–4972, 2001.

[56] D.M. Mitrinovic, S.M. Williams, and M.L. Schlossman. X-ray study of oil-microemulsion and oil-water interfaces in ternary amphiphilic systems. *Physical Review E (Statistical, Nonlinear, and Soft Matter Physics)*, 63(2):021601/1–11, 2001.

[57] M. Li, A. M. Tikhonov, D. J. Chaiko, and M. L. Schlossman. Coupled capillary wave fluctuations in thin aqueous films on an aqueous subphase. *Phys. Rev. Lett.*, 86(26):5934–5937, 2001.

[58] H. Kraack, B.M. Ocko, P.S. Pershan, E. Sloutskin, and M. Deutsch. Structure of a langmuir film on a liquid metal surface. *Science*, 298(5597):1404–7, 2002.

[59] M. Fukuto, R.K. Heilmann, P.S. Pershan, S.M. Yu, C.M. Soto, and D.A. Tirrell. Confinement-induced order of tethered alkyl chains at the water/vapor interface. *Physical Review E (Statistical, Nonlinear, and Soft Matter Physics)*, 66(1):010601/1–4, 2002.

[60] O. Gang, M. Fukuto, P. Huber, and P. Pershan. Wetting of hydrocarbon liquid surfaces by fluorocarbon vapor: a microscopic study. *Colloids and Surfaces A (Physicochemical and Engineering Aspects)*, 206(1-3):293–7, 2002.

[61] Q. Du, R. Superfine, E. Freysz, and Y. R. Shen. Vibrational spectroscopy of water at the vapor water interface. *Phys. Rev. Lett.*, 70(15):2313–2316, 1993.

[62] S. Dietrich. *Phase Trans. and Crit. Phen.*, volume 12. Acad. Press, NY, 1988.

[63] D. Ross, D. Bonn, and J. Meunier. Observation of short-range critical wetting. *Nature*, 400(6746):737–739, 1999.

[64] D. Ross, D. Bonn, A. I. Posazhennikova, J. O. Indekeu, and J. Meunier. Crossover from first-order to critical wetting: Short-range tricritical wetting. *Phys. Rev. Lett.*, 8717(17), 2001.

[65] C. Ebner and W. F. Saam. New phase-transition phenomena in thin argon films. *Phys. Rev. Lett.*, 38(25):1486–1489, 1977.

[66] H. T. Davis. *Statistical Mechanics of Phases, Interfaces, and Thin Films*. Wiley-VCH, New York, 1996.

[67] S. Dietrich and M. Schick. Wetting at a solid-liquid-liquid-vapor tetra point. *Surf. Sci.*, 382(1-3):178–181, 1997.

[68] C. Serre, P. Wynblatt, and D. Chatain. Study of a wetting-related adsorption transition in the ga-pb system: 1. surface energy measurements of ga-rich liquids. *Surf. Sci.*, 415(3):336–345, 1998.

# Chapter 2

# Theoretical and Experimental Overview

## 2.1 X-rays

The x-ray portion of the electromagnetic spectrum is generally taken to encompass wavelengths from $10^{-12}$ to $10^{-8}$ meters (0.01 to 100 $\mathring{A}$). Early in the 20th century Laue and Knipping[1,2] made use of the fact typical atomic and molecular scales are of the order of 1 to 10 $\mathring{A}$ to demonstrate the first x-ray diffraction pattern from a single crystal. Ever since then x-rays have naturally become one of the principal tools for studying atomic and molecular structures.

## 2.2 Index of Reflection

When Roentgen discovered X-rays in 1895, he immediately searched for a means to focus them[3,4]. On the basis of slight refraction in prisms he stated that the index of refraction of X-rays in materials cannot be much more than n = 1.05 if it differed at all from unity. Twenty years layer, Einstein proposed[5] that the refractive index for X-rays was $n = 1 - \delta$ where $\delta \approx 10^{-6}$, allowing for total external reflection at grazing

incidence angles. A simple classical model in which an electron of the material is considered to be accelerated by the electromagnetic field generated by x-rays shows that the complex dielectric constant $\varepsilon$ can be described as:

$$\epsilon = 1 - \frac{4\pi\rho Z e^2}{m\omega^2}\left(1 + \frac{i}{\mu\omega}\right) \tag{2.2.1}$$

where $\rho$ is the electron density of the material, $\omega$ is the frequency of the electromagnetic field, $\mu$ is the absorption length, $e$ is the electron charge, $m$ is the electron mass and Z is the atomic number of the element. The results of a more accurate quantum mechanical treatment are qualitatively similar:

$$n = \sqrt{\epsilon} = 1 - \delta + i\zeta \tag{2.2.2}$$

where the real and imaginary parts of the index of refraction, $\delta$ and $\zeta$, account for the and absorption of material, respectively. They are defined as:

$$\delta = \frac{r_e}{2\pi}\lambda^2 \sum_k \frac{Z_k + f'_k}{V_m} \tag{2.2.3}$$

and

$$\zeta = \frac{r_e}{2\pi}\lambda^2 \sum_k \frac{f''_k}{V_m} = \frac{\lambda}{4\pi}\mu \tag{2.2.4}$$

where $r_e = 2.813 \cdot 10^{-5}$ $\mathring{A}$ is the classical radius of the electron, $V_m$ is the volume of the unit cell, $Z_k$ is the number of electrons of atom $k$ in the unit cell, $f'$ and $f$" are the anomalous scattering coefficients [1], and $\lambda$ is the x-ray wavelength. If the x-ray wavelength $\lambda$ is low in comparison with the principal absorption energies, $f'_k \approx 0$ and $\delta \approx r_e\lambda^2\rho/(2\pi)$.

[1]For the relatively small angular range of the x-ray reflectivity measurements described in this thesis the angular dependence of the atomic form factor can be neglected.

## 2.3 Critical Angle of Reflection

In view of the fact that $\delta$ is positive, the refractive index of a material is always smaller than unity[6]. X-rays incident on the material surface from the vacuum will be refracted towards the surface. If the incident angle (measured from the surface) is less than a *critical angle* $\alpha_c$ that is given by:

$$\cos(\alpha_c) = n = 1 - \delta \tag{2.3.1}$$

the x-rays will be totally reflected. Since $1 \gg \delta > 0$ the expression for critical angle can be approximated as:[7]

$$\alpha_c^2 = 2\delta = \frac{r_e \lambda^2}{\pi} \rho \tag{2.3.2}$$

## 2.4 X-Ray Surface Techniques: Overview

Three major surface X-ray techniques are commonly used throughout the measurements described in this thesis - namely, X-ray specular reflectivity, X-ray diffuse scattering and X-ray grazing incidence diffraction. Each technique will be described in detail below. In the case of binary systems each of these techniques can be enhanced by tuning the x-ray energy through the absorption edge of one, or another of the elements. In this way the relative scattering amplitudes of individual elements can be changed by factors that are sometimes as large as a factor of two. In this thesis we have applied these resonance effects to specular reflectivity measurements. In addition, observation of characteristic x-ray fluorescence as a function of excitation energy can be used as a separate method for testing for the presence of different elements.

## 2.5 Reflectivity

### 2.5.1 Kinematics of Reflectivity Measurement

In order to introduce these x-ray techniques consider a simple case of a monochromatic x-ray beam with wavelength $\lambda$ reflected from a smooth, ideally flat and abruptly terminated (that is, having step-function-like density profile at the material-vapor interface) planar surface. Figure 2.1 provides a general description of kinematics for all of the x-ray surface techniques described in this work. For any incident angle $\alpha$ there will be a specular reflection observed at a detection angle $\beta = \alpha, \Delta\Theta = 0$, both incident and reflected beams located in the same (specular) plane perpendicular to the surface plane. This type of reflection will be referred to as *specular*. Later in this thesis we will discuss off specular scattering for which the detector is located out of the plane of incidence ($\Delta\Theta \neq 0$) and/or with $\beta \neq \alpha$. Conventional measurements of x-ray reflectivity from solid surfaces commonly make use of what is known as $\Theta - 2\Theta$ instruments in which the sample is rotated by an angle $\Theta$ while the detector is rotated by twice that, or $2\Theta$ in order to keep the incident angle $\alpha$ equal to the angle $\beta$. This is not possible for liquid surfaces and the X-ray reflectivity experiments described in this thesis require simultaneous scanning both the incident angle $\alpha$ and output angle $\beta$, while keeping $\beta = \alpha$, in the specular plane geometrically defined as $\Delta\Theta = 0$.

## 2.6 Ideal Surface: Fresnel Reflectivity

The intensity of the reflected specular signal from an ideal flat surface can be calculated by considering the usual boundary conditions for electromagnetic waves. The result is what is known as *Fresnel relationship*, which gives the amplitude of specular

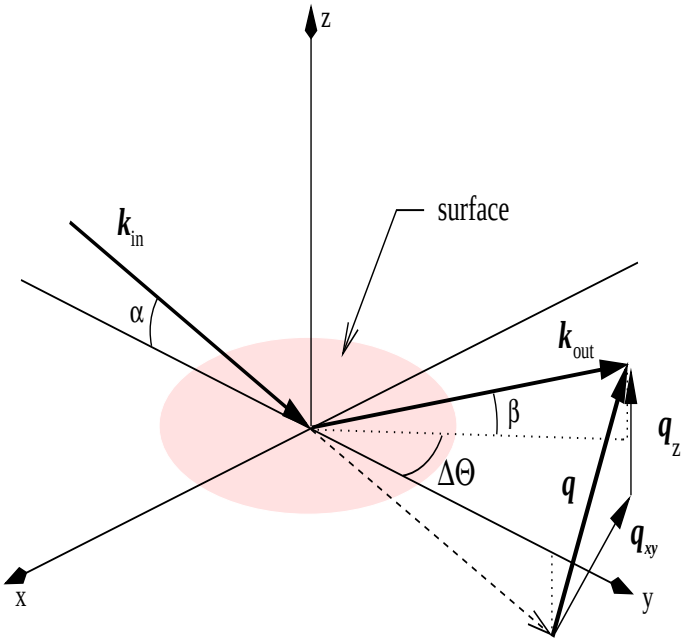



Figure 2.1: Kinematics of the x-ray measurement.

reflection for both s- and p-polarized waves as a function of incident angle $\alpha$. The reflectivity, defined as a ratio of the reflected beam intensity $I_r$ to the intensity of the direct beam $I_0$: $R_F(\alpha) = I_r(\alpha)/I_0$, is the modulus square of this amplitude. For small angles the Fresnel reflectivity is independent of the polarization[8]:

$$R_F(\alpha) = \left| \frac{sin\alpha - \sqrt{sin^2\alpha - sin^2\alpha_c - 2i\zeta}}{sin\alpha + \sqrt{sin^2\alpha - sin^2\alpha_c - 2i\zeta}} \right|^2 \tag{2.6.1}$$

Equation 2.6.1 can also be rewritten as a function of the vertical component of wavevector transfer, $q_z$ (for $\alpha = \beta$ and $\Theta = 0$, $\vec{q} = (0, 0, q_z)$)

$$R_F(q_z) = \left| \frac{q_z - \sqrt{{q_z}^2 - {q_c}^2 - 32i\pi^2\zeta/\lambda^2}}{q_z + \sqrt{{q_z}^2 - {q_c}^2 - 32i\pi^2\zeta/\lambda^2}} \right|^2 \tag{2.6.2}$$

where $q_z$ is defined as:

$$q_z = \frac{2\pi}{\lambda}(\sin\alpha + \sin\beta) \tag{2.6.3}$$

or, since $\alpha = \beta$

$$q_z = \frac{4\pi}{\lambda}\sin\alpha \tag{2.6.4}$$

If dispersion effects are neglected, i.e. if $f_k' \approx 0$, the critical wavevector can be written as

$$q_c = \frac{4\pi \sin\alpha_c}{\lambda} \approx 4\sqrt{\pi r_e \rho} \quad ^{2} \tag{2.6.5}$$

For large values of $q_z$, Fresnel reflectivity asymptotically approaches

$$R(q_z) = \left(\frac{q_c}{2q_z}\right)^4 \tag{2.6.6}$$

## 2.7 Reflectivity from a Structured Surface

### 2.7.1 Born Approximation vs. Dynamic Parratt Formalism

The kinematical theory or first Born approximation greatly simplifies the expression for the intensity of specular reflectivity for non-ideal surfaces that are either rough or have structure. The basic assumption of the Born approximation is that the amplitude of the transmitted wave is taken equal to that of the incident wave[8,9,10]. This amounts to neglecting refraction effects. The assumption is applicable for $q_z \gtrsim 5q_c$. In view of the fact that most of the interesting features to be discussed in this thesis occur for $q_z \gg q_c$, the majority of results will be analyzed using the Born approximation. The studies of tetra-point wetting in the binary GaBi alloy that will be discussed

[2]Note that unlike $\alpha_c$, $q_c$ is independent of $\lambda$, which is a reason why reflectivity is commonly expressed as a function of wavevector transfer component $q_z$ rather than incident angle $\alpha$.

in Chapter 7 involve features at values of $q_z \approx q_c$, and for these we will find it necessary to make use of the interactive matrix formalism developed by *Parratt*[11], which takes into account the refraction, or multiple scattering, that is neglected by Born approximation. For the first six chapters of this work we will limit ourselves with the simpler Born approximation result.

### 2.7.2 Master Formula

Within the first Born approximation, the x-ray reflectivity signal is a direct measure of the average electron density of the sample perpendicular to the surface normal $z$, $\rho(z)$. More specifically, the ratio of the x-ray reflectivity to the Fresnel reflectivity will deviate from unity by the absolute value of the square of amplitude of a *surface structure factor* $\Phi(q_z)$, that is defined as the Fourier transform of the derivative of the in-plane average of the electron density along the surface normal[12]:

$$\Phi(q_z) = \frac{1}{\rho_\infty} \int dz \frac{\langle d\rho(z) \rangle}{dz} \exp(\imath q_z z) \tag{2.7.1}$$

where $\rho_\infty$ is taken to be the electron density of the bulk. The reflectivity from a surface with structure is thus given by

$$R(q_z) = R_F(q_z) \cdot \left| \Phi(q_z) \right|^2 \tag{2.7.2}$$

The equations 2.7.1 and 2.7.2 are known as a *Master formula*[13].

## 2.8 Form Factor: Examples

In this section we will illustrate the application of Eq. 2.7.1 with a few heuristic examples of density profiles that are relevant to the measurements that are discussed later in this thesis.

### 2.8.1 Ideally sharp flat surface

An ideally flat surface in which the electron density transition from the bulk to the vacuum is abrupt can be represented by a density profile along the surface normal $\rho(z)$ which has a shape of a step function:

$$\frac{\langle\rho(z)\rangle}{\rho(\infty)} = \begin{cases} 1 & \text{if } x \geqslant 0; \\ 0 & \text{if } x < 0. \end{cases} \tag{2.8.1}$$

This corresponds to a $\delta$-function density derivative:

$$\frac{d}{dz}\left(\frac{\langle\rho(z)\rangle}{\rho(\infty)}\right) = \delta(z)$$

and according to Eq. 2.7.1, results in a structure factor

$$\left|\Phi(q_z)\right| = 1 \tag{2.8.2}$$

As should be expected, the predicted reflectivity from ideally flat surfaces follows Fresnel law.

### 2.8.2 Flat surface with a gradual interfacial profile

For an interface in which density profile undergoes a monotonic gradual transition from vacuum to bulk can be characterized by an error-function of width $\sigma$:

$$\frac{\langle\rho(z)\rangle}{\rho(\infty)} = \mathrm{erf}\left(\frac{z}{\sigma\sqrt{2}}\right) \tag{2.8.3}$$

The derivative of such an error function is the gaussian of width $\sigma$,

$$\frac{d}{dz}\left(\frac{\langle\rho(z)\rangle}{\rho(\infty)}\right) = \frac{1}{\sigma\sqrt{2\pi}} e^{-\frac{x^2}{2\sigma^2}} \tag{2.8.4}$$

and according to Eq. 2.7.1,

$$\Phi(q_z) = e^{-{q_z}^2\sigma^2/2} \tag{2.8.5}$$

It follows that

$$R(q_z) = R_F(q_z) \cdot \left|\Phi(q_z)\right|^2 = R_F(q_z)e^{-{q_z}^2\sigma^2} \tag{2.8.6}$$

Figure 2.2 (A) shows the two density profiles described so far along with the corresponding forms for $R(q_z)/R_F(q_z)$. In these plots the red line represents the density profile and $R(q_z)/R_F(q_z)$ of for the ideal abrupt surface. The blue lines illustrate the roughened density profile and reflectivity for the gradual interface.

### 2.8.3 Crystalline and Quasi-Crystalline Model

A slightly more complicated case is the surface structure factor from a periodic lattice of a finite-size crystal that terminates at atomic planes. If the atomic form factors are neglected the density profile perpendicular to the surface can be modeled by a series of N $\delta$-functions ($N \gg 1$) located at $z = d$, $2d$, $3d$, ... , $nd$, ... $Nd$, where d is the lattice spacing parameter. This model can be quantitatively described by a density function $\langle\rho(z)\rangle$:

$$\frac{\langle\rho(z)\rangle}{\rho(\infty)} = d\sum_{n=1}^{N}\delta(z-nd) \tag{2.8.7}$$

Applying this to Eq. 2.7.1 the structure factor becomes

$$\begin{aligned}\left|\Phi(q_z)\right| = q_z d\left|\int_{-\infty}^{\infty} dz \sum_{n=1}^{N}\delta(z-nd)\exp(\imath q_z z)\right| = \\ = q_z d\left|\sum_{n=1}^{N} e^{\imath q_z nd}\right| = q_z d\frac{\sin(\frac{Nq_z d}{2})}{\sin(\frac{q_z d}{2})}\end{aligned} \tag{2.8.8}$$

The function $q_z d\sin(Nq_z d/2)/\sin(q_z d/2)$ has sharp peaks at $q_z d = 2\pi$, $4\pi$, $6\pi$, etc. that are associated with constructive interference from planes with lattice spacing $d$

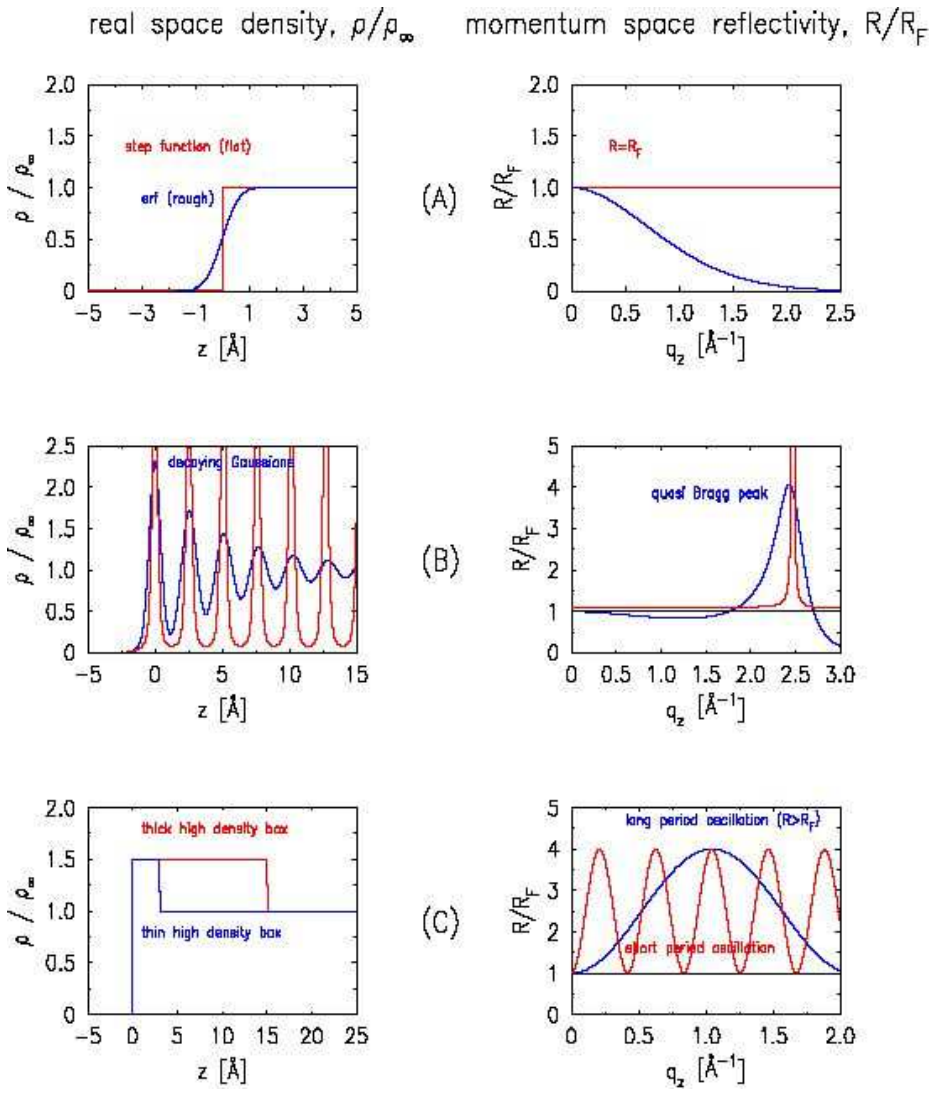



Figure 2.2: Density profiles $\rho(z)/\rho_\infty(z)$ and respective reflectivity curves $R(q_z)/R_F(q_z)$ for a smooth and roughened surfaces (A), crystalline and layering structure (B) and thin/thick high-density layers (C)

that are just the Bragg reflections from an array of parallel planes. For the finite N the scattering amplitude of these peaks increase and the widths decrease as the number of atomic layers N is increased[3];

The crystalline density model is illustrated in Figure 2.2 (B) for $N = 50$. The density profile (box on the left) drawn with a red line describes a set of well-defined atomic layers, and corresponds to the Bragg-like peak in the momentum reflectivity space (box on the right). The blue line in Figure 2.2 (B) corresponds to a model for surface induced atomic layering of the electron density that decays with distance from the surface. Details for this model which was first introduced to discuss the surface of liquid Hg will be discussed later in this thesis. In view of the fact that the layering is limited to just a few atomic layers at the surface, the surface structure peak associated with this density profile that is shown by the blue line in the box on the right is broader and less pronounced, than that of the crystal model shown by the red line. Such layering peak is commonly referred to as *quasi*-Bragg peak.

### 2.8.4 High-density surface layer

The final model to be discussed (Figure 2.2 (C)) is constructed with a surface slab whose electron density is higher than that of the bulk liquid. In this heuristic model atomic layering is neglected. The simplest mathematical representation of this is what is commonly referred to as a *two-box model*, a higher-density box of width $d$ and density $\rho_\infty(1 + A)$, built on top of a semi-infinite box of lower density $\rho_\infty$ described by a step-function:

[3]Even for an infinitely large N, the reflectivity corresponds to a finite number of layers typically determined among other things by the finite value of absorption length and energy bandwidth

$$\frac{\langle\rho(z)\rangle}{\rho(\infty)} = \begin{cases} 0 & \text{if } x < 0; \\ 1 + A & \text{if } 0 \leqslant x < d; \\ 1 & \text{if } d \leqslant x. \end{cases} \tag{2.8.9}$$

The derivative to this density profile consists of two $\delta$-functions, one located at $z = 0$ with amplitude of (1+A), and another one at $z = d$ with amplitude of $-A$:

$$\frac{d}{dz}\left(\frac{\langle\rho(z)\rangle}{\rho(\infty)}\right) = (1 + A)\delta(z) - A\delta(z - d) \tag{2.8.10}$$

$$\left|\Phi(q_z)\right| = \left|1 + A - Ae^{\imath q_z d}\right| \tag{2.8.11}$$

The resulting Fresnel-normalized reflectivity $R(q_z)/R_F(q_z)$ is an oscillatory function with a period of $2\pi/d$, maximum value of 1+2A and a minimum value of unity. These oscillations are commonly referred to in a literature as *Kiessig fringes*[14].

This density model is illustrated in Figure 2.2 (C) for A=0.5. Two profiles are shown - one with a thinner high density box and another one with a thicker density box. The thicker layer produces more frequent oscillations, as is expected since the period of oscillations $2\pi/d$ is inversely proportional to the thickness of the layer. In this model the density oscillates between values of 1 and $(1 + 2A)^2 = 4$. For both of these models the widths of the two interfaces have been neglected. For real surfaces with finite widths there are two effects. If the widths of the two interfaces are widely disparate, the amplitude of the oscillations decays as $q_z$ exceeds the reciprocal of the broader width and the reflectivity reaches a plateau of either $A^2$ or $(1 + A)^2$, depending on which of the two interfaces has the narrower width. Eventually as $q_z$ exceeds the narrower width the average reflectivity decreases. If both widths are comparable the oscillations and average reflectivity decay proportionally. As will be

shown later, systems studied in this thesis can be represented by a combination of the simple density models discussed above.

## 2.9 Thermal Capillary Wave Fluctuations

### 2.9.1 Solids vs. Liquids

The model surfaces that have been discussed in Section 2.8 tacitly assumed that the surface was perfectly flat. For some crystal surfaces this could be a reasonable approximation since the constraints on atomic positions that are associated with the crystalline structure keep the surface flat on atomic scale. Although surface roughness that is associated with miscuts, atomic steps and other similar defects gives rise to off specular diffuse scattering that reduces the intensity of the specular peak, this scattering is often weak. In addition the reciprocal of the correlation lengths that are associated with these defects are usually much broader than the spectrometer resolution. As a result for solid surfaces it is usually relatively easy to separate the specular reflectivity peak from the diffuse scattering. This is different in liquids for which the gravity determined length scale for roughness associated with thermally capillary waves is typically of the order of a millimeter. Since the reciprocal of this length is smaller than the spectrometer resolution, a major fraction of the intensity that is measured at the specular condition is due to diffuse scattering from thermal capillary waves.

### 2.9.2 Off-specular diffuse scattering

The manner in which surface roughness gives rise to off-specular diffuse scattering is best discussed in terms of differential cross section $d\sigma/d\Omega$. The geometry for

consideration of diffuse scattering is illustrated in Figure 2.1.The x-rays are incident at an angle $\alpha$ and collected by the detector at an elevation angle $\beta$ and azimuthal angle $\Delta\Theta$. The momentum transfer $\vec{q}$ can be decomposed into surface normal, $q_z$, and surface parallel, $q_{xy}$, components given by:

$$q_z = \frac{2\pi}{\lambda}(\sin\beta + \sin\alpha) \qquad \text{and} \qquad q_{xy} = \frac{2\pi}{\lambda}\sqrt{\cos^2\alpha + \cos^2\beta - 2\cos\alpha\cos\beta\cos\Delta\Theta}\,. \tag{2.9.1}$$

The general expression for the differential cross section for x-ray scattering from a three dimensional electron distribution $\rho(\vec{r})$ at a given location $\vec{r}$ can be expressed in terms of the electron density correlation function $\langle\rho(\vec{r})\rho(\vec{r\prime})\rangle = \langle\rho(\vec{r}-\vec{r\prime})\rho(0)\rangle$:[15]

$$\frac{d\sigma}{d\Omega} = V\left(\frac{e^2}{mc^2}\right)^2 \int d^3(\vec{r}-\vec{r\prime})\langle\rho(\vec{r}-\vec{r\prime})\rho(0)\rangle \exp\left[\imath\vec{q}\cdot(\vec{r}-\vec{r\prime})\right] \tag{2.9.2}$$

where $V$ is the illuminated volume. If the density distribution is homogeneous within the $x$-$y$ plane but inhomogeneous normal to the surface, the density correlation function depends on the relative distance $\vec{r}_{xy}-\vec{r}_{xy\prime}$ parallel to the surface and the distances $z$ and $z\prime$ from the surface. For an x-ray beam of a cross sectional area $A_0$ incident on the surface at an angle $\alpha$ relative to the $x$-$y$ plane, the illuminated area is $A_0/\sin(\alpha)$ and the differential cross section can be written as a half-space integral:[12]

$$\frac{d\sigma}{d\Omega} = \frac{A_0}{\sin(\alpha)}\left(\frac{e^2}{mc^2}\right)^2 \int_{z\geqslant 0} dz dz\prime d^2\vec{r}_{xy}\langle\rho(\vec{r}_{xy},z)\rho(0,z\prime)\rangle \exp\left[\imath q_z(z-z\prime) + \imath\vec{q}_{xy}\cdot\vec{r}_{xy}\right]. \tag{2.9.3}$$

The problem of converting this expression to a form that explicitly addresses surface capillary waves is that it is difficult to separate sort distance surface fluctuations from fluctuations within the bulk. Mecke and Dietrich[16] discuss this from a formal

theoretical perspective. From a somewhat more empirical point of view it is reasonable to consider defining a local average such as

$$\langle \rho(\vec{r}_{xy}, z) \rangle_\xi = \frac{1}{A_\xi} \int_{A_\xi} d^2\vec{r}'_{xy} \rho(\vec{r}_{xy} - \vec{r}'_{xy}, z) \tag{2.9.4}$$

where $A_\xi$ is an area in the xy plane with dimensions of the order of the bulk correlation length $\xi$. For non-critical liquids most of the capillary excitations are at wavelengths that are much larger than $\xi$ and $\langle \rho(\vec{r}_{xy}, z) \rangle_\xi$ is basically an average over all of the atomic scale fluctuations. Far from the surface it is just equal to the bulk electron density. A reasonable approximation in the hydrodynamic limit of long wavelength capillary waves is to assume that the dependence of $\langle \rho(\vec{r}_{xy}, z) \rangle_\xi$ on the z-coordinate is just a single local function of the distance from the position of the average surface, $h(\vec{r}_{xy})$:

$$\langle \rho(\vec{r}_{xy}, z) \rangle_\xi \approx \rho(z - h[\vec{r}_{xy}]) \tag{2.9.5}$$

Making this assumption

$$\rho(\vec{r}_{xy}, z) = \langle \rho(\vec{r}_{xy}, z) \rangle_\xi + \delta\rho(\vec{r}_{xy}, z) \tag{2.9.6}$$

where $\delta\rho(\vec{r}_{xy}, z)$ represents atomic scale fluctuations about the local average and

$$\langle \rho(\vec{r}_{xy}, z)\rho(0, z') \rangle_\xi = \rho(z - h[\vec{r}_{xy}])\rho(z - h[0]) + \langle \delta\rho(\vec{r}_{xy}, z)\delta\rho(0, z') \rangle \tag{2.9.7}$$

The approximation that we make in analyzing the effects of capillary fluctuations is to set

$$\langle \rho(\vec{r}_{xy}, z)\rho(0, z') \rangle = \langle \rho(\vec{r}_{xy}, z)\rho(0, z') \rangle_\xi \tag{2.9.8}$$

for all length scales with $|\vec{r}_{xy}| \gg \xi$. In fact, as we will see below the integrated physical effects associated with capillary waves only vary logarithmically with the smallest distance, or largest capillary wavevector. As a result the error in assuming that this is valid down to atomic length scales is minor. With this substitution

$$\frac{d\sigma}{d\Omega} = \frac{A_0}{\sin\alpha}\left(\frac{e^2}{mc^2}\right)^2 \int dz dz' d\vec{r}_{xy} \langle \exp[iq_z(z-z') + i\vec{q}_{xy}\cdot\vec{r}_{xy}]\rangle \times \\ \times\left\{\rho(z-h[\vec{r}_{xy}])\rho(z-h[0]) + \langle\delta\rho(\vec{r}_{xy},z)\delta\rho(0,z')\rangle\right\} \tag{2.9.9}$$

The second term in the integrand, which is only non-vanishing for regions $|\vec{r}_{xy}| \leqslant \xi$, gives rise to both the bulk diffuse scattering and surface scattering at momentum transfers with large $q_{xy}$[12]. Daillant et al.[17,18] discussed some of the problems that need to be addressed in order to try to separate surface and bulk scattering in this large $q_{xy}$ region. In any event, for discussion of diffuse scattering close to the specular condition $q_{xy} \ll 1/\xi$ and this term is not important and will be omitted. A change of variables yields

$$\frac{d\sigma}{d\Omega} \approx \frac{1}{16\pi^2}\left(\frac{q_c}{2}\right)^4 \frac{A_0}{\sin(\alpha)} \frac{|\Phi(q_z)|^2}{q_z^2} \int_{|\vec{r}_{xy}|>\xi} d^2\vec{r}_{xy} \langle \exp\{\imath q_z[h(\vec{r}_{xy}) - h(0)]\}\rangle \exp[\imath\vec{q}_{xy}\cdot\vec{r}_{xy}] \tag{2.9.10}$$

where the average appearing in Eq. 2.9.10 is the normal statistical average of the thermal height-height fluctuations. The quantity $q_c$ is the critical angle for total external reflection of x-rays. The structure factor $\Phi(q_z)$ previously described in Eq. 2.7.1 needs to be redefined with respect to the height fluctuations at the surface, $h(\vec{r}_{xy})$:

$$\Phi(q_z) \equiv \int dz \frac{\partial\left\langle\rho(\vec{r}_{xy},z)\right\rangle_\xi}{\partial z} \exp[iq_z(z - h(\vec{r}_{xy}))] = \int dz \frac{\partial\rho(z-h(\vec{r}_{xy}))}{\partial z} \exp[iq_z(z - h(\vec{r}_{xy}))] \tag{2.9.11}$$

For the case of thermally excited capillary waves on a liquid surface, the height fluctuations can be characterized by their statistical average[12]

$$\langle [h(\vec{r}_{xy}) - h(0)]^2 \rangle = \int_{|\vec{r}_{xy}|>\xi} d^2\vec{r}_{xy} \langle \exp\{\imath q_z [h(\vec{r}_{xy}) - h(0)]\} \rangle \exp[\imath \vec{q}_{xy} \cdot \vec{r}_{xy}] \quad (2.9.12)$$

Sinha et al.[19] have shown that integration over these height fluctuations yields the following dependence of the scattering on $q_{xy}$ and $q_z$:

$$\int_{|\vec{r}_{xy}|>\xi} d^2\vec{r}_{xy} \exp\left\{ \frac{q_z^2}{2} \left\langle [h(\vec{r}_{xy}) - h(0)]^2 \right\rangle \right\} \exp[\imath \vec{q}_{xy} \cdot \vec{r}_{xy}] = \frac{C}{q_{xy}^{2-\eta}} \quad (2.9.13)$$

where

$$\eta = \frac{k_B T}{2\pi\gamma} q_z^2 \quad (2.9.14)$$

and the value of $C$ can be determined with an approximate sum rule[20] that is obtained by integration over all surface capillary modes having wavevectors smaller than the upper wavevector cutoff $q_{max} \equiv \pi/\xi$:

$$\begin{aligned} C &= \int_{|\vec{q}_{xy}|<\pi/\xi} d^2\vec{q}_{xy} \int_{|\vec{r}_{xy}|>\xi} d^2\vec{r}_{xy} \left\langle \exp\{\imath q_z [h(\vec{r}_{xy}) - h(0)]\} \right\rangle \exp[\imath \vec{q}_{xy} \cdot \vec{r}_{xy}] \\ &= \int_{|\vec{q}_{xy}|<\pi/\xi} d^2\vec{q}_{xy} \int_{|\vec{r}_{xy}|>\xi} d^2\vec{r}_{xy} \exp\left\{ -\frac{q_z^2}{2} \langle [h(\vec{r}_{xy}) - h(0)]^2 \rangle \right\} \exp[\imath \vec{q}_{xy} \cdot \vec{r}_{xy}] \\ &= 4\pi^2 \lim_{\vec{r}_{xy}\to 0} \left[ \exp\left\{ -\frac{q_z^2}{2} \langle [h(\vec{r}_{xy}) - h(0)]^2 \rangle \right\} \right] = 4\pi^2 \end{aligned} \quad (2.9.15)$$

Therefore, the properly normalized differential cross section for scattering of x-rays from a liquid surface is:

$$\frac{d\sigma}{d\Omega} = \frac{A_0}{\sin\alpha} \left(\frac{q_c}{2}\right)^4 \frac{k_B T}{16\pi^2\gamma} |\Phi(q_z)|^2 \frac{1}{q_{xy}^2} \left(\frac{q_{xy}}{q_{\max}}\right)^{\eta}. \quad (2.9.16)$$

### 2.9.3 Specular Reflectivity and Local Density Profile

The intensity measured at a specific scattering vector $\vec{q}$ is obtained by integrating Eq. 2.9.16 over the solid angle $d\Omega$ defined by the detector acceptance of the experiment:

$$\frac{I}{I_0} = \int_{res} \frac{d\sigma}{d\Omega} = \frac{A_0}{\sin\alpha}\left(\frac{q_c}{2}\right)^4 \frac{k_B T}{16\pi^2\gamma}\left|\Phi(q_z)\right|^2 \int_{res} \frac{1}{q_{xy}^2}\left(\frac{q_{xy}}{q_{\max}}\right)^{\eta}. \tag{2.9.17}$$

For the specular reflection $\alpha = \beta$ and $\Theta = 0$ and the integral is centered at $q_{xy} = 0$. The projection of the detector resolution onto the $x$-$y$ plane is typically rectangular[12] and the above mentioned integration has to be done numerically. On the other hand a heuristically useful approximate analytical formula can be obtained for the specular reflectivity if the projection of detector resolution on liquid surface is assumed to be a circle of radius $q_{res}$[21]. In that case, integral over the circular resolution function defined as $|q_{xy}| < q_{res}$ can be easily calculated in polar coordinates:

$$\begin{aligned}\int_{res} \frac{1}{q_{xy}^2}\left(\frac{q_{xy}}{q_{\max}}\right)^{\eta} d^2 q_{xy} &= \left(\frac{1}{q_{\max}}\right)^{\eta} \int_{q_r}\int_{\phi} \frac{1}{q_r^{2-\eta}} q_r dq_r d\phi = \\ &= \frac{2\pi}{{q_{\max}}^{\eta}} \int_{q_r} \frac{1}{q_r^{1-\eta}} dq_r d\phi = \frac{2\pi}{{q_{\max}}^{\eta}} \frac{q_r^{\eta}}{\eta}\Big|_0^{q_{res}} = \frac{2\pi}{\eta}\left(\frac{q_{res}}{q_{\max}}\right)^{\eta}\end{aligned} \tag{2.9.18}$$

Substituting Eq. 2.9.18 into Eq. 2.9.16 results in:

$$\frac{R(q_z)}{R_F(q_z)} = \left|\Phi(q_z)\right|^2 \left(\frac{q_{\rm res}}{q_{\max}}\right)^{\eta} = \left|\Phi(q_z)\right|^2 \exp[-\sigma_{\rm cw}^2 q_z^2] \tag{2.9.19}$$

where $\Phi(q_z)$ is the local structure factor defined in Eq. 2.9.11, $R_F(q_z)$ is the Fresnel reflectivity from classical optics for a flat ($h(\vec{r}_{xy}) = h(0)$ for all $h(\vec{r}_{xy})$) and structureless ($|\Phi(q_z)|^2 = 1$) surface, defined in Eq. 2.6.2. The quantity $\sigma_{\rm cw}$ denotes an effective capillary wave roughness:

$$\sigma_{\rm cw}^2 = \frac{k_B T}{2\pi\gamma} \ln\left(\frac{q_{\rm res}}{q_{\max}}\right). \tag{2.9.20}$$

that increases with increasing $q_z$.

The implication of this is that a true specular reflection can not be properly defined for liquid surfaces. In fact it follows from Eq. 2.9.18 that the value of the signal that is measured at the specular condition ($\alpha = \beta, \Delta\Theta = 0$) depends on the resolution function[22]. One implication of the above analysis is that for a liquid surface there is not the same type of true specular reflectivity as would be obtained for a flat solid surface. For example, for a flat solid surface

$$\lim_{\vec{r}_{xy}\to 0} \langle [h(\vec{r}_{xy}) - h(0)]^2 \rangle \to 2\langle h[0]^2 \rangle \tag{2.9.21}$$

and one term in the integral of the Eq. 2.9.13 will be proportional to $\delta^2(q_{xy})$, which is just the specular signal. The signal observed at the specular signal that is dominated by this delta functions is not sensitive to the angular acceptance of the resolution function. In contrast the signal predicted from Eq. 14.4.1 from a liquid surface will generally depend on the resolution function. For small $\eta$, corresponding to small $q_z$ the dependence is weak and the specular reflectivity from the liquid surface is not very different from that of the signal due to the $\delta$-function of the solid surface; however, as $q_z$ and $\eta$ increase and, as demonstrated by Schwartz et al.[22] for the surface of water, the magnitude of the specular signal is dependent on the resolution. In fact, for $\eta \to 2$ the peak in intensity at the specular condition vanishes and at these angles there is no operational way to distinguish surface scattering from scattering that arises from the bulk. In view of the fact that $\eta \sim 1/\gamma$ this can be a problem for studies of low-surface tension systems, such as alkali metals and dielectric liquids.

Historically the reflectivity from liquid surfaces was originally discussed solely in terms of the Master formulae 2.7.1 and 2.7.2; however as shown by this discussion the

ratio of $R(q_z)$ to $R_F(q_z)$ depends on both an intrinsic structure factor and a thermal term that is not quite identical to the Debye-Waller factor used for solid surfaces. Nevertheless it is often convenient to define a quantity that we will refer to as the thermal structure factor:

$$\langle|\Phi(q_z)|^2\rangle_T = \frac{R(q_z)}{R_F(q_z)} \tag{2.9.22}$$

that corresponds to a macroscopically averaged, or *thermal* density profile $\langle\rho(z)\rangle_T$ which includes thermal fluctuations and is related directly to the measured reflectivity $R(q_z)$:

$$\frac{1}{\rho_\infty}\int dz \frac{\langle\rho(z)\rangle_T}{dz}\exp(\imath q_z z) = \frac{R(q_z)}{R_F(q_z)} \tag{2.9.23}$$

This macroscopically averaged thermal density profile, $\langle\rho(z)\rangle_T$, can be shown[23] to be the result of the convolution of the intrinsic density profile defined earlier in Eq. 2.9.5 for $h(x,y) = 0$, with the associated Gaussian distribution of thermal height fluctuations characterized by capillary roughness $\sigma_{cw}$.

Figure 2.3 illustrates the difference between the intrinsic density profile and its thermally roughened density profile equivalent for liquid gallium at room temperature: the solid line shows the intrinsic density profile extracted from experimental reflectivity data of liquid gallium by fitting it to atomic layering density model and taking into account the thermal fluctuations at the surface. The dashed line represents the thermally averaged density profile that is obtained from the best fit of Eq. 2.9.23 to the measured reflectivity at T=22°C.

As will be shown in Chapter 3, this intrinsic density profile for gallium has been found to be independent of temperature and resolution, while the thermal density

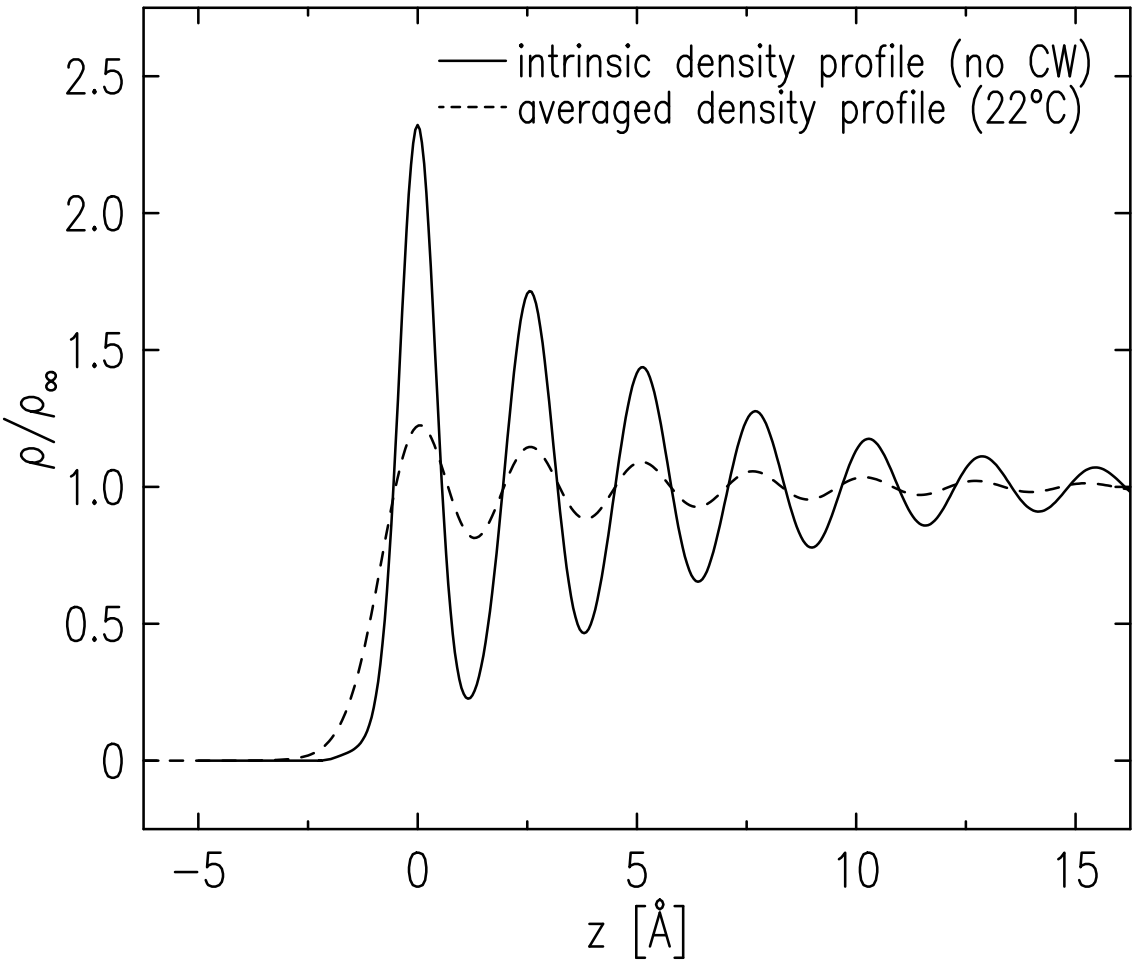



Figure 2.3: The difference between intrinsic and thermal profile, an example taken from experimental studies of liquid Gallium at room temperature.

profile which is essentially a local density profile convolved with thermal capillary excitations, does depend strongly on both the temperature and resolution effects.

### 2.9.4 Integration of the Resolution Function

The problem of calculating the effect of the resolution on the contributions of capillary excitations to the observed signal is to carry out an integration of the singular function ${1/q_{xy}}^{2-\eta}$ over a two-dimensional space defined by the detector resolution parameters. Although not impossible, the procedures that must be followed to carry out a 2D numerical integration over the region that encompasses a singularity slows down the integrations considerably. We circumvented this problem by analytically integrating the non-singular $q_r^{2-\eta} q_r dq_r$, where $q_r = \sqrt{q_x^2 + q_y^2}$ and only then doing a digital integral over the azimuthal angle $\phi$, taking $\phi = \arctan(q_y/q_x)$. The resultant integral that must be done numerically has the form:

$$\int_{res} \frac{1}{q_{xy}^2} \left( \frac{q_{xy}}{q_{\max}} \right)^{\eta} d^2 q_{xy} = \oint_{res} \frac{1}{q_r^2} \left( \frac{q_r}{q_{\max}} \right)^{\eta} q_r dq_r d\phi = \frac{1}{\eta} \oint_{\phi} \left( \frac{q_{res}(\phi)}{q_{\max}} \right)^{\eta} d\phi \quad (2.9.24)$$

where the piecewise continuous function $q_{res}(\phi)$ is defined by the border of the projection of the resolution function on the x-y plane of the liquid surface. With the singularity removed it is straightforward to carry out the one-dimensional integration over the variable $\phi$.

The practical situation corresponds to a rectangularly shaped detector resolution that is defined by pairs of horizontal and vertical slits. A pair of vertical slits with an opening of 2V and horizontal slits with an opening of 2H would accept scattering angles ranging from $\beta - \Delta\beta$ to $\beta + \Delta\beta$ vertically and $\Theta - \Delta\Theta$ to $\Theta + \Delta\Theta$ horizontally, where $\Delta\beta$ and $\Delta\Theta$ are defined in low angle approximation ($\Delta\beta$, $\Delta\Theta \ll 1$) as

$$\begin{aligned} \Delta\beta &= \tfrac{V}{L} \\ \Delta\Theta &= \tfrac{H}{L} \end{aligned} \tag{2.9.25}$$

The quantity L is the distance from the center of the sample to the position of the detector slits.

According to 2.9.1, the projection of resolution function in $q_{xy}$ space is the rectangle of the size $2Q_x$ by $2Q_y$, where

$$\begin{aligned} Q_x &= \tfrac{2\pi}{\lambda}\Delta\Theta\cos\beta = \tfrac{2\pi}{\lambda}\tfrac{H}{L}\cos\beta \\ Q_y &= \tfrac{2\pi}{\lambda}\sin\beta\Delta\beta = \tfrac{2\pi}{\lambda}\tfrac{V}{L}\sin\beta \end{aligned} \tag{2.9.26}$$

We assume that the detector accepts all radiation for which $q_{xy}$ falls within this rectangular shape and rejects all that falls outside. A representation of such rectangular resolution function $\Xi(q_x, q_y)$ with the detector slits centered at an arbitrary position $(q_{x0}, q_{y0})$ is:

$$\Xi(q_x, q_y) = \begin{cases} 1 & \text{if } |q_x - q_{x0}| \leqslant Q_x \\ 0 & \text{if } Q_x < |q_x - q_{x0}| \\ 1 & \text{if } |q_y - q_{y0}| \leqslant Q_y \\ 0 & \text{if } Q_y < |q_y - q_{y0}| \end{cases} \tag{2.9.27}$$

For the spectrometer either centered at the specular, or close to it $q_{res}(\phi)$ defines a rectangle that encloses the specular position, $q_{xy} = 0$. For the spectrometer at an off specular position the situation is slightly more complicated.

Consider the first case when $|q_{x0}| < Q_x$ and $|q_{y0}| < Q_y$, which implies that the singularity is located inside the resolution function. The diagram describing the resolution function integration procedure in this case is shown in Figure 2.4. Point O corresponds to a singularity located at $q_x = q_y = 0$. The center of the rectangular resolution box is $(q_{x0}, q_{y0})$. We designate the corners of the rectangle as $A_1, A_2, A_3$ and $A_4$. The points $B_{12}, B_{23}, B_{34}$ and $B_{41}$ are defined by the perpendicular projections

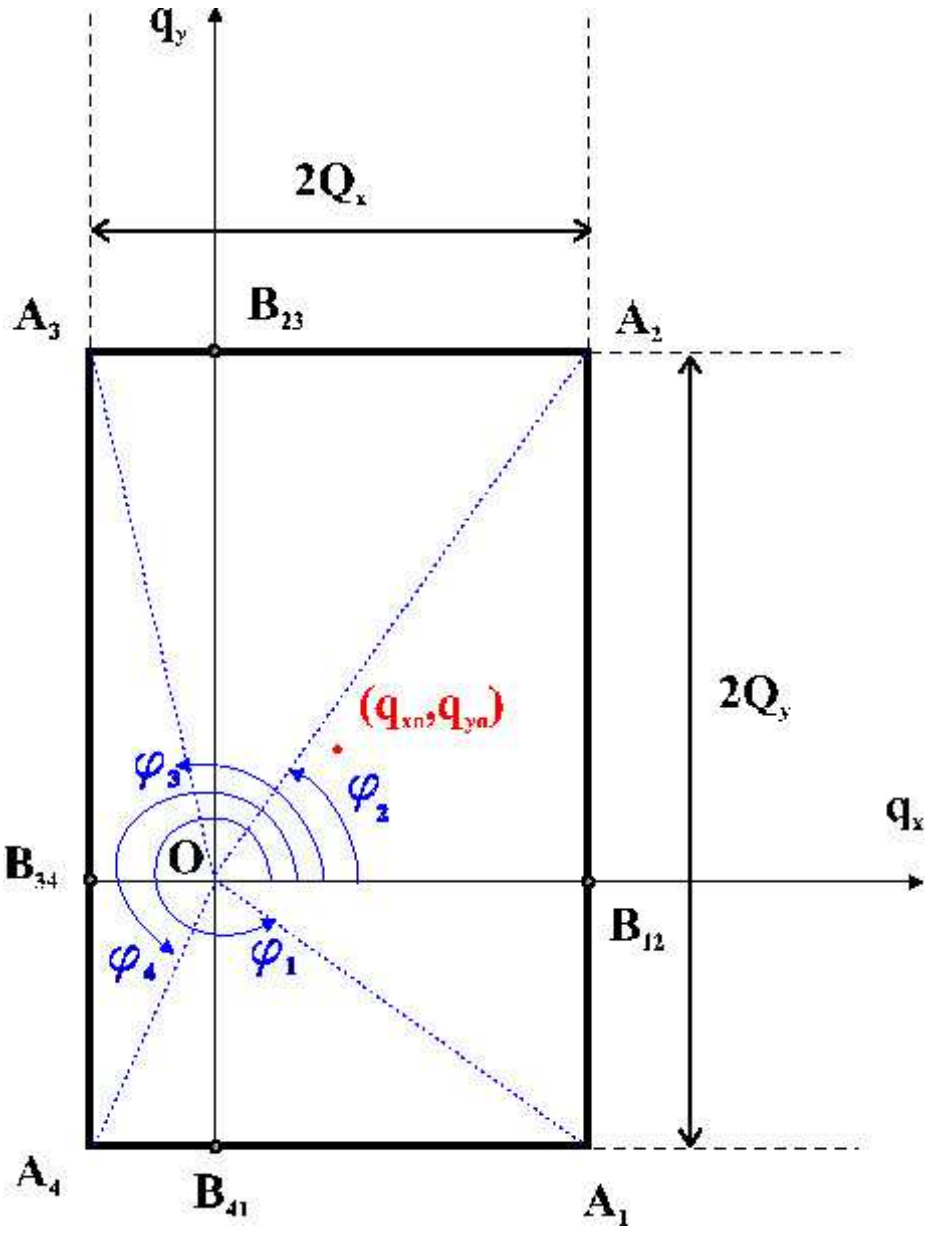



Figure 2.4: The schematic describing the integration of capillary wave contributions over the rectangular resolution function in $q_{xy}$ space, for the case when the singularity O is located *inside* the resolution volume.

$OB_{12}, OB_{23}, OB_{34}$ and $OB_{41}$. Additionally, we define the angles that are formed by the lines $OA_1, OA_2, OA_3$ and $OA_4$ relative to the $q_x$ axis as $\phi_1, \phi_2, \phi_3$ and $\phi_4$ respectively. From basic geometry,

$$\begin{aligned} OB_{12} &= Q_x + q_{x0} \\ OB_{23} &= Q_y + q_{y0} \\ OB_{34} &= Q_x - q_{x0} \\ OB_{41} &= Q_y - q_{y0} \end{aligned} \tag{2.9.28}$$

$$\begin{aligned} \phi_1 &= 2\pi - \arctan(\tfrac{OB_{41}}{OB_{12}}) = 2\pi - \arctan(\tfrac{Q_y - q_{y0}}{Q_x + q_{x0}}) \\ \phi_2 &= \arctan(\tfrac{OB_{23}}{OB_{12}}) = \arctan(\tfrac{Q_y + q_{y0}}{Q_x + q_{x0}}) \\ \phi_3 &= \pi - \arctan(\tfrac{OB_{23}}{OB_{34}}) = \pi - \arctan(\tfrac{Q_y + q_{y0}}{Q_x - q_{x0}}) \\ \phi_4 &= \pi + \arctan(\tfrac{OB_{41}}{OB_{34}}) = \pi + \arctan(\tfrac{Q_y - q_{y0}}{Q_x - q_{x0}}) \end{aligned} \tag{2.9.29}$$

Note that $\arctan(x)$ is defined for the region $-\frac{\pi}{2} < x \leq \frac{\pi}{2}$. Then $q_{res}(\phi)$ described in 2.9.24 can be written as:

$$q_{res}(\phi) = \begin{cases} \frac{OB_{12}}{\cos\phi} & \text{if } \phi_1 < \phi \leqslant \phi_2 \\ \frac{OB_{23}}{\sin\phi} & \text{if } \phi_2 < \phi \leqslant \phi_3 \\ -\frac{OB_{34}}{\cos\phi} & \text{if } \phi_3 < \phi \leqslant \phi_4 \\ -\frac{OB_{41}}{\sin\phi} & \text{if } \phi_4 < \phi \leqslant \phi_1 \end{cases} \tag{2.9.30}$$

The negative signs on the third and fourth line are necessary because the $\cos(\phi)$ and $\sin(\phi)$ are negative for the relevant angles. Equation 2.9.24 can be rewritten as

$$\begin{aligned} &\oint_{res} \tfrac{1}{q_{xy}^2} \left(\tfrac{q_{xy}}{q\max}\right)^\eta d^2 q_{xy} = \tfrac{1}{\eta} \oint_\phi \left(\tfrac{q_{res}(\phi)}{q\max}\right)^\eta d\phi = \\ &= (\eta q_{\max}^\eta)^{-1} \left[ \int_{\phi_1 - 2\pi}^{\phi_2} \left(\tfrac{Q_x + q_{x0}}{\cos\phi}\right)^\eta d\phi + \int_{\phi_2}^{\phi_3} \left(\tfrac{Q_y + q_{y0}}{\sin\phi}\right)^\eta d\phi + \int_{\phi_3}^{\phi_4} \left(\tfrac{Q_x - q_{x0}}{-\cos\phi}\right)^\eta d\phi + \int_{\phi_4}^{\phi_1} \left(\tfrac{Q_y + q_{y0}}{-\sin\phi}\right)^\eta d\phi \right] \end{aligned} \tag{2.9.31}$$

A similar treatment can be applied for the case when the singularity is outside of the rectangular resolution box. One example of this is illustrated schematically

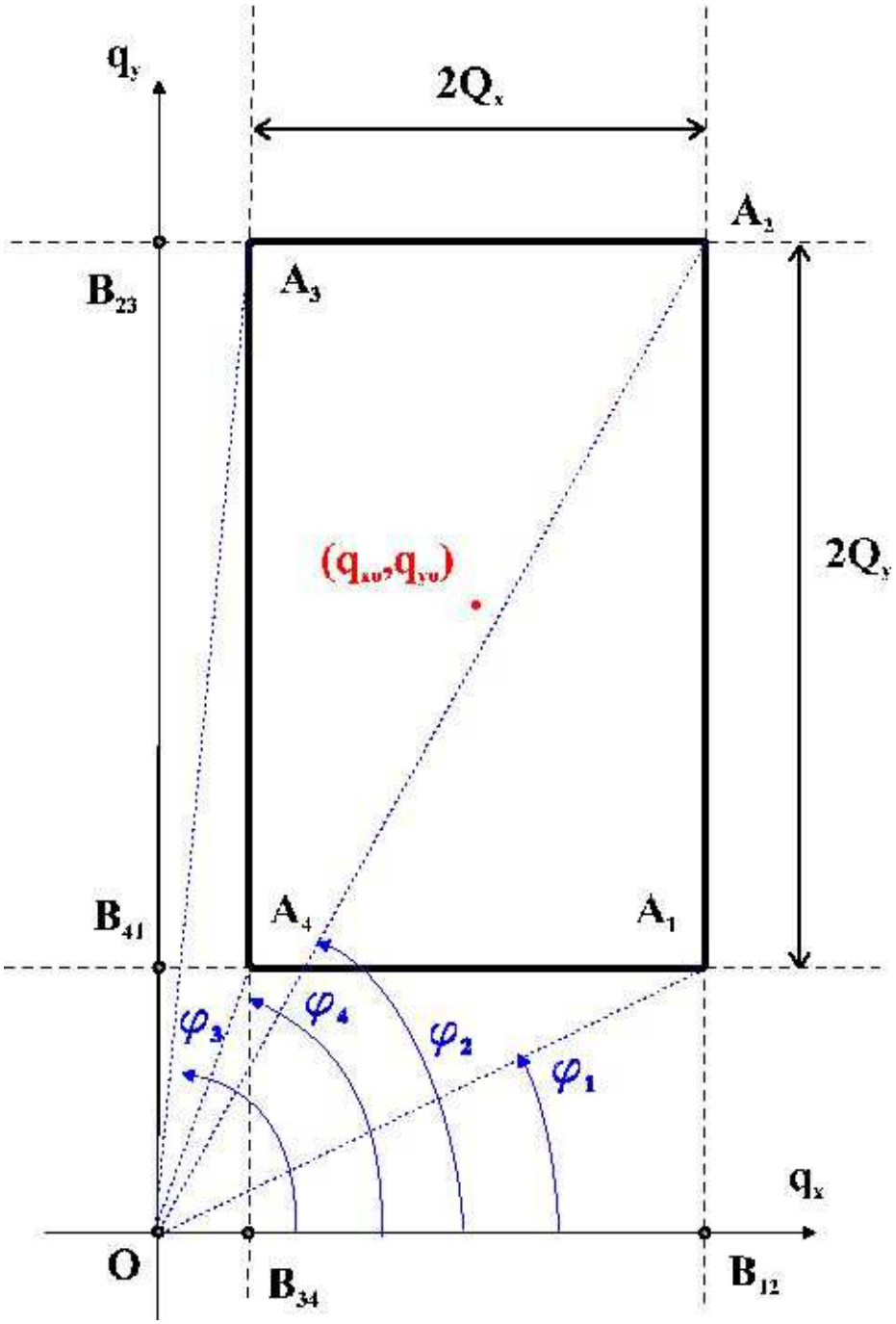



Figure 2.5: A schematic describing the procedure integration of capillary wave contributions over the rectangular resolution function in $q_{xy}$-space for the case when the singularity O is located *outside* of the resolution volume.

by Figure 2.4. In this case the projections $OB_{12}, OB_{23}, OB_{34}$ and $OB_{41}$, as well as corresponding angles $\phi_1, \phi_2, \phi_3$ and $\phi_4$ can be defined in a similar way:

$$\begin{aligned} OB_{12} &= q_{x0} + Q_x \\ OB_{23} &= q_{y0} + Q_y \\ OB_{34} &= q_{x0} - Q_x \\ OB_{41} &= q_{y0} - Q_y \end{aligned} \tag{2.9.32}$$

and

$$\begin{aligned} \phi_1 &= \arctan(\tfrac{OB_{41}}{OB_{12}}) = \arctan(\tfrac{q_{y0}-Q_y}{q_{x0}+Q_x}) \\ \phi_2 &= \arctan(\tfrac{OB_{23}}{OB_{12}}) = \arctan(\tfrac{q_{y0}+Q_y}{q_{x0}+Q_x}) \\ \phi_3 &= \arctan(\tfrac{OB_{23}}{OB_{34}}) = \arctan(\tfrac{q_{y0}+Q_y}{q_{x0}-Q_x}) \\ \phi_4 &= \arctan(\tfrac{OB_{41}}{OB_{34}}) = \arctan(\tfrac{q_{y0}-Q_y}{q_{x0}-Q_x}) \end{aligned} \tag{2.9.33}$$

For the geometry illustrated in Figure 2.5 the final integral is:

$$\begin{aligned} &\oint_{res} \tfrac{1}{q_{xy}^2} \left(\tfrac{q_{xy}}{q\max}\right)^{\eta} d^2 q_{xy} = \tfrac{1}{\eta} \oint_{\phi} \left(\tfrac{q_{res}(\phi)}{q\max}\right)^{\eta} d\phi = \\ &= (\eta q_{\max}^{\eta})^{-1} \left[ \int_{\phi_1}^{\phi_2} \left(\tfrac{q_{x0}+Q_x}{\cos\phi}\right)^{\eta} d\phi + \int_{\phi_2}^{\phi_3} \left(\tfrac{q_{y0}+Q_y}{\sin\phi}\right)^{\eta} d\phi - \int_{\phi_4}^{\phi_3} \left(\tfrac{q_{x0}-Q_x}{\cos\phi}\right)^{\eta} d\phi - \int_{\phi_1}^{\phi_4} \left(\tfrac{q_{y0}-Q_y}{\sin\phi}\right)^{\eta} d\phi \right] \end{aligned} \tag{2.9.34}$$

Note that if the spectrometer is sufficiently far off of the specular condition $q_{x0} \pm Q_x$ and/or $q_{y0} \pm Qy$ can be negative. Nevertheless this form for the resolution integration is valid.

## 2.10 Experimental Details

In this section we will discuss a number of practical considerations in performing x-ray measurements on liquid surfaces.

### 2.10.1 Synchrotron Radiation Sources

A study of surface layering requires a reflectivity measurement out to the values of vertical component that are at least of the order of wavevector transfer for which the

layering peak maximum is expected, $q_z^{peak} = \pi/a$,[24] where $a$ is the atomic radius. For liquid metals $a$ is typically on the order of $1.0-1.5$ $\mathring{A}$,[25] making $q_z^{peak} \approx 2.0-3.0$ $\mathring{A}^{-1}$. If we neglect the reflectivity enhancement due to the layering and consider just the Fresnel reflectivity $R(q_z) \approx (q_c/2q_z)^4$ (Eq. 2.6.6). For liquid metals, typical value of critical wavevector $q_c$ is on the order of 0.05 $\mathring{A}^{-1}$. Therefore Fresnel reflectivity at $q_z = q_z^{peak} \approx 2.5$ $\mathring{A}^{-1}$ and $R_F(q_z^{peak}) = (q_c/2q_z^{peak})^4 \approx 10^{-7}$. The effect of thermally excited capillary wave fluctuations reflectivity is to reduce the reflectivity by an additional Debye-Waller-like factor: $DW = \exp(-\sigma_{cw}^2(q_z^{peak})^2)$. For a typical value of $\sigma_{cw} = 1.0$ $\mathring{A}$, $DW = 10^{-3}$, which reduces the reflectivity by additional three orders of magnitude. Therefore, in order to obtain reasonable signals while measuring the specular reflectivity signal out to the layering peak, one needs an x-ray source capable of providing on the order of $10^{10}$ photons per second. In addition, since liquid metal samples in the experimental chamber can not be too large (typically $<$ 2 to 4 cm) the x-ray beam must be relatively small and well-collimated. This also requires monochromatic radiation.

Advances in synchrotron radiation over the past twenty years made it possible to satisfy all of these conditions. Figure 2.6 shows the comparison between the advances in x-ray source brightness and the growth of computing power which occurred over the past half a century.

### 2.10.2 Liquid Surface Spectrometer

Measurement of the angular dependence of the reflectivity from a solid sample can be achieved by simply rotating the sample with respect to the incident beam. This is obviously unacceptable for studying bulk liquids, since the surfaces must remain horizontal. Therefore, studying liquids requires a specially designed goniometer that

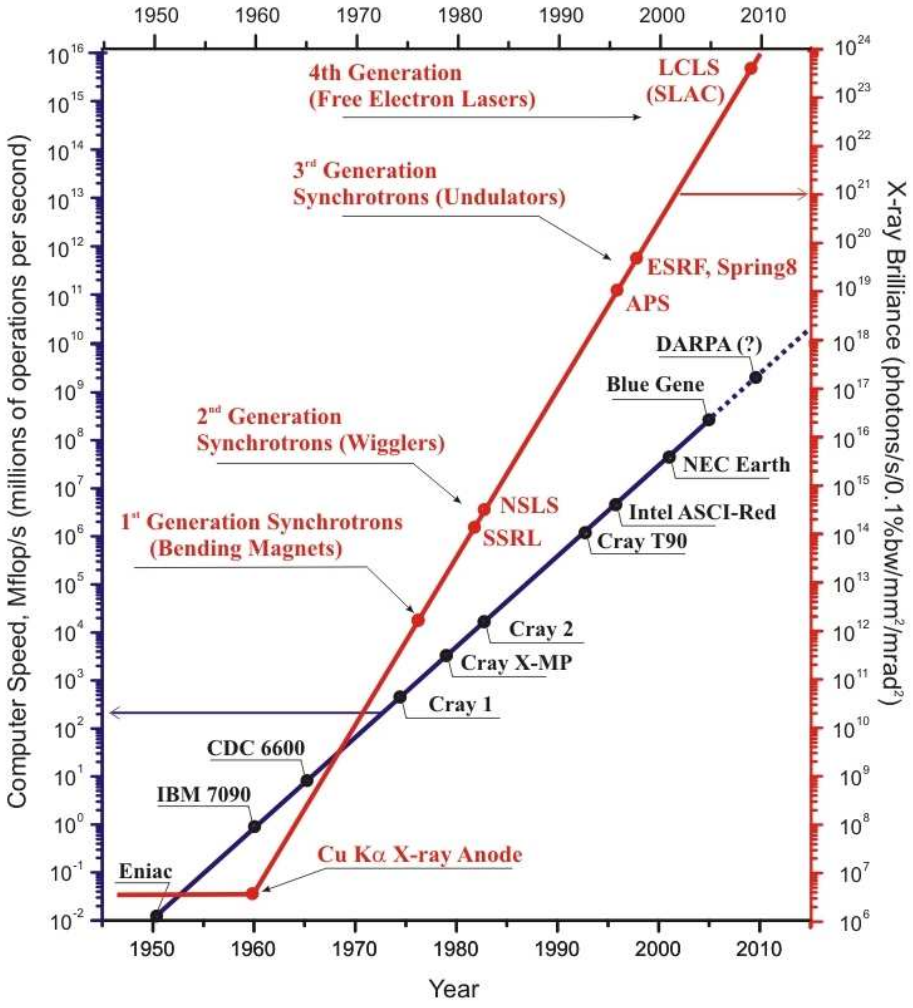



Figure 2.6: A comparison between synchrotron radiation development (x-ray source brightness, expressed in photons/sec/0.1% bandwidth $/mm^2/mrad^2$ and the growth in leading-edge computing speed (expressed in millions of operations/sec) which occurred over the past 60 years

is commonly called *liquid surface spectrometer* [4].

In Figure 2.7 we present a sketch of the instrumentation for realizing the kinematics that was shown in Figure 2.1 for a liquid surface. A horizontal monochromatic beam from the synchrotron source (a) is Bragg-reflected by a *steering crystal* (b) that can be rotated around the axis parallel to the incident beam by an angle $\chi$ while keeping the angle between the incident beam and the reciprocal lattice vector $\overrightarrow{G}$ of the crystal fixed. In this way the angle $\alpha$ that the Bragg-reflected beam makes with respect to the horizontal plane of the sample changes such that

$$G \sin \chi = \frac{2\pi}{\lambda} \sin \alpha \tag{2.10.1}$$

Not shown on the figure is the incident arm located between the steering crystal and the sample, containing the slits defining the size of the beam and the normalization monitor. The size of the slit is smaller than the size of the beam and is usually on the order of 10 microns for low incident angles and opened up to 300-500 microns for higher angles to increase the flux. The normalization monitor is used to measure the intensity of the incident beam, which is then used to normalize the scattered signal. In view of the fact that the beam follows a cone the incident arm as well as the sample stage containing the sample (c) have to move both vertically and horizontally in order to follow the beam.

The beam reflected from the sample is registered by a detector (e) that must also move horizontally in order to follow the reflection. If the distance from (b) to (c) is equal to the distance from (c) to (e) the vertical position of the detector can be held

[4] A more appropriate name for this instrument is liquid surface *reflectometer*, or perhaps liquid surface *diffractometer*, however, historically the name 'liquid surface *spectrometer*' has been established, even though x-ray energy spectra is virtually never measured by such 'spectrometer'

fixed.

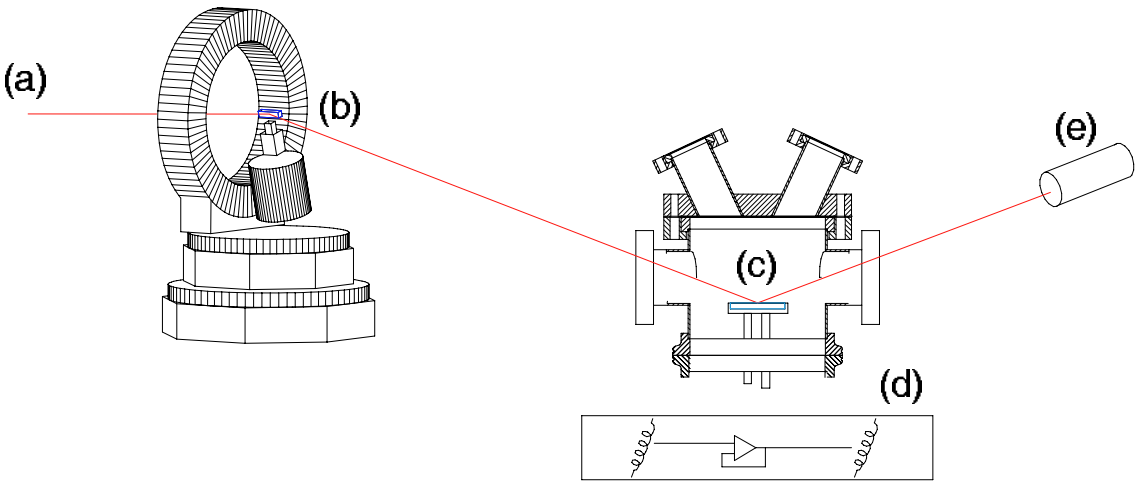



Figure 2.7: A schematic picture of liquid spectrometer setup. Shown are: the incoming synchrotron beam (a), the steering crystal (b), the liquid sample within the UHV chamber (c), temperature control and the active vibration isolation system (d) and the detector (e)

In fact, the actual mechanical implementation of what might appear a rather simple instrument is quite sophisticated. Depending on the particular setup, a typical liquid surface spectrometer requires motion of more than twenty individual motors, some of which require precision in the range of 1$\mu$m - 100$\mu$m for linear motors and a few millidegrees for rotational motors. These include motors responsible for movement of monochromator crystal, sample height (which is defined by the incident angle $\alpha$), detector height and detector rotation (which determines output angle $\beta$, as well as various motors responsible for optical delivery of the beam (mirrors and slits). In addition there are two sets of motorized slits before the sample and two on the detector side, each of which has four separate motors. The motion of most of the spectrometer motors is controlled by commands issued through a computer interface, according to

a liquid surface geometry code [26,27]. However, for the geometry code to work properly, the exact positions of these motors have to be individually aligned with respect to both the x-ray beam and the positions of other motors. Furthermore several tracking parameters, such as the distances that relate the linear displacement of the sample and detector to the various angles, have to be carefully determined before liquid surface spectrometer can be used. Also, in the course of the measurement there is often slight drifts in the position of the incident beam, the shape of the liquid sample, etc. As a consequence key motor positions and tracking parameters have to be periodically checked during the experiment, and if necessary adjusted[28,29].

### 2.10.3 Active Vibration Isolation System

One of the experimental difficulties in dealing with liquids is that even minor vibrational noise disturb the sample, causing ripples on the surface that deflect the reflected beam away from the detector. It is therefore crucial to isolate the liquid from vibrations coming from either outside of the experimental hutch, or from the movements of liquid spectrometer itself. Suppression of external vibrations are accomplished by a commercially available (Halcyonics GmbH) *active vibration isolation system* (d). The motion of the table top containing the sample is detected by a highly sensitive piezoelectric accelerometer consisting of a mass resting on a piezoelectric disc. The acceleration signal obtained by accelerometer is processed by analog control circuit and amplifier. A correction signal is then supplied to a magnetic actuator that is located on the movable table that supports the liquid sample. Active feedback systems such as the MOD-1M provided by Halcyonics is capable of suppressing external vibrations in all 6 degrees of freedom with frequencies $> 0.6Hz$ while supporting up to 90kg of equipment[30]. Minimization of the effect of vibrations caused by the

movements of the spectrometer is further achieved with a pre-determined *sleep time*, normally on the order of 5 to 10 seconds, is used between the completion of the motor movement and the beginning of signal detection count.

### 2.10.4 Ultra High Vacuum Chamber

A study of atomic structure at the surface would be impossible unless the surface can be kept atomically clean. Most metallic liquids oxidize very easily, and in order to maintain the surfaces free of oxide and other contaminants, the sample has to be kept in the atmosphere with sufficiently small partial pressures of oxygen, water vapor and other non-inert gases. The way to achieve this is by using an *Ultra High Vacuum* (UHV) system. A schematic design of the UHV chambers used in liquid metal experiments described in this thesis is shown in Figure 2.8. The chamber contains a sample (A) placed in Mo holder (B) mounted on top of the heater (not shown), with thermocouple and heater wires accessible through bottom flange M. Be windows (C) are capable of withholding a pressure differential of more than $10^5$ Pa, yet at the same time are 99% transparent to the x-rays. The vacuum inside the chamber is produced by ion pump (D) and turbo pump (E) backed up by a rotary station, connected to the turbo pump through a hose (F), and is monitored by vacuum gauge and RGA system which can be connected at flange (K). Ion sputtering system (G) is used to clean the surface of the sample, and is connected to the Ar gas line (H) [5]. The sample can be monitored through the glass window on a view port window (I). A linear transfer mechanism (L) provides the ability of wiping the sample and moving the radiation shield in and out with the help of bellow system

[5]During the x-ray measurements only the ion pump is used and the turbo pump is turned off to reduce vibrations, however, during sputtering ion pump is turned off and only turbo pump is used

(J). The chamber components are supported by a rigid frame (N). The photo (top inset of Figure 2.8) shows the smaller of the two chambers actively used in the x-ray experiments. The design of the two chambers is quite similar, the advantage of the larger chamber is a larger volume and higher "ceiling" which allows for a greater range of motion of linear transfer mechanism (which can be mounted both vertically and horizontally), as well as providing for an additional port, while the disadvantage is the increased weight and size of the chamber. These UHV systems are capable of sustaining the 1 atm pressure differential to the room, with the partial pressures of oxygen and other major contaminants two orders of magnitude lower.

### 2.10.5 Liquid Metal Sample preparation

A typical liquid metal sample is produced from melting 50g-200g of metal, of the highest purity that is commercially available (typically on the order of 99.9999% purity). The metal can be supplied in form of ingots, powder or a single briquette. The metal is melted in glass hardware which has been chemically cleaned after being soaked in an ultrasonic bath (Branson Ultrasonic Cleaner, Model 1510). The melting is done in a glove box filled with either an inert gas atmosphere in case of a binary alloy, or in the UHV chamber itself, in case of a pure system. Despite these precautionary measures, the surface of the metal typically contains a macroscopic amount of oxide, which must be mechanically removed by scraping the liquid surface with a clean glass or Mo wiper. The wiper is typically a Mo foil mounted on the linear transfer mechanism (J-L in Figure 2.8) that allows manipulation of the wiper inside the chamber. Wiping the sample works well for removing macroscopic quantities of oxide, but when the contamination is present in a form of just a few monolayers cleaning is better accomplished by means of an *ion sputtering* process described

below. The sample is then frozen and is kept under inert gas atmosphere or under vacuum until the UHV chamber is mounted on the sample stage of surface spectrometer where it undergoes what is known as a *bakeout* process during which the chamber and its components are gradually heated up to 150-200 °C, effectively degassing the chamber walls of any substances absorbed there. During this procedure the system is continuously pumped by 100 L/min turbo pump (Varian, Model: DS-102) (the pump is connected to chamber through the port indicated by part E in Figure 2.8). After the completion of the bakeout, the chamber is cooled down to room temperature and the pressure is lowered further by switching to the ion pump (part D in Figure 2.8), which is more efficient at low pressures. During initial stages of pumping and bakeout the atmosphere inside the chamber is periodically checked by a residual gas analyzer (RGA) system (connected through port K), capable of distinguishing individual chemical species present in the UHV chamber by a method of mass spectroscopy. Typically the bakeout procedure has to be performed at least twice - the sample is usually prepared at Harvard, several weeks prior to the experiment and transported to one of the synchrotron facility under vacuum. In view of the fact that the Be x-ray windows are brittle, for this first bake out and for transportation to the synchrotron they are replaced with thick (2 mm) glass windows. On arrival at the synchrotron the vacuum is briefly broken and the glass windows are replaced by the Be windows. The window replacement can be performed within 20-30 minutes, but to further minimize exposure to air, prior to opening the chamber it is backfilled with nitrogen atmosphere which prevents oxygen and water from absorbing at the chamber walls. After the windows are replaced and the chamber is evacuated, the second bake out is done. In view of the preliminary first bakeout and the short exposure to air,

this second bakeout can be typically completed in 10-15 hours, as compared to 24 hours for the first.

### 2.10.6 Surface Cleaning by Ion Sputtering

Despite the efforts to minimize the exposure to contaminants described in the previous section, the surface of the sample is frequently covered by a thin native film of oxide that cannot be removed by scraping. Moreover, the bakeout process described previously always results in some of the contamination desorbed from the walls being deposited on the surface of the sample. To minimize this contamination the sample is protected with a radiation shield during bakeout. During ion sputtering the chamber is backfilled with an inert gas atmosphere of $\approx 10^{-6}$ Torr, in our case Argon. The ion sputtering gun system uses high voltage (2-5 kV)to first ionize Ar atoms, then accelerate the resulting $Ar^+$ ions to form a high-energy ion beam, which is directed onto the sample. When the primary $Ar^+$ ions strike the sample their energy is transferred to the target atoms of the sample, which is sufficient to eject them from the surface. The sputtering $Ar^+$ beam can be de-focused to cover the entire area of the sample, normally on the order of a few $cm^2$, or focused on a particularly contaminated part of the surface of the sample. Because the surfaces of liquid metals are highly reflective, presence of even a single monolayer of oxide can be easily detected by eye, making it possible to monitor the sputtering progress through a viewport (I) shown on Figure 2.8. Presence of impurities can be also checked with x-ray reflectivity or fluorescence measurements.

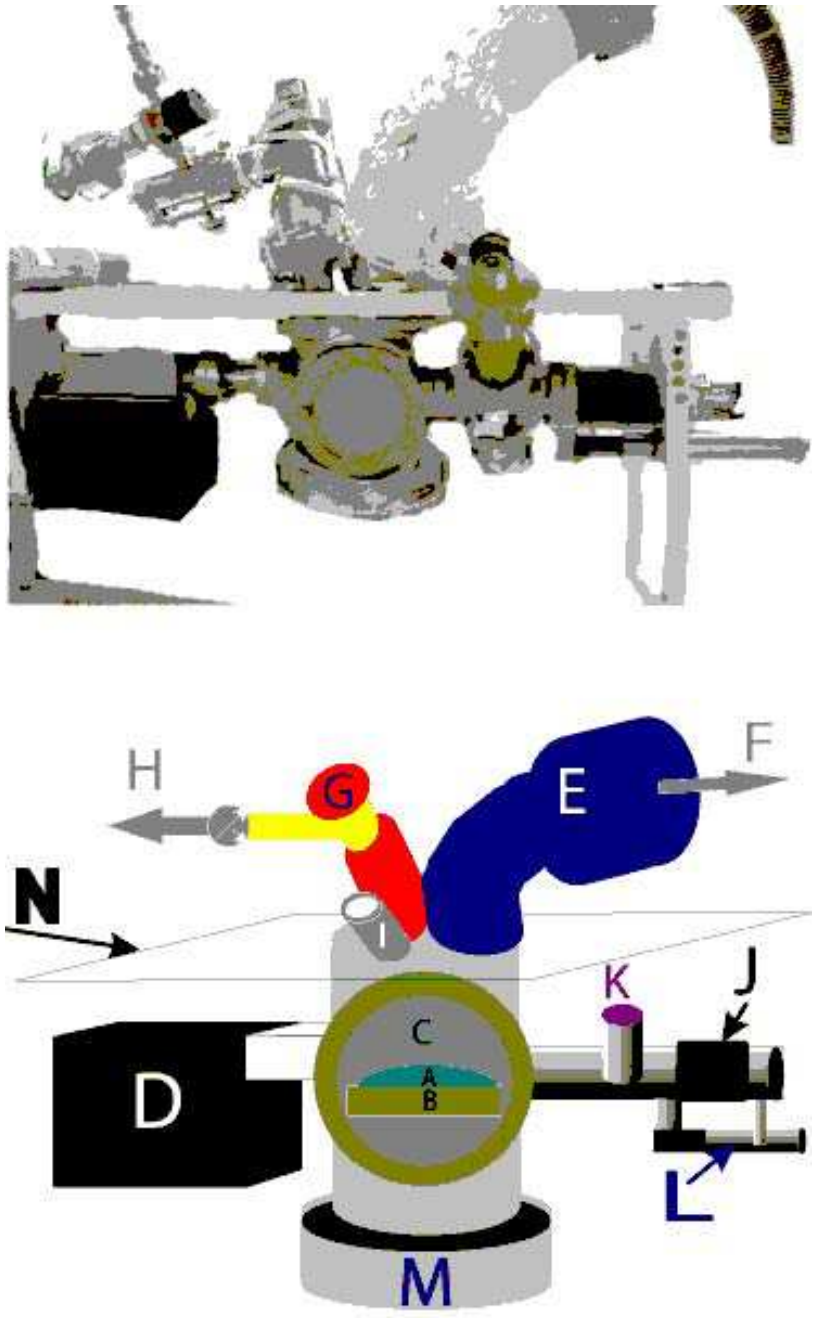



Figure 2.8: A photo and schematic of a typical UHV chamber setup: Liquid Sample (A) contained in sample holder (B), output Be window (C) (input Be window is located on the other side of the chamber), ion pump (D), turbo pump (E), hose leading to rotary pump (F), ion sputtering gun (G), a hose leading to Ar cylinder (H), viewport for monitoring the sample (I), a bellow (J), vacuum gauge and a port for RGA system (K), linear transfer mechanism (L), bottom flange containing thermocouple, heater and electrical contacts feedthroughs (M) and chamber frame (N).

### 2.10.7 Temperature control

The temperature of the sample is controlled by a heater mounted directly below the sample holder, that is capable of achieving temperatures well in excess of 400 °C. A Eurotherm temperature controller with a feedback loop maintains temperature drifts well under 0.1°C. In order to reduce temperature gradients that arise from radiation losses to the relatively cool chamber walls, a special radiation shield could be installed to maintain the sample in a thermally isotropic environment. The shield construction is shown in Figure 2.9. The shield is mounted on a linear transfer mechanism (part L of Figure 2.8) which allows for the shield to be moved by 5-7 cm during sputtering or wiping. Care must be taken to avoid touching the sample as it would inevitably introduce oxide, impurities or formation of amalgam at the surface. The radius of the cover is designed to be $\approx$ 5mm larger than that of the sample. The radius of the typical sample holder is 25-30mm, and the height of the sample is 3-5 mm. The height of the shield is 15 mm. The shield is made out of copper to improve thermal equilibration time. For studies involving high-temperature measurements the shield temperature can be controlled by a separate heater. In experiments which do not require a high degree of temperature control the radiation shield construction can be replaced by a 0.5mm thick sheet of Mo foil, approximately 4cm $\times$ 4cm in size which can be mounted on the same linear transfer mechanism.

### 2.10.8 Curvature Effects

The liquid metals that we have studied do not seem to wet non-reactive substrates such as Si, or metals such as Mo and W. As a result the finite contact angles that they make with the sample pan always lead to samples with finite curvature. To some

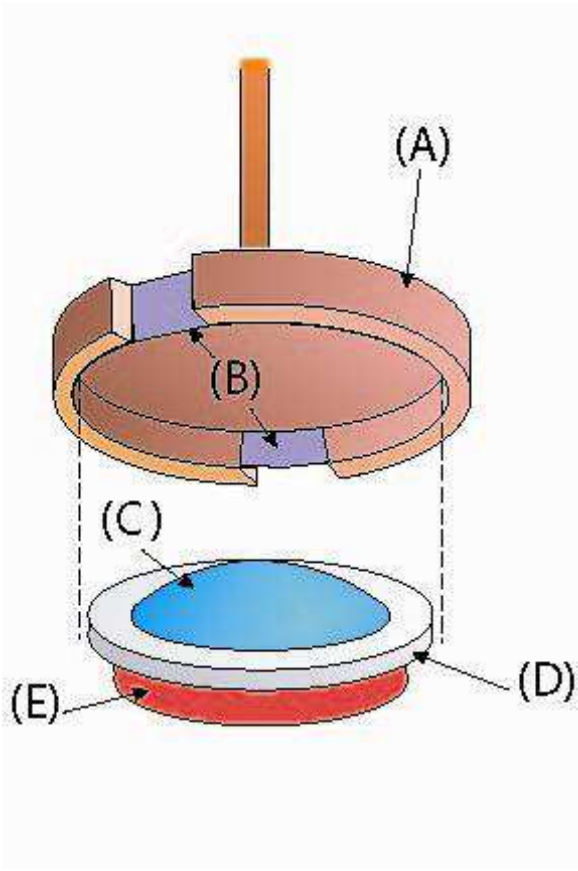



Figure 2.9: A schematic picture describing radiation shield setup: radiation shield (A) with Be foil walls (B), liquid sample (C) contained in a Mo sample pan (D), positioned directly on top of a Boralectric resistive heater (E). For the measurement the shield is lowered so that the sample is completely surrounded by the shield and its' walls

extent this effect could have been mitigated if the diameter of the metallic liquid was sufficiently large; however, the fact that the sample must be mounted in a UHV chamber places restrictions on sample size. In this section we will describe a method for measuring the macroscopic surface curvature profile.

Consider a well-collimated x-ray beam of vertical size $\Delta H$ incident on a surface of a curved liquid sample at angle $\alpha$, as shown on Figure 2.10. If the local radius of curvature $R$ is sufficiently large, and if the curvature is sufficiently uniform, the resulting footprint (distance between points A and B on the surface) on the sample can be expressed as:

$$AB = \frac{\Delta H}{\tan\alpha} \tag{2.10.2}$$

The angle $\delta\phi$ between surface normals at A and B therefore can be written as:

$$\delta\phi = \frac{AB}{R} = \frac{\Delta H}{R\tan\alpha} \tag{2.10.3}$$

and the rays reflected from A and B - AA' and BB' will diverge by an angle $\Delta\beta = 2\delta\phi$ or

$$\Delta\beta = \frac{2\Delta H}{R\tan\alpha} \tag{2.10.4}$$

as a result the height $\Delta H'$ of the beam observed a distance L away from the sample is

$$\Delta H' = L\Delta\beta = \frac{2L\Delta H}{R\tan\alpha} + \Delta H \tag{2.10.5}$$

The local radius of curvature (average curvature over the illuminated part of the sample) can be determined from a measurement of $\Delta H'$ for a fixed incident angle $\alpha$. By repeating the measurement of $\Delta H'$ while moving the beam across the sample (by scanning the sample height, for example) we can obtain information on the local

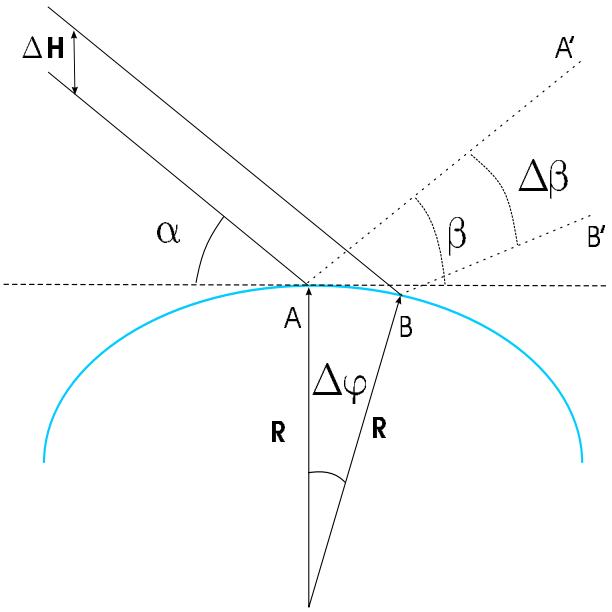



Figure 2.10: Illustration of reflection geometry from curved sample.

curvature at different points on the sample surface. In addition, from the variation in the average scattering angle "beta" one can obtain a measure of the global curvature.

In view of the fact that the local curvature measurement is affected by beam divergence, non-uniform beam profile and diffuse scattering from the sample, local curvature measurements typically produce higher numbers than global curvature values.

A series of such scans is called a *walking scan* because the beam walks across the surface of the sample. To illustrate consider what happens when the sample height is increased by a value $\Delta sh$. If the sample surface was ideally flat, then the position of the reflected beam observed at the detector position would change by double that value, $2\Delta sh$. On the other hand, because of the sample curvature, the average reflected angle $\beta$ will be changed by a value $\Delta\beta$ given by an expression similar

to 2.10.4:

$$\Delta\beta = \frac{2\Delta sh}{R\tan\alpha} \tag{2.10.6}$$

Note that in this case the sample height displacement $\Delta sh$ replaces the height of the beam $\Delta H$, but otherwise the geometry remains the same.

The shift in the vertical position of reflected beam, or 'detector height', $DH$, due to sample height displacement $\Delta sh$ can be expressed as:

$$\Delta DH = 2\Delta sh + L\Delta\beta = 2\Delta sh + \frac{2L\Delta sh}{R\tan\alpha} \tag{2.10.7}$$

Figure 2.11 provides an illustration of a typical walking scan. The sample height was incrementally changed by 0.2mm in both directions from the nominal position of spectrometer geometry ($\Delta sh = 0$), and the detector height was taken at each position of sample height. The scans were performed for $\alpha = 74$ mrad with detector L=402mm away from the sample. The vertical opening of the detector slit was 1mm. As can be seen qualitatively from this figure, the detector height scans centered around $\Delta sh = 0$ are the narrowest, have the highest intensity, and smallest spacing between the adjacent scan. As the beam travels further from the sample's center on either side, the scans become broader, peak intensity decreases while the distances between the neighboring scans increases. This implies that the radius of curvature is largest around nominal position $\Delta sh = 0$ and decreases to the sides, as is expected. This particular sample is completely convex, but depending on the size and the wetting angles the sample can become concave in the middle.

A more quantitative approach consists of plotting the values $\Delta DH - 2\Delta sh$ as a

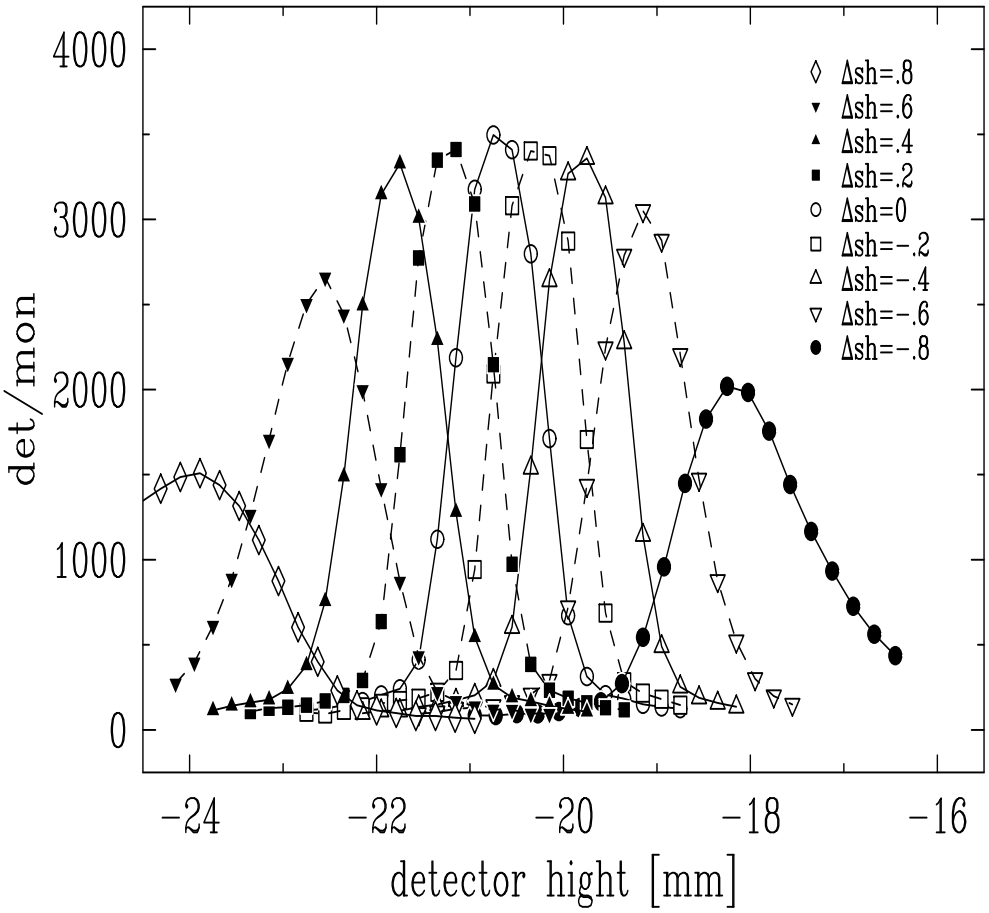



Figure 2.11: Graphical representation of a "walking scan" procedure: a series of detector height scans for various sample height position, taken on a sample of liquid GaBi alloy. Sample height position was changed in increments of 0.2mm, see legend for more details.

function of $\Delta sh$, since according to Eq. 2.10.7

$$\Delta DH - 2\Delta sh = \frac{2L\Delta sh}{R\tan\alpha} \tag{2.10.8}$$

the sample curvature $R^{-1}$ is therefore proportional to the derivative of such plot:

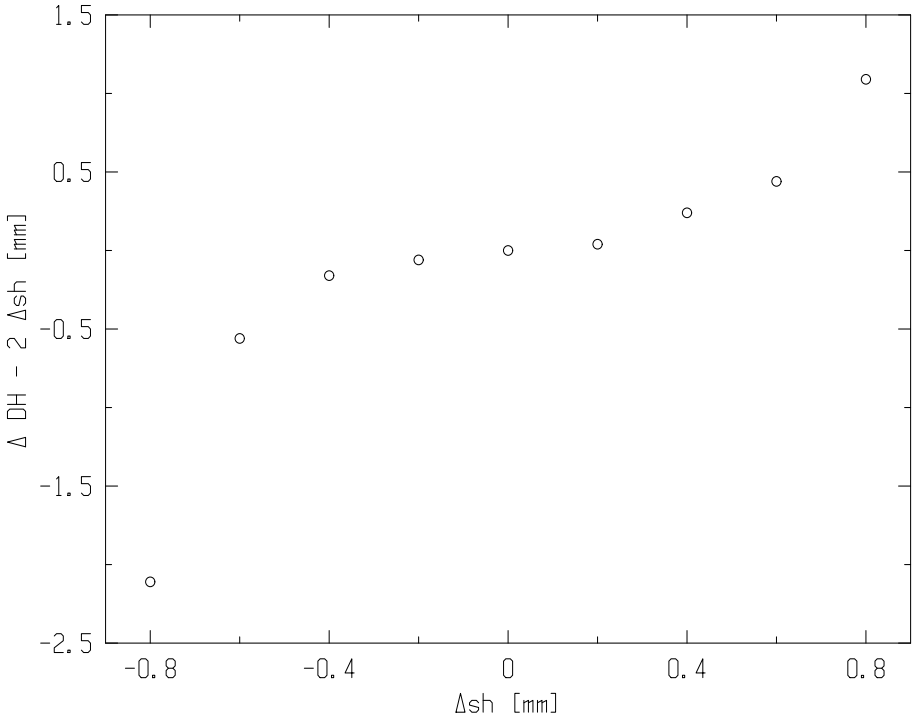



Figure 2.12: The displacements of the center positions of detective height scans from the walking scan shown in Figure 2.11, adjusted for twice the amount of the sample height displacement to account for a geometrical change in position of the beam for an ideally flat reflecting surface, as a function of sample height position. The derivative of this plot is the effective measure of the local surface curvature, $R^{-1}$.

$$\frac{1}{R} = \frac{\tan\alpha}{2L}\frac{\delta(\Delta DH - 2\Delta sh)}{\delta\Delta sh} \tag{2.10.9}$$

Plugging in the values for incident angle $\alpha = 74$ mrad and the distance from the sample L=402mm, the slope of the plot of $\delta(\Delta DH - 2\Delta sh)/\delta\Delta sh = 0.45$ at $\Delta sh \approx 0$

corresponds to a value of $R^{-1} \approx 9 \cdot 10^{-5} m^{-1}$ or $R \approx 11$ meters. On the other hand, the slope corresponding to $\Delta sh = -0.8$mm, as well as the respective sample curvature at this position on the sample, are an order of magnitude higher.

# Bibliography


[1] W. Freidrich, P. Knipping, and M. Von Laue. Interferenz-erscheinungen bei rontgenstrahlen. *Proc. Bavarian Acad. Sci.*, pages 303–322, 1912.

[2] M. Laue. Eine quantitative prufung der theorie fur die interferenzerscheinungen beirontgenstrahlen. *Proceedings of the Bavarian Academy of Sciences*, pages 363–373, 1912.

[3] W. C. Roentgen. Uber eine neue art von strahlen. vorlufige mittheilung. *Sber. Phys.-Med. Ges. Wurzb.*, 137:132–141, 1895.

[4] W. C. Roentgen. On a new kind of rays. *Nature*, 53:274–276, 1896.

[5] A. Einstein. Lassen sich brechungsexponenten der korper fur roentgenstrahlen experimentell ermitteln? *Verh. Dtsch. Phys. Ges.*, 20:86–87, 1918.

[6] A. H. Compton. *Philos. Mag.*, 45(112), 1923.

[7] J. Als-Nielsen and D. McMorrow. *Elements of Modern X-Ray Physics*. John Wiley & Sons, New York, 1st edition, 2001.

[8] M. Tolan. X-ray scattering from soft-matter thin films - materials science and basic research - introduction. *X-Ray Scattering from Soft-Matter Thin Films*, 148:1–+, 1999.

[9] M. Born and E. Wolf. *Principles of Optics*. Pergamon Press, Bath, 1964.

[10] J. Daillant and A. Gibaud. *X-Ray and Neutron Reflectivity: Principles and Applications*. Lecture Notes in Physics. Springer-Verlag, Berlin Heidelberg, 1999.

[11] L. G. Parratt. Surface studies of solids by total reflection of x-rays. *Physical Review*, 95(2):359–369, 1954.

[12] A. Braslau, P. S. Pershan, G. Swislow, B. M. Ocko, and J. Als-Nielsen. Capillary waves on the surface of simple liquids measured by x- ray reflectivity. *Phys. Rev. A*, 38(5):2457–2470, 1988.

[13] P.S. Pershan and J. Als-Nielsen. X-ray reflectivity from the surface of a liquid crystal: surface structure and absolute value of critical fluctuations. *Phys. Rev. Lett.*, 52(9):759–62, 1984.

[14] H. Kiessig. "interfernz von rontgenstrahlen an dunnen schichten,". *Ann. Phys. , Leipzig*, 10:769–778, 1931.

[15] A. Guinier. *X-Ray Diffraction*. Freeman, San-Francisco, 1963.

[16] K. R. Mecke and S. Dietrich. Effective hamiltonian for liquid-vapor interfaces. *Phys. Rev. E*, 59(6):6766–6784, 1999.

[17] C. Fradin, A. Braslau, D. Luzet, D. Smilgies, M. Alba, N. Boudet, K. Mecke, and J. Daillant. investigating liquid surfaces down to the nanometer scale using grazing incidence x-ray scattering. *Physica-B*, 248:310, 1998.

[18] C. Fradin, A. Braslau, D. Luzet, D. Smilgies, M. Alba, N. Boudet, K. Mecke, and

J. Daillant. Reduction in the surface energy of liquid interfaces at short length scales. *Nature*, 403(6772):871–874, 2000.

[19] S. K. Sinha, E. B. Sirota, S. Garoff, and H. B. Stanley. X-ray and neutron-scattering from rough surfaces. *Phys. Rev. B*, 38(4):2297–2311, 1988.

[20] H. Tostmann, E. DiMasi, P. S. Pershan, B. M. Ocko, O. G. Shpyrko, and M. Deutsch. Surface structure of liquid metals and the effect of capillary waves: X-ray studies on liquid indium. *Phys. Rev. B*, 59(2):783–791, 1999.

[21] M.J. Regan, H. Tostmann, P.S. Pershan, O.M. Magnussen, E. DiMasi, B.M. Ocko, and M. Deutsch. X-ray study of the oxidation of liquid-gallium surfaces. *Physical Review B (Condensed Matter)*, 55(16):10786–90, 1997.

[22] D.K. Schwartz, M.L. Schlossman, E.H. Kawamoto, G.J. Kellogg, P.S. Pershan, and B.M. Ocko. Thermal diffuse x-ray-scattering studies of the water-vapor interface. *Physical Review A (Statistical Physics, Plasmas, Fluids, and Related Interdisciplinary Topics)*, 41(10):5687–90, 1990.

[23] M.J. Regan, E.H. Kawamoto, S. Lee, P.S. Pershan, N. Maskil, M. Deutsch, O.M. Magnussen, B.M. Ocko, and L.E. Berman. Surface layering in liquid gallium: an x-ray reflectivity study. *Phys. Rev. Lett.*, 75(13):2498–501, 1995.

[24] O. M. Magnussen, B. M. Ocko, M. J. Regan, K. Penanen, P. S. Pershan, and M. Deutsch. X-ray reflectivity measurements of surface layering in liquid mercury. *Phys. Rev. Lett.*, 74(22):4444–4447, 1995.

[25] *CRC Handbook of Chemistry and Physics*. CRC Press, Boca Raton, FL, 1985.

[26] EPICS: Experimental Physics and Industrial Control System, `http://www.aps.anl.gov/epics/`, 2003.

[27] Gerry Swislow. CSS, Certified Scientific Software: SPEC. URL: `http://www.certif.com/spec.html`, 2003.

[28] Notes on Alignment of Liquid Surface Spectrometer, URL: `http://liquids.deas.harvard.edu/x22bnotes.html`, 2000.

[29] E. DiMasi. X22B Liquid Surface Spectrometer, URL: `http://www.solids.bnl.gov/lss/`, 2001.

[30] L. Gaul and U. Stoebener. Active control of structures. *Proceedings of NATO-Advanced Study Institute 'Modal Analysis & Testing'*, pages pp. 565–604, 1998.

# Chapter 3

# Surface-Induced Atomic Layering

## 3.1 Theoretical predictions

The experimental studies described in Chapters 4 through 7 of this thesis were motivated by the theoretical prediction by Rice[1] of the existence of a well-defined atomic layering structure at the liquid/vapor interface of a liquid metal. The effect is the most prominent at the first surface layer, with each subsequent layer becoming less and less ordered such that deep in the bulk of the liquid all memory of the surface is lost. By this prediction the average local electron density introduced in Eq. 2.9.5, $\langle\rho(z)\rangle_\xi$, along the surface normal can be represented by a decaying oscillating function such as in Figure 3.1. On the other hand for a dielectric liquid consisting of relatively small molecules, such as $H_2O$, $CCl_3$, $C_6H_2$ etc., the $\langle\rho(z)\rangle_\xi$ is believed to be a simple monotonic rise from zero on the vapor side to bulk value on the liquid side.

### 3.1.1 Velasco's Theory

Recent theoretical and computer simulations by Velasco et al.[2] offer a somewhat different interpretation of the atomic layering phenomena than by Rice. Their principal argument is that the layering phenomena found in atomic liquids up until now is

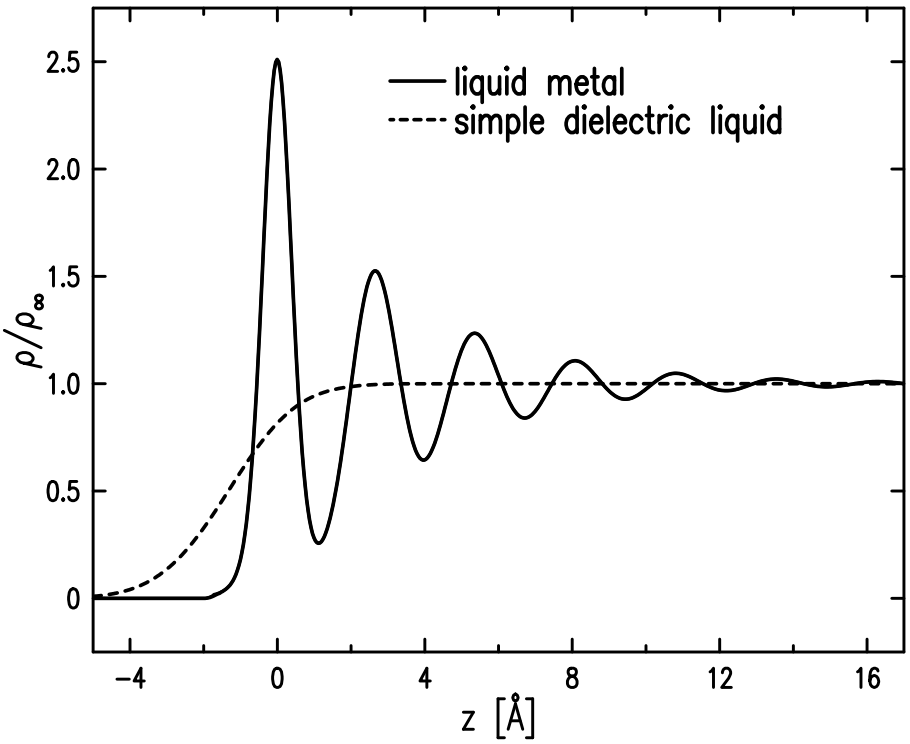



Figure 3.1: Surface-normal average of the density at the surfaces of liquid metal (solid line) and dielectric liquid (broken line).

of more universal nature, and that the many-body character of metallic interactions may not necessarily play a leading role in forming layering. Velasco et al. claim that one should expect surface-induced atomic layering in any liquid for which the ratio of the melting temperature $T_m$ to the critical temperature $T_c$, $T_m/T_c$ is sufficiently small. Another way to rephrase this hypothesis: the surface layering will appear in every liquid at low enough temperature, if it is not first preempted by solidification, below which the liquid becomes metastable and the free liquid-vapor interface cannot be observed at equilibrium. In fact this is similar to the criteria for which liquid crystals will form if they are not precluded by crystallization. This explanation of layering phenomenon, therefore, does not rely on nonadditive particle interactions, as does Rice's theory, but depends solely on thermodynamic stability of the liquid-vapor interface. The potential shortfall of the theory offered by Velasco is that the potentials they use to describe the layering phenomena are not realistic, in the sense that they may not be capable of explaining some of the other thermodynamic properties of liquids.

## 3.2 Candidates for X-ray Study of Atomic Layering

In this section we will consider the conditions which might be used to define good candidates for x-ray reflectivity study of surface-induced atomic layering. To study atomic surface layering phenomena one has to start with a surface that is atomically clean. While a combination of chemical procedures and ion sputtering may produce samples that produce an atomically clean surface, this condition must also be maintained throughout the length of the experiment. For most metallic systems

the principal surface contamination is the surface oxide that will form in the presence of even small amounts of oxygen or water in the system. Oxide layers that a visible to the eye will usually form at oxygen pressures as low as $10^{-8}$ Torr. The only way to achieve and maintain a clean surface for these metals is to study them under ultra high vacuum (UHV) conditions, which implies that the candidate for such study must have a low enough vapor pressure for UHV techniques to be applied successfully. The alkali metals are exceptions to this since the surface oxides seem to dissolve in the bulk.[3,4] Similarly liquid Hg can be kept relatively clean under slightly reducing atmospheres.

The second problem is to have sufficient intensity to measure the reflectivity at values of $q_z$ that are of the order of the value at which the surface layering structure peak is expected, $q_{peak} \approx 2\pi/a$ where $a$ is the atomic or molecular radius. In view of the fact that the bare Fresnel reflectivity falls off rapidly with increasing $q_z$, i.e. $R_F(q_z) \approx (q_c/2q_z)^4$ where $q_c$ is the critical wavevector, there is some advantage to studying materials with larger atomic numbers for which both $q_c$ is larger and $a$ is smaller. Thermal capillary excitations add to the problem since, as discussed in Sect. 2.9, the capillary reduced roughness causes the reflectivity to fall exponentially with $q_z^2$. The single parameter that best summarizes this effect is $\eta = (k_B T/2\pi\gamma)q_z^2$ (Eq. 2.9.14). Thus another advantage in material property is a low melting temperature and high surface tension.

The relative effect of capillary fluctuations on the reflectivity from different materials with comparable surface structure factors can be most easily estimated by considering the effect of the capillary waves on just the Fresnel reflectivity at the value of $q_z = q_{peak} = 2\pi/a$ for which the layering peak is expected, where $a$ is the

atomic size: $R(q_z)/|\Phi(q_z)|^2 = R_F(q_z)\exp(-\sigma_{cw}^2 q_z^2)$. Although the square of the surface structure factor $|\Phi(q_{peak})|^2$ will enhance $R(q_{peak})$ by a factor $\sim 100$, this factor is about the same for all of the pure metals that have been studied thus far. The effect on the Fresnel reflectivity at $q_z = q_{peak}$ can be approximated by

$$\frac{R(q_{peak})}{|\Phi(q_peak)|^2} \sim \left(\frac{q_c}{q_{peak}}\right)^4 \exp\left[-\frac{k_B T_m q_{peak}^2}{2\pi\gamma}\ln\left(\frac{q_{\rm res}}{q_{\rm max}}\right)\right] \sim \rho_e^2 a^4 \exp\left[-\frac{T_m}{\gamma a^2}\ constant\right] \tag{3.2.1}$$

Table 3.1 contains a list of relevant material parameters for a number of pure elements. The elements are listed in the decreasing order of $R(q_{peak})/|\Phi(q_{peak})|^2$, the estimated reflectivity at $q_{peak}$ obtained by multiplying Fresnel Reflectivity $R_F$ by Debye-Waller capillary wave factor. Not surprisingly, the first three elements for which the atomic layering has been experimentally observed - mercury, gallium and indium (in that order) can be found at the top of the list. In the rest of this chapter we will review some of the experimental data obtained during these measurements and its interpretation.

## 3.3 Distorted Crystal Density Model

In view of the fact that the phase information is lost in a reflectivity measurement, it is impossible to extract $\langle\rho(z)\rangle_\xi$ from a single reflectivity measurement[10] by simply performing a reverse Fourier transform of the x-ray reflectivity data (see Eq. 2.9.11). So-called model independent methods[10,11,12] have been developed that purport the ability to extract average local density profile defined in Eq. 2.9.5, $\langle\rho(z)\rangle_\xi$; however, as has been shown by Pershan[13] there is a certain degree of ambiguity that can not be avoided. As a result our solution is to assume a model for the density profile, which

| **Z** | **Name** | $T_m$, $^\circ$ K | $\gamma$, mN/m | $P_{vap}$, Torr | $q_{peak}$, $\mathring{A}^{-1}$ | $\sigma_{cw}$, $\mathring{A}$ | $\eta(q_{peak})$ | $R(q_{peak})/\|\Phi(q_{peak})\|^2$ |
|---|---|---|---|---|---|---|---|---|
| 80 | Mercury | 234.28 | 498 | 2.e-06 | 2.3 | 0.72 | 0.53 | 3.9e-09 |
| 31 | Gallium | 302.93 | 718 | <1e-11 | 2.6 | 0.68 | 0.61 | 4.0e-10 |
| 49 | Indium | 429.32 | 556 | <1e-11 | 2.2 | 0.92 | 0.80 | 3.8e-10 |
| 48 | Cadmium | 594.1 | 570 | 1.e-01 | 2.1 | 1.07 | 1.02 | 1.7e-10 |
| 50 | Tin | 505.12 | 560 | <1e-11 | 2.2 | 1.00 | 0.99 | 1.2e-10 |
| 81 | Thallium | 576.6 | 464 | 3.e-08 | 2.1 | 1.17 | 1.22 | 1.1e-10 |
| 82 | Lead | 600.65 | 458 | 3.e-09 | 2.1 | 1.20 | 1.23 | 1.0e-10 |
| 79 | Gold | 1337.6 | 1338 | 2.e-05 | 2.5 | 1.05 | 1.34 | 7.5e-11 |
| 83 | Bismuth | 544.5 | 378 | 2.e-10 | 2.1 | 1.26 | 1.43 | 3.0e-11 |
| 30 | Zinc | 692.73 | 782 | 1.e-01 | 2.6 | 0.99 | 1.33 | 1.2e-11 |
| 55 | Cesium | 301.6 | 70 | 2.e-06 | 1.4 | 2.18 | 1.73 | 1.5e-12 |
| 29 | Copper | 1356.6 | 1300 | 3.e-04 | 2.8 | 1.07 | 1.83 | 1.1e-12 |
| 37 | Rubidium | 312.2 | 85 | 1.e-06 | 1.5 | 2.01 | 1.71 | 8.4e-13 |
| 47 | Silver | 1235.1 | 828 | 2.e-03 | 2.5 | 1.28 | 2.06 | 6.7e-13 |
| 19 | Potassium | 336.8 | 110 | 1.e-06 | 1.5 | 1.83 | 1.59 | 4.9e-13 |
| 56 | Barium | 1002 | 277 | 1.e-01 | 1.6 | 1.99 | 2.10 | 3.4e-13 |
| 11 | Sodium | 371 | 191 | 1.e-07 | 1.9 | 1.46 | 1.54 | 3.3e-13 |
| 12 | Magnesium | 922 | 559 | 2.e+00 | 2.3 | 1.35 | 1.85 | 1.1e-13 |
| 3 | Lithium | 453.7 | 398 | 1.e-10 | 2.3 | 1.12 | 1.36 | 9.1e-14 |
| 20 | Calcium | 1112 | 361 |  | 1.8 | 1.84 | 2.27 | 2.3e-14 |
| 51 | Antimony | 903.9 | 367 |  | 2.3 | 1.64 | 2.79 | 1.2e-14 |
| 32 | Germanium | 1210.6 | 621 | 8.e-07 | 2.6 | 1.46 | 2.98 | 2.0e-15 |
| 14 | Silicon | 1683 | 865 | 3.e-04 | 2.7 | 1.46 | 3.20 | 1.5e-16 |
| 52 | Tellurium | 722.7 | 180 | 1.e-01 | 2.5 | 2.10 | 5.71 | 2.6e-21 |
| 34 | Selenium | 490 | 106 | 2.e-03 | 2.6 | 2.25 | 6.76 | 6.8e-24 |
| 18 | Argon | 83.8 | 13 |  | 4.1 | 2.65 | 23.64 | 2.1e-62 |
| 10 | Neon | 24.56 | 5 | 4.e+00 | 7.1 | 2.28 | 52.05 | 6.6e-125 |

Table 3.1: Comparison of candidates for Surface-induced layering study.[5,6,7,8,9]

is then Fourier transformed and fitted to the experimentally determined structure factor.

### 3.3.1 Model Description

The simplest approximation for the oscillating electron density profile describing the surface-induced layering phenomena in single component liquid metals can be constructed by considering a physical model which consists of a series of well-defined atomic 2D layers ordered parallel to the surface, so-called *distorted crystal model*[14]. The layers are separated from each other by a distance $d$. The width of each subsequent layer is gradually increased, causing an overlap between layers as one goes deeper into the bulk, until eventually the liquid approaches a common bulk-like liquid behavior with no sign of layering. Mathematically, the electron density can be described by a semi-infinite sum of equally spaced Gaussians, with identical total integrated density: [1]

$$\frac{\langle\rho(z)\rangle}{\rho_\infty} = \sum_{n=0}^{\infty} \frac{d/\sigma_n}{\sqrt{2\pi}} \exp\left[-(z - nd - z')^2/2\sigma_n^2\right] \tag{3.3.1}$$

As will be shown below, if the widths have the form $\sigma_n^2 = n\bar{\sigma}^2 + \sigma_0^2$, and $\bar{\sigma}$ and $\sigma_0$ are constants, the sum of the Fourier transforms will have a simple analytic form. The model density approaches the bulk density $\rho_\infty$ for $\sigma_n \gg d$.

### 3.3.2 An Alternative Density Model

An alternative model for the layering profile can be built from superposition of an error-function and an exponentially decaying sinusoidal:

[1] This neglects the changes in scattering form factor amplitude, $f(q)$, which are typically small for small $q$.

$$\frac{\langle\rho(z)\rangle}{\rho_\infty} = \left[1 + A\ \exp\left(-\frac{z-z'}{\lambda}\right)\sin\left(\frac{2\pi(z-z_0-z')}{d}\right)\right] erf\left(\frac{z}{\sigma_0}\right) \qquad (3.3.2)$$

Although the profiles produced by this model are very similar to those of the distorted crystal model, there are some disadvantages. For example, if an empirical model is to be used it should have the fewest number of arbitrary parameters. This model contains five parameters ($A, \lambda, d, z_0$ and $\sigma_0$), as opposed to just three in the case of a distorted crystal model ($\sigma_0, \bar{\sigma}, d$). Another disadvantage of this model is that in contrast to the distorted crystal model, it cannot be clearly cast in terms of atomic distributions. However, the best fit electron density functions from both of these empirical models are essentially identical[15] and the only arguments to favor one or the other are really subjective.

### 3.3.3 Fitting Functions

In order to extract a real space density profile from the experimental data it is necessary to construct a computer code that relates the reflectivity to the model. There are three things that must be included in this code. The first is a numerical expression that will accurately represent the surface structure factor $|\Phi(q_z)|$ associated with the electron density model (Eq. 2.9.11). The second is a numerical function that takes account of the integral over the singular function that describes the capillary effects. The method that was used to achieve this was discussed in Sect. 2.9.4. The third, and final ingredient is to subtract from scattering at the specular condition the intensity of the theoretically predicted diffuse scattering at the position where the off-specular background scattering is measured. This code is then fit to the measured data using

Table (a)

| **Variable** | **Name** | **Units** | **Typical Value** | **Fit?** |
|---|---|---|---|---|
| vdh | vertical slit size | mm | 0.1-4 | no |
| hdh | horizontal slit size | mm | 0.1-4 | no |
| L | sample-to-detector | mm | 400 | no |
| $\Delta\Theta$ | background offset | degree | 0.1-0.3 | no |
| $\alpha$ | incident angle | degree | 0.1-10 | no |
| $\lambda$ | wavelength | $\mathring{A}$ | 0.6-1.6 | no |

Table (b)

| **Variable** | **Name** | **Units** | **Typical Value** | **Fit?** |
|---|---|---|---|---|
| $Q_c$ | Critical Wavevector | $\mathring{A}^{-1}$ | 0.05 | no |
| $Q_{max}$ | $Q_{max}$ | $\mathring{A}^{-1}$ | 1.0-3.0 | no |
| $\gamma$ | surface tension | dyn/cm | 70-700 | sometimes |
| T | temperature | K | 250-500 | no |

Table (c)

| **Variable** | **Name** | **Units** | **Typical Value** | **Fit?** |
|---|---|---|---|---|
| $\sigma_0$ | avg atomic width | $\mathring{A}$ | 0.3-1.0 | yes |
| $\overline{\sigma}$ | broadening width | $\mathring{A}$ | 0.3-3.0 | yes |
| d | interatomic spacing | $\mathring{A}$ | 2.0-3.0 | yes |

Table 3.2: A listing of typical fitting parameters related to atomic layering model described here. Table (a) contains parameters describing the spectrometer geometry, table (b) lists parameters relevant to the studied material and table (c) includes parameters describing the density profile

the C-PLOT non-linear least square fitting procedures with varying numbers of self adjusting parameters.

The parameters used by these functions can be divided into three general categories. The first corresponds to the constraints imposed by the spectrometer. These include details such as the x-ray wavelength, the dimensions of the detector slits, the lengths of the various arms of the spectrometer. These are necessary in order to implement the digital integration over the spectrometer resolution. Some of these parameters are listed in Table 3.2 (a). The second has to do with the thermal capillary excitations that were discussed in Section 2.9. These include the surface tension $\gamma$ and the temperature $T$ of the material, as well as the critical wavevector $q_c$ and are listed in Table 3.2 (b). Finally there are the parameters in Table 3.2 (c) that are needed to model the intrinsic electron density profile. The parameters in Table 3.2 (a) and (b) are known and the measurements are analyzed by fitting the distorted crystal model to the data by varying only the parameters in Table 3.2 (c).

In view of the fact that at least approximate values for the surface tension for most systems are known the first step is to use these values for obtain a first best fit of the structure factor $\Phi(q_z)$ to the reflectivity. This form for $\Phi(q_z)$ is then used to more precisely define the value of the surface tension that was used to account for the capillary effects by fitting the diffuse scattering data. If necessary, the reflectivity data fitting may have to be adjusted with the revised surface tension, as the entire process is reiterated until a self-consistent density model and surface tension values accurately describing both reflectivity and diffuse scattering data are found. This procedure is slightly more complicated for alloys since the density profiles depend on the relative concentration of the two species. Additionally, the simple distorted

crystal model is often not sufficient to describe layering in binary alloys, the structure of which can be complicated by surface segregation. These effects will be discussed in detail when the data for the alloys are presented.

## 3.4 X-Ray Measurements of Liquid Mercury, Gallium and Indium

### 3.4.1 X-Ray Reflectivity Comparison

The raw reflectivity data from Hg[16], Ga[15] and In[17] is shown in Figure 3.2. For clarity of representation, the data sets for indium and mercury have been offset by multipliers of 10 and 0.1, respectively. The lines represent Fresnel reflectivity curves, without taking into account capillary roughening or any surface structure or capillary contributions. Figure 3.3 shows the reflectivity data for these three metals normalized to the respective Fresnel reflectivities.

Although the prominence of local maxima at the position of the layering peaks decreases in moving from Hg through Ga to In, this does not reflect the true strength of the intrinsic, or local layering that was discussed in Section 2.9.4. As can be seen in Table 3.1, when the values of $q_{peak}$ are taken into account, this ordering of the three metals happens to coincide with the order of the increasing melting temperatures ($-35$°C for Hg, 25°C for Ga and 170°C for In), and consequently the value of $\eta(q_{peak})$ at the melting temperature also increases in the order of Hg, Ga and In. In fact, when the thermal effects are removed the intrinsic layering is comparable for all three metals.

The effects of thermal capillary waves on the reflectivity can be most directly seen by measuring the temperature dependence of the reflectivity for any one metal. This

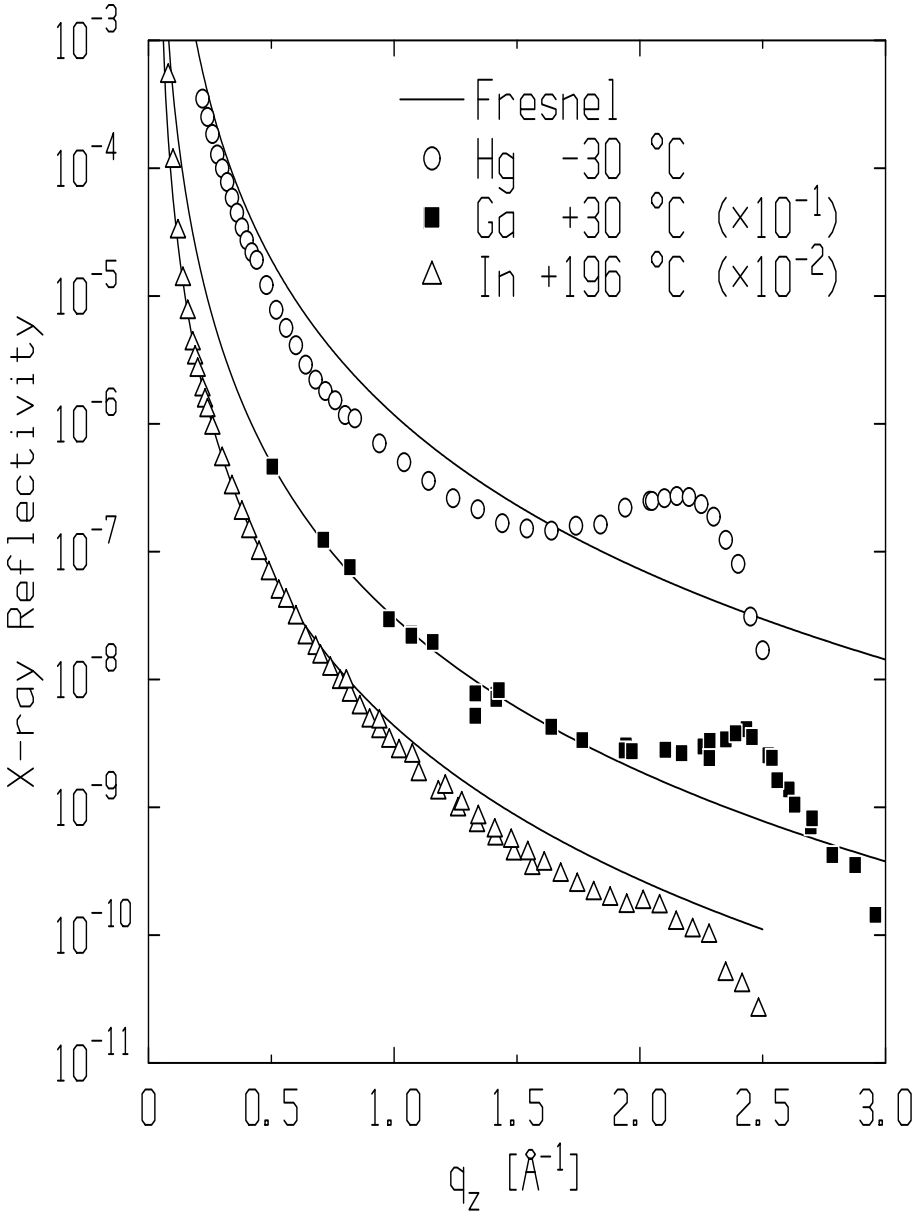



Figure 3.2: The plot showing x-ray reflectivity data taken from liquid Hg (circles), Ga (squares) and In (triangles), along with theoretically predicted Fresnel curves (lines).

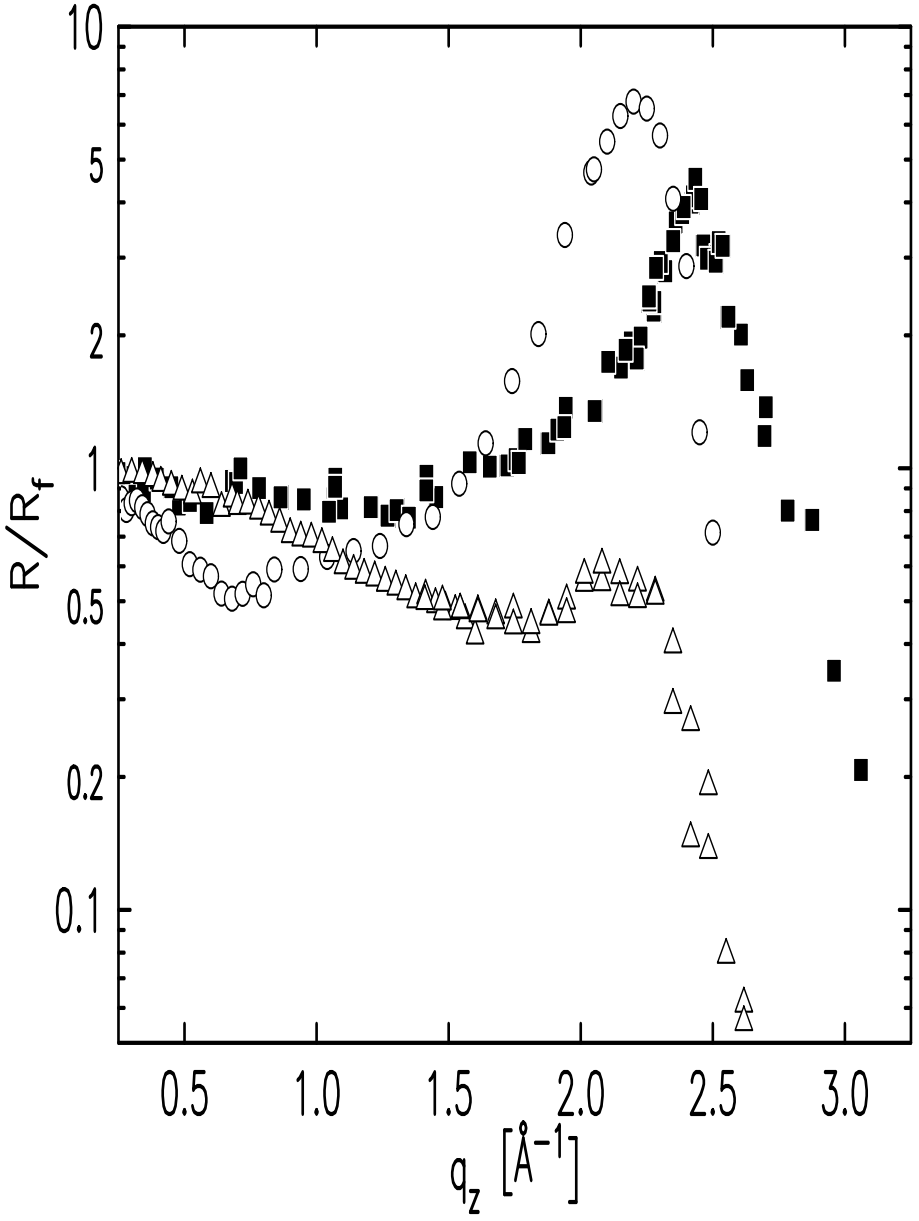



Figure 3.3: The plot showing Fresnel-normalized x-ray reflectivity data taken from liquid Hg (circles), Ga (squares) and In (triangles).

has now been done for the two metals with the lowest melting temperatures (Ga[15], and Hg[16]) since it is for these metals that the practical range of temperatures is largest. In the next section we will illustrate this effect for Ga. Although we will not show them, the results for Hg are similar.

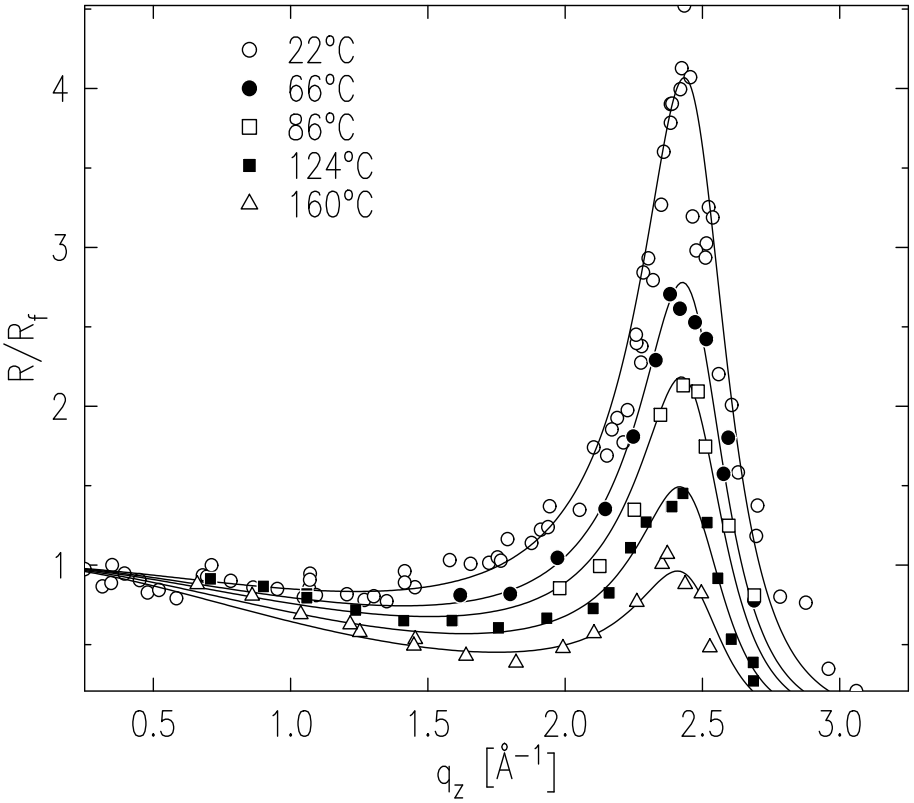



Figure 3.4: Fresnel-normalized x-ray reflectivity data measured for liquid Ga in the temperature range of 22°C to 160°C.

### 3.4.2 Temperature-Dependent Reflectivity: Liquid Ga

In Figure 3.4 we show Fresnel-normalized reflectivity data sets measured for liquid Ga at 22°C, 66°C, 86°C, 124°C and 160°C. The layering peak is most prominent for the lowest temperature and gradually decreases as the temperature increases.

In Figure 3.5 we show the intrinsic surface structure factor that is obtained by dividing the data by the predicted effect of capillary excitations (Eq. 2.9.16) using the published surface tension value of 718 mN/m. As can be seen, with the predicted capillary effects removed the intrinsic structure factor is independent of temperature.

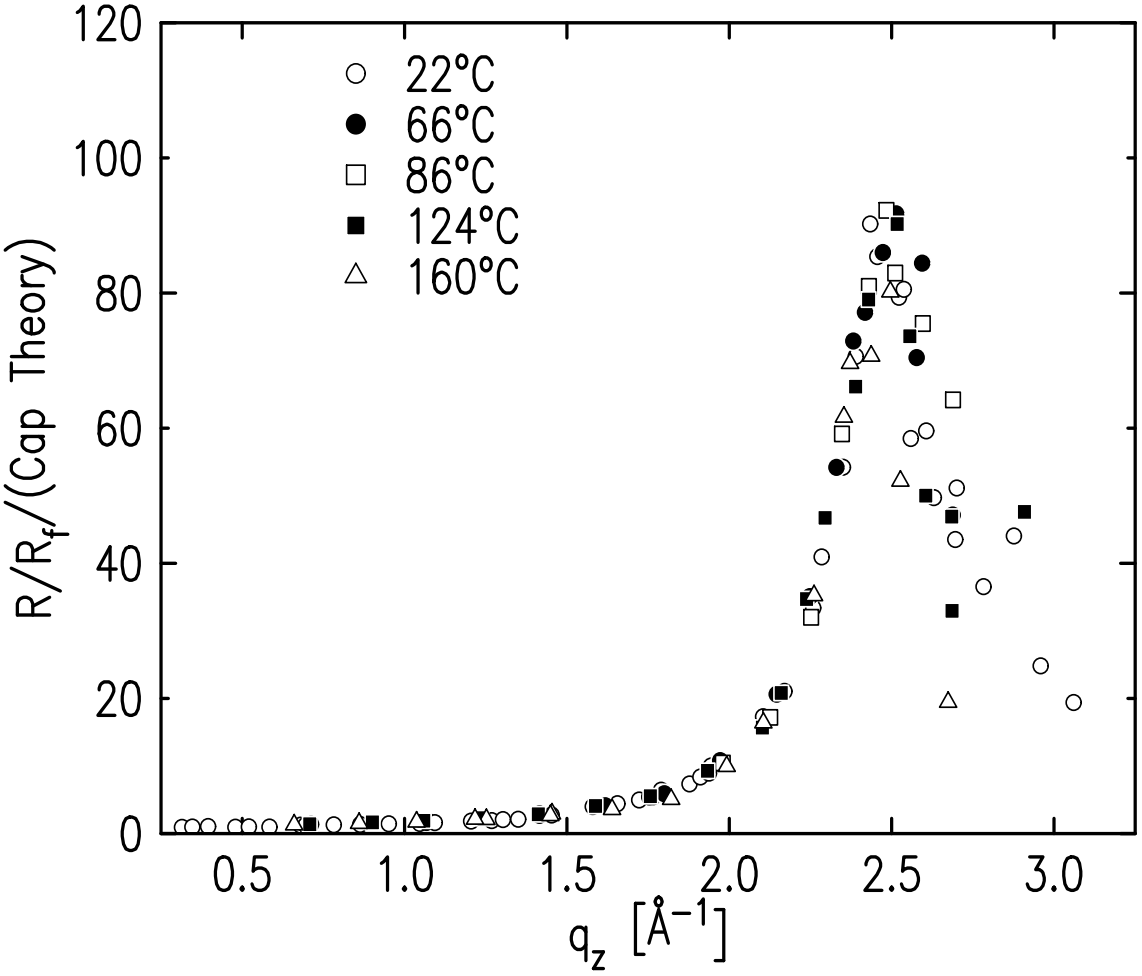



Figure 3.5: The temperature-dependent reflectivity datasets pictured in Figure 3.4 normalized to the thermal capillary wave fluctuations.

### 3.4.3 X-Ray Diffuse Scattering Data: Liquid In

In this thesis a *diffuse scattering scan* implies a measurement of signal as a function of $\beta$ at $\Delta\Theta = 0$ while keeping incident angle $\alpha$ fixed. The observed scattering therefore follows a trajectory in the $(q_x, q_z)$ plane with $dq_z/dq_x = \tan\beta$ and $q_y$=0. The signal measured in the specular reflectivity and diffuse scattering geometries are, however, related since the signal measured at $\beta = \alpha$ in the diffuse measurement is the specular signal.

The results of diffuse scattering scans that illustrate confirmation of the capillary wave prediction for liquid In are shown in Figure 3.6, which shows a set of diffuse scattering scans taken at various values of incident angle $\alpha$ (symbols), along with theoretical predictions of the capillary wave theory. For all experimental measurements, the signal originating at the surface was separated from the bulk diffuse background by subtracting intensities measured with the detector moved approximately 0.4° transverse to the reflection plane. The solid lines are the intensities that are theoretically predicted by numerically integrating the capillary prediction (Eq. 2.9.16) over the known resolution function, using the method described in Section 2.9.3, while also taking into account the background subtraction procedure.

The excellent agreement between the experimental data and theoretical predictions demonstrated in Figure 3.6 is a strong indication that one can rely on elements of capillary wave theory in order to successfully deconvolve the surface structure factor information related to the intrinsic atomic structure of the liquid surfaces. This method of deconvolving thermal contribution is going to be discussed in great details in Chapter 4 of this work.

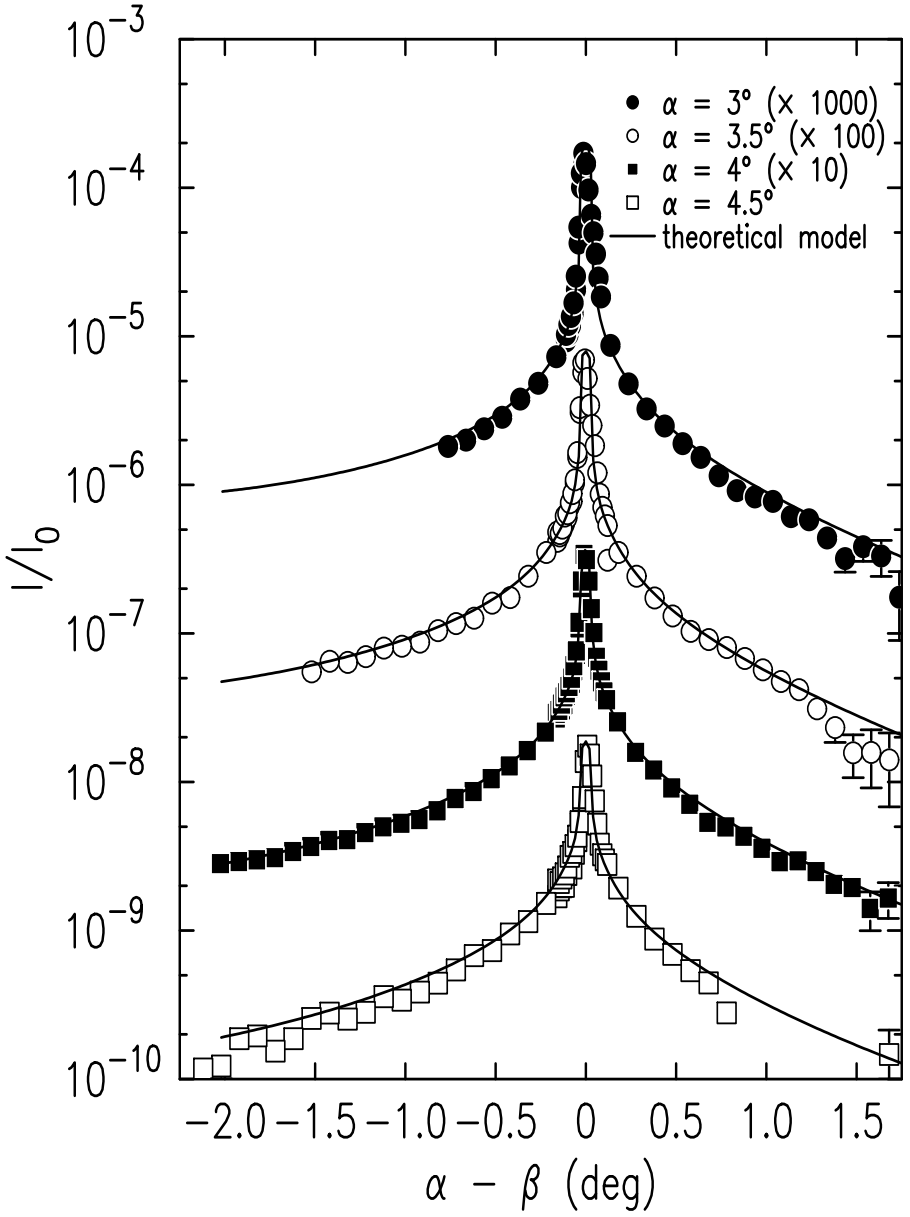



Figure 3.6: Diffuse scattering data for liquid indium (symbols), along with the theoretical simulations which follow from capillary wave theory (lines), taken at 3.0, 3.5, 4.0 and 4.5 degrees, which correspond to $\eta$ values of 0.049, 0.066, 0.087 and 0.110 respectively.

# Bibliography


[1] S.A. Rice, D. Guidotti, and H.L. Lemberg. Some comments on the electronic properties of liquid metal surfaces. In S.A. Prigogine, I.; Rice, editor, *Aspects of the study of surfaces. vol.27*, pages 543–633, Chichester, Sussex, UK, 1974. Wiley.

[2] E. Velasco, P. Tarazona, M. Reinaldo-Falagan, and E. Chacon. Low melting temperature and liquid surface layering for pair potential models. *Journal of Chemical Physics*, 117(23):10777–88, 2002.

[3] C.C. Addison. *The Chemistry of the Liquid Alkali Metals*. John Wiley and Sons, New York, 1984.

[4] H. U. Borgstedt and C. K. Mathews. *Applied Chemistry of the Alkali Metals*. Plenum Press, New York, 1987.

[5] *CRC Handbook of Chemistry and Physics*. CRC Press, Boca Raton, FL, 1985.

[6] Michael de Podesta. *Understanding the Properties of Matter*. Taylor & Francis, London, 2002.

[7] T. Iida and R. I. L. Guthrie. *The Physical Properties of Liquid Metals*. Oxford University Press, Oxford, 1993.

[8] G. W. C. Kaye and T. H. Laby. *Tables of physical and chemical constants and some mathematical functions*. Wiley, New York, 15th edition, 1986.

[9] John Emsley. *The Elements*. Clarendon PRess, Oxford, 3rd edition, 1998.

[10] M. Tolan. X-ray scattering from soft-matter thin films - materials science and basic research - introduction. *X-Ray Scattering from Soft-Matter Thin Films*, 148:1–+, 1999.

[11] C. H. Chou, M. J. Regan, P. S. Pershan, and X. L. Zhou. Model-independent reconstruction of smooth electron density profiles from reflectivity data of liquid surfaces. *Phys. Rev. E*, 55(6):7212–7216, 1997.

[12] Songyan Zheng, Joseph Strzalka, Che Ma, Stanley J. Opella, Benjamin M. Ocko, and J. Kent Blasie. Structural studies of the hiv-1 accessory protein vpu in langmuir monolayers: Synchrotron x-ray reflectivity. *Biophys. J.*, 80(4):1837–1850, 2001.

[13] P.S. Pershan. Effects of thermal roughness on x-ray studies of liquid surfaces. *Colloids and Surfaces A (Physicochemical and Engineering Aspects)*, 171(1-3):149–57, 2000.

[14] O. M. Magnussen, B. M. Ocko, M. Deutsch, M. J. Regan, P. S. Pershan, D. Abernathy, G. Grubel, and J. F. Legrand. Self-assembly of organic films on a liquid metal. *Nature*, 384(6606):250–252, 1996.

[15] M.J. Regan, E.H. Kawamoto, S. Lee, P.S. Pershan, N. Maskil, M. Deutsch, O.M. Magnussen, B.M. Ocko, and L.E. Berman. Surface layering in liquid gallium: an x-ray reflectivity study. *Phys. Rev. Lett.*, 75(13):2498–501, 1995.

[16] O. M. Magnussen, B. M. Ocko, M. J. Regan, K. Penanen, P. S. Pershan, and M. Deutsch. X-ray reflectivity measurements of surface layering in liquid mercury. *Phys. Rev. Lett.*, 74(22):4444–4447, 1995.

[17] H. Tostmann, E. DiMasi, P. S. Pershan, B. M. Ocko, O. G. Shpyrko, and M. Deutsch. Surface structure of liquid metals and the effect of capillary waves: X-ray studies on liquid indium. *Phys. Rev. B*, 59(2):783–791, 1999.

# Chapter 4

# Temperature Dependent Surface Structure of Liquid Mercury

## 4.1 Abstract

In this chapter we present x-ray reflectivity measurements of liquid mercury between $-36°$C and $+25°$C. The surface structure can be described by a layered density profile convolved with a thermal roughness $\sigma_T$. The layering has a spacing of 2.72 Å and an exponential decay length of 5.0 Å. Surprisingly, $\sigma_T$ is found to increase considerably faster with temperature than the $\sqrt{T}$ behavior predicted by capillary wave theory, in contrast with previous measurements on Ga and dielectric liquids.

## 4.2 Introduction

The effect of temperature on the surface structure of a liquid is quite different from that of a solid surface. In the liquid, thermal surface waves are excited at all wavelengths from the particle spacing to a long wavelength gravitational cutoff, and produce a surface roughness on the order of the particle spacing. For non-metallic liquids,

these capillary waves broaden the liquid–vapor interface, which is a monotonically decreasing density profile with a width of several Å.[1]

Metallic liquids exhibit a more complex surface structure in which the atoms are stratified parallel to the liquid–vapor interface in layers that persist into the bulk for a few atomic diameters. This layering arises from the strongly density dependent non-local interionic potential[2] and is unique to metallic liquids. Nevertheless, the effect of temperature is still expected to be principally in the form of capillary waves, which roughen the surface-normal profile and diminish the layering amplitude. X-ray reflectivity measurements have confirmed the existence of surface layering in liquid Hg,[3] Ga,[4] In,[5] and several alloys.[6,7] Models based on capillary waves as the only mechanism for surface roughening were found to describe the temperature dependent layering of liquid Ga[8] as well as diffuse scattering measured from the liquid In surface.[5]

In previous comparisons of the x-ray reflectivity of liquid Hg and Ga,[9] two important differences were identified. Although reflectivities for both metals exhibit quasi–Bragg peaks indicative of surface layering, the Hg data have a minimum at low momentum transfer ($q_z \approx 0.6$ Å$^{-1}$) not found in Ga (see Fig. 2 in Ref. 9). To describe this minimum, the model for the surface structure had to be more complex than that of Ga. One successful model incorporated a low density region persisting a few Å into the vapor side of the interface. This feature was taken to be intrinsic to Hg. In addition, the room temperature layering peak appeared to be broader for Hg than for Ga, leading to the conclusion that in Hg, surface layering decayed over a much shorter length scale.

Subsequent measurements yielded variations in this low-$q_z$ minimum, prompting us to address the possible effect of impurities at the surface. An important difference

between experiments on Hg and Ga is that due to the low vapor pressure, Ga can be measured under ultra high vacuum (UHV) conditions and cleaned in situ by argon sputtering, which is not possible for Hg. In this work, we compare Hg measured in a reducing $H_2$ atmosphere[10] to measurements taken in a UHV compatible chamber having a very low oxygen partial pressure.

The present temperature dependent study has an important advantage over previous room temperature measurements. Near the melting point, the layering peak has a large amplitude and is easily distinguished from the region of the low-$q_z$ minimum. This allows a robust determination of the layering decay length that is not affected by the details of the models in the near-surface region. This is not the case at room temperature, where the shallow peak and pronounced minimum yield more ambiguous fits. We conclude in the present work that Ga and Hg have comparable layering decay lengths. This underscores the value of temperature dependent measurements for comparisons of liquid metals' surface structure.

## 4.3 Experimental Details

X-ray reflectivity measurements[1] were carried out using the liquid surface spectrometer at beamline X22B at the National Synchrotron Light Source, at an x-ray wavelength of 1.24 Å and resolution of 0.035 $Å^{-1}$.[11] The background intensity, due mainly to scattering from the bulk liquid, was subtracted from the specular signal by rocking the detector out of the reflection plane.

## 4.4 Sample Preparation

Liquid mercury was prepared in two different sample chambers. In the first, the Hg sample[12] was contained in a glass reservior with a teflon stopcock and glass filling capillary, mounted on a high vacuum chamber comprised of a cylindrical thin-walled Be can mating to stainless steel flanges with viton o-ring seals. After several cycles of evacuating the chamber to $10^{-4}$ Torr and backfilling with 900 Torr of dry $H_2$ gas, the liquid Hg was poured from the reservoir into a ceramic sample pan. Surfaces appeared clean to the eye and yielded reproducible reflectivity measurements for as long as four days. When the sample was deliberately exposed to air, the reflectivity exhibited deep oscillations characteristic of rapid oxide formation.[13]

A second Hg reservoir, capillary and valve made from stainless steel was mounted on top of a UHV chamber. Following a bakeout, the sample was poured, with the Hg vapor pressure of about $10^{-2}$ Torr then determining the total pressure in the chamber. Small patches of oxide were initially observed, but disappeared from the surface within a few hours. Hg oxide is expected to decompose due to the low oxygen partial pressure in this pseudo UHV environment.[14] In addition, we observe a continuous evaporation and recondensation of Hg, constantly renewing the Hg surface.[15] The resulting Hg surface was stable, as determined by x-ray reflectivity, for eleven days.

In both chambers, a copper cold finger extended from the bottom of the sample pan into a liquid nitrogen dewar. Temperature was monitored near the sample pan, and calibrated in separate experiments with a sensor immersed in the Hg. Corrected sample temperatures are reported with relative errors of $\pm 1$°C. For the UHV chamber, the gradient between sample and thermometer was greater, and there is an additional systematic error which may be as large as 8°C. Both chambers rested on an active

vibration isolation unit.

## 4.5 X-Ray Reflectivity Measurements

Our x-ray reflectivity measurements reveal that the surface induced layering is strongly temperature dependent. Fig. 4.1(a) shows the reflectivity as a function of $q_z$ measured in the glass chamber for three temperatures between $-35°$C and room temperature. The quasi–Bragg peak observed at $q_z \approx 2.2$ Å$^{-1}$ indicates that the liquid metal is stratified near the surface. The peak position, amplitude and width give the length scales for the surface induced layering, which extends several Å into the bulk liquid. The other main feature of the data is the minimum in the reflectivity at $q_z \approx 0.6$–1.2 Å$^{-1}$, the depth of which differs between samples. This minimum is much more pronounced under the high pressure $H_2$ environment (900 Torr) than under the Hg vapor pressure of $10^{-2}$ Torr, as shown for two sets of room temperature measurements in Fig. 4.1(b). These low-$q_z$ data indicate that the details of the electron density within 5 Å of the surface are affected by the sample environment.

## 4.6 Electron Density Model

We have quantified the surface layering by constructing a model for the surface-normal density profile, parameterized as reported previously,[3,4,8] and fitting the reflectivity calculated from the model to the experimental data. The surface-normal density profile is constructed from slabs of electron density parallel to the liquid–vapor interface. The slabs represent planes of atoms separated by a distance $d$, which are disordered in-plane, and which have mean-squared surface-normal displacements increasing with

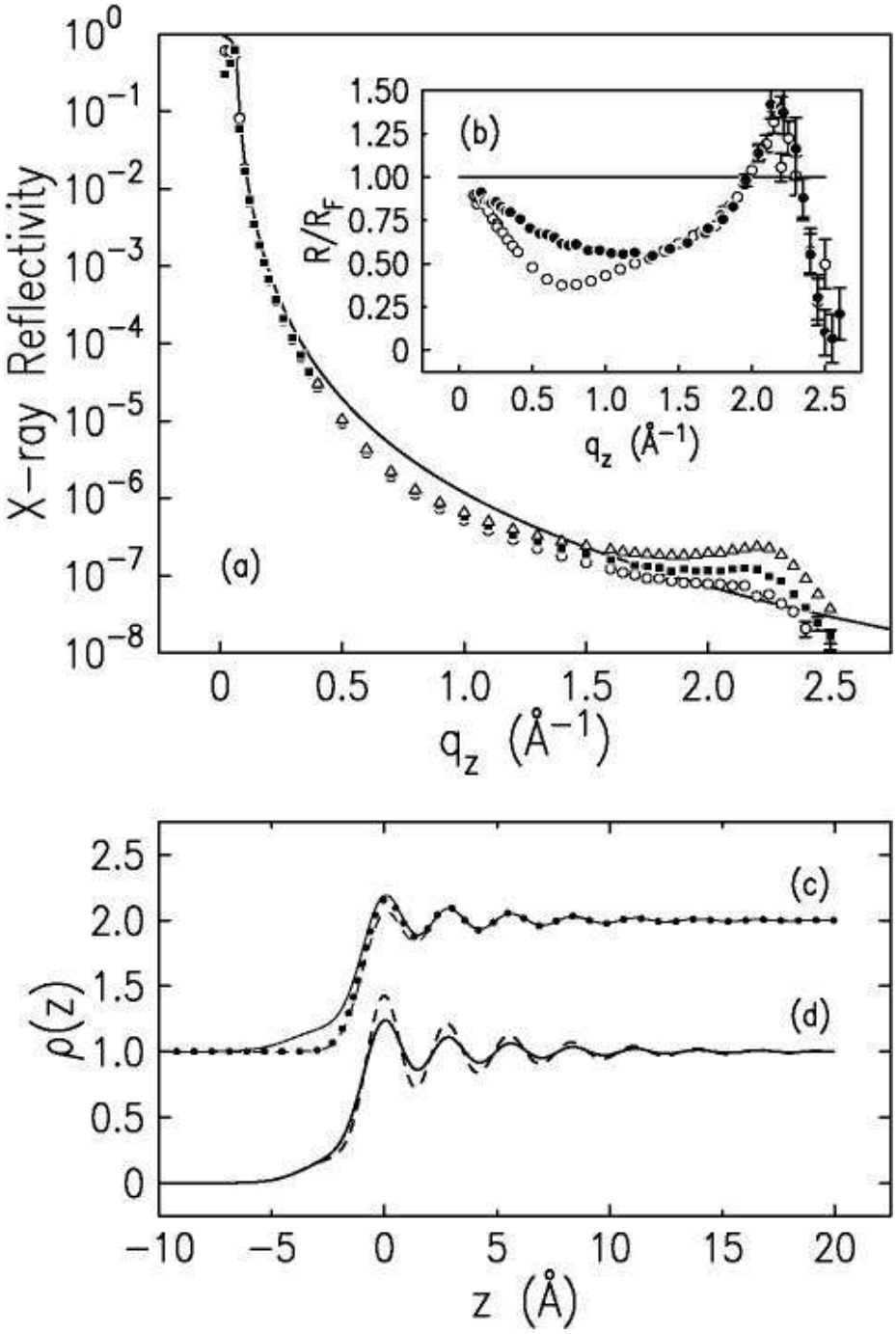



Figure 4.1: (a) X-ray reflectivity of liquid Hg. △: −35°C; ■: 0°C; ○: +23°C; (—): calculated Fresnel reflectivity $R_F$. (b) Room temperature reflectivity normalized by $R_F$ (—) for two Hg samples. ○: glass chamber with $H_2$ gas. ●: UHV chamber. (c) Calculated local layering profiles having $d = 2.72$ Å, $\overline{\sigma} = 0.46$ Å, and $\sigma_T = 1.0$ Å. $(\cdots)$: no surface modification. (—): adlayer model. (- - -): surface depletion model. (d) Best fit profiles for vacuum data. (—): Room temperature ($\sigma_T = 1.0$ Å). (- - -): $T = -36$°C ($\sigma_T = 0.8$ Å).

depth. The electron density profile is composed of a sum of Gaussian terms:

$$\rho(z) = \rho_\infty \sum_{n=0}^{\infty} \frac{d/\sigma_n}{\sqrt{2\pi}} \exp\left[-(z-d)^2/2\sigma_n^2\right] \ ,$$

where $\rho_\infty$ is the electron density of bulk Hg, and we represent the mean-squared displacements in the $n$th layer by $\sigma_n^2 = n\overline{\sigma}^2 + \sigma_T^2$, where $\sigma_T$ characterizes the roughness of the layer nearest the surface. Far into the bulk, $n\overline{\sigma}^2$ becomes large, and no layering is present, so that $\overline{\sigma}$ quantifies a layering decay length. With this form for $\rho(z)$, the reflectivity, proportional to the Fresnel reflectivity $R_F$ of an abruptly terminated homogeneous electron density, can be calculated analytically and yields

$$\begin{aligned} \frac{R(q_z)}{R_F} &= \left| \frac{1}{\rho_\infty} \int_{-\infty}^{+\infty} (\partial\rho/\partial z) \exp(iq_z z)\, dz \right|^2 \\ &= F^2 (q_z d)^2 \exp(-\sigma_T^2 q_z^2) \times \\ &\quad \left[1 - 2\exp(-q_z^2\overline{\sigma}^2/2)\cos(q_z d) + \exp(-q_z^2\overline{\sigma}^2)\right]^{-1} \ , \end{aligned}$$

where the reduced scattering form factor $F = (f(q_z) + f')/(Z + f')$ has been inserted, as presented previously.[16]

The parameters $\sigma_T$, $\overline{\sigma}$, and $d$ control the height, width and position of the layering peak, and characterize a simple local layering profile (Fig. 4.1(c), dotted line). Although this model is sufficient for liquid Ga[4,8] and In,[5] it does not yield a good fit to the the low-$q_z$ reflectivity of liquid Hg. To account for the low-$q_z$ reflectivity we have considered profiles which incorporate density terms in addition to the layered model, modifying the first Hg layer, the first several layers, and/or the region several Å towards the vapor side of the interface. These additional features are independent of temperature. The modification having the best fit for all data is a single additive Gaussian term $f_A\rho_\infty(d/\sigma_A\sqrt{2\pi})\exp[-(z-z_A)/2\sigma_A^2]$, positioned a few Å into the vapor region, with a width $\sigma_A \approx 1.5$ Å and a density $f_A$ relative to the bulk varying

from 0.1–0.3 between samples. (Fig. 4.1(c), solid line). However, this model is difficult to distinguish mathematically from one in which the density of the first Hg layer is decreased. In particular, the data with the most exaggerated low-$q_z$ minima can be fit by models with a broadened, depleted first Hg layer and an expanded spacing between the first two layers (Fig. 4.1(c), dashed line). Models having alternating long and short layer spacings, as might result from atomic pairing, do yield destructive interference at low $q_z$ but do not fit the data well.

Deviations from the simple oscillatory profile are smaller for samples poured in a UHV chamber at $10^{-7}$ Torr following a bakeout than for measurements in a glass chamber evacuated to only $10^{-4}$ Torr. To explain this difference, we attribute the modified density profile to the presence of impurities. In recent self-consistent quantum monte carlo simulations of the Hg-vapor interface, no vapor-side tail or appreciable modification of the surface layer was observed in the computed density profile.[17] As discussed above, we believe the presence of macroscopic oxide is unlikely, although oxygen, water or other contaminants introduced with the Hg sample may be present in small amounts. These may form a passivated, low-density adlayer or incorporate themselves into the first Hg layer to alter its density.

## 4.7 Discussion

Although the available x-ray data do not allow a unique determination of the near-surface region, we obtain reliable information on the temperature dependence of the surface-normal density profile. All Hg data are described by local layering parameters $d = 2.72 \pm 0.02$ Å and $\overline{\sigma} = 0.46 \pm 0.05$ Å. These values are obtained for both $H_2$ and vacuum measurements, and are independent of the model surface modification. The

temperature dependence of the reflectivity can be quantified solely by the variation of $\sigma_T$, as shown in Fig. 4.2(a) for measurements in $H_2$ atmosphere. This parameter controls the amplitude of the layering peak and is directly related to the amplitude of the density oscillations at the surface, as shown in Fig. 4.1(d) for vacuum measurements, varying from 0.8 Å near the melting point to about 1.0 Å at room temperature. The other parameters, if allowed to vary for each temperature independently, show no systematic dependence on $T$.

In particular, this means that the layering decay length of $5.0 \pm 0.5$ Å for Hg is independent of temperature, as was previously shown for Ga.[8] This is somewhat surprising, since it is not obvious that layering should persist over essentially the same length scale in the face of thermal roughening which effectively broadens the interfacial width. Such a model, in which the local surface-normal density profile is independent of the surface height fluctuations, is intrinsic to the analyses long used for calculating the scattering cross section from rough surfaces.[18,19] Previous observations on liquid metals demonstrated that such an interpretation appears to be justified.[5,8] In fact, it has been thought that the liquid metal surface may provide the best justification of this approach, since the measured reflectivity peak is a dramatic structural feature that is both straightforward to characterize and strongly affected by surface height fluctuations that vary considerably with temperature.

In the capillary wave model, thermally excited surface waves produce mean-squared displacements for which the restoring force is due to the surface tension $\gamma$:

$$\sigma_{\mathrm{cw}}^2(T) = \frac{k_B T}{2\pi\gamma} \ln\left(\frac{k_{\max}}{k_{\min}}\right) ,$$

where $k_{\max} = 1.2$ Å$^{-1}$ and $k_{\min} = 7.4 \times 10^{-3}$ Å$^{-1}$ are wavevector cutoffs determined

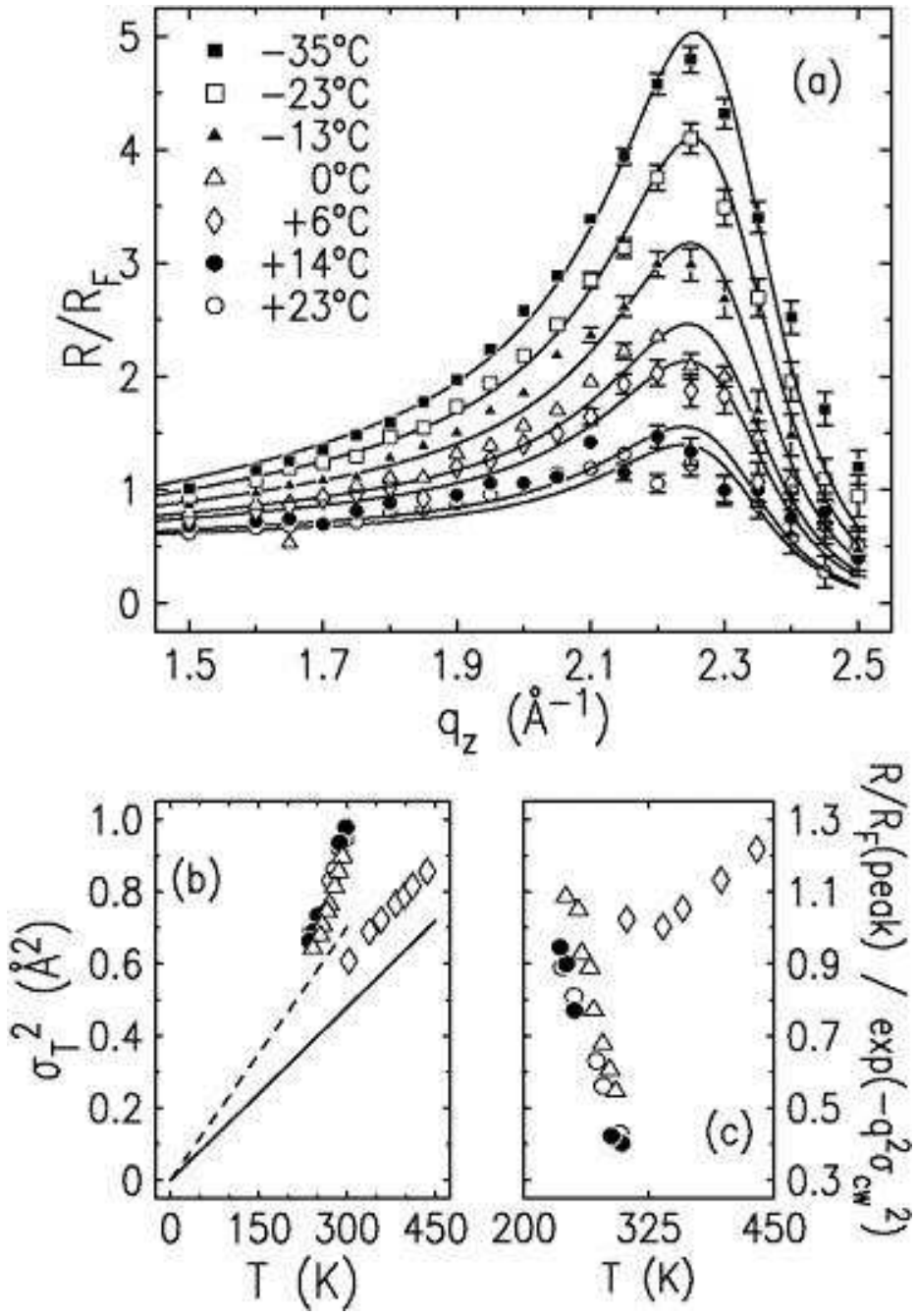



Figure 4.2: (a) $R/R_F$ for different temperatures, from sample measured in $H_2$ atmosphere. Solid lines are fit curves for which $\sigma_T$ has been varied. (b) Temperature dependence of $\sigma_T^2$. △: Measurement in vacuum). ○: Measurement in $H_2$ gas). •: Second sample measured in $H_2$ gas. ◇: Ga data from Ref. 8. Lines: Capillary wave form $\sigma_{cw}^2(T)$ for Hg (- - -) and Ga (—). (c) Temperature dependence of $(R/R_F)/\exp(-q^2\sigma_{cw}^2)$ at the layering peak, normalized at the melting point, for Ga (◇) and Hg (symbols as in (b)).

by the atomic size and the instrumental resolution, respectively.[1] This model has been successfully applied to dielectric liquids[1,20] and to liquid Ga.[8] Fig. 4.2(b) compares $\sigma_{\rm cw}^2$ calculated as a function of temperature for Hg and Ga (dashed and solid lines), for appropriate values of the surface tension,[21] bulk interatomic spacing,[21] and instrumental resolution, to the surface roughness $\sigma_T$ extracted from reflectivity measurements of Hg and Ga (symbols). The temperature dependence of $\sigma_T$ differs fundamentally between Hg and Ga. For Ga, the slope of the experimental points matches that of the capillary wave model, offset only by a constant term $\sigma_0 \approx 0.3$ Å, attributed to an intrinsic roughness.[8] This allows the quantity $\sigma_T$ for Ga (denoted in Ref. 8 by $\sigma_c$) to be written as $\sigma_T^2 = \sigma_0^2 + \sigma_{\rm cw}^2$. Liquid Ga, therefore, has a temperature independent local surface layering profile, roughened by capillary waves.

By contrast, $\sigma_T^2(T)$ for Hg has a much steeper slope than predicted by capillary wave theory, exhibiting an additional temperature dependent roughness. This result is independent of the local layering model, as shown in Fig. 4.2(c), where we plot $(R/R_F)/\exp(-q^2\sigma_{\rm cw}^2)$ for Hg and Ga at their layering peaks vs. $T$, normalized at the melting point. The Ga data increase only slightly with $T$, within their scatter of about 15%. The Hg data exhibit a steep slope far exceeding the $\approx 15\%$ scatter. The temperature dependence of the Hg–vapor interface roughness has also been extracted from recent self-consistent quantum monte carlo simulations.[17] While similar linear behavior of $\sigma_T^2(T)$ is observed, direct comparison of the slope is complicated by the differences in capillary wave cutoffs and surface tension between the experimental and simulation samples.

The temperature dependence of $\gamma$, even considering the possible effects of impurities, can be ruled out as a cause. For pure Hg, $d\gamma/dT \approx -0.2 \times 10^{-3}$ N/mK,[21]

an order of magnitude too small to explain our observations. Optical measurements on Hg surfaces with varying degrees of cleanliness have found $d\gamma/dT$ in the range of $-0.7 \times 10^{-3}$ to $+0.3 \times 10^{-3}$ N/mK depending on the method of sample preparation.[22] The observation that oxide or contamination can produce $d\gamma/dT > 0$ for Hg is notable, but this would cause a reduction of $\sigma_T$ with increasing $T$ rather than the increase observed, and so can not account for our results.

## 4.8 Summary

We have measured specular x-ray reflectivity from liquid mercury between $-36$°C and $+25$°C. The longitudinal density profile exhibits density oscillations due to strongly temperature dependent surface induced layering, as well as a sample dependent low-density feature near the liquid–vapor interface, independent of $T$. We conclude that the surface structure of liquid Hg has a temperature dependent component in addition to capillary wave roughening. This may take the form of temperature dependent height fluctuations which increase the mean-squared atomic displacements beyond the effect of capillary waves, or of a temperature dependent local density profile. The specular reflectivity measurements presented here can not distinguish between these two cases. Measurements of diffuse scattering from the Hg surface may provide further information. These results re-emphasize the fact that roughness intrinsic to the surface-normal density profile in general can not be unambiguously separated from height fluctuations, despite previous treatments of scattering from the liquid surface.

# Bibliography


[1] A. Braslau *et al*, Phys. Rev. A **38**, 2457 (1988).

[2] S. A. Rice, J. Non-Cryst. Solids, **205–207**, 755 (1996).

[3] O. M. Magnussen *et al*, Phys. Rev. Lett. **74**, 4444 (1995).

[4] M. J. Regan *et al*, Phys. Rev. Lett. **75**, 2498 (1995).

[5] H. Tostmann *et al*, submitted to Phys. Rev. B (July 1998).

[6] H. Tostmann *et al*, Ber. Bunsenges. Phys. Chem., to appear September 1998.

[7] N. Lei *et al*, J. Chem. Phys. **104**, 4802 (1996); N. Lei em et al, J. Chem. Phys. **107**, 4051 (1997); M. J. Regan *et al*, Phys. Rev. B **55**, 15874 (1997).

[8] M. J. Regan *et al*, Phys. Rev. B **54**, 9730 (1996).

[9] M. J. Regan *et al*, J. Non-Cryst. Solids **205–207**, 762 (1996).

[10] D. Turnbull, private communication. More recently it has been recognized that passivation of Hg oxide occurs only at elevated temperatures: V. Kolevzon, private communication.

[11] The reflectivity measured for $q_z \gtrapprox 1.2$ Å$^{-1}$ varies by a few percent depending on the choice of vertical detector resolution, due to diffuse scattering near the specular

condition which arises from surface fluctuations. We have not incorporated this small effect into our analysis of the reflectivity. A detailed discussion is given in Ref. 5.

[12] Quadruple distilled Hg with $< 1$ ppm metal impurities, Bethlehem Apparatus Co., Inc., Front and Depot Streets, Hellertown PA 18055

[13] H. Tostmann *et al*, J. Non-Cryst. Sol., submitted August 1998.

[14] B. N. Thomas *et al*, J. Chem. Phys. **86**, 1036 (1987).

[15] B. C. Lu and S. A. Rice, J. Chem. Phys. **68**, 5558 (1978).

[16] In this paper, we consistently use $n = 0$ to refer to the surface layer. This produces discrepancies with the equations given in Ref. 3.

[17] D. S. Chekmarev *et al*, submitted to Phys. Rev. E (July 1998).

[18] S. K. Sinha *et al*, Phys. Rev. B **38**, 2297 (1988).

[19] M. K. Sanyal *et al*, Phys. Rev. Lett. **66**, 628 (1991).

[20] M. Fukuto *et al*, submitted to Phys. Rev. Lett. (April 1998).

[21] T. Iida and R. I. L. Guthrie, *The Physical Properties of Liquid Metals*, Oxford University Press, 1993.

[22] V. Kolevzon and G. Pozdniakov, J. Phys.: Condens. Matter **9**, 6815 (1997) and references therein.

# Chapter 5

# X-ray Studies on Liquid Indium

## 5.1 Abstract

In this chapter we describe x-ray reflectivity (XR) and small angle off-specular diffuse scattering (DS) measurements from the surface of liquid Indium close to its melting point of 156°C. From the XR measurements we extract the surface structure factor convolved with fluctuations in the height of the liquid surface. We present a model to describe DS that takes into account the surface structure factor, thermally excited capillary waves and the experimental resolution. The experimentally determined DS follows this model with no adjustable parameters, allowing the surface structure factor to be deconvolved from the thermally excited height fluctuations. The resulting local electron density profile displays exponentially decaying surface induced layering similar to that previously reported for Ga and Hg. We compare the details of the local electron density profiles of liquid In, which is a nearly free electron metal, and liquid Ga, which is considerably more covalent and shows directional bonding in the melt. The oscillatory density profiles have comparable amplitudes in both metals, but surface layering decays over a length scale of $3.5 \pm 0.6$ Å for In and $5.5 \pm 0.4$ Å for Ga. Upon controlled exposure to oxygen, no oxide monolayer is formed on the

liquid In surface, unlike the passivating film formed on liquid Gallium.

## 5.2 Introduction

The structure of the free surface of a liquid metal is fundamentally different from that of a dielectric liquid such as water or Argon. For dielectric liquids, the interatomic or intermolecular potential is long-ranged and the nature of the interactions does not change significantly across the liquid–vapor interface. Theoretical modeling and molecular dynamics studies result in an interfacial density profile that varies monotonically from the bulk liquid density to the bulk vapor density.[1] This can be contrasted with results of computer simulations of dielectric liquid noble gases in contact with their solid phase.[2] There, the hard wall provided by the solid phase is shown to induce surface layering in the liquid with a well defined lamellar structure.

In liquid metals, the potential energy function changes drastically from a screened short-ranged Coulomb potential in the bulk liquid phase where the conduction electrons are delocalized to a long-ranged van der Waals type potential in the vapor phase where all electrons are localized.[3] In this case, density functional calculations[4,5] and computer simulations[6] indicate an oscillatory surface-normal density profile. This surface induced layering can be attributed to the fact that strong Coulomb interactions between the abruptly truncated conduction electrons at the surface and the ion cores impose a constraint ordering the surface in a well defined lamellar structure. This constraint can be thought of as an effective hard wall ionic potential at the surface where the conduction electron density abruptly terminates.

The existence of surface layering in liquid metals has only recently been verified

unambiguously by experiment, first for liquid Hg[7] and then for liquid Ga.[8] Comparison of the temperature dependence of this layering, however, reveals qualitative differences between the two metals.[9,10] This observation indicates that details of the interactions such as the degree of covalency in the metal may affect the surface structure.

For crystalline metals that can be described by weak pseudo–potentials, electron–ion scattering is relatively weak and the non localized or itinerant electrons can be treated as if they were essentially free.[11] Alkali metals with their nearly parabolic energy bands are the prime example of this class of nearly free electron (NFE) like metals. In analogy with this, the term NFE metals applies to liquid metals whose conduction electrons have similar itinerant character and are only weakly perturbated by a small ionic pseudopotential.[12] NFE liquid metals can be contrasted with those whose conduction electrons are partially localized in covalent bonds.[13] Evidence for such covalent character in liquid metals may be obtained from measurements of the optical properties as well as from the bulk liquid structure factor.[14]

In fact, both liquid Ga and Hg show substantial deviations from NFE behavior. In liquid Ga, a shoulder in the bulk liquid structure factor indicates the presence of directional bonding in the melt.[15,16,17,18] Liquid Hg displays a pronounced asymmetry in the first peak of the bulk liquid structure factor, and the optical constants of liquid Hg deviate markedly from the predictions of the Drude theory for free electrons,[19] which, for example, adequately describes the optical constants of the alkali metals.[20,21] In order to understand which aspects of surface layering may be affected by deviations from NFE character, it is necessary to investigate liquid metals with less tendency towards covalent bonding. The alkali metals would be ideal candidates

in this regard. Unfortunately, the very low surface tension of liquid alkali metals will result in a large thermally induced surface roughness, making it extremely difficult to observe the surface layering experimentally. This is exacerbated by the fact that alkali metals are very reactive in air but cannot be investigated under Ultra High Vacuum (UHV) conditions due to their high vapor pressure. Liquid Indium, which has a high surface tension, reasonably low melting point and low vapor pressure does not suffer from these shortcomings. Moreover, it is considered to be NFE like for the following reasons. First, the first peak in the bulk structure factor of liquid In is highly symmetric, indicating the absence of significant orientational bonding in the melt.[22] Second, quantitative analysis of the shape of the bulk liquid structure factor yields a twelve-fold coordination with an interatomic distance that decreases with increasing temperature.[23] This is precisely what is expected for a liquid that can be described by an ideal hard sphere model. Third, the measured optical properties of liquid In agree with the Drude free electron theory over a large range of wavevectors.[24] Even more interesting, the optical constants of mixtures of liquid Hg and In differ appreciably from free electron behavior for Hg rich compositions, but gradually approach free electron behavior with increasing In content.[25] A main objective of this study is to compare the surface structure of the more NFE like liquid metal In to that of the more covalent liquid Ga.

This fundamental interest in the relationship between the surface structure and electronic properties of liquid metals bears directly on the topic of surface reactions, which is of considerable practical importance. This is especially true for liquids, where the atoms are mobile, and reactions at the surface can directly affect alloying, phase formation and other properties of the bulk. For this reason, surfaces and reactions

at surfaces play a critical role in process and extractive metallurgy.[26] We previously demonstrated that on exposure to oxygen the surface of liquid Ga becomes coated with a uniform 5 Å thick passivating oxide film that protects the underlying bulk phase from further oxidation.[27] We will show below that the oxidation behavior of liquid In is fundamentally different from that of Ga.

## 5.3 Experimental Details

The experiments reported here were primarily performed at the beamline X25 at the National Synchrotron Light Source (NSLS). Following a toroidal focussing mirror, a Ge (220) crystal was used to select the x-ray wavelength $\lambda = 0.653$ Å and to tilt the beam downward onto the horizontal liquid metal surface. The geometry of this liquid spectrometer has been described elsewhere.[28] Additional data were acquired at beamline X22B at the NSLS, using a similar scattering geometry and an x-ray wavelength of 1.24 Å. The size of the x-ray beam striking the liquid metal surface was determined by 1 mm (horizontal) $\times$ 0.1 mm (vertical) slits downstream of the monochromator and the measured signal was normalized to the incoming beam intensity.

The experimental resolution, determined primarily by slits in front of the detector, was varied for different experimental configurations. Specular reflectivity was primarily measured using a conventional NaI scintillation detector. Typical slit settings for measuring this specular reflectivity at X25 were 4 mm (h) $\times$ 4 mm (v). At 600 mm from the sample this yields a $q_z$ resolution of 0.06 Å$^{-1}$. For comparable resolution at the longer wavelength at X22B, a vertical detector slit of 8 mm was used. Small angle

off-specular surface diffuse scattering was measured using a position sensitive detector (PSD) aligned within the reflection plane.[29] For a given incident angle, the PSD detects both the specular reflection and off-specular diffuse intensity in the reflection plane up to $\approx 0.5^\circ$ away from the specular peak. We used a coarse vertical resolution for the PSD in the multi channel mode (64 channels on 20 mm). Away from the specular peak, where the intensity varies slowly with position, data from neighboring channels were averaged together for improved statistics. Counting all photons hitting the detector, and disregarding the positional information, the PSD can be used as a conventional counter. In this "single channel" mode the slit settings were 20 mm vertically and 3 mm horizontally, corresponding to a $q_z$ resolution of 0.32 $\text{Å}^{-1}$. For all experimental arrangements, the signal originating at the surface was separated from the bulk diffuse background by subtracting intensities measured with the detector moved approximately $\pm 0.4^\circ$ (corresponding to $\approx 0.67\,\mathring{A}^{-1}$) transverse to the reflection plane.[28]

The linearity of the PSD was checked by comparison of diffuse scans taken with the PSD to diffuse data taken by moving the scintillation detector within the reflection plane, and by measuring the specular reflectivity with the stationary PSD in a single-channel mode. As we will discuss below, once scaled for the different resolution, the different types of scans perfectly overlap each other.

Indium of 99.9995% purity was contained in a Molybdenum pan within an Ultra High Vacuum (UHV) chamber to maintain a clean surface.[30] Details of the UHV chamber design can be found elsewhere.[28] The sample was heated above the melting point of liquid In to $170 \pm 5$ °C. After a three day bakeout, the pressure was $8 \times 10^{-10}$ Torr, with a partial oxygen pressure $< 8 \times 10^{-11}$, for which the formation

time for an oxide monolayer is calculated to be several days.[31] Although patches of oxide were present on the In ingot when it was introduced into the chamber, this oxide was removed by Argon ion sputtering (2.5 keV, 20 $\mu$A ion current) at an Ar partial pressure of about $5 \times 10^{-5}$ Torr. The impact of the ion beam induced mass flow along the surface that transported the oxide patches towards the ion beam, thus cleaning the entire liquid–vacuum interface and not only the area hit directly by the $Ar^+$ ions.[32] Data presented here were always taken within one to two hours of sputter cleaning the sample. Since data acquired without sputtering but within a few hours reproduced each other, and because of the unique growth properties of oxide on liquid In which will be presented below, we are confident that the measured scattering is intrinsic to a clean liquid Indium surface.

A major improvement over experiments described previously is the incorporation of active vibration isolation. Previous measurements eliminated mechanically induced surface waves by utilizing the viscous drag at the bottom of thin samples. These samples had curved surfaces, requiring a time consuming technique to measure the reflectivity[28] and making it very difficult to measure at grazing incidence, important for the detection of in-plane ordering. In this work, the rigid UHV chamber and ion pump assembly were mounted on an active vibration isolation unit,[33] similar to that used previously in our studies of liquid Hg.[7] With this system we were able to use a sample pan 5 mm deep and 60 mm in diameter, resulting in flat samples where the angular deviation of the surface normal from the vertical across the surface was negligible compared to the critical angle for total external reflection of x-rays.

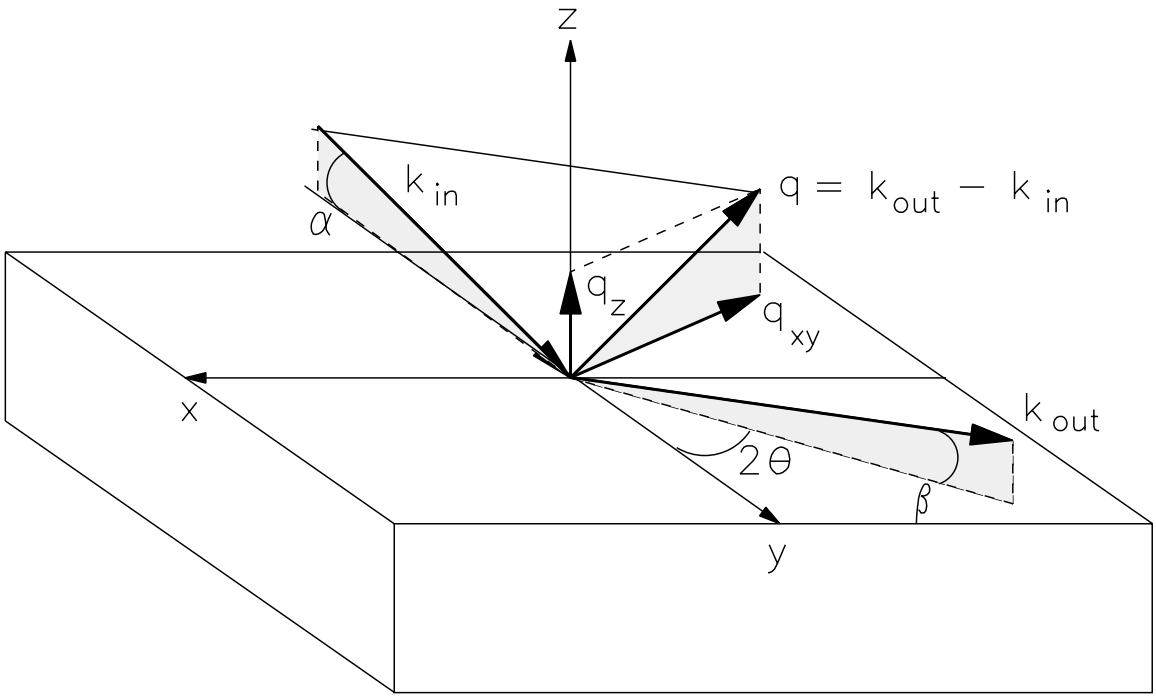



Figure 5.1: Sketch of the geometry of x-ray scattering from the liquid surface with $\alpha$ and $\beta$ denoting incoming and outgoing angle, the incoming and outgoing wavevector $\vec{k}_{in}$ and $\vec{k}_{out}$ respectively and the azimuthal angle $2\theta$. The momentum transfer $\vec{q}$ has an in-plane component $q_{xy}$ and a surface-normal component $q_z$.

## 5.4 Theory

The scattering geometry is given in Figure 5.1, defining the liquid surface to be lying in the $x$-$y$ plane, with x-rays incident at an angle $\alpha$ and collected by the detector at an elevation angle $\beta$ and azimuthal angle $2\theta$. The momentum transfer $\vec{q}$ can be decomposed into surface normal, $q_z$, and surface parallel, $q_{xy}$, components given by:

$$q_z = \frac{2\pi}{\lambda}(\sin\beta + \sin\alpha) \qquad \text{and} \qquad q_{xy} = \frac{2\pi}{\lambda}\sqrt{\cos^2\alpha + \cos^2\beta - 2\cos\alpha\cos\beta\cos 2\theta}\,. \tag{5.4.1}$$

In the following, we develop a formula for the differential cross section $d\sigma/d\Omega$ for x-ray scattering from a rough and structured liquid surface. The general expression

for the differential cross section for x-ray scattering from a three dimensional electron distribution $\rho(\vec{r})$ at a given location $\vec{r}$ can be expressed in terms of the electron density correlation function $\langle\rho(\vec{r})\rho(\vec{r}\prime)\rangle = \langle\rho(\vec{r}-\vec{r}\prime)\rho(0)\rangle$:[34]

$$\frac{d\sigma}{d\Omega} = V\left(\frac{e^2}{mc^2}\right)^2 \int d^3(\vec{r}-\vec{r}\prime)\langle\rho(\vec{r}-\vec{r}\prime)\rho(0)\rangle \exp\left[\imath\vec{q}\cdot(\vec{r}-\vec{r}\prime)\right] \tag{5.4.2}$$

where $V$ is the illuminated volume. If the density distribution is homogeneous within the $x$-$y$ plane but inhomogeneous normal to the surface, the density correlation function depends on the different positions $\vec{r}_{xy} - \vec{r}_{xy}\prime$ on the surface and the distances $z$ and $z\prime$ from the surface. For an x-ray beam of a cross sectional area $A_0$ incident on the surface at an angle $\alpha$ relative to the $x$-$y$ plane, the illuminated area is $A_0/\sin(\alpha)$ and the differential cross section can be written:[35]

$$\frac{d\sigma}{d\Omega} = \frac{A_0}{\sin(\alpha)}\left(\frac{e^2}{mc^2}\right)^2 \int dz dz\prime d^2\vec{r}_{xy}\langle\rho(\vec{r}_{xy},z)\rho(0,z\prime)\rangle \exp\left[\imath q_z(z-z\prime) + \imath\vec{q}_{xy}\cdot\vec{r}_{xy}\right]. \tag{5.4.3}$$

For a homogeneous liquid that is sufficiently far away from any critical region, the only long wavelength excitations that give rise to significant scattering are thermally excited surface capillary waves. In this case, there is some length $\xi$ such that for $|\vec{r}_{xy}| > \xi$ the density density correlation function can be expressed in terms of a density profile $\tilde{\rho}[z - h(\vec{r}_{xy})]$ defined relative to the local position of the liquid surface $h(\vec{r}_{xy})$ and capillary wave induced relative variations of the height, $h(\vec{r}_{xy}) - h(\vec{r}_{xy}\prime)$.[36]

$$\langle\rho(\vec{r}_{xy},z)\rho(0,z\prime)\rangle \overset{|\vec{r}_{xy}|\geq\xi}{\longrightarrow} \tilde{\rho}(z-[h(\vec{r}_{xy})-h(0)])\tilde{\rho}(z\prime) \tag{5.4.4}$$

Defining $\delta\rho(\vec{r}_{xy},z) = \rho(\vec{r}_{xy},z) - \tilde{\rho}(z-h(\vec{r}_{xy}))$, the differential cross section from a liquid surface can now be written:

$$\begin{aligned}\frac{d\sigma}{d\Omega} = \frac{A_0}{\sin(\alpha)}\left(\frac{e^2}{mc^2}\right)^2 &\int dz dz\prime d^2\vec{r}_{xy} \exp\left[\imath q_z(z-z\prime) + \imath\vec{q}_{xy}\cdot\vec{r}_{xy}\right] \\ &\times\left\{\tilde{\rho}(z-[h(\vec{r}_{xy})-h(0)])\tilde{\rho}(z\prime) + \langle\delta\rho(\vec{r}_{xy},z)\delta\rho(0,z\prime)\rangle\right\}.\end{aligned} \tag{5.4.5}$$

The second term in the integrand is only non-vanishing for regions $|\vec{r}_{xy}| \leq \xi$. This term gives rise to both the bulk diffuse scattering and surface scattering at momentum transfers having large $q_{xy}$ components.[35] The effect of this term can be separated experimentally from the specular reflection and may be omitted in the following discussion of scattering close to the specular condition. A change of variables yields

$$\frac{d\sigma}{d\Omega} \approx \frac{1}{16\pi^2}\left(\frac{q_c}{2}\right)^4 \frac{A_0}{\sin(\alpha)}\frac{|\Phi(q_z)|^2}{q_z^2}\int_{|\vec{r}_{xy}|>\xi} d^2\vec{r}_{xy}\langle\exp\{\imath q_z h(\vec{r}_{xy})\}\rangle \exp[\imath\vec{q}_{xy}\cdot\vec{r}_{xy}] \tag{5.4.6}$$

where $q_c$ is the critical angle for total external reflection of x-rays and the surface structure factor

$$\Phi(q_z) = \frac{1}{\rho_\infty}\int dz \frac{d\tilde{\rho}(z)}{dz}\exp(\imath q_z z) = \frac{-\imath q_z}{\rho_\infty}\int dz\tilde{\rho}(z)\exp(\imath q_z z) \tag{5.4.7}$$

is the Fourier transform of the local or intrinsic density profile $\tilde{\rho}(z)$, independent of $\vec{r}_{xy}$. In this equation, $\rho_\infty$ is the bulk electron density.

For the case of thermally excited capillary waves on a liquid surface, the height fluctuations can be characterized by their statistical average $\langle|h(\vec{r}_{xy})|^2\rangle$.[35] Sinha et al. have shown that integration over these height fluctuations yields the following dependence of the scattering on $q_{xy}$ and $q_z$:[37]

$$\int_{|\vec{r}_{xy}|>\xi} d^2\vec{r}_{xy}\langle\exp\{\imath q_z h(\vec{r}_{xy})\}\rangle \exp[\imath\vec{q}_{xy}\cdot\vec{r}_{xy}] = \frac{C}{q_{xy}^{2-\eta}} \tag{5.4.8}$$

with $C$ to be determined and

$$\eta = \frac{k_B T}{2\pi\gamma}q_z^2.$$

The value of $C$ can be determined by integration over all surface capillary modes having wavevectors smaller than the upper wavevector cutoff $q_{max} \equiv \pi/\xi$:

$$\begin{aligned} C &= \int_{|\vec{q}_{xy}|<\pi/\xi} d^2\vec{q}_{xy}\int_{|\vec{r}_{xy}|>\xi} d^2\vec{r}_{xy}\langle\exp\{\imath q_z h(\vec{r}_{xy})\}\rangle \exp[\imath\vec{q}_{xy}\cdot\vec{r}_{xy}] \\ &\approx 4\pi^2 \lim_{\vec{r}_{xy}\to 0}\langle\exp\{\imath q_z h(\vec{r}_{xy})\}\rangle = 4\pi^2 \end{aligned} \tag{5.4.9}$$

Therefore, the properly normalized differential cross section for scattering of x-rays from a liquid surface is:

$$\frac{d\sigma}{d\Omega} = \frac{A_0}{\sin\alpha}\left(\frac{q_c}{2}\right)^4 \frac{k_B T}{16\pi^2\gamma}\left|\Phi(q_z)\right|^2 \frac{1}{q_{xy}^2}\left(\frac{q_{xy}}{q_{\max}}\right)^{\eta} . \tag{5.4.10}$$

The intensity measured at a specific scattering vector $\vec{q}$ is obtained by integrating Eq. 5.4.10 over the solid angle $d\Omega$ defined by the detector acceptance of the experiment. For the specular reflection $q_{xy} = 0$ ($\alpha = \beta$ and $2\theta = 0$), the integral is centered at $q_{xy} = 0$. The projection of the detector resolution onto the $x$-$y$ plane is rectangular[35] and the above mentioned integration has to be done numerically. However, an analytical formula can be obtained for the specular reflectivity if the detector resolution is assumed to be a circle of radius $q_{res}$, independent of $q_z$[28]:

$$\frac{R(q_z)}{R_f(q_z)} = \left|\Phi(q_z)\right|^2 \left(\frac{q_{\rm res}}{q_{\max}}\right)^{\eta} = \left|\Phi(q_z)\right|^2 \exp[-\sigma_{\rm cw}^2 q_z^2] \tag{5.4.11}$$

where

$$R_f(q_z) = \left|\frac{q_z - \sqrt{q_z^2 - q_c^2}}{q_z + \sqrt{q_z^2 - q_c^2}}\right|^2 \approx \left(\frac{q_c}{2q_z}\right)^4 \qquad for \;\; q_z \gtrsim 5q_c$$

is the Fresnel reflectivity from classical optics for a flat ($h(\vec{r}_{xy}) = h(0)$ for all $h(\vec{r}_{xy})$) and structureless ($|\Phi(q_z)|^2 = 1$) surface. The quantity $\sigma_{\rm cw}$ denotes the capillary wave roughness:

$$\sigma_{\rm cw}^2 = \frac{k_B T}{2\pi\gamma}\ln\left(\frac{q_{\rm res}}{q_{\max}}\right) . \tag{5.4.12}$$

In the experiments presented here, the measured specular reflectivity was analyzed by numerical integration of the theoretical model over the rectangular resolution defined by the detector slits. In practice, the specular reflection is measured with coarse resolution and the results based on Eq. 5.4.11 fall within 5% of the exact values obtained from integrating over Eq. 5.4.10. On the other hand, the off specular

diffuse scattering is measured with much finer resolution and near the specular peak, $\vec{q}_{xy} = 0$, it has to be analyzed by numerical integration of Eq. 5.4.10 over the slit defined resolution. In addition, numerical integration of Eq. 5.4.10 is necessary to obtain the correct ratio of specular reflectivity to off-specular diffuse scattering.

In Eq.(5.4.7) we have introduced a local structure factor which is the Fourier transform of the local or intrinsic density profile. An alternative representation is to define a macroscopically averaged density profile $\langle\rho(z)\rangle_T$ such that

$$\frac{1}{\rho_\infty}\int dz \frac{\langle\rho(z)\rangle_T}{dz}\exp(\imath q_z z) = \Phi(q_z)\exp(-1/2\sigma_{cw}^2 q_z^2)$$

This macroscopically averaged density profile, $\langle\rho(z)\rangle_T$, can be shown to be equal to the convolution of the local density profile, $\tilde{\rho}(z)$, with the associated Gaussian distribution of height fluctuations characterized by

$$\sigma_{cw}^2 = \langle|h(\vec{r}_{xy})|^2\rangle = \frac{k_B T}{2\pi\gamma}\ln\left(\frac{1}{|\vec{r}_{xy}|q_{max}}\right).$$

Unfortunately, it is difficult to extract a precisely defined $\langle\rho(z)\rangle_T$ from a single reflectivity measurement because of the above mentioned problem of the variation of the resolution with $q_z$.

A second difficulty with reflectivity measurements, even when $|\Phi(q_z)|^2$ can be separated from the thermal effects, is that the direct inversion of $|\Phi(q_z)|^2$ in order to obtain $\tilde{\rho}(z)$ is not possible because the phase information necessary to perform the Fourier transform in Eq. 5.4.7 is lost in any intensity measurement. The common practice to overcome this problem is to assume a model for the density profile, which is then Fourier transformed and fitted to the experimentally determined structure factor. In this study, the liquid metal is modelled by layers of different electron densities parallel to the surface. The layers represent planes of atoms, separated

by a distance $d$, and having increasing width the further they are below the surface. Mathematically, the electron density is described by a semi-infinite sum of Gaussians, normalized to the bulk density $\rho_\infty$:

$$\tilde{\rho}(z) = \rho_\infty \sum_{n=0}^{\infty} \frac{d/\sigma_n}{\sqrt{2\pi}} \exp\left[-(z-nd)^2/2\sigma_n^2\right] \otimes F_{\mathrm{In}}(z). \tag{5.4.13}$$

Here $\otimes$ denotes convolution, $F_{\mathrm{In}}(z)$ is the atomic x-ray scattering form factor of In, and $\sigma_n^2 = n\bar{\sigma}^2 + \sigma_0^2$, where $\bar{\sigma}$ and $\sigma_0$ are constants. This form for $\sigma_n$ produces a quadratic increase in the Gaussian width with distance $z$ below the surface, so that the parameter $\bar{\sigma}$ is related to the decay length for surface layering and the model density approaches the bulk density $\rho_\infty$ for $\sigma_n \gg d$. An advantage of using Gaussian functions to model $\tilde{\rho}(z)$ is that an expression for $\langle\rho(z)\rangle_T$ is obtained from Eq. 5.4.13 by replacing $\sigma_n$ with $\sigma_n^T$ and defining $(\sigma_n^T)^2 = \sigma_{cw}^2 + \sigma_n^2$. Note that the effective width of the individual layers becomes $(\sigma_n^T)^2$ which explicitly demonstrates the additivity of the different contributions to the surface roughness from capillary modes (for which $q_{xy} < q_{max}$) and short wavelength modes (for which $q_{xy} > q_{max}$) that are incorporated into the model for $\tilde{\rho}(z)$.

## 5.5 Experimental Results

The specular reflectivity measured from liquid In at $170 \pm 5$ °C demonstrates the presence of surface layering. Figure 5.2 shows the reflectivity as a function of $q_z$, normalized to the Fresnel reflectivity of a sharply terminated In surface with a critical angle $q_c = 0.052$ Å$^{-1}$. The circles show the data taken with the scintillation detector, with a $q_z$ resolution of 0.06 Å$^{-1}$. Open circles represent the small angle data taken at X22B ($\lambda$=1.24 Å) whereas the closed circle data have been taken at X25 ($\lambda$=0.65 Å).

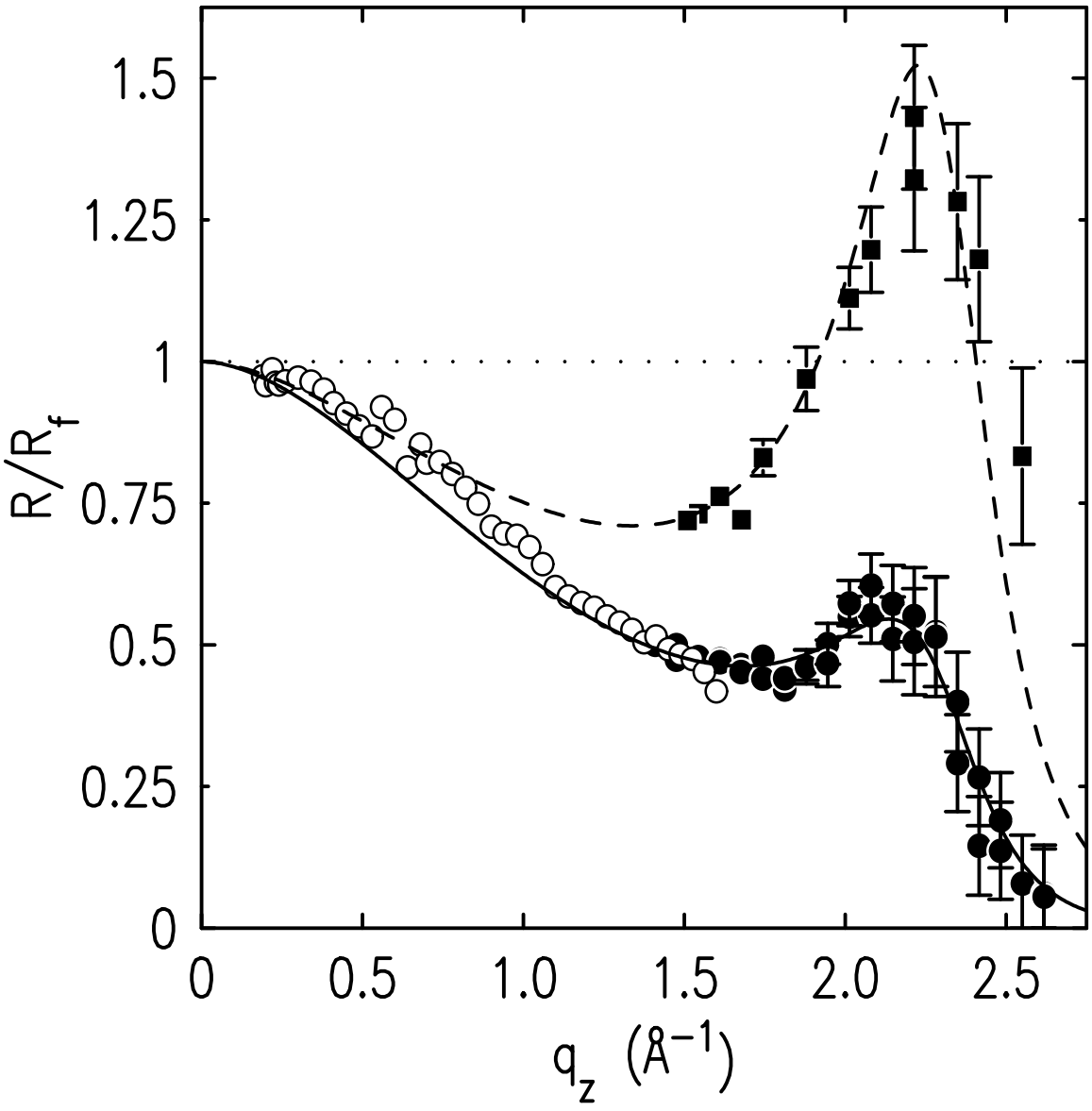



Figure 5.2: Specular x-ray reflectivity for liquid Indium at 170 °C taken with vertical detector resolutions of 0.06 $Å^{-1}$ (scintillation detector; open circles: X22B, closed circles: X25) and 0.32 $Å^{-1}$ (PSD in single channel mode; squares: X25). The reflectivity is normalized to the Fresnel reflectivity $R_f$ of a flat In surface. Solid lines are fits as described in the text. Data from X22B was not incorporated in any fits.

Filled squares represent data taken with the PSD in a single channel mode, with the vertical resolution coarser by a factor of 5. The large increase in signal with decreasing resolution immediately demonstrates the significance of the diffuse scattering. The reflectivity at small and intermediate wavevectors falls below the Fresnel value calculated for an ideally flat and abruptly terminated surface. This is due to the roughness of the liquid In surface which scatters photons out of the specular condition. The most prominent feature in these data is the broad peak centered near 2.2 $\mathring{A}^{-1}$. This peak is due to constructive interference of x-rays from layers ordered parallel to the surface. This very distinctive structural feature of liquid metal surfaces has been observed earlier for Hg[7] and Ga.[8] The two data sets show the same features, although as a consequence of integrating the diffuse scattering over coarser resolution, the intensity is greater for data taken with the PSD.

The lines in Figure 5.2 illustrate fits of the density profile model discussed above to these data. Three surface layering parameters, $d$, $\overline{\sigma}$, and $\sigma_0$, determine the form of $\Phi(q_z)$, which is then used in Eq. 5.4.10 along with $T = 170°$C and the experimentally determined value for the surface tension of liquid In at that temperature, $\gamma = 0.556$ N/m.[38] As discussed above, we assign the short wavelength cutoff for capillary waves, $q_{max} \approx \pi/\xi$ , to be $\sim 1\mathring{A}^{-1}$ where $\xi$ was taken to be the nearest neighbor atomic distance in the bulk melt.[39] The integral over Eq. 5.4.10 is then performed numerically over the known resolution volume. Surface layering parameters obtained from the scintillation detector data are $d = 2.69 \pm 0.05$ Å, $\overline{\sigma} = 0.54 \pm 0.06$ Å, and $\sigma_0 = 0.35 \pm 0.04$ Å (solid line in Figure 5.2). Essentially the same parameters (with larger error due to poorer statistics) result from a fit of the model to the PSD data (broken line in Figure 5.2).

Although the resolution dependence of the reflectivity of liquid metals provides a test of the thermal capillary wave theory prediction, a more rigorous test is the measurement of the spectral density of the off specular diffuse scattering. We have measured diffuse intensity over a $\beta$ range straddling the specular condition. Intensities normalized to the direct beam are shown in Figure 5.3 for several choices of $\alpha$. Data at extreme values of $(\beta-\alpha)$ are limited by the intense background due to bulk scattering at large $\beta$ and by the scattering geometry at small $\beta$. The asymmetry of the wings centered around the specular ridge ($\beta - \alpha = 0$) arises from the $\beta$ dependence of both the exponent $\eta$ and the surface structure factor $\Phi(q_z)$.

The solid lines are obtained by calculating the intensity from Eq. 5.4.10, integrating numerically over the resolution function and subtracting a similar calculation for the background scan taken out of the reflection plane. The calculation incorporates the surface structure factor $\Phi(q_z)$ determined from the reflectivity measurements along with the other fixed quantities ($\gamma$, $k_BT$, and $q_{\max}$), without further adjustable parameters. We find excellent agreement between this model and the experimental data for the entire range studied, including the wings (Figure 5.3) and the specular region (inset of Figure 5.3). The implications of this agreement will be discussed in the next section.

To study the oxidation properties of liquid Indium we exposed the In surface to controlled amounts of oxygen through a bakeable UHV leak valve. During oxidation, macroscopic oxide clumps, large enough to be observed by eye, formed at the edges of the sample, while the center remained clean. X-ray reflectivity measured during oxidation showed no changes until the floating oxide regions grew large enough to reach the area illuminated by the x-ray beam, at which point the macroscopically

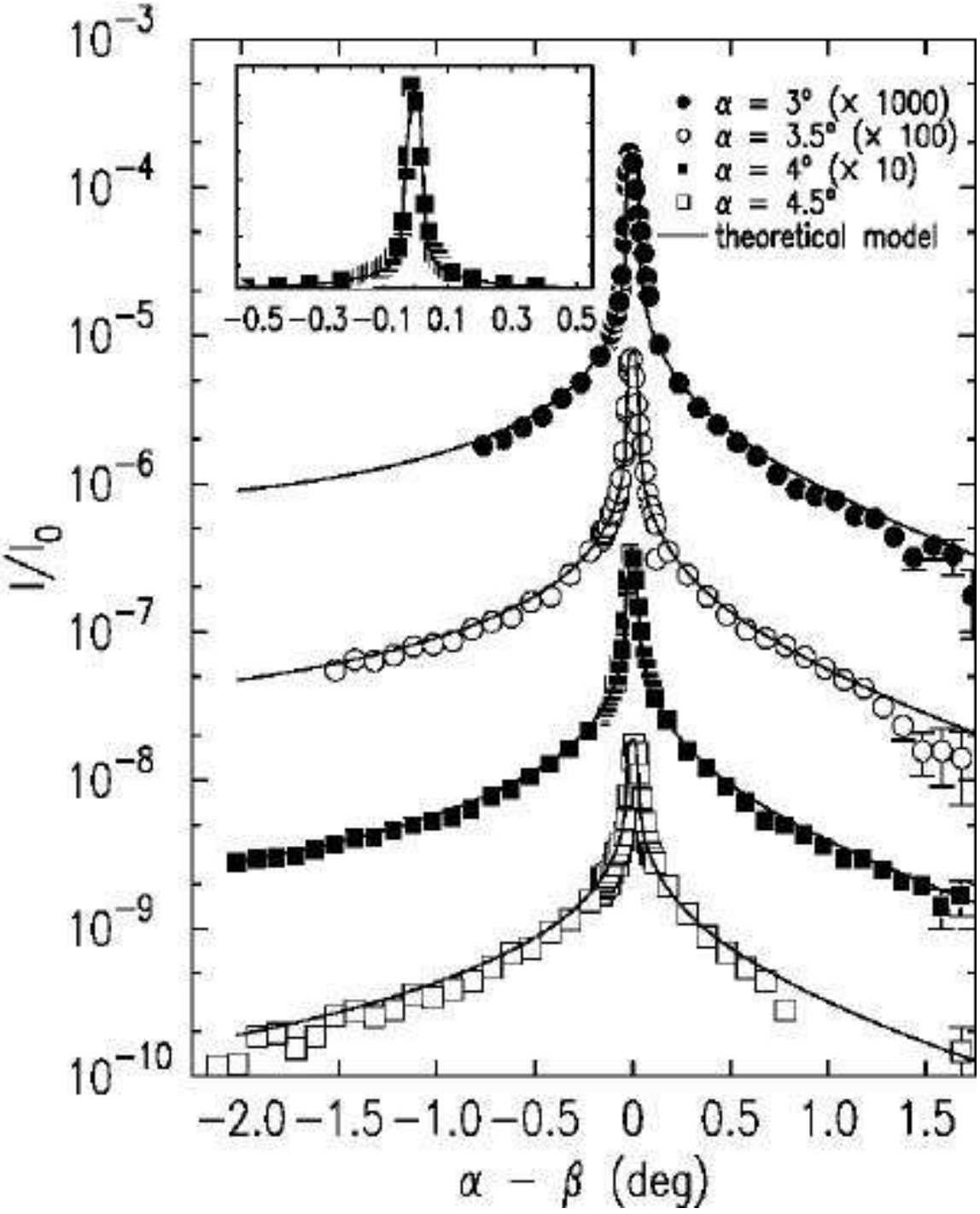



Figure 5.3: Diffuse scattering as a function of scattering angle $\beta$ for different fixed incoming angles $\alpha$. Solid lines: Diffuse scattering calculated from the experimentally determined structure factor with no further adjustable parameters. Inset: linear plot emphasizing the fit near the specular peak for $\alpha = 4.5°$

rough surface scattered the reflected signal away from the specular condition. This result is in sharp contrast to the formation of the highly uniform, 5 Å thick, passivating oxide layer we previously observed to form on liquid Ga under the influence of the same amount of oxygen.[27]

## 5.6 Discussion

The macroscopic density profile extracted from the reflectivity measurements is resolution dependent since the density oscillations are smeared out by thermally activated capillary waves as described in the Theory section. This smearing depends on the temperature and surface tension and hence also varies for different liquids. The macroscopic density profile directly extracted from the experiment is the averaged density profile $\langle\rho(z)\rangle_T$ shown in previous publications.[7,8,9,28] In order to compare the intrinsic layering properties in different liquid metals, it is necessary to remove these thermal effects that vary from metal to metal and experiment to experiment and to obtain the intrinsic or local density profile $\tilde{\rho}(z)$. Previous temperature dependent reflectivity measurements of liquid Ga around the specular position have shown that the resolution dependent roughness is well described by the capillary wave (CW) prediction.[9] Similar conclusions were reached from $T$-dependent measurements of liquid paraffins.[40] Here, we employed a different approach to verify that the CW prediction holds for liquid In, performing diffuse scattering measurements at a single temperature at different angles of incidence. The magnitude and the angular dependence of the diffuse scattering is in full compliance with the predictions of the capillary wave model without using any adjustable parameters. This is demonstrated by the perfect agreement of the diffuse scattering profiles with the theoretical curves in Figure 5.3.

This allows us to directly calculate the local density profile $\tilde{\rho}(z)$ by simply setting $\eta = 0$. A comparison between the local density profile $\tilde{\rho}(z)$ and the temperature averaged density profile $\langle\rho(z)\rangle_T$ is made in Figure 5.4(a).

In this single-$T$ approach the effects of the intrinsic, $T = 0$, roughness $\sigma_0$ and the cutoff $q_{\max}$ cannot be unambiguously separated,[41] as was possible for the $T$-dependent measurements in alkanes[40] and Ga.[9] However, this does not affect our main conclusion that the surface roughness, as probed by the DS, is entirely due to thermally activated capillary waves.

The local density profile of liquid In is compared with that of Ga in Figure 5.4(b). Profiles derived from the extremal parameters of fits to $R(q_z)$ and from extremal values for temperature, surface tension and resolution function are indistinguishable on the scale of the figure. The amplitude of the first density peak for In is comparable to that of Ga. This reflects the fact that in the region nearest the surface, the density oscillations are determined primarily by $\sigma_0$, which has similar values for the two metals. Further towards the bulk, layering is seen to decay faster for In than for Ga. We quantify this observation by the excellent fit of the peak amplitude of the electron density profile to the form $\exp(-z/l)$. The decay lengths $l = 3.5$ Å$\pm 0.6$ for In and $l = 5.5$ Å$\pm 0.4$ for Ga differ by an amount well outside of the experimental error. This is illustrated in the inset of Figure 5.4(b), a semilogarithmic plot of the maxima of the density oscillations as a function of distance from the first surface layer. The lines represent the fit of the peak amplitude to the exponential form and the slope represents the decay length.

It is also instructive to compare the surface structure factor measured in the reflectivity experiments to the bulk structure factor measured by standard x-ray or

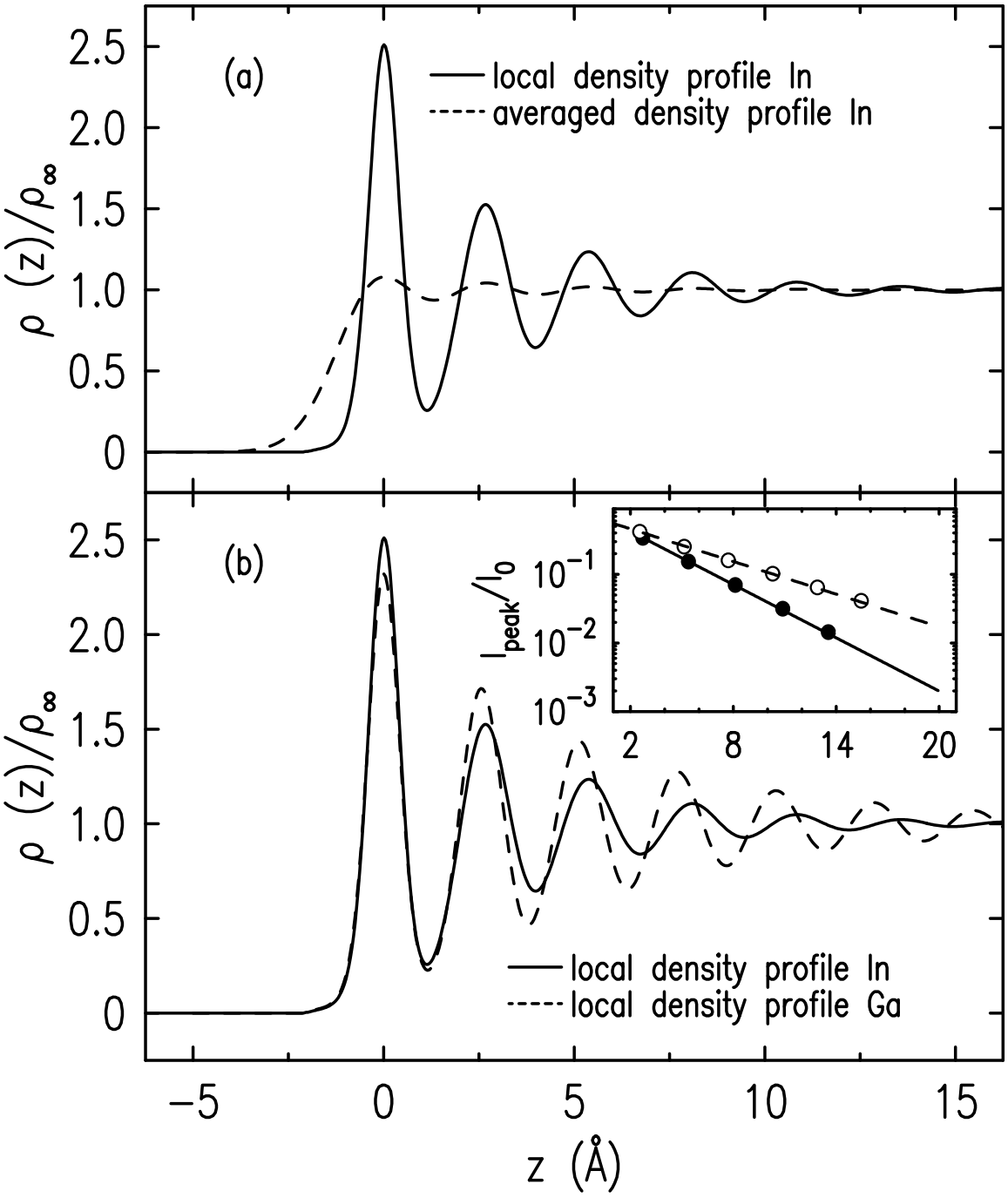



Figure 5.4: (a) Comparison of the local real space density profile for liquid Indium (—) with the thermally averaged density profile for the same metal (- - -). The averaged density profile is directly accessible by experiment and has been measured at 170° C. (b) Real space local density profile for liquid Gallium (- - -) and liquid Indium (—) after the removal of thermal broadening. Densities $\tilde{\rho}(z)$ are normalized to the bulk densities $\rho_\infty$ of liquid Gallium and Indium. Inset: Decay of the amplitude of the surface–normal density profile for liquid Ga (open circles) and liquid In (filled circles). The lines represent the fit of this decay of the surface layering to the form $\exp(-z/l)$ for liquid Ga (—) and In (- - -).

neutron diffraction (Figure 5.5(a): Indium; Figure 5.5(b): Gallium). The widths of the peaks shown are inversely proportional to the decay lengths of the corresponding correlation functions: the pair correlation function $g(r)$[42] of the bulk and the layered density profile $\tilde{\rho}(z)$ of the surface. Plotting the amplitudes of $g(r)$ and $\tilde{\rho}(z)$ on a semi-log scale (inset of Figure 5.5) shows that they lie on straight lines. This indicates that the correlations decay exponentially, and the decay lengths are obtained as the negative inverses of the slopes. The inset plots show clearly that while the surface and bulk decay lengths are about the same for In, in Gallium the surface induced layering decays much more slowly than the bulk pair correlation function. This is consistent with the NFE nature of In. For Ga, by contrast, the tendency towards covalency may disrupt the hard sphere packing and enable surface correlations that differ from those in the bulk.

Another piece of evidence suggesting that directional bonding in the melt might have an effect on surface induced layering stems from the ratio between the surface layer spacing and the bulk nearest neighbor distance. This nearest neighbor distance is taken from the analysis of the pair correlation function which is the Fourier transform of the structure factor depicted in Figure 5.5. Due to truncation problems and related subtleties with the data analysis, the bulk nearest neighbor distance cannot be directly inferred from the maximum in the bulk liquid structure factor and we use the nearest neighbor distance given by Iida and Guthrie.[38] For liquid In, this ratio of surface layer spacing to bulk nearest neighbor distance is 2.69 Å/3.14 Å = 0.86, close to the value of $\sqrt{2/3} \approx 0.82$ for the hard sphere packing that would be expected for a NFE liquid metal. For liquid Ga, this ratio is larger, 2.56 Å/2.78 Å = 0.92. In this case, formation of directional bonds, eventually leading to $Ga_2$ dimers, may prevent close

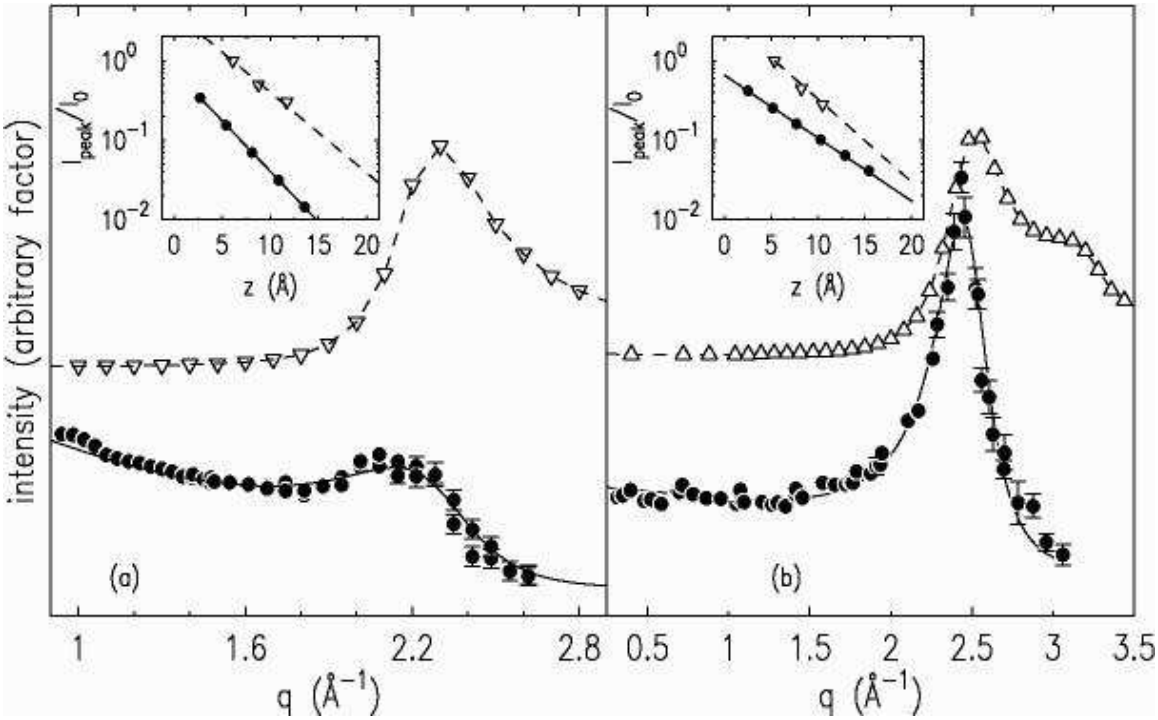



Figure 5.5: (a) Bulk (△) and surface (•) structure factors for liquid In. The bulk structure factor data are taken from Orton et al.[22] The solid line is a fit of the model explained in the text to the experimentally determined surface structure factor. The broken line is a guide for the eye. The inset compares the decay of the longitudinal surface density oscillations (filled circles; solid line represents fit to an exponential) to the decay of the bulk pair correlation function (open triangles; broken line represents fit to exponential). The coordinate $z$ of the x-axis represents the distance from the surface in the case of the decaying surface layering and the radial distance from a reference atom in the bulk liquid in the case of the decaying bulk pair correlation. The data for the bulk pair correlation function are taken from Waseda.[42] (b) Bulk (△) and surface (•) structure factors for liquid Ga. The bulk structure factor data are taken from Narten et al.[15] Solid lines are fits to reflectivity data, broken lines are guides for the eye. The inset compares the decay of the longitudinal surface density oscillations (filled circles; solid line represents fit to exponential) to the decay of the bulk pair correlation function (open triangles; broken line represents fit to exponential). The data for the bulk pair correlation function are taken from Waseda.[42]

packing.

Tomagnini et al. recently considered a possible relationship between surface induced layering in LM and the stability of crystal facets at metal surfaces. Although premelting of crystalline interfaces is quite common in non-metallic crystals, most metals have at least one close packed face which does not premelt, remaining solid up to the melting temperature[43]. /indexTomagnini Tomagnini et al. use Molecular Dynamics simulations to demonstrate that when the period of the surface induced layering at the liquid surface, which they assumed to be $2\pi/q_0$ where $q_0$ is the position for the peak in the bulk liquid structure factor, is commensurate with the distance between lattice planes along the normal to the crystal facet, this particular facet is stabilized and resistant to premelting. It would be interesting to correlate the premelting properties of Ga and In crystals with our results for the period of the surface layering and in particular, to examine if the effect of directional bonding that affects the surface structure in the liquid affects premelting of the solid as well.

We see here that for both Ga and In the period of the layering at the liquid surface is significantly longer than $2\pi/q_0$. Further, for In the period is reasonably close to the value that would have been expected between the close packed layers if the crystal structure of NFE In was such a crystal. In fact the crystal structure of In is tetragonal, space group I4/mmm.

Our diffuse scattering measurements show that the roughness of the liquid In surface can be attributed entirely to thermally excited capillary waves. This indicates that there are no other detectable inhomogeneities on the surface, such as might be caused by microscopic oxide patches. This observation is in concert with independent

experiments on organic Langmuir monolayers on water. If the monolayer is homogeneous[44,45], the DS can be described by Eq.(5.4.10) with no adjustable parameters and no excess scattering is observed — just as is the case for metallic liquid In. On the other hand, if the organic monolayer is compressed beyond its elasticity limit and becomes inhomogeneous, Eq.(5.4.10) no longer describes the experimentally determined DS, and excess scattering is observed that must originate from sources other than thermally activated capillary waves.[44] This demonstrates the viability of diffuse scattering as a tool for studying surface inhomogeneities. This is of particular interest for investigations on liquid alloys where — depending on the type of alloy — a rich surface behaviour is expected, ranging from concentration fluctuations for alloys displaying surface segregation to critical fluctuations for alloys with a critical consolute point.[46]

Controlled oxidation of the liquid metal surfaces reveals a further striking difference between Ga and In. Although exposure of liquid Ga to air or to a large amount of oxygen leads to the formation of a macroscopically thick and rough oxide film, exposure to controlled amounts of oxygen under UHV conditions produces a well defined uniform 5 Å thick oxide film.[27] This film protects the underlying bulk phase to a certain extent from further corrosion, as further dosage at low oxygen pressures ($< 2 \times 10^{-4}$ Torr) was found to have no effect on the oxide thickness or coverage fraction. This pasivating of the surface is rather unusual for solid metals, Al being prominent among the few examples. Liquid In, unlike Ga, was not found to form a passivating oxide film. Instead, macroscopic clumps of oxide formed which did not wet the clean In surface. This corrosion mechanism is rather common for solid metal surfaces, the oxidation of Fe being the best known example. It is not clear to what

extent this fundamental difference in the mechanism for corrosion is related to differences in the structure of the liquid surface and to what extent to the chemical affinity for oxidation of the respective liquid metal.

## 5.7 Summary

We have measured the x-ray reflectivity and small angle off specular surface diffuse scattering from liquid In at 170°C. Our results can be quantitatively explained by the convolution of thermally excited surface waves and a temperature independent surface structure factor, corresponding to theoretically predicted surface layering. The absence of excess diffuse scattering beyond that due to thermally excited capillary waves demonstrates that the liquid–vapor interface is homogeneous in the surface-parallel direction. The intrinsic layering profile of liquid In, obtained by removing the capillary wave roughening, is compared to that previously reported for liquid Ga. For Ga, surface layering persists farther into the bulk than is the case for In. This may be attributed to directional bonding in the Ga bond stabilizing surface induced layering over a larger distance than is the case for liquid In. Further evidence suggesting a correlation between the degree of covalency in the melt and the surface structure stems from the observation that the compression of the surface layer spacing relative to the bulk nearest neighbor distance is close to the behavior expected for an ideal hard sphere liquid for In but considerably different for Ga. Controlled oxidation of liquid In results in the formation of a macroscopic rough oxide, unlike the passivating microscopic uniform oxide film that forms on liquid Ga.

# Bibliography


[1] F. F. Abraham, Rep. Prog. Phys. **45** 1113, (1982).

[2] G. A. Chapella et al., J. Soc. Faraday II **73** 1133, (1977).

[3] S. A. Rice et al., Adv. Chem. Phys. **27** 543, (1974).

[4] R. Evans, M. Hasegawa, J. Phys. C: Solid State Phys. **14** 5225, (1981).

[5] M. Iwamatsu, S. K. Lai, J. Phys.: Condens. Matter **4** 6039, (1992).

[6] J. G. Harris, J. Gryko, S. A. Rice, J. Chem. Phys. **87** 3069, (1987).

[7] O. M. Magnussen, B. M. Ocko, M. J. Regan, K. Penanen, P. S. Pershan, M. Deutsch, Phys. Rev. Lett. **74** 4444, (1995).

[8] M. J. Regan, E. H. Kawamoto, S. Lee, P. S. Pershan, N. Maskil, M. Deutsch, O. M. Magnussen, B. M. Ocko, L. E. Berman, Phys. Rev. Lett. **75** 2498, (1995).

[9] M. J. Regan, P. S. Pershan, O. M. Magnussen, B. M. Ocko, M. Deutsch, L. Berman, Phys. Rev. B **54** 9730, (1996).

[10] Some pecularities of the Hg surface structure may be due to the fact that Hg cannot be studied under ultra high vacuum (UHV). In the present report, we compare the In results to measurements of liquid Ga, both performed under UHV

conditions. A detailed discussion of the temperature dependent surface layering of liquid Hg will be given elsewhere: E. DiMasi, H. Tostmann, B. M. Ocko, P. S. Pershan, and M. Deutsch, submitted to Phys. Rev. B.

[11] N.W.Ashcroft and N.D.Mermin, *Solid State Physics*, Harcourt Brace, Orlando, 1976.

[12] J.M.Ziman, Phil.Mag. **6** 1013, (1961).

[13] G.A.deWijs, G.Pastore, A.Selloni and W.van der Lugt, Phys.Rev.Lett. **75** 4480, (1995).

[14] N.H.March, *Liquid Metals*, Cambridge University Press, Cambridge, 1990.

[15] A. H. Narten *et al*, J. Chem. Phys. **56** 1185, (1972).

[16] M.C. Bellissent-Funel, P. Chieux, D. Levesque and J.J. Weiss, Phys.Rev. A **39** 6310, (1989).

[17] X. G. Gong *et al*, Europhys. Lett. **21** 469, (1993).

[18] A. DiCicco and A. Filipponi, Europhys. Lett. **27** 407, (1994).

[19] E. D. Crozier, E. Murphy, Can. J. Phys. **50** 1914, (1972).

[20] H.Mayer and M.H.El Naby, Z.Physik **174** 280, (1963).

[21] D.Nattland, H.Heyer and W.Freyland, Z.Physikal.Chemie NF **149** 1, (1986).

[22] B. R. Orton, S. P. Smith., Phil. Mag. **14** 873, (1966).

[23] H. Ocken, C. N. J. Wagner, Phys. Rev. **149** 122, (1966).

[24] L. G. Schulz, Advan. Phys. **6** 102, (1957).

[25] J. N. Hodgson, Advan. Phys. **16** 675, (1967).

[26] F. A. Richardson, *Physical Chemistry of Melts in Metallurgy*, Academic Press, London, 1974.

[27] M. J. Regan, H. Tostmann, P. S. Pershan, O. M. Magnussen, E. DiMasi, B. M. Ocko, M. Deutsch, Phys. Rev. B **55** 10786, (1997).

[28] M. J. Regan, P. S. Pershan, O. M. Magnussen, B. M. Ocko, M. Deutsch, and L. E. Berman, Phys. Rev. B **55** 15874, (1997).

[29] G. C. Smith, J. Fischer, V. Radeka, IEEE Trans. Nuc. Sci. **NS-32** 521, (1985). The PSD was designed at Brookhaven National Laboratory (BNL) and consists of an 8 cm anode wire with 40 psi Kr/10% $CO_2$ gas optimized for x-ray absorption at 19 keV.

[30] X-ray Photoelectron Spectroscopy (XPS) shows that no impurity segregates at the surface of liquid In contained in a Mo pan. The sample was heated up to 300° C for several days and the XPS was taken after cooling the sample. The surface sensitivity of the XPS spectrometer is 1% given a penetration depth of about 30 Å. This is in accordance with the In–Mo phase diagram which predicts no Mo solubility in In at these temperatures (T.B. Massalski, *Binary Alloy Phase Diagram*, ASM International, Materials Park, Ohio, 1990).

[31] A. Roth, *Vacuum Technology*, Elsevier, Amsterdam, 1990.

[32] J. Fine, S. C. Hardy, T. D. Andreadis, J. Vac. Sci. Technol. **18** 1310, (1981).

[33] JRS Scientific Instruments, Affoltern a.A., Switzerland.

[34] A. Guinier, *X-Ray Diffraction*, Freeman, San-Francisco, 1963.

[35] A. Braslau, P. S. Pershan, G. Swislow, B. M. Ocko, J. Als-Nielsen, Phys.Rev.A **38** 2457, (1988).

[36] The microscopic definition of the local density profile $\tilde{\rho}(z - h(\vec{r}_{xy}))$ requires averaging over density fluctuations with wavelengths shorter than $\xi$. It follows that fluctuations with surface wavevectors $q_{xy} \leq \pi/\xi$ are contained in the definiton of $\tilde{\rho}(z - h(\vec{r}_{xy}))$.

[37] S. K. Sinha, E. B. Sirota, S. Garoff, H. B. Stanley, Phys. Rev. B **38** 2297, (1988).

[38] T.Iida, R.I.L.Guthrie, *The Physical Properties of Liquid Metals*, Clarendon Press, Oxford, 1993.

[39] This cutoff is selected such that the number of capillary modes is equal to the number of surface atoms. Choice of a larger cutoff length would imply that the local density profile includes contributions from averaging over the capillary waves with the shortest wavelengths. First principle arguments that might support such a larger cutoff length are beyond the scope of this paper. A smaller cutoff length on the other hand would imply capillary waves with wavelengths smaller than the particle size which is not physically reasonable.

[40] B. M. Ocko, X. Z. Wu, E. B. Sirota, S. K. Sinha, M. Deutsch, Phys. Rev. Lett. **72** 242, (1994).

[41] M. P. Gelfand, M. E. Fisher, Physica A **166** 1, (1990).

[42] Experimentally determined data for the bulk structure factor $S(Q)$ and the pair correlation function $g(R)$ calculated from $S(Q)$ can be found in: Y. Waseda, *The Structure of Non-Crystalline Materials*, McGraw-Hill, New York, 1980; an electronic database can be found at `http://www.iamp.tohoku.ac.jp/database/scm/index.html`.

[43] O. Tomagnini, F. Ercolessi, S. Iarlori, F.D. Di Tolla and E. Tosatti, Phys. Rev. Lett. **76** 1118, (1996).

[44] M. Fukuto, R.K. Heilmann, P. S. Pershan, J.A. Griffiths, S.M. Yu and D.A. Tirrell, Phys.Rev.Lett (accepted).

[45] C. Gourier et al., Phys. Rev. Lett. **78** 3157, (1997).

[46] H. Tostmann, E. DiMasi, P.S. Pershan, B.M. Ocko, O.G. Shpyrko and M. Deutsch, Ber.Bunsenges.Phys.Chem, to appear september 1998.

# Chapter 6

# Surface Structure of KNa alloy

## 6.1 Abstract

In this chapter we describe an x-ray scattering study of the microscopic structure of the surface of a liquid alkali metal. The bulk liquid structure factor of the eutectic $K_{67}Na_{33}$ alloy is characteristic of an ideal mixture, and so shares the properties of an elemental liquid alkali metal. Analysis of off-specular diffuse scattering and specular x-ray reflectivity shows that the surface roughness of the K-Na alloy follows simple capillary wave behavior with a surface structure factor indicative of surface induced layering. Comparison of the low-angle tail of the $K_{67}Na_{33}$ surface structure factor with the one measured for liquid Ga and In previously suggests that layering is less pronounced in alkali metals. Controlled exposure of the liquid to $H_2$ and $O_2$ gas does not affect the surface structure, indicating that oxide and hydride are not stable at the liquid surface under these experimental conditions.

## 6.2 Introduction

The structure of the free surface of a liquid metal (LM) is fundamentally different from that of a dielectric liquid, due to the strong coupling between conduction electrons and

ion cores.[1] At the liquid-vapor interface of a LM, the Coulomb interaction between the free electron Fermi gas and the classical gas of charged ions acts like an effective hard wall and forces the ions into ordered layers parallel to the surface. The existence of surface-induced layering in LM has been verified unambiguously by experiment for liquid Hg[2], Ga[3] and In.[4] Layering is also present in liquid binary alloys, even though it may be suppressed by surface segregation[5] or the formation of surface phases.[6,7]

Even though surface layering appears to occur in LM in general, comparison of the detailed surface structure reveals qualitative differences between different LM.[4,8] In fact, very little is understood about how the surface induced layering predicted for an ideal LM is affected by the details of the more complicated electronic structure exhibited by the polyvalent metals studied so far. One important goal therefore is to study the surface structure of those LM which show the most ideal electronic structure in the bulk phase, characterized by itinerant conduction electrons which are only weakly perturbed by a small ionic pseudopotential. These LM are referred to as nearly-free electron or NFE-type liquid metals.[9] In a previous study we have compared the surface structure of liquid In, which is considered to be a NFE-type liquid metal, with the surface structure of liquid Ga, which displays a considerable degree of covalency in the bulk.[4] However, even though liquid In has less tendency towards covalent bonding than Ga, it is trivalent, and the most simple models do not adequately describe its electronic structure or metallic properties.[11] The most ideal NFE-type liquid metals are the monovalent alkali metals (AM) which have a half-filled *s*-band and an almost spherical Fermi surface.[10] The metallic properties of the AM are explained by the most simple solid state models such as the Drude theory.[11] The fact that the conduction band is primarily formed from *s*-electron states

and that the electron-ion interaction can be modeled by a weak pseudopotential have led to numerous theoretical studies on the electronic structure. In fact, as far as the surface structure of LM is concerned, most of the theoretical studies and computer simulations have been applied to liquid Na, K and Cs.[1,12]

A particularly interesting question concerns the possible correlation between surface tension and surface structure. In general, LM have surface tensions that are at least an order of magnitude higher than the surface tensions of all other types of liquids.[7] Liquid alkali metals are the only exception to this pattern. For example, Ga and Cs melt at about the same temperature but the surface tension of Ga is greater than that of Cs by about an order of magnitude. If the high surface tension of liquid metals is related to surface induced layering, it would be reasonable to expect that liquid AM should display weak or no layering at the surface. This is contradicted by computer simulations showing pronounced layering for liquid Cs.[1]

The alkali alloy $K_{67}Na_{33}$ is more suitable experimentally for such a study than are the elemental liquid AM. Among the elemental alkali metals, Li deviates from NFE-type behavior,[11,13] while the high equilibrium vapor pressures of the other elemental AM prevents the use of an ultra-high vacuum (UHV) environment over a long period of time without noticeable evaporation of material. Experiments under UHV conditions are mandated by the high reactivity of liquid AM towards water and oxygen.[13] When liquid K and Na are alloyed in the eutectic composition (67 at%K), however, a vapor pressure well below $10^{-10}$ Torr is obtained. The low melting point of this alloy ($-12.6°$C) is an additional advantage, since the thermal surface roughness is considerably reduced.[4] This binary alloy appears to be well suited for emulation of the properties of an elemental liquid AM. The total structure factor $S(q)$ of bulk

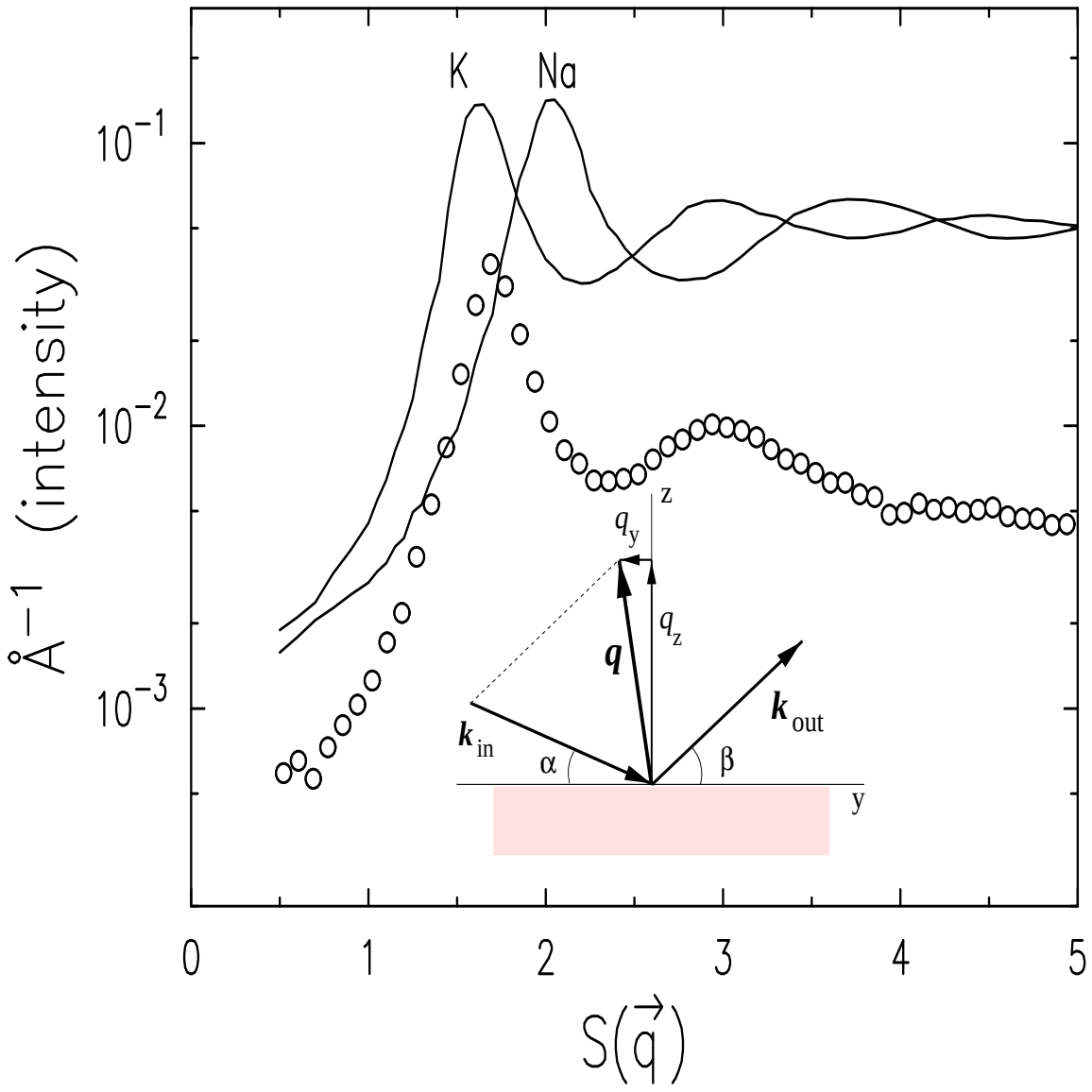



Figure 6.1: Bulk liquid structure factor measured for liquid $K_{67}Na_{33}$ (∘) compared to the bulk structure factors of pure liquid K and Na from Ref. 14 (—). Inset: geometry for x-ray reflectivity and off-specular diffuse scattering as described in the text.

liquid $K_{67}Na_{33}$, shown in Figure 6.1, is characteristic of random mixing, without sub-peak or asymmetry of the first peak.[14] The first peak of $S(q)$ for the alloy lies between those of pure K and Na, as expected for an ideal mixture.[14] More importantly, the electronic structure of the homovalent K-Na alloys is as NFE-like as the electronic structure of the pure components.[15] Even if there were some homocoordination or surface enrichment of K driven by the lower surface tension of K as compared to Na, it would not be discernible in our structural measurements, since x-ray scattering is sensitive to the distribution of the electron density, which is virtually identical for K and Na (0.25 e/Å$^3$ and 0.27 e/Å$^3$ respectively).

## 6.3 Sample Preparation

The eutectic alloy was prepared by mixing liquid K and Na in an inert atmosphere glove box ($<$ 2 ppm $H_2O$, $<$1 ppm $O_2$). The alloy was transferred into a stainless steel reservoir and sealed with a Teflon O-ring. The design of the reservoir is similar to the one used in recent Hg experiments.[8] The reservoir is connected to a stainless steel UHV valve which is attached to a UHV flange. This assembly was connected to the UHV chamber, which was baked out at 150° C until a vacuum in the $10^{-10}$ Torr range resulted. After reaching this pressure, the Mo sample pan (20 mm diameter, 1 mm depth) in the UHV chamber was sputtered clean with $Ar^+$ ions. Sputtering removes the native Mo-oxide layer and facilitates the wetting of the sample pan by the AM. After sputtering, the UHV valve to the reservoir was opened and the liquid alloy metered into the sample pan. As we will show below, our measurements under these conditions are consistent with a surface free of oxide on an atomic level.

## 6.4 Experimental geometry

Experiments were carried out using the liquid surface spectrometer at beamline X25 at the National Synchrotron Light Source, operating with an x-ray wavelength $\lambda$ =0.65 Å and a resolution of $\Delta q_z \approx 0.05$ Å$^{-1}$. In the x-ray reflectivity (XR) geometry, incident angle $\alpha$ and reflected angle $\beta = \alpha$ are varied simultaneously with $\beta$ detected within the plane of incidence. The background intensity, due mainly to scattering from the bulk liquid, is subtracted from the specular signal by displacing the detector out of the reflection plane by slightly more than one resolution width.[4,5,16] The specular reflectivity from the surface, $R(q_z)$, is a function of the normal component, $q_z = (4\pi/\lambda)\sin\alpha$, of the momentum transfer $\vec{k}_{out} - \vec{k}_{in} = (0,0,q_z)$. $R(q_z)$ yields information about surface roughness and surface-normal structure and may be approximated as[4]

$$R(q_z) = R_f(q_z)\,|\Phi(q_z)|^2 \left(\frac{q_{res}}{q_{max}}\right)^{\eta} \tag{6.4.1}$$

where $R_f(q_z)$ is the Fresnel reflectivity of a flat, laterally homogeneous surface. The surface structure factor, $\Phi(q_z)$, is the Fourier transform of the gradient of the intrinsic surface-normal density profile. The power-law term with $\eta = (k_B T/2\pi\gamma)q_z^2$ accounts for roughening of the intrinsic density profile by capillary waves (CW). Scattering of x-ray photons by CW outside of the detector resolution $q_{res}$ result in a loss in observed intensity. The short-wavelength cutoff $q_{max}$ is determined by the particle size $a$ with $q_{max} \approx \pi/a$. The observed reflectivity is reduced when either the temperature $T$ is increased or the surface tension $\gamma$ is reduced.

For off-specular diffuse scattering (DS), the incoming angle $\alpha$ is kept constant while $\beta$ is varied, straddling the specular condition (see inset of Figure 6.1). The bulk diffuse background has to be subtracted from the measured overall intensity. An acurate

description of the theoretical diffuse scattering requires inclusion of the contribution of the surface to the bulk background scattering.[4,16] The lineshape of the DS scans is determined principally by the power-law term in Eq. 6.4.1. Analysis of DS gives access to in-plane correlations of the surface and surface inhomogeneities that might be present.[16] Simultaneous analysis of XR and DS allows for a consistent determination of surface roughness and structure. As has been pointed out recently,[17] it is only for $\eta < 2$ that the reflected intensity displays the cusp-like singularity centered at the specular condition $\alpha = \beta$. For $\eta \geq 2$, it is not possible to distinguish surface scattering from bulk diffuse scattering since both are dominated by correlations of the same length scale. The value of $q_z$ at which $\eta$ reaches the limit of 2 at room temperature is about 1.7 $\text{Å}^{-1}$ for $K_{67}Na_{33}$.

## 6.5 X-Ray Diffuse Scattering Measurements

Diffuse scattering measurements from the surface of $K_{67}Na_{33}$ taken at different incoming angles $\alpha$ (Figure 6.2(a)) show that the liquid alloy has a uniform surface roughened by capillary waves. The solid lines through the data are calculated from CW theory (power-law term in Eq. 6.4.1) with the surface roughness entirely due to thermally activated surface waves. This model has no adjustable parameters, and the surface tension of 0.110±0.003 N/m is consistent with macroscopic measurements.[18] The agreement between the data and CW theory is excellent. The only limitation is in the low-angle region ($\alpha = 0.9°$ and $\beta < \alpha$), where the footprint of the incoming beam is larger than the flat part of the sample. Apart from this deviation, the sample shows no excess scattering which would be expected from an inhomogeneous surface.[4,16] The absence of excess diffuse scattering indicates that the alloy surface

is free of microscopic patches or islands of possible contaminants such as oxide or hydride.

## 6.6 X-Ray Reflectivity Measurements

As a result of this excellent agreement between CW theory and DS, the reflectivity from the alloy surface shown in Figure 6.3 (open squares) can be compared to the calculated reflectivity from a $K_{67}Na_{33}$ surface which is roughened by CW but displays no structure (i.e. $\Phi(q_z) = 1$). The dashed line in Figure 6.3 displays this theoretical prediction and it is obvious that the data rise above it, consistent with the low-angle behavior of surface induced layering observed previously.[3,4] exist. This point is emphasized further in the inset where the measured $R(q_z)$ is divided by $R_f$ and the power-law CW term in Eq. 6.4.1 to obtain a direct measure of the surface structure factor $\Phi(q_z)$. As can be seen, the value of $\Phi(q_z)$ rises above unity with increasing $q_z$ as expected when constructive interference of x-rays due to surface layering is present. The low angle tail of the surface structure factor of $K_{67}Na_{33}$ is now compared with that of liquid Ga and In reported previously .[3,4] To normalize $q_z$ to the atomic size, $q_z$ has been divided by $q_z^{max}$ of the first maximum of $S(q)$. For $K_{67}Na_{33}$, $q_z^{max} \approx 1.7$ Å$^{-1}$ whereas for Ga and In $q_z^{max} \approx 2.4$ Å$^{-1}$. It is evident that the surface structure factor indicative of surface-normal layering does not increase as quickly for $K_{67}Na_{33}$ as for Ga or In. Assuming that the same layering model that successfully describes the surface of Ga[3] and In[4] also applies to the KNa alloy the measurement indicates that either the surface layering of the alloy is significantly weaker than that of both Ga or In, or the length over which the layering decays into the bulk is signficantly shorter. One can speculate that there might be a correlation between these layering length scales

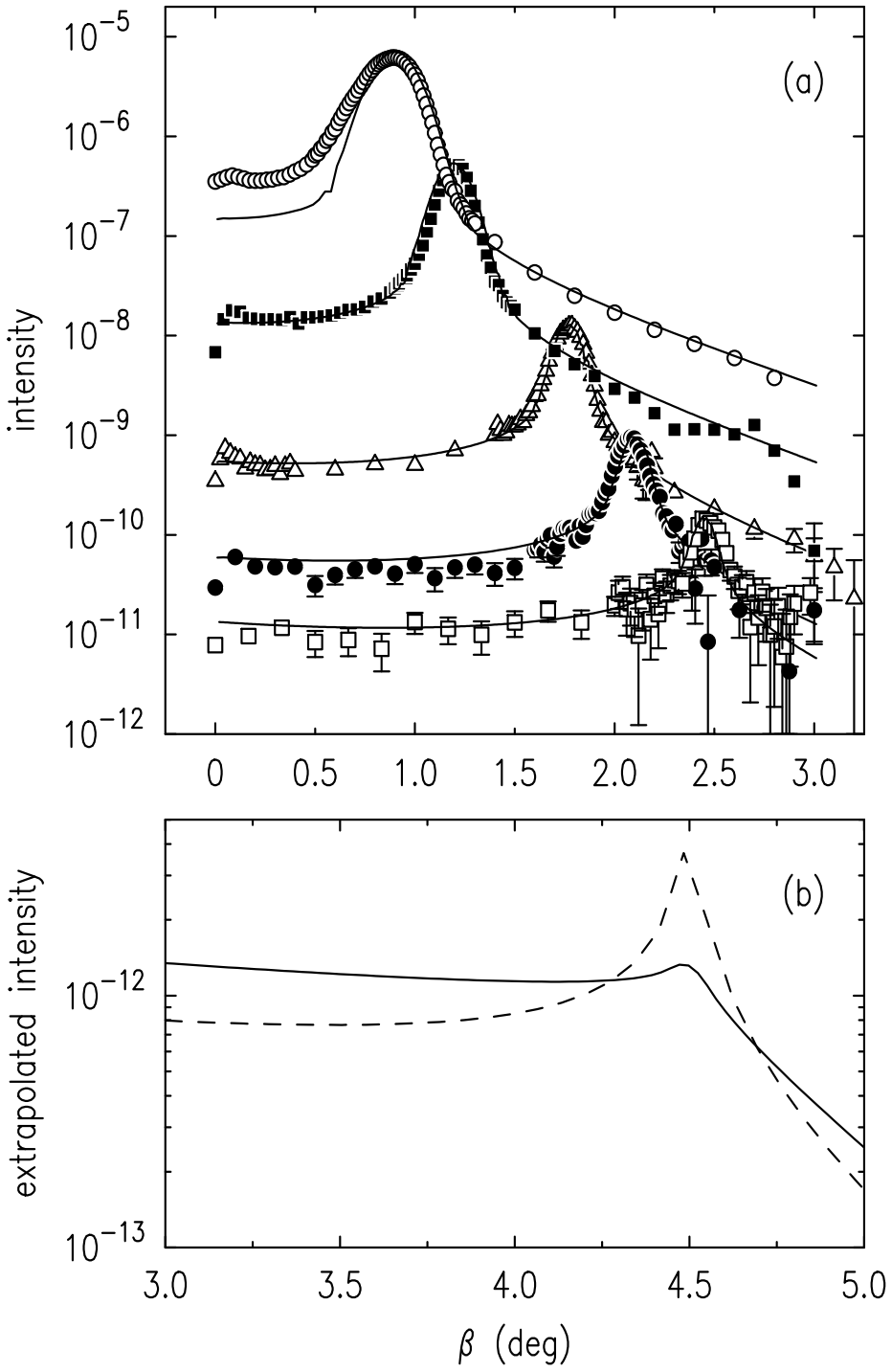



Figure 6.2: (a) Off-specular diffuse scattering from the surface of liquid $K_{67}Na_{33}$ for different incoming angles $\alpha$: (○): 0.9° (multiplied by 25 for clarity), (■): 1.2° (× 5), (△): 1.77°, (●): 2.1° (× .2), (□): 2.45° (× .1). (b) Extrapolated diffuse scattering (assuming no surface layering) for $\alpha = 4.5$ °: (—) resolution of the present experiment ($\Delta q_z \approx 0.03$ Å$^{-1}$). ( - - - ) assuming the resolution attainable at a low divergence x-ray source: ($\Delta q_z \approx 3 \times 10^{-4}$ Å$^{-1}$). (intensity × 100).

and the surface tension. This would mean that weak or quickly decaying layering is expected for LM with exceptionally low surface tension. Clearly, data extending well beyond $q_z = 1$ Å$^{-1}$ are needed to support this conclusion.

## 6.7 Capillary Wave Contributions

Several factors contribute to the difficulty of extending reflectivity measurements to values of $q_z$ large enough to cover the expected position of the layering peak. The reflected intensity falls over almost ten orders of magnitude, while the background from the bulk structure factor increases, as this value of $q_z$ is approached. We must also consider that the exponent $\eta$ approaches its limiting value of 2 for $q_z \to 1.7$ Å$^{-1}$ so that the specular cusp becomes broadened and ultimately lost in the diffuse background. Because of these effects, simply increasing the photon flux is not sufficient to improve the measurement substantially. A better approach is to significantly improve the resolution. This is illustrated in Figure 6.2(b), where the calculated DS for $\alpha = 4.5$ degrees (corresponding to $q_z = 1.5$ Å$^{-1}$) is shown for the current experimental resolution (solid line) and for a resolution sharper by a factor of 200 (dashed line). Although the intensity is much reduced in the latter case, the peak is much better defined. Reflectivity measurements conducted at low divergence synchrotron x-ray sources that are presently becoming available may make such extensions of the $q_z$ range possible.

## 6.8 Oxidation Studies

To explore the effect of possible contaminants on the surface structure, we deliberately exposed the liquid alloy surface to controlled amounts of pure oxygen and hydrogen

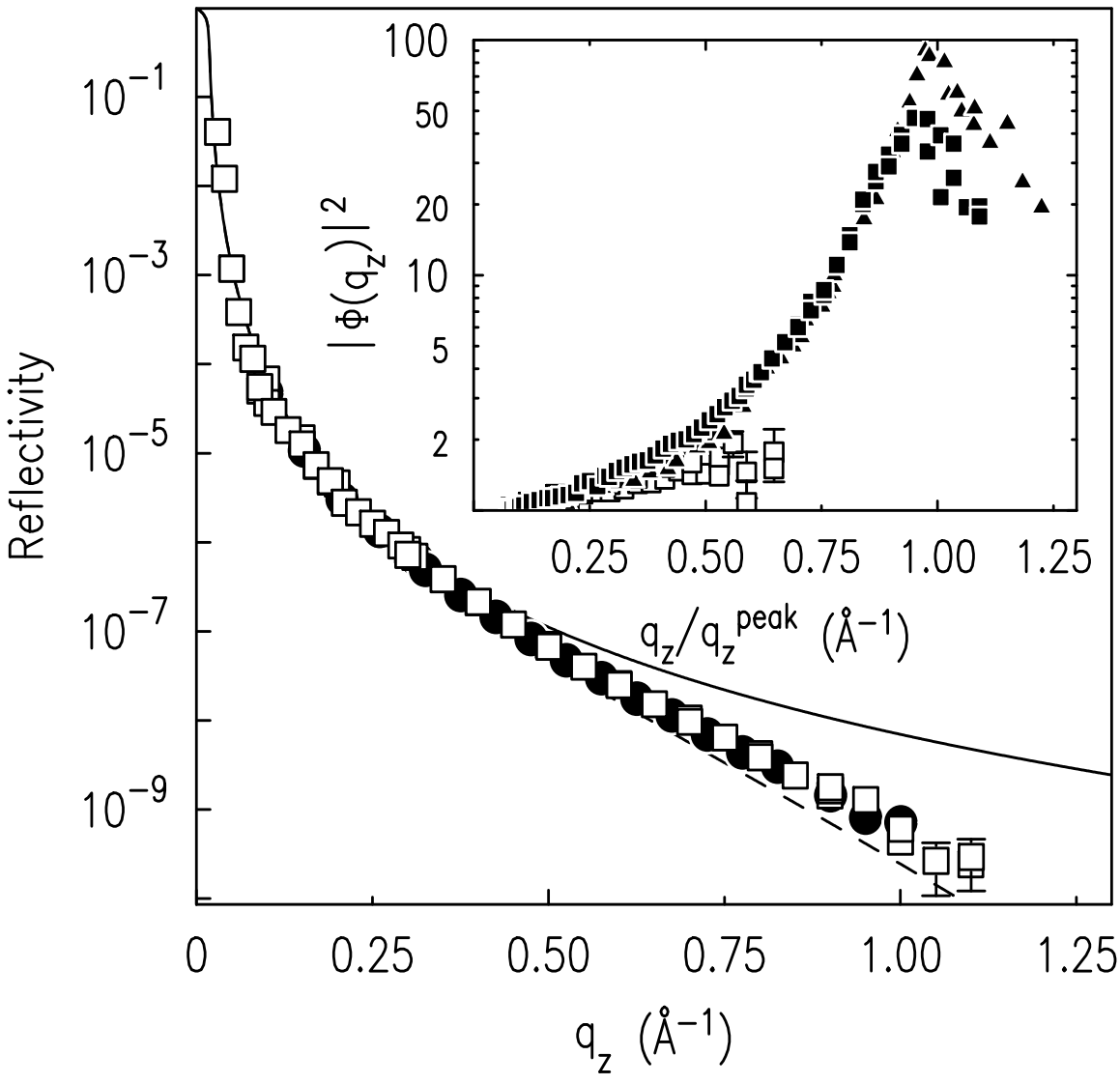



Figure 6.3: X-ray reflectivity from a clean liquid $K_{67}Na_{33}$ surface at room temperature (□) and $K_{67}Na_{33}$ following an exposure to 3000 L of oxygen (•) Also included for reference: (—) calculated Fresnel reflectivity from an ideal $K_{67}Na_{33}$ surface; (- - -) calculated reflectivity $R_{cw}$ from a $K_{67}Na_{33}$ surface roughened by capillary waves at room temperature. Inset: Surface structure factor $|\Phi(q_z)|^2$ of liquid $K_{67}Na_{33}$ at room temperature (□). For comparison the surface structure factors for liquid Ga (closed triangles) and In (closed boxes) are included. $q_z$ is normalized to the position of the first peak in the bulk $S(q)$

gas, measured in units of monolayer surface coverage (Langmuir).[20] The liquid alkali surface has been exposed to up to 3000 L oxygen and up to 6000 L hydrogen. As an example,$R(q_z)$ at the maximum exposure of $O_2$ is shown as filled circles in Figure 6.3. In no case was a measurable effect on $R(q_z)$ observed, indicating no change in the surface-normal structure. This insensitivity of the liquid $K_{67}Na_{33}$ surface to small amounts of oxygen is in striking contrast to similar experiments on liquid Ga[20] and Hg[21] where the formation of a thin homogeneous oxide film has been observed upon exposure of the liquid surface to as little as 200 L of oxygen. This difference is due to the fact that the low surface tension of liquid AM precludes segregation of oxide from the bulk. By contrast, high surface tension LM such as Ga or Hg lower their high overall surface energy by segregation of a contaminant film. These results are also in agreement with photoelectron spectroscopy experiments requiring a similarly clean liquid AM surface.[22]

## 6.9 Summary

In summary, we have shown that it is possible to investigate the surface structure of an atomically clean liquid AM under UHV conditions. Exposing the sample to up to 6000 L of $H_2$ or $O_2$ has no effect on the atomic surface structure since the exceptionally low surface tension of AM precludes contaminant segregation. From DS we extract the surface roughness, which agrees well with capillary wave theory, and with the macroscopic surface tension reported in the literature. The $q_z$-dependence of the surface structure factor determined from the XR is consistent with constructive interference of x-rays due to surface-normal layering. This surface-induced layering in liquid $K_{67}Na_{33}$ appears to be much weaker than that found in high surface tension

LM such as In or Ga.

# Bibliography


[1] J. G. Harris, J. Gryko and S. A. Rice, J. Chem. Phys. **87** 3069, (1987).

[2] O. M. Magnussen, B. M. Ocko, M. J. Regan, K. Penanen, P. S. Pershan, M. Deutsch, Phys. Rev. Lett. **74** 4444, (1995).

[3] M. J. Regan, E. H. Kawamoto, S. Lee, P. S. Pershan, N. Maskil, M. Deutsch, O. M. Magnussen, B. M. Ocko, L. E. Berman, Phys. Rev. Lett. **75** 2498, (1995).

[4] H. Tostmann, E. DiMasi, P. S. Pershan, B. M. Ocko, O. G. Shpyrko, and M. Deutsch, Phys. Rev. B **59** 783, (1999).

[5] M. J. Regan, P. S. Pershan, O. M. Magnussen, B. M. Ocko, M. Deutsch, and L. E. Berman, Phys. Rev. B **55** 15874, (1997).

[6] H. Tostmann, E. DiMasi, P.S. Pershan, B.M. Ocko, O.G. Shpyrko and M. Deutsch, Ber. Bunsenges. Phys. Chem. **102** 1136, (1998).

[7] E. DiMasi and H. Tostmann, Synchrotron Radiation News **12** 41, (1999).

[8] E. DiMasi, H. Tostmann, B.M. Ocko, P.S. Pershan and M. Deutsch, Phys. Rev. B **58** 13419, (1998).

[9] J.M.Ziman, Phil.Mag. **6** 1013, (1961).

[10] N.H.March, *Liquid Metals*, Cambridge University Press, Cambridge, 1990.

[11] N. W. Ashcroft and N. D. Mermin, *Solid State Physics*, Saunders College Publishing, Orlando (1976).

[12] M. Hasegawa and M. Watabe, J. Phys. C **15** 353, (1982); E. Chacon, F. Flores and G. Navascues, J. Phys. F **14** 1587, (1984); M. A. Gomez and E. Chacon, Phys. Rev. B **49** 11405, (1994).

[13] C. C. Addison, *The Chemistry of the Liquid Alkali Metals*, Wiley-Interscience, New York (1984).

[14] Y. Waseda, *The Structure of Non-Crystalline Materials*, McGraw Hill, New York (1980).

[15] M. Shimoji, *Liquid Metals*, Academic Press, London (1977) p. 142-148.

[16] M. Fukuto, R.K. Heilmann, P. S. Pershan, J.A. Griffiths, S.M. Yu and D.A. Tirrell, Phys.Rev.Lett **81** 3455, (1998).

[17] P. S. Pershan, Synchrotron Radiation News, **12**, 10 (1999).

[18] V. K. Sheriev, T. P. Osiko and O. G. Ashkhotov, High Temperature **29** 85, (1991).

[19] The position of the layering peak is expected to be close to that of the first peak of the bulk $S(q)$.

[20] M. J. Regan, H. Tostmann, P. S. Pershan, O. M. Magnussen, E. DiMasi, B. M. Ocko, M. Deutsch, Phys. Rev. B **55** 10786, (1997).

[21] H. Tostmann, E. DiMasi, P.S. Pershan, B.M. Ocko, O.G. Shpyrko and M. Deutsch, J. Non. Cryst. Solids, in print (1999).

[22] G. Indlekofer and P. Oelhafen, J. Non-Cryst. Solids **156-158** 226, (1993).

# Chapter 7

# Layering in Alkali Metals: Liquid Potassium

## 7.1 Abstract

In this chapter we present x-ray reflectivity and diffuse scattering measurements from the liquid surface of pure potassium. They strongly suggest the existence of atomic layering at the free surface of a pure liquid metal with low surface tension. Prior to this study, layering was observed only for metals like Ga, In and Hg, the surface tensions of which are 5-7 fold higher than that of potassium, and hence closer to inducing an ideal "hard wall" boundary condition. The experimental result requires quantitative analysis of the contribution to the surface scattering from thermally excited capillary waves. Our measurements confirm the predicted form for the differential cross section for diffuse scattering, $d\sigma/d\Omega \sim 1/q_{xy}^{2-\eta}$ where $\eta = k_B T q_z^2/2\pi\gamma$, over a range of $\eta$ and $q_{xy}$ that is larger than any previous measurement. The partial measure of the surface structure factor that we obtained agrees with computer simulations and theoretical predictions.

## 7.2 Introduction

In contrast to measurements of dielectric liquids, which show a monotonically varying density profile at the liquid-vapor interface, liquid metals exhibit a phenomenon known as surface-induced layering[1,2]. This had been thought to occur because the Coulomb interactions between two constituents of the liquid metal, the free electron Fermi gas[3] and the classical gas of positively charged ions, suppress local surface fluctuations that would otherwise conceal the layered atomic ordering that occurs at hard walls[4]. On the other hand recent molecular simulations by Chacon et al.[5] argue that surface layering should occur in any liquid for which the ratio of melting temperature $T_m$ and critical temperature $T_c$, $T_m/T_c$, is sufficiently small. Until this measurement the only experimental observations of surface-induced atomic layering have been accomplished in a number of high surface tension metals - pure liquid metallic systems such as Hg[6], Ga[7], In[8] as well as in binary alloys[9,10]. In fact, for Ga, Hg and K $T_m/T_c \approx 0.13 - 0.15$ and these observations are consistent with Chacon et al.[5]. From another point of view, all but one of the metallic systems studied so far exhibit relatively high values of surface tension, a few hundred mN/m, leaving unanswered the fundamental question of whether the surface-induced layering is caused by the high surface tension, which suppresses the long wavelength capillary waves, or whether it is caused by the intrinsic metallic properties of the studied systems. In the later case surface-induced layering should also be found in low-surface tension metals. Monovalent alkali metals have a surface tension comparable to that of water (72 mN/m) and their study should, therefore, shed light on this issue. Moreover, monovalent alkali metals are the best available examples of an ideal nearly-free-electron metal[11], therefore, they are particularly well suited for studying surface induced layering in an ideal,

simple liquid metal. The same properties which make alkali metals ideal for studies of layering have also been the motivation for the numerous computer simulations of liquid Na, K and Cs[1,2,11,12,13,14,15,16].

Until recently, experimental surface studies of the pure liquid alkalis were thought to be impossible because of two fundamental experimental problems. First, their high evaporation rates which lead to high values of vapor pressure[17], and high reactivity[18] to water and oxygen implied that their surfaces could not be maintained atomically clean for extended periods of time even under UHV conditions. Therefore, the first study of alkali metal systems performed by us[8] employed a binary KNa alloy that preserves most of the characteristic features typical of a nearly-free-electron metal, but for which the vapor pressure and melting temperature were both lower than those of the pure metals. Contrary to expectations, no measurable changes were detected in that study in the x-ray reflectivity of the alloy's surface over periods of many hours or after intentional exposure to large doses of oxygen. This lack of surface contamination is believed to be due to the high solubility of the oxides of these metals in the bulk liquid[18,19], and to the low surface tension of liquid alkali metals which does not promote segregation of the oxide at the surface. The fact that the surface of the KNa alloy was found to remain atomically clean for extended periods of time suggests that the same might be true for the pure metals. The second experimental problem is that the large capillary-wave-induced roughness due to the low surface tension renders the x-ray reflectivity peak weak and inseparable from its' diffuse wings. Thus, a clear layering peak in the measured reflectivity curve, such as found in the high-surface-tension liquid metal studies[6,7,8,9,10], can not be observed here. We demonstrate here that this problem can be resolved by a subtle application of diffuse scattering and

reflectivity measurements. A significant aspect of this chapter pertains, therefore, to the methods of measurement and analysis that are necessary in order to separate the effects due to the thermal capillary waves from those of the surface-induced layering. Using these methods, the present study clearly demonstrates the existence of surface induced layering in liquid K, with properties similar to those of the high-surface-tension liquid metals studied previously[6,7,8,9,10].

## 7.3 Experimental Details

The sample preparation procedure and the experimental setup were similar to our previous experiment on the KNa alloy[8]. The sample was prepared in an Argon-filled glove box ( $<$ 2ppm $H_20$, $<$ 1 ppm $O_2$). The K with purity of 99.999 %, which was contained in a glass ampoule, was melted and then transferred into a sealed stainless steel reservoir inside the glove box using a glass syringe. The reservoir was sealed with a Teflon o-ring and then mounted onto a UHV chamber.

After a 24-hour bakeout of the entire chamber to 150 $^\circ$C, a base pressure of $10^{-9}$ Torr has been established inside the UHV chamber. The K in the reservoir was then heated above the melting temperature $T_m$=63$^\circ$ C and dropped through a capillary into a Mo sample pan mounted inside the UHV chamber by opening the valve V shown on Figure 7.1. Previous to filling the pan with liquid K, the pan was cleaned by sputtering with $Ar^+$ ions for several hours in order to remove the native Mo oxide. This latter procedure significantly improves the wetting of the sample pan by liquid K and therefore helps to achieve a larger area of macroscopically flat liquid surface than it has been possible for high surface tension metals[7]. The sample pan was kept at a constant temperature of 70 $^\circ$C. Pure K has a vapor pressure of about

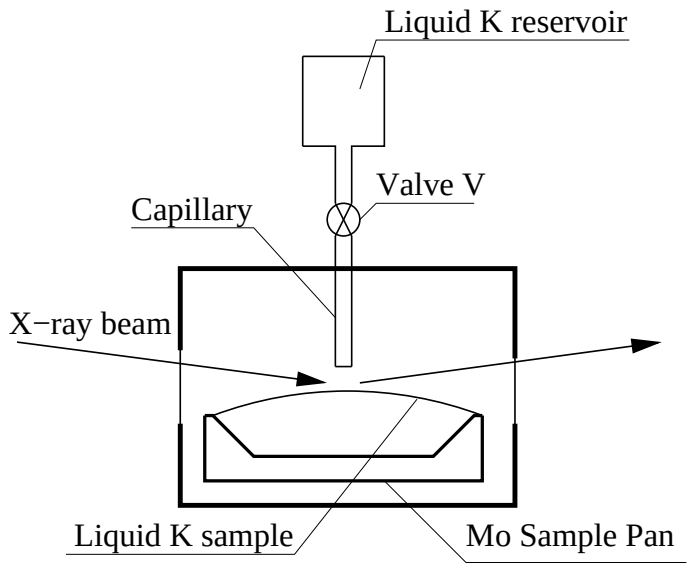



Figure 7.1: Schematic description of the experimental setup.

$10^{-6}$ Torr at this temperature, which renders the requested UHV conditions almost impossible. We circumvented this problem by a differential pumping setup, where we used a permanently attached ion pump. By constantly pumping at the sample chamber, we were able to achieve a base pressure of about $10^{-9}$ Torr in the chamber, three orders of magnitude lower than vapor pressure of potassium.

Measurements were carried out using the liquid surface reflectometer at CMC-CAT beamline at the Advanced Photon Source, Argonne National Laboratory, operating at an x-ray wavelength of 1.531 $\mathring{A}^{-1}$. The kinematics of the measurement is illustrated in Figure 7.2. Two different surface-sensitive x-ray techniques were applied - specular x-ray reflectivity and x-ray diffuse scattering. In the specular x-ray reflectivity geometry, the incident angle $\alpha$ and the reflection angle $\beta$=$\alpha$ are varied simultaneously while keeping $\Delta\Theta = 0$ constant. The signal is measured as a function of the surface-normal momentum transfer $q_z = 2\pi/\lambda\,(\sin\alpha + \sin\beta)$ with the in-plane

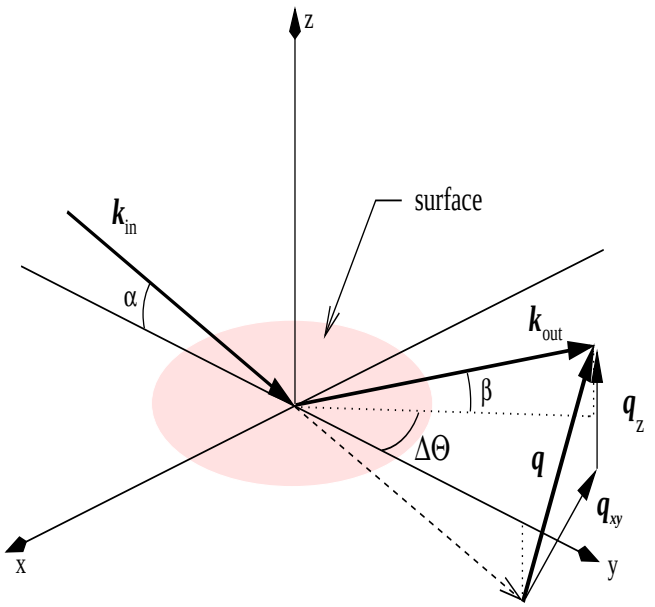



Figure 7.2: Kinematics of the x-ray measurement.

momentum transfer $q_{xy} = 0$.

In the x-ray diffuse scattering geometry, the detection angle $\beta$ is varied within the plane of incidence $\Delta\Theta = 0$, while the incident angle $\alpha$ stays fixed. The observed scattering therefore follows a trajectory in the $(q_x, q_z)$ plane with $dq_z/dq_x = \tan\beta$ and $q_y$=0. The signals measured in the two geometries are, however, related since the signal measured at $\beta = \alpha$ in the diffuse measurement is the specular signal.

The differential cross-section of the diffuse scattering signal is given by[20]:

$$\frac{d\sigma}{d\Omega} = \frac{A_0}{\sin\alpha}\left(\frac{q_c}{2}\right)^4 \frac{k_B T}{16\pi^2\gamma} \mid \Phi(q_z) \mid^2 \frac{1}{q_{xy}^{2-\eta}} \left(\frac{1}{q_{\max}}\right)^{\eta} \tag{7.3.1}$$

where $q_c$[21] is the critical angle for total external reflection of x-rays, $\gamma$ is the surface tension, $q_{max} \approx \pi/\xi$ is the value of the upper cutoff for capillary wave contributions[20]. The value for $\xi$ is empirically taken to be the nearest neighbor atomic distance in the

bulk[21]. The scattering lineshape exponent $\eta$ is given by[20]

$$\eta = \frac{k_B T}{2\pi\gamma} q_z^2 \tag{7.3.2}$$

The principal goal of the present surface x-ray scattering measurements is to determine the surface structure factor[7]

$$\Phi(q_z) = \frac{1}{\rho_\infty} \int dz \frac{\langle d\rho(z) \rangle}{dz} \exp(\imath q_z z) \tag{7.3.3}$$

which is given by the Fourier transform of the $(x, y)$-averaged intrinsic density profile $\langle \rho(z) \rangle$ along the surface normal $z$ in the absence of capillary waves. In this equation, $\rho_\infty$ is the bulk electron density. The fact that the peak of the differential cross section at the specular condition is algebraic, rather than a $\delta$-function complicates the determination of $\Phi(q_z)$ from the measured intensity. This can be done, however, when both specular reflectivity and diffuse scattering measurements are available.

## Practical Considerations

It follows from Eq. 7.3.1 that the nominal specular reflectivity signal, observed at $\alpha = \beta$ and $\Delta\Theta = 0$ corresponds to the integral of the $(1/q_{xy})^{2-\eta}$ over the area $\Delta q_{xy}^{res}(q_z) = \Delta q_x^{res} \times \Delta q_y^{res}$ which is the projection of the instrumental resolution function on the horizontal plane of the liquid surface. The $q_z$-dependence of $\Delta q_{xy}^{res}(q_z)$ is due to the increase of the projected width of the detector resolution $\mid \Delta q_y^{res} \mid = (2\pi/\lambda) \sin\beta \Delta\beta$ on the plane of the surface as $\beta$ increases. The integration results in the reflectivity scaling as $\left(\Delta q_y^{res}/q_{max}\right)^\eta / \eta$ and since $\eta$ scales as $q_z^2$, the net effect is a Debye-Waller-like decrease in the reflectivity as $q_z$ increases. For example, if one defines a mean square surface roughness by taking an average over a length scale

$\approx (\Delta q_y^{res})^{-1}$, this roughness can be written as[22]

$$\sigma^2(q_z) = (k_b T/2\pi\gamma)\ln(q_{max}/\Delta q_y^{res}) \tag{7.3.4}$$

From this one can show that the reflectivity is proportional to a Debye-Waller factor $\exp[-q_z^2\sigma^2(q_z)]$. The important point to note is that for liquid surfaces the signal measured at the specular condition $q_{xy} = 0$ depends on the resolution of the reflectometer.

The validity of the simple capillary wave model in the high $q$-range remains controversial and untested. Although the model assumes that the energy for surface excitations can be described by the capillary form $\approx \gamma/q_{xy}^2$ with a constant surface tension, $\gamma$, over the entire range of length scales from the macroscopic to a microscopic length of the order of $\xi = \pi/q_{max}$, where $\xi$ is normally taken to be of the order of the interatomic/molecular spacing $a$, this is certainly not strictly true for lengths that are shorter than a length that we might designate as $\xi_{cutoff} = \pi/q_{cutoff} > a$. Nevertheless, the basic physics is not changed if we replace $q_{max}$ by the smaller $q_{cutoff}$ since the differences engineered by this are really just a matter of accounting, in the sense that it determines the relative contributions between the capillary wave and structure factor terms given in Eq. 7.3.1. Nevertheless this is not a serious objection to the present treatment, since the capillary wave model is certainly accurate for values of $q_{xy}$ covered by the present measurements. Even if the model were to fail for values of $q_{xy} > q_{cutoff}$, the shorter wavelength fluctuations could be incorporated into the definition of a $q_{cutoff}$-dependent structure factor $\Phi(q_z)$. On the other hand, the fact that the intensity of off-specular diffuse scattering predicted by Eq. 7.3.1 has been shown to be in satisfactory quantitative agreement with measurements for a number of liquids over a wide range of $q_y$ and $q_z$ implies that $q_{cutoff}$ is reasonably close to

$q_{max} = \pi/a$ and the extracted structure factor $\Phi(q_z)$ is a reasonable measure of the local profile.

There are three practical considerations involved in these measurements.

The first is that it is necessary to insure that the measurement corresponding to the integral over the resolution does not include a diffuse scattering contribution from sources other than the surface. For flat surfaces, for which the specular reflectivity can be described by a $\delta$-function at $q_{xy}$=0, this can be accomplished by subtracting the scattering measured at some finite value of $q_{xy}$ from the signal measured at $q_{xy}$=0. For liquid surfaces this separation is complicated by the fact that the signal measured at finite $q_{xy}$ includes scattering from the $1/q_{xy}^{2-\eta}$ tails of the cross-section. We circumvent this problem in the present study by comparing the difference between measurements at $q_{xy}$ =0 and at some $q_{xy} \neq 0$ with the same difference as predicted by the theoretical differential cross section (Eq. 7.3.1). Thus, we present all data in this study as differences between a signal measured at $\{\alpha, \beta, 0\}$ and at $\{\alpha, \beta, \Delta\Theta_{offset}$ = 0.2 degrees$\}$. For specular reflectivity $\alpha = \beta$; however, for off-specular diffuse measurements $\beta \neq \alpha$. diffuse scattering from all sources other than the surface are essentially constant over this range of $\Delta\Theta_{offset}$. This is because these other sources of scattering, such as diffuse scattering from either the bulk liquid or from the vapor above the surface, only depend on the absolute value of the total momentum transfer $\mid q \mid$ and this is essentially unchanged for small offsets in $\Delta\Theta_{offset}$.

The second practical consequence of the $1/q_{xy}^{2-\eta}$ form is that as $\eta$ increases it becomes increasingly difficult to distinguish the singular specular peak from the off-specular power-law wings. At $\eta \geq 2$ this distinction is no longer possible[20], even with infinitely sharp resolution. Unfortunately, for liquid K, $\eta$ reaches the limit of 2

at $q_z$=1.74 $\mathring{A}^{-1}$, which is comparable to $q_z$=1.6 $\mathring{A}^{-1}$, where the quasi-Bragg surface layering peak is expected to be observed. However, in the following paragraph we show that as a result of resolution effects, the limit at which the specular cusp can no longer be distinguished from the background in practice is even lower.

The impact of the finite resolution can be easily seen by considering a simple example of a rectangular resolution function of infinite length along the x axis but with a very small width along the y axis. For small values of $\alpha$ this is often an excellent approximation to the real resolution functions[23]. With this approximation, the integration over the $q_x$ component yields a $1/{q_y}^{1-\eta}$ dependence for the diffuse scattering, placing the value of $\eta$ where the specular ridge disappears to be $\eta$=1 instead of $\eta$=2 . For K, this $\eta$=1 limit is reached at $q_z$=1.2 $\mathring{A}^{-1}$. The detector slit dimensions which provide an optimal compromise between intensity and resolution were discussed by one of us[20] and are $(width) \approx (height) \times \sin\alpha$, where $\alpha$ is the incident angle.

The third practical problem in extending x-ray reflectivity measurements to large $q_z$ is the fast fall-off of the reflected intensity. Much more serious is the Debye-Waller-like factor that was discussed above. Since the surface tension $\gamma$ for K (110 mN/m at 70 $^\circ$C) is much lower than that of a metal like Ga (770 mN/m)[17], the factor of $\exp[-\sigma^2 q_z^2]$ with $\sigma^2 \sim 1/\gamma$ is orders of magnitude smaller than that of Ga at the same values of $q_z$. Even at high-flux synchrotron facilities such as the Advanced Photon Source the low count rates of the reflectivity signal observed at $q_z \approx 1.0 - 1.1$ $\mathring{A}^{-1}$ are among the dominant limiting factors of the $q_z$ range accessible in this experiment.

## 7.4 Measurements

### 7.4.1 Advantages of Linear Detector

To partially compensate for the low intensity the off-specular diffuse scattering measurements were carried out using a linear position sensitive detector (PSD), rather than a point detector.

In Figure 7.3 we show a diffuse scattering profile as a function of $q_{xy}$. The specular condition corresponds to $q_z = 0.3\ \mathring{A}^{-1}$. The profile exhibits a sharp peak whose width is dominated by the instrumental resolution, however the long tails are an intrinsic property of the capillary wave surface roughness. We note that the data shown represents the intensity difference for data obtained at $\Delta\Theta = 0$ and $\Delta\Theta = \pm\Delta\Theta_{offset}$ with either a position sensitive detector (PSD) or with a point detector. An advantage of the PSD configuration is that it permits the entire profile to be acquired simultaneously for a wide range of the output angles $\beta$ for a fixed $\alpha$. We carefully checked for possible instrumental errors associated with the PSD (saturation or nonlinear effects) by comparing data obtained with both the PSD and a point detector. As shown, in Figure 7.3, data obtained with both configurations are indistinguishable. Further, this comparison allowed an accurate determination of the PSD spatial resolution, about 0.22 mm vertically. To provide for a reasonable comparison with the point detector, the vertical slit was set to match the resolution of the PSD. The solid line in Figure 7.3 represents the theoretical prediction for the different intensity, obtained by numerically integrating $d\sigma/d\Omega$ in Eq. 7.3.1 over the known resolution. The known values of the incident angle $\alpha$, temperature T, surface tension $\gamma$, x-ray energy and detector resolution, were used without any adjustable parameters. The

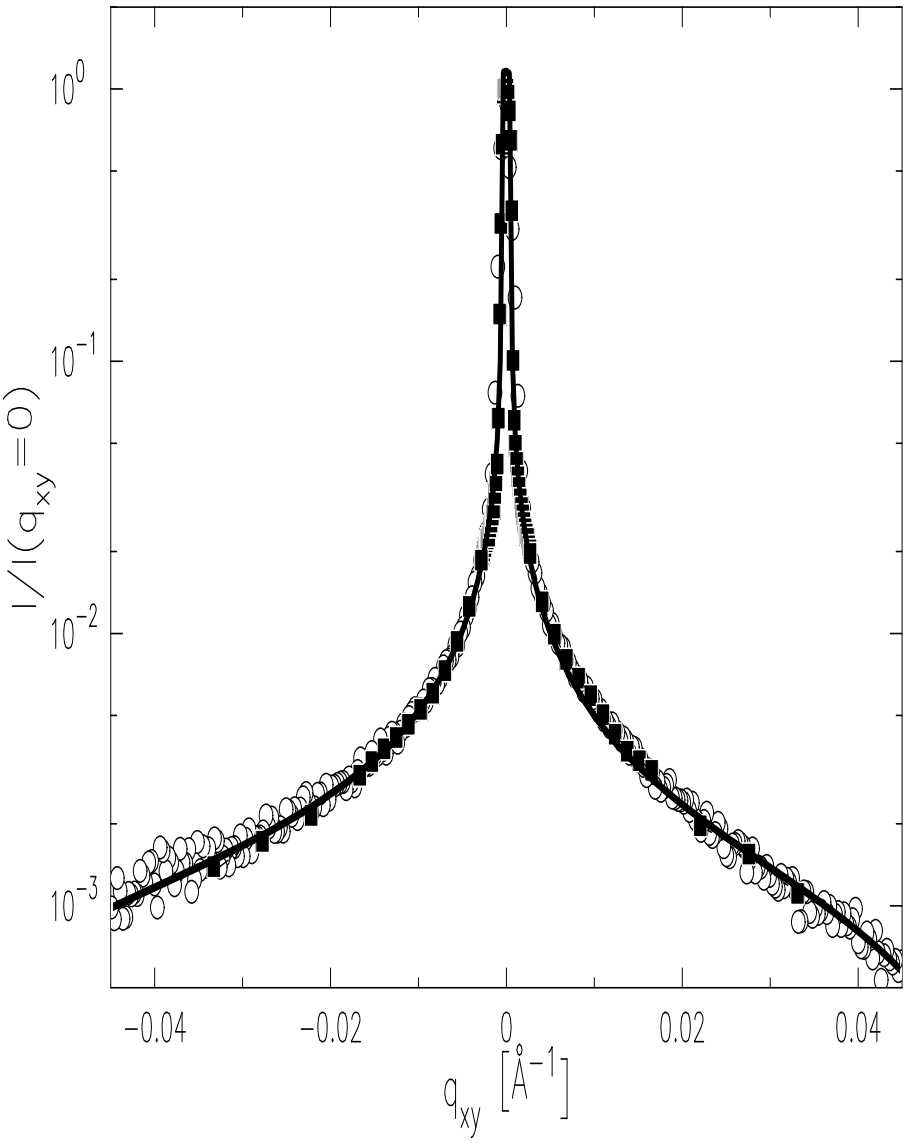



Figure 7.3: Comparison of an X-ray diffuse scattering scans taken with point detector - filled squares, and position sensitive detector (PSD) - open circles. The specular condition corresponds to $q_z$=0.3 $\mathring{A}^{-1}$. The resolution of the bicron detector (0.22mm vertically and 2.5mm horizontally) was chosen to match that of a PSD. Also shown is a line which represents theoretical modeling using the capillary-wave theory for given resolution, temperature (70°$C$) and surface tension (110 mN/m).

essentially perfect agreement between both experimental data sets and the theoretical simulations strongly supports the theoretical model for the effect of the thermally induced surface excitation on the diffuse x-ray scattering from the surface.

### 7.4.2 Diffuse Scattering Data: Eta Effect

Further diffuse scattering data was collected with the PSD, which proved to be especially useful at higher values of $q_z$, where the weaker scattering makes it increasingly more difficult to separate the specular signal from the power-law wings as $\eta$ approached 1. Figure 7.4 shows a set of diffuse scattering scans measured with a PSD and the corresponding calculated theoretical predictions, for several $q_z$ values (0.3, 0.4, 0.6, 0.8, 1.0 and 1.1 $\mathring{A}^{-1}$). Each curve represents a difference between a diffuse measurement in the plane of incidence ($\Delta\Theta = 0$) and an average of two measurements taken by displacing the detector out of the plane of incidence by an angle of $\Delta\Theta_{offset} = \pm$ 0.2 degrees. Theoretical simulations include the same subtraction operation as well. All data sets are normalized to unity at $q_{xy}$=0 for easier comparison. As $q_z$ gets larger, the ratio of specular signal to the diffuse wings decreases, and the specular peak eventually disappears under the off-specular diffuse wings. In the curve measured at $q_z = 1.2$ $\mathring{A}^{-1}$), shown in the inset to Figure 7.4, the specular peak is all but disappeared. The solid lines that represent numerical integration of the capillary-wave theory (Eq. 7.3.1) show a remarkably good agreement with experimental data. The only adjustable quantity in these theoretical curves is the form of $\Phi(q_z)$. As discussed below, one common form was used for all data sets.

This agreement provides additional support for the absence of surface contamination, since the presence of any kind of inhomogeneous film at the surface would manifest itself in extra x-ray diffuse signal which could not be explained by capillary

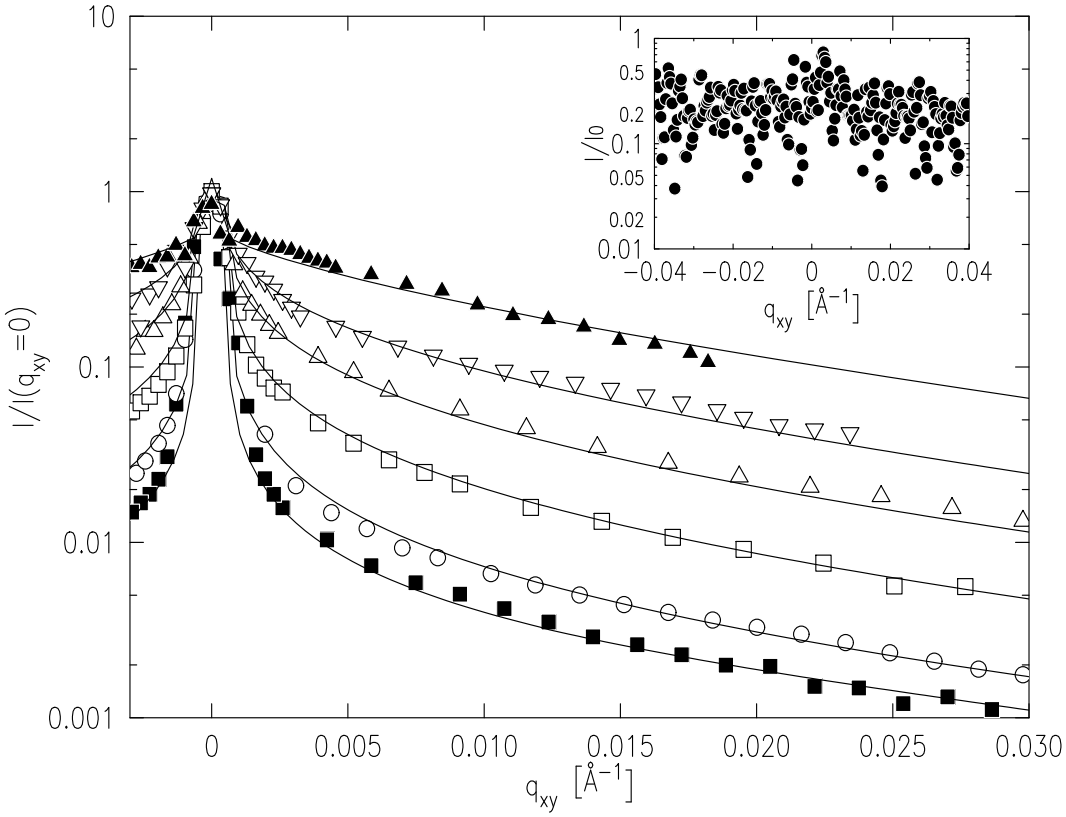



Figure 7.4: X-Ray diffuse scattering scans taken with PSD, as a function of wavevector transfer component $q_{xy}$. Specular condition corresponds to values of $q_z$ (bottom to top): 0.3, 0.4, 0.6, 0.8, 1.0 and 1.1 $\mathring{A}^{-1}$. For comparison, the scans are normalized to unity at $q_{xy}$=0. Lines represent theoretically simulated scans for given values of $q_z$. The inset shows a similar scan taken at 1.2 $\mathring{A}^{-1}$, for which the specular peak is marginally observable.

wave theory alone.

### 7.4.3 Resolution Effects

Figure 7.5 shows the effect of varying the shape of the detector resolution on the diffuse scattering data. Changing the horizontal size of the slit in front of the PSD has little effect on either the measured intensity of the specular peak, because of the intrinsic property of the singularity, or on the diffuse scattering at small $q_{xy}$, because it is sharply peaked around $q_{xy} = 0$. However, far away from the specular condition, the signal is directly proportional to the area of the resolution function, and scales with the size of the slits.

### 7.4.4 Specular Reflectivity Data

The excellent agreement between the experimental measurements and the theoretical simulations strongly support our conclusion that by the methods above one can account properly and accurately for both the capillary-wave-induced diffuse scattering in, and the resolution effects on, the measured data. We have, therefore, employed these results to analyze the specular reflectivity data, to find out whether surface-induced layering exists at the surface of K.

Specular reflectivity measurements were made by scanning $\alpha = \beta$ at both $\Delta\Theta = 0$ and $\Delta\Theta = \pm\Delta\Theta_{offset}$. The $\beta$-resolution, $\Delta\beta = 0.2$ degrees, was set by fixing the height of the detector slit at 2.5 mm, located 714 mm away from the center of the sample. Likewise, the horizontal resolution was defined by a 2.5 mm wide slit located at the same position. The ratio of the difference between the specular signal measured at $\Delta\Theta = 0$ and at $\Delta\Theta = \pm\Delta\Theta_{offset}$ to the theoretical Fresnel reflectivity from the K liquid-vapor interface is shown in Figure 7.6. As expected, there is a Debye-Waller

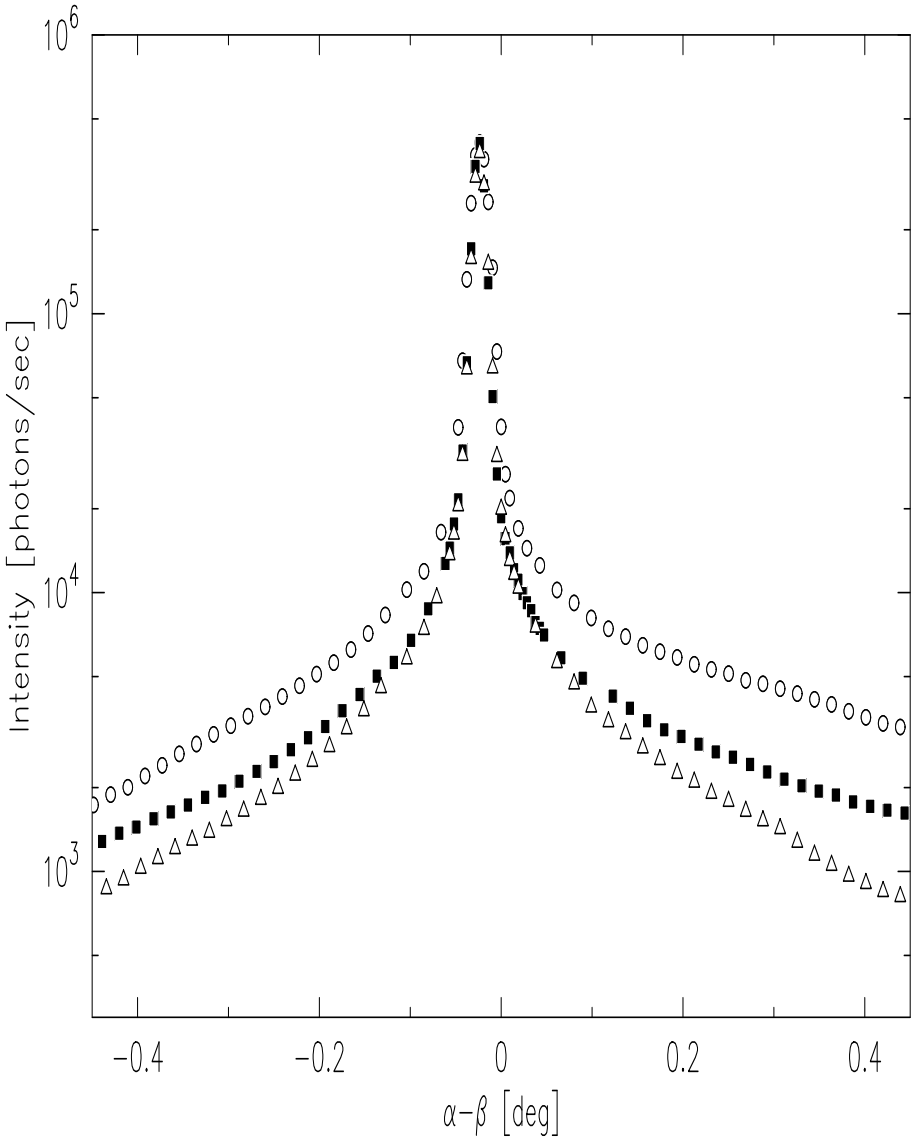



Figure 7.5: Effects of varying the horizontal resolution function on the diffuse scattering data. Diffuse scans taken with PSD, peak position corresponding to $q_z$=0.4 $\mathring{A}^{-1}$, as a function of angular deviation from specular condition $(\alpha - \beta)$ with fixed vertical resolution (.22mm), while horizontal resolution was changed (bottom to top: 2mm, 4mm, 8mm).

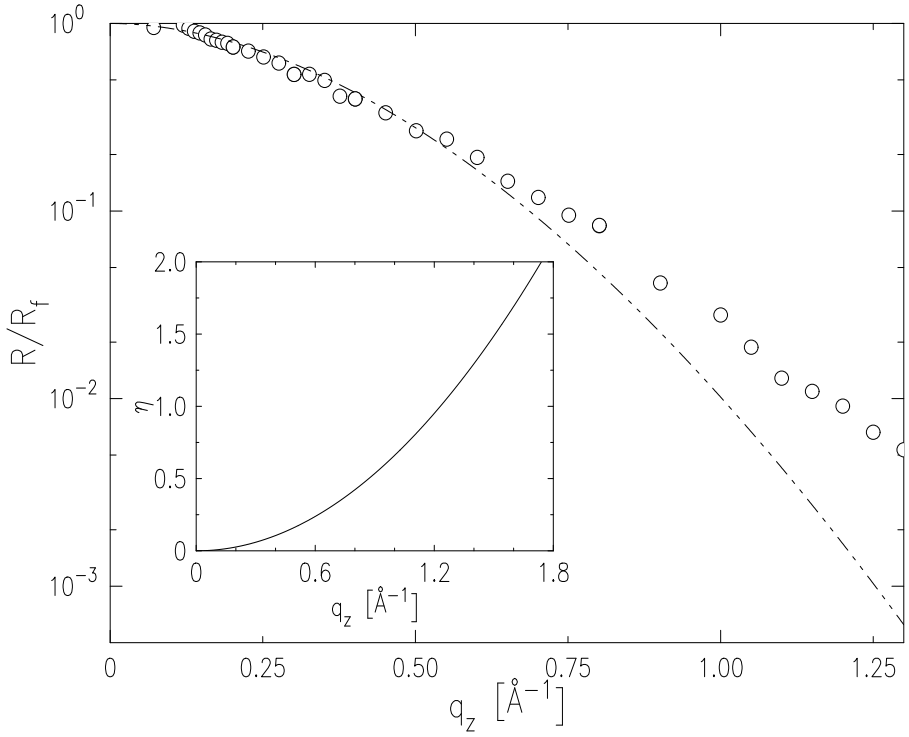



Figure 7.6: Fresnel-normalized reflectivity signal $R/R_f(q_z)$ for liquid K (circles) compared to capillary wave predictions (dashed line). The inset shows the capillary wave factor $\eta$ for liquid K as a function of $q_z$.

type effect that causes the data to fall below unity with increasing $q_z$. However, the measured curve (points) decreases slower than the theoretical prediction (dashed line) for the Debye-Waller-like factor in Eq. 7.3.1 convolved with the resolution function.

### 7.4.5 Surface Structure Factor Data

Figure 7.7 shows the form factor $\Phi(q_z)$, obtained by dividing the data in Figure 7.6 by the integral of the Debye-Waller factor (see Eq. 7.3.1) over the resolution function. In order to compare it with the surface structure factors measured previously for other liquid metals, we have normalized $q_z$ by the value of $q_{peak}$ - the value of $q_z$ at which the layering peak is observed or is expected to be observed. In fact we are comparing the electron density structure factors of the different metals. Alternatively we might have compared the atomic densities; however, none of the atomic form factors vary by more than a few percent over the measured range of $q_z$. The surface structure factor of the pure K is found here to rise clearly above unity and shows a similar functional behavior to that of the pure Ga and In, metals for which the surface-induced layering has been well-documented[7,8]. The inset shows the same plot comparing the surface structure factors extracted from the specular reflectivity measurements of pure Ga, pure In and pure K over an extended $q_z/q_{peak}$ range. Even though experimental and intrinsic limitations (such as the "$\eta$ effect" discussed above) prevents us from resolving the layering peak in its' entirety, it seems clear that liquid K exhibits surface layering similar to that observed in other metals. These experimental results are supported by computer simulations predicting a surface-induced layering in pure potassium[24].

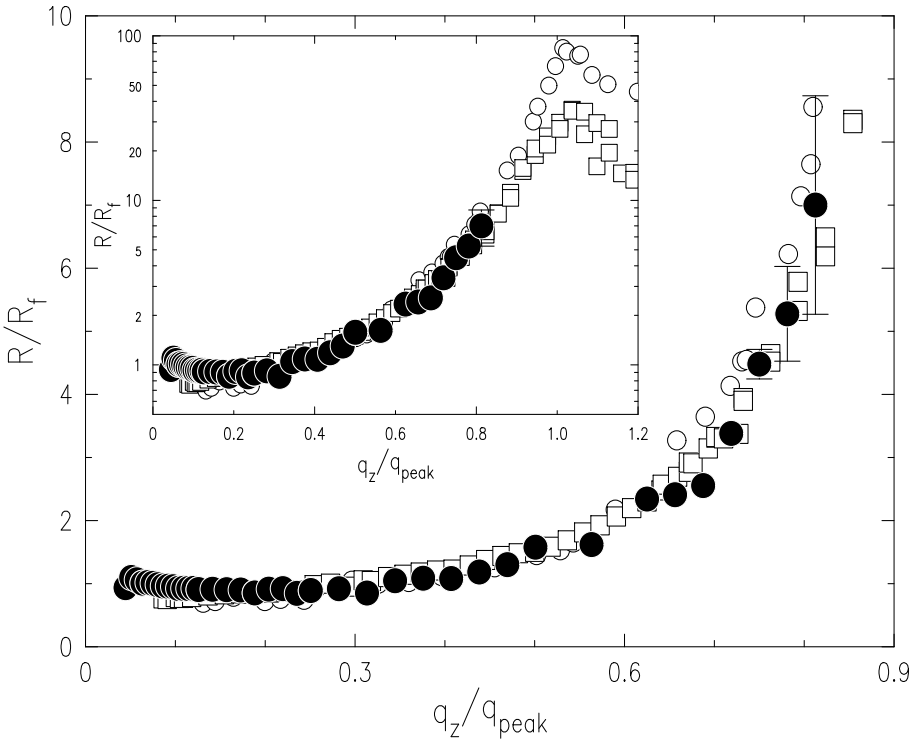



Figure 7.7: Surface structure factor $\Phi(q_z)$ for liquid Ga (open circles), liquid In (open squares) and liquid K (filled circles) obtained from X-ray reflectivity data by deconvolving resolution, Fresnel reflectivity and capillary wave contributions, shown here as a function of $q_z/q_{peak}$, here $q_{peak}$ is the value of $q_z$ at which the layering peak is observed (2.4 $\mathring{A}^{-1}$ for Ga and 2.2 $\mathring{A}^{-1}$ for In) or is expected to be observed (1.6 $\mathring{A}^{-1}$ for K). The inset shows the same three sets of data extended to a greater range.

## 7.5 Summary and Discussion

In this work we have expressed the x-ray scattering from the liquid surface, both specular and diffuse, in terms of the product of a thermal fluctuation term and a surface structure term (Eq. 7.3.3). This is analogous to the usual treatment of Bragg scattering from three-dimensional crystals for which the intensity is expressed as a product of a structure factor and a phonon-induced Debye-Waller factor. For the liquid surface we have assumed that the thermal fluctuations could be described by capillary waves over all length scales extending from a distance $\xi \approx \pi/q_{max}$ that is of the order of the atomic or molecular size, to a macroscopic distance that is determined by the reciprocal of the reflectometer resolution. The gravitationally determined capillary length is ignored since it is many orders of magnitude longer than the resolution-determined length. In fact the capillary wave model is strictly true only for long wavelengths and the assumption that it can be invoked for lengths as small as $\xi$ is only justified empirically[6,7,8,9,10]. However, the good agreement between the measured diffuse scattering and that predicted by Eq. 7.3.1, found for a number of liquids including the present one provides a rather general justification for adopting this limit.

In the present study we generalized the methods that were previously used for liquid surfaces by simultaneously carrying out detailed measurements along and transverse to the specular axis. As in these earlier studies we have been able to verify the $1/q_{xy}^{2-\eta}$ behavior of the capillary wave form of the surface fluctuations to values of $\eta = 0.82$ and to obtain a measure of the surface structure factor. Aside from recent work by Mitrinovic, Williams and Schlossman[23] which were carried out to $\eta = 0.62$, the largest values of $\eta$ attained in any of the previous studies on liquids were less than

half of our value. In view of the fact that the measured value of $\Phi(q_z)$ depends on proper isolation of the capillary diffuse scattering our confirmation of the capillary model for diffuse scattering from K is essential.

The most significant limitation to the present measurement came about as a result of the fact that due to the thermally excited capillary wave Debye-Waller-like effect, the largest value of $q_z$ at which the specular peak can be observed is smaller than 1.6 $\mathring{A}^{-1}$ at which $\Phi(q_z)$ is expected to have a peak. This limitation can be expressed in terms of the capillary model of Eq. 7.3.1 since as $\eta \rightarrow 2$ the specular peak no longer exists. Another way to see the same thing is that the scattering at the peak of $\Phi(q_z)$ will be difficult to observe when the product $\sigma^2(q_{peak})q_{peak}^2 \gg 1$. In essence, this condition occurs when the effective surface roughness approaches that of the surface layer spacing. Although the precise value of $\sigma(q_{peak})$ depends on the resolution, for the resolutions used to study K, $\sigma^2(q_{peak})q_{peak}^2 = 13.8$. Nevertheless, in this chapter we demonstrated by careful measurement of the diffuse scattering with a number of different resolution configurations that it was possible to quantitatively extract values of $\Phi(q_z)$ for K over a significant range of $q_z$. These measurements establish that over the measured range the $q_z$-normalized surface structure factor for pure liquid K is nearly identical to that found in Ga and In, with a well defined rise above unity as the peak in $q_z$ is approached from below. This strongly suggests that the layering in K is identical to that of other liquid metals, as implied by Chacon et al.[5]. Finally, we note that the present method could also be applied to non-metallic liquids having similar surface tensions[25,26,27]. The unresolved and intriguing question of whether the local surface layering in metallic systems is different from that of non-metallic liquids when the surface tensions involved are similar will have to await future studies.

# Bibliography


[1] S.A. Rice, D. Guidotti, and H.L. Lemberg. Some comments on the electronic properties of liquid metal surfaces. In S.A. Prigogine, I.; Rice, editor, *Aspects of the study of surfaces. vol.27*, pages 543–633, Chichester, Sussex, UK, 1974. Wiley.

[2] R. Evans and M. Hasegawa. *J. Phys. C: Solid State Phys.*, 14(5225), 1981.

[3] N.H. March. *Liquid Metals*. Cambridge University Press, Cambridge, 1990.

[4] M. Iwamatsu and S.K. Lai. Evidence of an oscillatory density profile in liquid metal surfaces: an asymptotic solution. *Journal of Physics: Condensed Matter*, 4(28):6039–46, 1992.

[5] E. Velasco, P. Tarazona, M. Reinaldo-Falagan, and E. Chacon. Low melting temperature and liquid surface layering for pair potential models. *Journal of Chemical Physics*, 117(23):10777–88, 2002.

[6] O. M. Magnussen, B. M. Ocko, M. J. Regan, K. Penanen, P. S. Pershan, and M. Deutsch. X-ray reflectivity measurements of surface layering in liquid mercury. *Phys. Rev. Lett.*, 74(22):4444–4447, 1995.

[7] M.J. Regan, E.H. Kawamoto, S. Lee, P.S. Pershan, N. Maskil, M. Deutsch, O.M.

Magnussen, B.M. Ocko, and L.E. Berman. Surface layering in liquid gallium: an x-ray reflectivity study. *Phys. Rev. Lett.*, 75(13):2498–501, 1995.

[8] H. Tostmann, E. DiMasi, P. S. Pershan, B. M. Ocko, O. G. Shpyrko, and M. Deutsch. Surface structure of liquid metals and the effect of capillary waves: X-ray studies on liquid indium. *Phys. Rev. B*, 59(2):783–791, 1999.

[9] H. Tostmann, E. DiMasi, O. G. Shpyrko, P. S. Pershan, B. M. Ocko, and M. Deutsch. Surface phases in binary liquid metal alloys: An x-ray study. *Ber. Bunsen-Ges. Phys. Chem. Chem. Phys.*, 102(9):1136–1141, 1998.

[10] E. DiMasi, H. Tostmann, O.G. Shpyrko, M. Deutsch, P.S. Pershan, and B.M. Ocko. Surface-induced order in liquid metals and binary alloys. *Journal of Physics: Condensed Matter*, 12(8A):A209–14, 2000.

[11] N. W. Ashcroft and N. D. Mermin. *Solid State Physics*. Saunders College Publishing, Orlando, 1976.

[12] J.G. Harris, J. Gryko, and S.A. Rice. Self-consistent monte carlo simulations of the electron and ion distributions of inhomogeneous liquid alkali metals. i. longitudinal and transverse density distributions in the liquid-vapor interface of a one-component system. *Journal of Chemical Physics*, 87(5):3069–81, 1987.

[13] M. Hasegawa and M. Watabe. *J. Phys. C*, 15(353), 1982.

[14] E. Chacon, F. Flores, and G. Navascues. *J. Phys. F*, 14(1587), 1984.

[15] M.A. Gomez and E. Chacon. Role of the surface electronic response function on treatments of the liquid-vapor interface of alkali metals. *Physical Review B (Condensed Matter)*, 49(16):11405–8, 1994.

[16] J. Goodisman and M.-L. Rosinberg. Density functional calculations for liquid metal surfaces. *Journal of Physics C (Solid State Physics)*, 16(6):1143–52, 1983.

[17] T. Iida and R. I. L. Guthrie. *The Physical Properties of Liquid Metals*. Oxford University Press, Oxford, 1993.

[18] H. U. Borgstedt and C. K. Mathews. *Applied Chemistry of the Alkali Metals*. Plenum Press, New York, 1987.

[19] C.C. Addison. *The Chemistry of the Liquid Alkali Metals*. John Wiley and Sons, New York, 1984.

[20] P.S. Pershan. Effects of thermal roughness on x-ray studies of liquid surfaces. *Colloids and Surfaces A (Physicochemical and Engineering Aspects)*, 171(1-3):149–57, 2000.

[21] J. Als-Nielsen and D. McMorrow. *Elements of Modern X-Ray Physics*. John Wiley & Sons, New York, 1st edition, 2001.

[22] D.K. Schwartz, M.L. Schlossman, E.H. Kawamoto, G.J. Kellogg, P.S. Pershan, and B.M. Ocko. Thermal diffuse x-ray-scattering studies of the water-vapor interface. *Physical Review A (Statistical Physics, Plasmas, Fluids, and Related Interdisciplinary Topics)*, 41(10):5687–90, 1990.

[23] D.M. Mitrinovic, S.M. Williams, and M.L. Schlossman. X-ray study of oil-microemulsion and oil-water interfaces in ternary amphiphilic systems. *Physical Review E (Statistical, Nonlinear, and Soft Matter Physics)*, 63(2):021601/1–11, 2001.

[24] D. Chekmarev, M. Zhao, and S. A. Rice. Structure of the liquid-vapor interface of a metal from a simple model potential: Corresponding states of the alkali metals. *Journal of Chemical Physics*, 109(2):768–778, 1998.

[25] E. Chacon, M. Reinaldo-Falagan, E. Velasco, and P. Tarazona. Layering at free liquid surfaces. *Phys. Rev. Lett.*, 87(16):166101/1–4, 2001.

[26] J.M. Soler, G. Fabricius, and E. Artacho. Surface layering and local structure in liquid surfaces. *Surf. Sci.*, 482-485:1314–18, 2001.

[27] G.A. Chapela, G. Saville, S.M. Thompson, and J.S. Rowlinson. Computer simulation of a gas-liquid surface. i. *Journal of the Chemical Society Faraday Transactions II*, 73:1133–44, 1977.

# Chapter 8

# Search for Layering in Non-metallic Liquids: Water

## 8.1 Abstract

Recent measurements show that the free surfaces of liquid metals and alloys are always layered, regardless of composition and surface tension, a result supported by three decades of simulations and theory. Recent theoretical work claims, however, that at low enough temperatures the free surfaces of *all* liquids should become layered, unless preempted by bulk freezing. Using x-ray reflectivity and diffuse scattering measurements we show that there is no observable surface-induced layering in water at T=298 K, thus highlighting a fundamental difference between dielectric and metallic liquids. The implications of this result for the question in the title are discussed.

## 8.2 Introduction

The free surface of liquid metals and alloys were demonstrated experimentally over the last few years to be layered, i.e. to exhibit an atomic-scale oscillatory surface-normal density profile.[1,2,3,4] This is manifested by the appearance of a Bragg-like

peak in the x-ray reflectivity (XR) curve, $R(q_z)$, as shown in Fig. 8.1 for Ga.[2] The wave-vector transfer position of the peak, $q_{peak}$ is related to the layering period $d$ by $q_{peak} = 2\pi/d$. The layered interface is in a marked contrast with the theoretical description of the liquid-vapor interface of a simple liquid. This theory, prevailing for over a century, depicts the density profile as a monotonic increase from the low density of the vapor and the high density of the bulk liquid.[5,6] This view was supported by XR measurements on many non metallic liquids measured over the last two decades, including water,[7] alkanes,[8] and quantum liquids,[9] which showed no Bragg-like peaks. However, as discussed below, the measurements in all of these studies were restricted to the small q range, i.e. $q_z \ll \pi$/atomic size, and would not have detected surface layering if it existed.

Early simulations on non-metallic liquids demonstrate that atomic layering is ubiquitous near a hard flat surface and this has been observed for liquid Gallium.[10] On the other hand, for the liquid vapor interface it is tempting to think that the large surface tension $\gamma$ of liquid metals such as Hg ($\gamma \approx 500$ mN/m), Ga ($\gamma \approx 750$ mN/m), and In ($\gamma \approx 550$ mN/m) might be the explanation for the SL observed at their surface. This assumption is partially mitigated by the observation of SL at the free surface of liquid K where $\gamma \approx 100$ mN/m only. Here we report x-ray scattering results showing that the free surface of water, which has nearly the same surface tension as K, does not exhibit SL features in the reflectivity profiles, thereby suggesting that surface tension by itself does not explain SL. This conclusion rests on the validity of the capillary wave theory (discussed below).

Rice *et al.*[11] first predicted SL in liquid metals three decades ago. They argued

that the layered interface structure for liquid metals is a consequence of the strong dependence of the effective ion-potential energy on the steeply varying electron density across the liquid/vapor interface. At the low density vapor phase the electrically neutral atoms interact through a van der Waals interaction only. In the metallic, higher density, liquid phase the electrons are delocalized, and the much more complex interactions involve an interplay between a quantum Fermi fluid of free electrons and a classical liquid of charged ion cores. Rice concludes that this substantive change in the effective-ion-potential stabilizes the short range surface fluctuations with the result that the atoms near the surface form a layered structure.[11] Calculations employing the glue model of metallic cohesion support these conclusions.[12] By contrast, Soler *et al.*[13] claim that SL is solely due to the formation of a dense layer at the surface. This layer is not restricted to metallic liquids, but may form also in nonmetallic liquids due to nonisotropic interactions, such as remnant covalent bonding in liquid Si[13] and the highly directional interactions in liquid crystals,[14] or in non-uniform Lennard-Jones fluids with unbalanced attractive forces.[15] Additionally, the SL has been found in colloidal systems,[16] which suggests that layering phenomenon may be more fundamental than previously thought. More recently, based on extensive simulations, Chacón *et al.*[17] argued that SL does not require the many-body, delocalize-electron interactions of a liquid metal at all. Rather, according to them, SL is a universal property of all liquids at low enough temperatures, $T \lesssim T_c/a$, whenever not preempted by bulk solidification. Here $T_c$ is the critical temperature of the liquid, and $a \approx 4 - 5$.

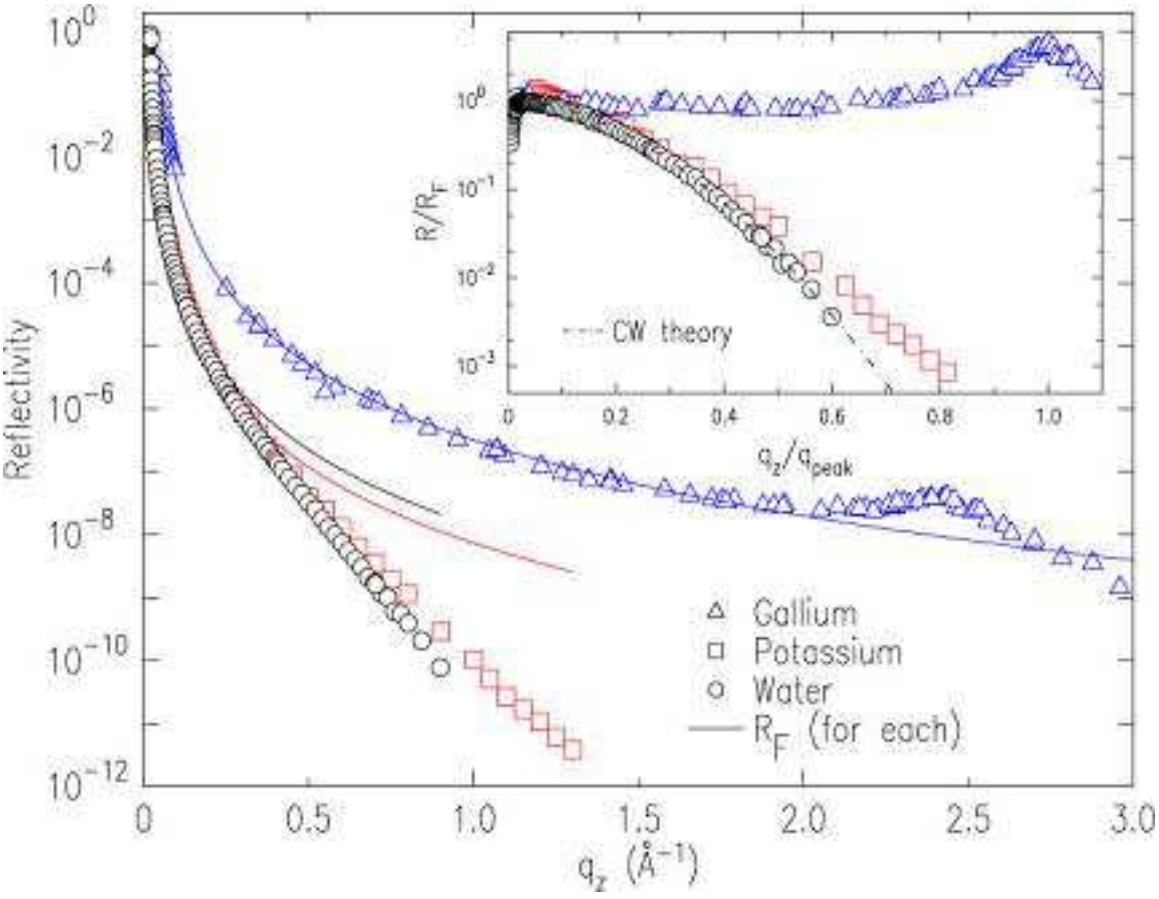



Figure 8.1: X-ray reflectivity from free liquid surfaces of the indicated samples. Points - measured $[R(q_z)]$, lines - calculated for an ideally flat and steplike interface $[R_F(q_z)]$. The inset shows the ratio of the two.

## 8.3 Effect of Capillary Waves

The dichotomy between these two views could be resolved, in principle, by XR measurements on selected materials[18] to see which exhibit, or not, a layering peak at some $q_{peak}$. Unfortunately, practical considerations limit the number of elemental liquids that can be studied to a relatively few. One of the major problems is that the measurable $q_z$ range is more often than not limited to values much less than $q_{peak}$ by the strong off-specular diffuse scattering caused by thermal capillary waves. The effect of the capillary waves is to induce a surface roughness $\sigma \sim \sqrt{T/\gamma}$, where $\gamma$ is the surface tension. The consequence of this, which is shown in Fig. 8.1, for three liquids at room temperature, is to reduce the reflectivity $R(q_z)$ below that of the theoretical Fresnel reflectivity from an interface with an idealized flat, steplike surface-normal density profile. For low-$\gamma$ liquids such as water ($\sim$ 70 mN/m) and K ($\sim$100 mN/m) the reduction is significant. For Ga, where $\gamma \approx 750$ mN/m the effect is almost negligible at room temperature. Even that small reduction is almost completely offset at room temperature by the SL effect that peaks at $q_z \approx 2.5$ Å$^{-1}$. At higher temperatures, however, the effect is quite prominent.[2]

Although the rapid falloff in $R/R_F$ of water prevents its measurements out to $q_z \approx q_{peak} = 2.0$ $\mathring{A}^{-1}$, our recent studies of liquid K[19] demonstrated that if surface layering is present its signature can still be observed clearly at $q_z << q_{peak}$ even for low $\gamma \lesssim 100$ mN/m liquids. This is accomplished by carefully accounting for the effects of capillary waves, based on diffuse x-ray scattering (DS) measurements. We present here an x-ray study of the surface structure of water over the most extended $q_z$-range published to date, and including diffuse scattering[7,20]. For the present measurements the intrinsic surface structure factor of water can be extracted directly from the

raw $R(q_z)$ without resorting to any structural model for the interface. Comparison between the water surface structure factor, for which there is no evidence of SL, and that of K and Ga suggests that surface tension is not the dominant cause of the SL observed in liquid metals.

## 8.4 Experimental Details

X-ray measurements were carried out on the CMC-CAT liquid surface diffractometer, APS, Argonne National Laboratory, at a wavelength of $\lambda = 1.531$ $\mathring{A}$. The purified water sample was contained in a Langmuir trough[21] mounted on the diffractometer. The surface was periodically swept with a teflon barrier, monitoring $\gamma$ with a film balance, to ensure a clean surface.[22]

Both XR[18] and DS[23] are well documented techniques. Experimental geometry setup employed in the experiments described in this work is shown in Fig. 8.2. For x-rays striking the surface at a grazing angle $\alpha$ and detected at an output angle $\beta$ *in the specular plane*, the surface-normal ($z$) and in-plane surface-parallel ($y$) components of the wavevector transfer are $q_z = (2\pi/\lambda)(\sin\alpha + \sin\beta)$ and $q_y = (2\pi/\lambda)(\cos\alpha - \cos\beta)$. In a XR measurement both angles are varied, keeping $\alpha = \beta$, so that $q_y = 0$, and the reflected signal, measured vs $q_z$ and divided by the incident intensity $I_0$, yields $R(q_z)$. In a DS measurement, $\beta$ is varied for a fixed $\alpha$, and hence both $q_z$ and $q_y$ vary.

Within the Born approximation,[18] $R(q_z)/R_F(q_z) = |\Phi(q_z)|^2 W(\eta, q_z)$, where $\Phi(q_z) = (\rho_\infty)^{-1} \int [\mathrm{d}\langle\rho(z)\rangle/\mathrm{d}z] \exp(\imath q_z z)\mathrm{d}z$ is the conventional structure factor of the liquid-vapor interface, $\langle\rho(z)\rangle$ is the *intrinsic* (i.e. in the absence of capillary wave smearing) surface-parallel-averaged electron density profile along the surface-normal $z$ direction,

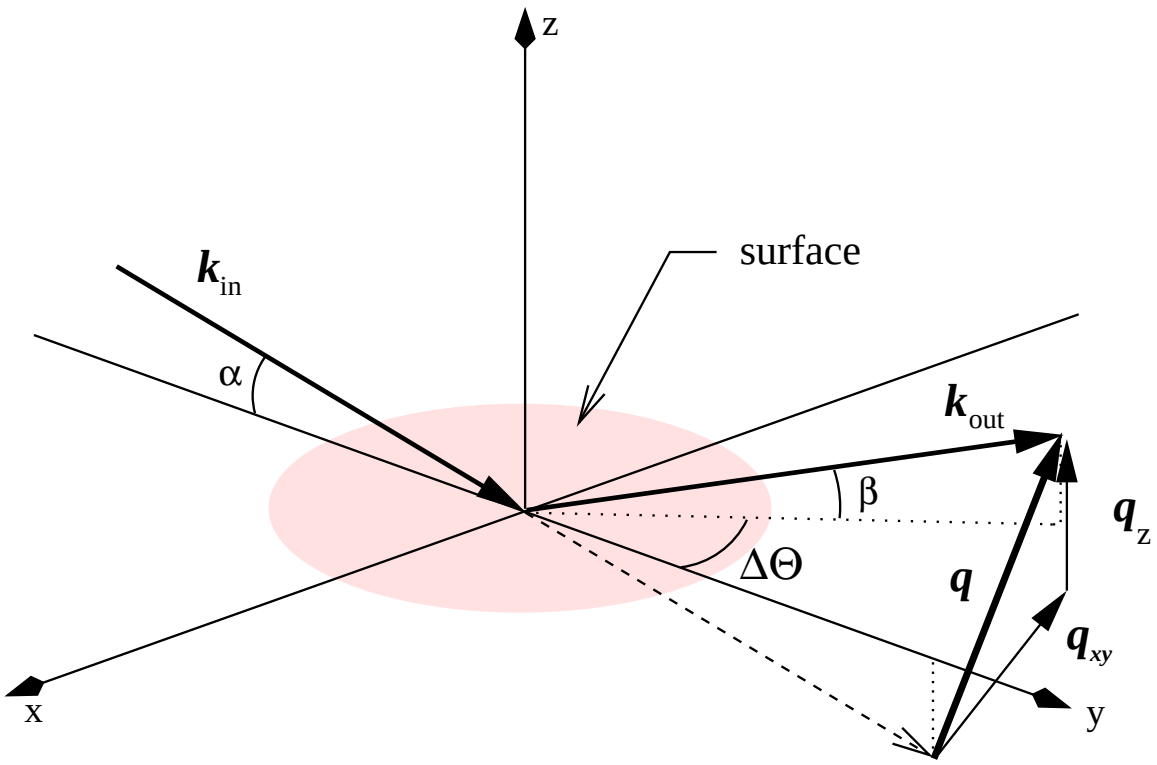



Figure 8.2: Schematic description of the experimental setup.

and $W(\eta, q_z)$ accounts for the smearing of the intrinsic density profile by capillary waves. The aim of our XR measurement is to determine $\Phi(q_z)$ to observe a possible layering peak. Since both $\Phi(q_z)$ and $W(\eta, q_z)$ depend on $q_z$, extracting $\Phi(q_z)$ directly from the measured $R(q_z)$ is possible as $|\Phi(q_z)|^2 = R(q_z)/W(\eta, q_z)$ only if $W(\eta, q_z)$ is known independently. For this we use the DS data.

## 8.5 X-ray Diffuse Scattering Data

The measured DS, shown in Fig. 8.3, is given by theory as $I_{DS} = \int [\mathrm{d}\sigma(q_x - q'_x, q_y - q'_y, q_z - q'_z)/\mathrm{d}\Omega]\mathrm{d}\omega(q'_x, q'_y, q'_z)$, where $\mathrm{d}\omega$ is the angular resolution of the diffractometer and

$$\frac{d\sigma}{d\Omega} = \frac{A_0}{8\pi \sin\alpha} q_z^2 R_F(q_z) \mid \Phi(q_z) \mid^2 \frac{\eta}{q_{xy}^{2-\eta}} \left(\frac{1}{q_{max}}\right)^{\eta} \tag{8.5.1}$$

is the scattering cross-section. Here $q_c$ is the critical angle for total external reflection of x rays, $q_{max} \approx \pi/\xi$ is the upper cutoff for capillary wave contributions, with $\xi$ of order of the atomic diameter, and $\eta = (k_B T)/(2\pi\gamma)q_z^2$.

Two subtle complications are encountered in analyzing the DS data. First, non-surface DS contributions (scattering from the bulk, sample chamber windows, etc.) can significantly distort the shape of the DS scans. These background contributions are measured by offsetting the detector by $\Delta\Theta = \pm 0.3^\circ$ from the plane of incidence, and are already subtracted from the data shown in Fig. 8.3. Second, in the fixed-$\alpha$ DS scans, carried out by scanning $\beta$, $q_z$, and thus $|\Phi(q_z)|^2$, also vary. Fortunately, $\delta q_z \approx \delta q_y/\beta$ and for the range of $q_y$ displayed in Fig. 8.3 and typical $q_z$ values, the changes are small enough to be neglected, e.g. a maximal $\delta q_z \approx 0.06\ \mathring{A}^{-1}$ at the largest $\beta$ for $\alpha = 3.5^\circ$. Thus, it is a good approximation for each of the DS scans to treat $\Phi(q_z)$ as a fixed function of $\alpha$. $\mid \Phi(q_z) \mid^2$ is then obtained by dividing the measured

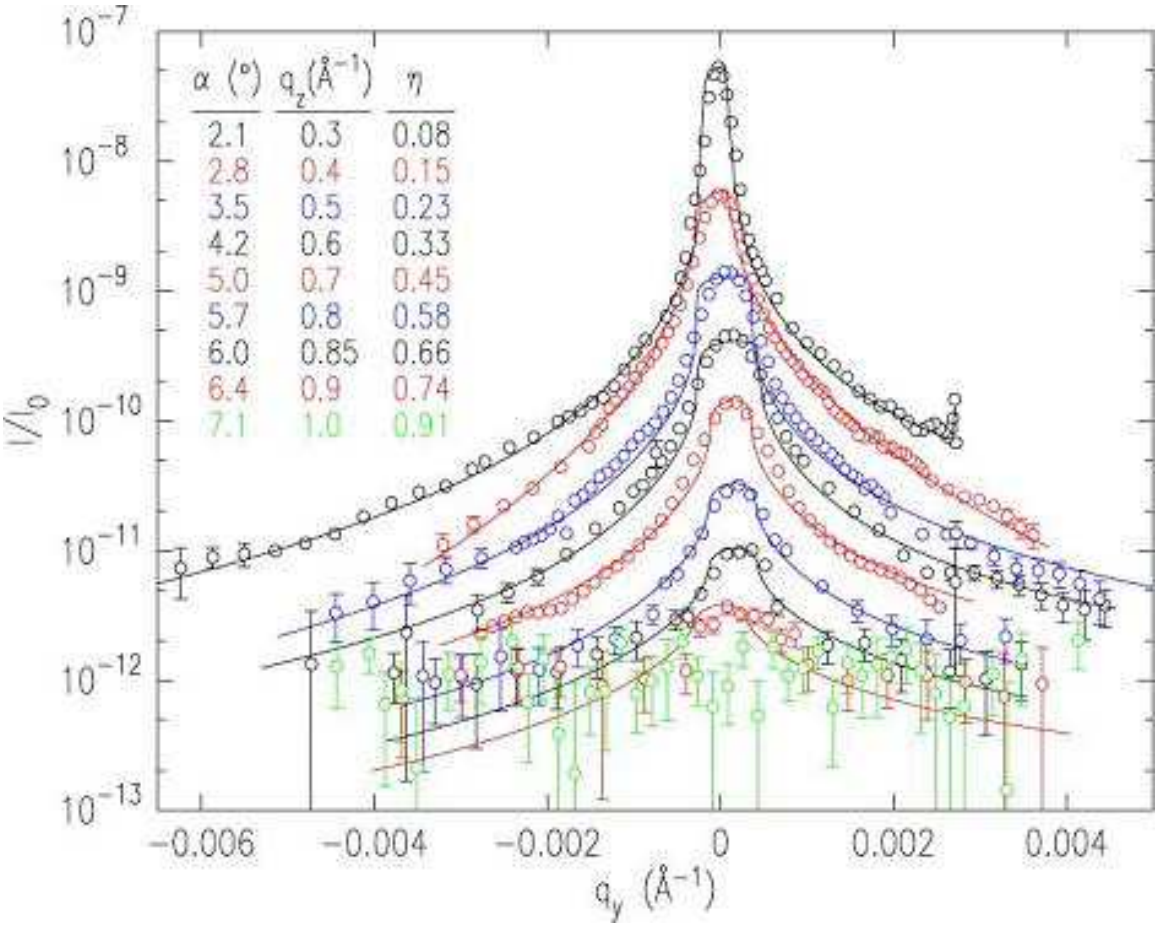



Figure 8.3: Comparison of measured diffuse scattering with capillary wave theory predictions for the angles of incidence $\alpha$ (top to bottom): 2.1°, 2.8°, 3.5°, 4.2°, 5.0°, 5.7°, 6.0°, and 6.4°. The last data set corresponding to 7.1° shown in the inset no longer exhibits a distinguishable specular peak. The $q_z$ values corresponding to the specular condition $q_y = 0$ Å$^{-1}$ are 0.3, 0.4, 0.5, 0.7, 0.8, 0.85, 0.9, and 1.0 $\mathring{A}^{-1}$, respectively.

DS and XR curves by $W(\eta, q_z) = \int [A_0/(8\pi \sin\alpha)] q_z^2 R_F(q_z)(\eta/q_y^{2-\eta}) q_{max}^{-\eta} \mathrm{d}\omega$.[19]

The theoretical curves calculated using Eq. 8.5.1 with $T = 298\ K$ and $\gamma = 72$ mN/m are shown as lines in Fig. 8.3. As $q_z$ increases, so do both $\eta \propto q_z^2$ and the intensity of the off-specular power-law wings relative to that of the specular peak at $q_y = 0$. The curve at $q_z = 1\ \mathring{A}^{-1}$ demonstrates the capillary-wave-imposed limit where the specular signal at $q_y = 0$, which contains the surface structure information, becomes indistinguishable from the DS signal at $\pm q_y > 0$. In principle, this limit arises from the fact that for $\eta \geq 2$ the singularity at $q_y = 0$ in $d\sigma/d\Omega$ vanishes and there is no longer any criterion by which the surface scattering can be differentiated from other sources of diffuse scattering. In practice, the fact that the projection of the resolution function on the horizontal x-y plane is very much wider transverse to the plane of incidence than within the plane of incidence reduces this limit to a value closer to $\eta \approx 1$.[19] Figure 8.3 exhibits excellent agreement between the theoretical DS curves calculated from Eq. 8.5.1 with the measured DS over several decades in intensity and one decade in $\eta$, *without any adjustable parameters*. This confirms the applicability of the capillary wave theory for the surface of water over the $q_z$ range studied here, $0 \leq q_z \leq 0.9\ \mathring{A}^{-1}$. Measurements of diffuse scattering for small $q_z$ (i.e. small $\eta$) to values of the surface parallel component of the wave vector transfer $q_x$ of the order of $\pi$/atomic size have been done by Daillant *et. al*[24,25] by moving the detector out of the plane of incidence for grazing incident angles. At such large wave vectors the observed scattering must be interpreted as the superposition of scattering due to surface capillary waves and bulk diffuse scattering from the liquid below the surface. The separation of these two contributions is rather subtle and was only accomplished through nontrivial calculations of the noncapillary terms. Eventually

Daillant *et. al* concluded that as the value of $q_x$ approaches the atomic scale (i.e., $\pi$/atomic size) the surface tension varies with $q_x$.[26] In principle, this dispersion should affect the sum rule that is the origin of the $1/q_{xy}^{\eta}$ in the differential cross section in Eq.(8.5.1). On the other hand, considering that the dispersion is a relatively small effect that will only change the argument of a logarithmic term, its effect on the present analysis can be neglected.

## 8.6 X-ray Reflectivity Data

Fig. 8.4 shows a specular reflectivity data taken for liquid water, normalized by Fresnel function. Low angle data was taken with a point bicron detector, but at high angles we used a position sensitive, wire detector in order to effectively resolve specular peak along with diffuse wings. Bicron detector has a higher efficiency than linear detector and is therefore preferable at low angles where $\eta$-effect is negligible. Due to slightly different resolution functions of the two detectors, the x-ray reflectivity data does not match precisely. Shown with blue and red lines are the theoretical predictions for the x-ray reflectivity signal assuming capillary wave contributions according to Eq.(8.5.1. Red line corresponds to resolution function used for data taken with bicron detector, and blue (dashed) line used resolution function of wire detector. Since the data doesn't deviate significantly from these theoretical curves, one can conclude that the surface of water does not exhibit a strong structure factor observed in metallic liquids.

$|\Phi(q_z)|^2$ is then obtained directly from the measured XR curve, as $R(q_z)/W(\eta, q_z)$ as discussed above. It is shown in Fig. 8.5 (circles) along with previously measured results for K (squares) and Ga (triangles).

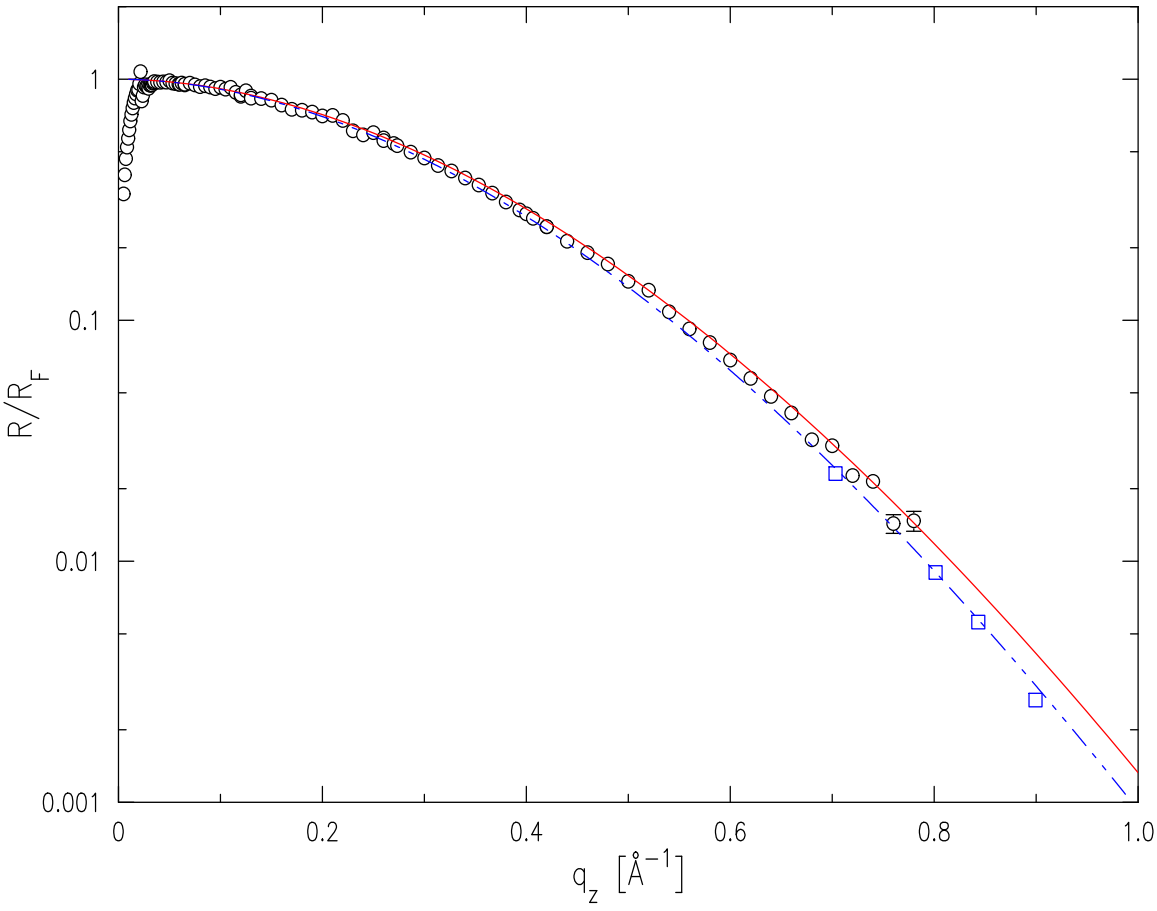



Figure 8.4: Fresnel-normalized X-ray reflectivity from free liquid surfaces water, taken for two different values of resolution with bicron detector (circles) and linear detector (squares). Blue and red lines show theoretical expected values for the two measurements, respectively, assuming no surface structure.

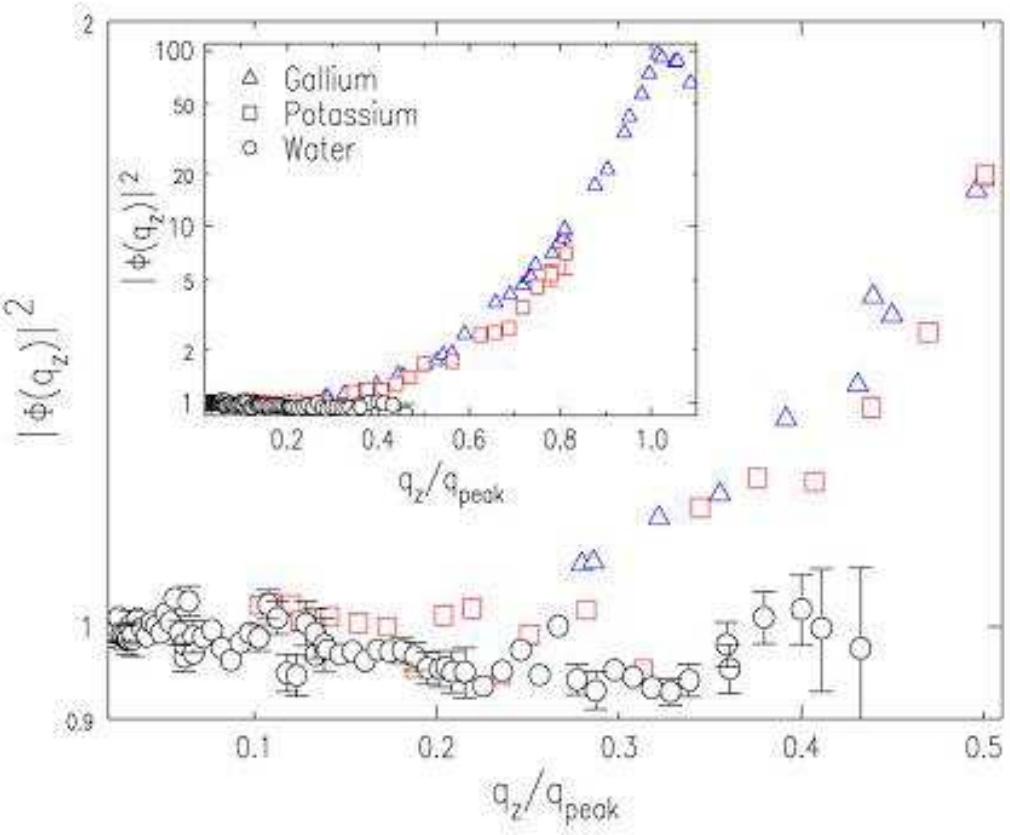



Figure 8.5: Comparison of the structure factor squared $\mid \Phi(q_z) \mid^2$ for water (circles), liquid potassium (squares), and liquid gallium (triangles). The wavevector $q_z$ is normalized to the expected position of the layering peak $q_{peak}$ of each sample. The inset shows the data on an extended scale. For discussion see text.

The rise of the Ga $|\Phi(q_z)|^2$ to $\sim$100 at $q_{peak}$ due to layering can be clearly seen on the inset of Fig. 8.5. For K, the capillary-wave-imposed limit only allows obtaining $|\Phi(q_z)|^2$ for $q_z \lesssim 0.8 q_{peak}$. Nevertheless, the value of $|\Phi(q_z)|$ for K starts to deviate from unity for values of $q_z/q_{peak} \approx 0.3$. Furthermore, over the range for which it can be measured it is basically identical to the structure factor of Ga. This is a clear indication that the surface of liquid K has essentially the same SL as that of Ga, which is also nearly identical to that of the other liquid metals that have been studied to date, e.g., In[27] and Sn[28]. For water, however, no deviation of $|\Phi(q_z)|^2$ from unity is observed even at the highest measurable $q_z/q_{peak} \approx 0.5$. This suggests that surface-induced layering does not occur at the surface of water. The different behavior, in spite of the similar $\gamma$ of water and K, leads to the conclusion that the surface layering in K, and by implication in other liquid metals, is not merely a consequence of its surface tension.

The absence of layering in water, and its presence in potassium, seems at first sight to corroborate the claim of Rice *et al.*[11] that layering is a property arising from the metallic interaction of the liquid. On the other hand, Chacón *et al.*[17], who maintain that surface-induce layering is a general property of all liquids, regardless of their interactions, predict that layering should occur only at temperatures $T/T_c \lesssim 0.2$, where $T_c$ is the critical temperature of the liquid. Although supercooling is often possible, the practical limit for most reflectivity measurements is the melting temperature $T_m$. Thus the smallest $T/T_c$ for any liquid is on the order of $T_m/T_c$. For liquid metals $T_m/T_c \approx 0.15$ (K), 0.13 (Hg), 0.07 (In), 0.066 (Sn), and 0.043 (Ga). Since these values are $< 0.2$, by Chacón's criteria surface layering is expected, and indeed demonstrated experimentally to occur, in all of them.[1,2,19,27,28] By contrast,

for water, where $T_m/T_c = 0.42 \gg 0.2$, Chacón's criteria predict that the appearance of surface layering is preempted by bulk freezing, and thus no SL should occur at room temperature, as indeed found here.

## 8.7 Summary

In summary, we have shown that the surface of water does not exhibit SL even though its surface tension is not significantly different from that of liquid K for which SL was observed. Thus the atomic layering of liquid K cannot be the result of surface tension alone. Although this seems to support Rice's argument that the metallic phase is essential for SL, we note that SL is exhibited by both liquid crystals[14] and other intermediate-size organic molecules.[29] Consequently, there can be other criteria for SL, in addition to those proposed by Rice. One possibility, proposed by Chacón *et. al*, is that SL should be ubiquitous for all liquids that can be cooled to temperatures of the order of $0.2T_c$. Unfortunately, this is difficult to explore experimentally since suitable liquids are rather scarce. For example, liquid noble gases, the archetypical van der Waals liquids, have all $T_m/T_c > 0.55$. For liquid helium the ratio is lower but in view of both the presence of the superfluid transition and the low scattering cross section this is a difficult system to study. X-ray reflectivity measurements at 1 K, i.e., $T_m/T_c \sim 0.2$, did not exhibit evidence for SL[9]. Similarly, the polar liquids oxygen and fluorine have $T_m/T_c$ of only 0.38 and 0.37. There are, however, some low melting organic van der Waals liquids, e.g. propane and 1-butene, that have $0.2 < T_m/T_c < 0.25$, and may be suitable for addressing this issue. It would be also very interesting to measure the surface structure of materials such as Se ($T_m/T_c = 0.28$), Te (0.3), Sc (0.28), and Cd (0.22), for which $T_m/T_c > 0.2$. If it were

possible to probe surface layering in these high $T_m/T_c$ materials such experiments could test Chacón's argument. Unfortunately, these materials have relatively high vapor pressure and that precludes the use of UHV methods for insuring atomically clean surfaces. The surfaces of some alkalis and mercury can be kept clean without UHV methods. For most of the experimentally accessible metals this is not true.

# Bibliography


[1] O. M. Magnussen, B. M. Ocko, M. J. Regan, K. Penanen, P. S. Pershan, and M. Deutsch, Phys. Rev. Lett. **74**, 4444 (1995).

[2] M. J. Regan, E. H. Kawamoto, S. Lee, P. S. Pershan, N. Maskil, M. Deutsch, O. M. Magnussen, B. M. Ocko, and L. E. Berman, Phys. Rev. Lett. **75**, 2498 (1995).

[3] H. Tostmann, E. DiMasi, P. S. Pershan, B. M. Ocko, O. G. Shpyrko, and M. Deutsch, Physical Review B 61, 7284 (2000) ; E. DiMasi, H. Tostmann, O. G. Shpyrko, P. Huber, B. M. Ocko, P. S. Pershan, M. Deutsch, and L. E. Berman, Phys. Rev. Lett. **86**, 1538 (2001).

[4] B. Yang, D. Gidalevitz, D. X. Li, Z. Q. Huang, and S. A. Rice, Proc. Nat. Acad. of Sc. USA **96**, 13009 (1999) ; B. Yang, D. X. Li, Z. Q. Huang, and S. A. Rice., Phys. Rev. B **62**, 13111 (2000).

[5] F. P. Buff, R. A. Lovett, and F. Stilling, Phys. Rev. Lett. **15**, 621 (1965) ; F. H. Stillinger and J. D. Weeks, J. Phys. Chem. **99**, 2807 (1995).

[6] J. S. Rowlinson and B. Widom, "Molecular Theory of Capilarity" (Oxford University Press, Oxford, 1982).

[7] A. Braslau, M. Deutsch, P. S. Pershan, A. H. Weiss, J. Als-Nielsen, and J. Bohr, Phys. Rev. Lett. **54**, 114 (1985).

[8] B. M. Ocko, X. Z. Wu, E. B. Sirota, S. K. Sinha, and M. Deutsch, Phys. Rev. Lett. **72**, 242 (1994).

[9] L. B. Lurio, T. A. Rabedeau, P. S. Pershan, I. F. Silvera, M. Deutsch, S. D. Kosowsky, and B. M. Ocko, Phys. Rev. Lett. **68**, 2628 (1992) ; Phys. Rev. B **48**, 9644 (1993).

[10] W. J. Huisman, J. F. Peters,M. J. Zwanenburg et al., Nature **390**, 107, 379 (1997).

[11] S. A. Rice, D. Guidotti, and H. L. Lemberg, W. C. Murphy and A. N. Bloch, in "Advances in Chemical Physics XXVII" edited by I. R. Prigogine, and S. A. Rice (Wiley, Chichester, 1974) p. 543 ; M. P. D'Evelyn and S. A. Rice, J. Chem. Phys. **78**, 5225 (1983) ; S. A. Rice, Mol. Simul. **29**, 593 (2003).

[12] F. Celestini, F. Ercolesi and E. Tosatti, Phys. rev. Lett. **78**, 3153 (1997) ; S. Iarlori, P. Carnevali, F. Ercolesi and E. Tosatti, Surf. Sci **211/212**, 55 (1989).

[13] G. Fabricius, E. Artacho, D. Sanchez-Portal, P. Ordejon, D. A. Drabold and J. M. Soler, Phys. Rev. B (Rapid) **60**, R16283 (1999) ; J. M. Soler, G. Fabricius, and E. Artacho, Surf. Sci. **482-485**, 1314 (2001).

[14] P. S. Pershan, Physics Today **35**(5), 34 (1982).

[15] K. Katsov and J. D. Weeks, J. Phys. Chem. B **106**, 8429 (2002).

[16] A. Madsen,O. Konovalov, A. Robert and G. Grubel, Phys. Rev. E **64**, 061406 (2001)

[17] E. Chacon, M. Reinaldo-Falagan, E. Velasco, and P. Tarazona, Phys. Rev. Lett. **87**, 166101 (2001) ; E. Velasco, P. Tarazona, M. Reinaldo-Falagan, and E. Chacon, J. Chem. Phys. **117**, 10777 (2002).

[18] M. Deutsch and B. M. Ocko, in "Encyclopedia of Applied Physics", edited by G. L. Trigg (VCH, New-York, 1998), Vol. 23, p. 479 ; J. Als-Nielsen and D. McMorrow, "Elements of Modern X-Ray Physics" (Wiley, New York, 2001).

[19] O. G. Shpyrko, P. Huber, A. Grigoriev, P. S. Pershan, B.M. Ocko, H. Tostmann, and M. Deutsch, Phys. Rev. B **67**, 115405 (2003).

[20] D. K. Schwartz, M.'L. Schlossman, E.'H. Kawamoto, G. J. Kellogg, P. S. Pershan, and B. M. Ocko, Phys. Rev. A **41**, 5687 (1990).

[21] D. K. Schwartz, M. L. Schlossman, and P. S. Pershan, J. Chem. Phys. **96**, 2356 (1992).

[22] G. L. Gaines, "Insoluble Monolayers at Liquid-Gas Interfaces" (Wiley, New York, 1966).

[23] P. S. Pershan, Coll. Surf. A **171**, 149 (2000).

[24] C. Fradin, A. Braslau, D. Luzet, D. Smilgies, M. Alba, N. Boudet, K. Mecke, J. Daillant, Nature **403**, 871 (2000)

[25] S. Mora, J. Daillant, K. Mecke, D. Luzet, A. Braslau, M. Alba, B. Struth, Phys. Rev. Lett. **90**, 216101 (2003).

[26] K. R. Mecke and S. Dietrich, Phys. Rev. E 59, 6766 (1999)

[27] H. Tostmann, E. DiMasi, P. S. Pershan, B. M. Ocko, O. G. Shpyrko, and M. Deutsch, Phys. Rev. B **59**, 783 (1999).

[28] O. G. Shpyrko, A. Grigoriev, P. S. Pershan, C. Steimer, B.M. Ocko, M. Deutsch, B. Lin, M. Meron, T. Graber, and J. Gerbhardt, ( to be published).

[29] C. J. Yu, A. G. Richter, A. Datta, M. K. Durbin and P. Dutta, Phys. Rev. Lett. **82**, 2326 (1999).

# Chapter 9

# Surface of Liquid Sn: Anomalous layering

## 9.1 Abstract

X-ray reflectivity measurements on the free surface of liquid Sn are presented in this chapter. They exhibit the high-angle peak, indicative of surface-induced layering, also found for other pure liquid metals (Hg, Ga and In). However, a low-angle peak, not hitherto observed for any pure liquid metal, is also found, indicating the presence of a high-density surface layer. Fluorescence and resonant reflectivity measurements rule out the assignment of this layer to surface-segregation of impurities. The reflectivity is modelled well by a 10% contraction of the spacing between the first and second atomic surface layers, relative to that of subsequent layers. Possible reasons for this are discussed.

## 9.2 Introduction

Rice and coworkers[1] predicted that the atoms at the free surface of a liquid metal should be stratified to a depth of a few atomic diameters. This layering phenomenon

has been experimentally confirmed two decades later by x-ray reflectivity measurements for three high surface-tension metals: Hg,[2] Ga[3] and In,[4] and the low-surface tension K.[5] The signature of layering in the x-ray reflectivity curve is the appearance of a quasi-Bragg peak at a wavevector transfer $q_z = 2\pi/d$, where $d$ is the atomic spacing between the layers. The peak arises from constructive interference of waves diffracted by the ordered subsurface layers. These measurements are complicated by several technical issues, in particular the need to use UHV conditions to preserve surface cleanliness for highly reactive liquid metals surfaces.

Both Ga and In were found to Regan et al.[3] comprising equal-density, periodically-spaced atomic layers. Liquid Hg[2,6] shows a more complicated surface structure. However, unlike Ga and In, the high vapor pressure of Hg did not allow its study under UHV conditions, and the possibility that the more complicated structure originates in chemical interactions with foreign atoms at the surface cannot be definitively ruled out. For Ga, in particular, the decay length of the layering into the bulk was found to be slightly larger than that expected, and found, for other liquid metals. This was tentatively assigned to the enhanced Ga-Ga pairing tendency,[3] reflected also in the appearance of a small shoulder on the first, nearest-neighbor, peak of the bulk radial distribution function,[7,8] and in the ordering of Ga at the liquid-solid interface.[9] A similarly strong pairing tendency has been reported also for Sn, the subject of the present study.[10,11,12]

The motivation of the present study was to investigate whether atomic layering exists in liquid Sn, and, if it does, to find out whether or not the layering follows the classic behavior of Ga and In, or do new effects appear, e.g. due to the strong pairing. The relatively low melting temperature, $T_m = 232$ °C, and vanishingly

low vapor pressure at $T_m$ render such measurements possible. As shown below, the measured x-ray reflectivity off the Sn surface indeed exhibits an anomalous feature that is not present for either Ga or In. Additional experiments were carried out to rule out the possibility that this anomalous feature is not intrinsic, but caused by chemical impurities at the surface. The origin of this structure is identified as a $\sim 10\%$ contraction in the first to second interlayer distance.

## 9.3 Experimental

The UHV chamber and the preparation procedures of the liquid Sn sample had been described previously.[4,13] Prior to placing an Sn sample inside the Mo sample pan, the surface of the pan was sputtered clean. In the sputtering process the sample's surface is bombarded by $Ar^+$ ions, which break up and sputter away the oxidized material covering the surface. Ingots of solid Sn with purity of 99.9999 % were placed in the Mo sample pan inside a UHV chamber evacuated to $10^{-9}$ Torr and were then melted by a Boralectric heating element mounted underneath the pan. After the molten Sn filled the pan it was cooled to the solid phase, a 24-hour bakeout process was performed. In the bakeout process the walls of the chamber and its components are gradually heated up to $100-200°$C and then cooled down to room temperature. Following this procedure the sample was melted again and the macroscopic native oxide, as well as any possible contaminations, at the surface were removed by a mechanical scraping of the liquid surface with Mo foil wiper. After this, the residual microscopic surface oxide layer was removed by further sputtering by the $Ar^+$ ion beam for several hours. If there are impurities in the bulk with surface energies that are lower than that of Sn the Gibbs adsorption rule implies that they would segregate at the surface. We

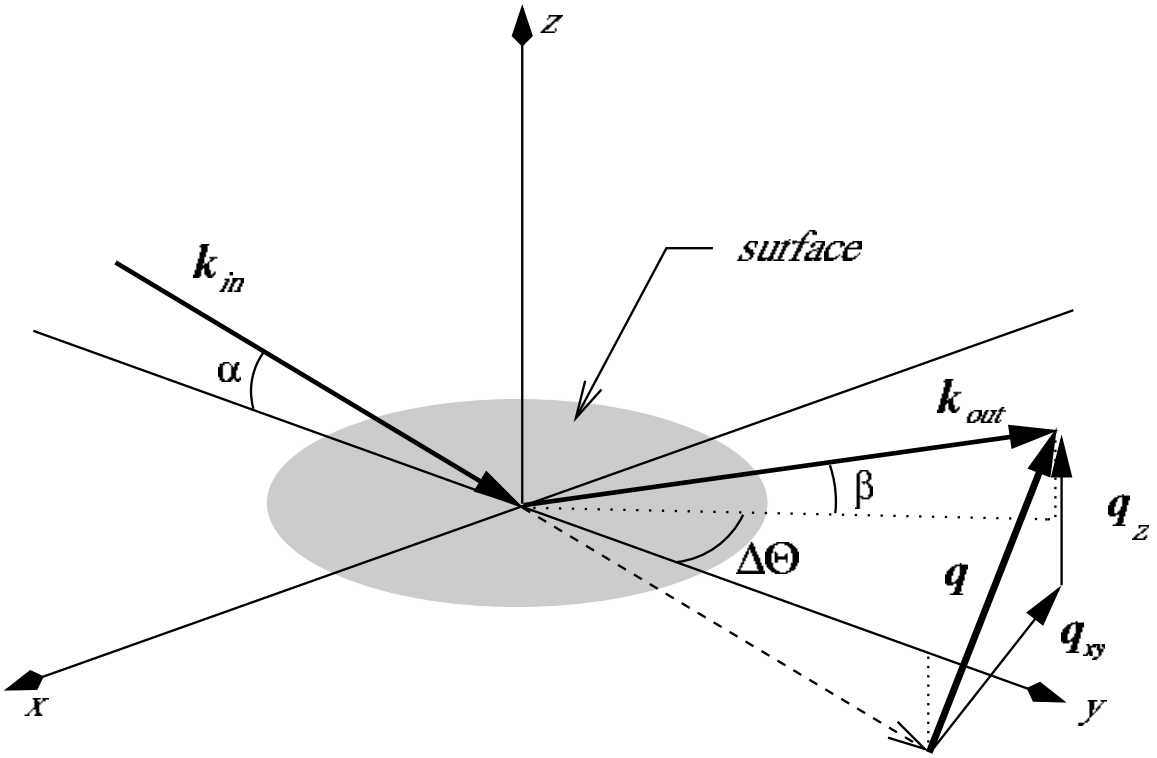



Figure 9.1: Kinematics of the x-ray measurement. $k_{in}$ and $k_{out}$ are the wavevectors of the incident and detected x-rays, respectively.

will demonstrate below that even though Sn has a relatively high surface tension impurities are not present at the surface.

## 9.4 X-ray reflectivity measurements

The measurements were carried out at the liquid surface spectrometer facility of the ChemMAT CARS beamline at the Advanced Photon Source, Argonne National Laboratory, Argonne, IL. The kinematics of x-ray measurements described in this work are illustrated in Fig. 9.1. X-rays with a wavevector $k_{in} = 2\pi/\lambda$, where $\lambda = 0.729\ \mathring{A}$ is the x-ray's wavelength, are incident on the horizontal liquid surface at an angle $\alpha$. The detector selects, in general, a ray with an outgoing wavevector $k_{out}$. The

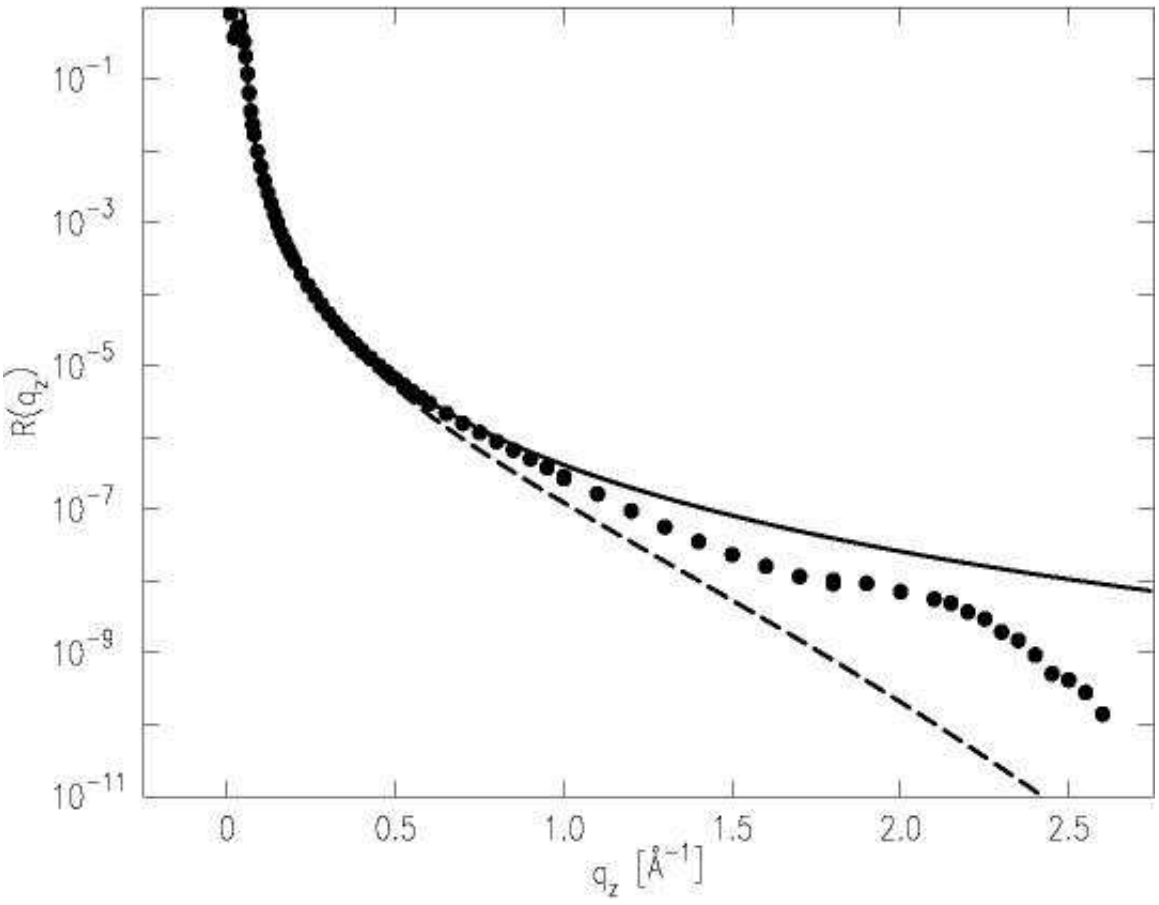



Figure 9.2: The measured x-ray specular reflectivity (points) of the surface of liquid Sn. The Fresnel reflectivity (solid line) of an ideally flat and abrupt surface, and the reflectivity of an ideal surface roughened by thermally-excited capillary waves (dashed line) are also shown.

reflectivity $R(q_z)$ is the intensity ratio of these two rays, when the specular conditions, $\alpha = \beta$ and $\Delta\Theta = 0$, are fulfilled. In this case the surface-normal momentum transfer is $q_z = (2\pi/\lambda)(\sin\alpha + \sin\beta) = (4\pi/\lambda)\sin\alpha$.

The x-ray specular reflectivity shown with circles in Fig. 9.2 is the difference between the specular signal recorded with Oxford scintillation detector at $\alpha = \beta, \Delta\Theta = 0$ and the off-specular background signal recorded at the same $q_z$, but at $\Delta\Theta = \pm 0.1°$. The data is then normalized to the measured incident intensity. This background

subtraction procedure is particularly important because the bulk scattering function peaks at approximately the same $q_z$ as the quasi-Bragg surface layering peak, since both peaks correspond roughly to the interatomic distance. As a result the background is particularly strong at the $q_z$ values corresponding to the layering peak. Since the measured $\Delta\Theta \neq 0$ intensity includes contributions from the capillary-wave-induced diffuse surface scattering, all of the theoretical simulations discussed below include a similar background subtraction procedure. The Fresnel reflectivity curve, $R_F(q_z)$, due to an ideally flat and abrupt surface, is shown in a solid line in Fig. 9.2. The dashed line is $R_F(q_z)$ modified by the theoretically predicted thermal capillary wave contributions, which depend only on the known values of the resolution function, surface tension and temperature. The quasi-Bragg layering peak, as well as the deviation of the measured $R(q_z)$ from the capillary-wave-modified $R_F(q_z)$ are unambiguous proof of the existence of local structure at the surface. The quasi-Bragg peak at $q_z \approx 2.2$ Å$^{-1}$ corresponds to an atomic layering of close packed spheres with the $d \approx 2.8$ Å spacing of the atomic diameter of Sn. An additional new feature, a subtle but significant peak at $q_z \approx 0.9$ Å$^{-1}$ is not discernible in this figure, and is revealed only upon removal of the effects of the capillary waves from the measured Fresnel-normalized reflectivity, as we show below.

## 9.5 The Surface Structure Factor

To obtain a quantitative measure of the intrinsic surface structure factor the effects of thermal capillary excitations must be deconvolved from the reflectivity curve shown in Fig. 9.2. As mentioned above, the method for doing this has been described in detail in earlier papers on the surface layering in Ga,[3] In,[4] K[5] and water.[14] The

principal result of this analysis is that the measured reflectivity can be expressed as

$$R(q_z) = R_F(q_z) \cdot |\Phi(q_z)|^2 \cdot CW(q_z) \tag{9.5.1}$$

where $\Phi(q_z)$ is the intrinsic structure factor of the surface and CW($q_z$) accounts for the effects of the thermally-excited capillary waves on $R(q_z)$. The surface scattering cross section yielding the CW($q_z$) term depends on $T$, $q_z$, the surface tension and the geometric parameters defining the reflectometer's resolution function. It is understood well enough to allow us to fully account analytically for the effects of capillary waves on the measured $R(q_z)$. This is demonstrated in Fig. 9.3 where we plot the background-subtracted and incident-intensity-normalized intensity scattered by the surface capillary waves measured as a function of $\beta$ for a fixed incidence angle $\alpha$ in the reflection plane ($\Delta\Theta = 0°$). The agreement between the measured values (points) and the theoretical cross section (line) is very good over more than 3 decades in intensity.

For this scan the incident beam is 100 $\mu$m high and the detector is 0.5 mm high and 1 mm wide. Integration of the intensity in this figure over the $\beta$-range spanned by the resolution function of the reflectivity measurements shown in Fig. 9.2 yields a value identical with that obtained in the reflectivity measurements at $q_z = 0.48$ Å$^{-1}$. This further strengthens our claim that the effects of the capillary waves' scattering on the reflectivity are well understood, and can be separated out confidently from the measured $R(q_z)$.

The iterative procedure by which the theoretical line in Fig. 9.3 is calculated is the following. We first obtain a measure of the structure factor from a best fit of Eq. 9.5.2 to the reflectivity (Fig. 9.2) using values for $CW(q_z)$ that are calculated from published values for the surface tension. This form of the surface structure factor is then used to fit measured diffuse scattering curves similar to that shown in

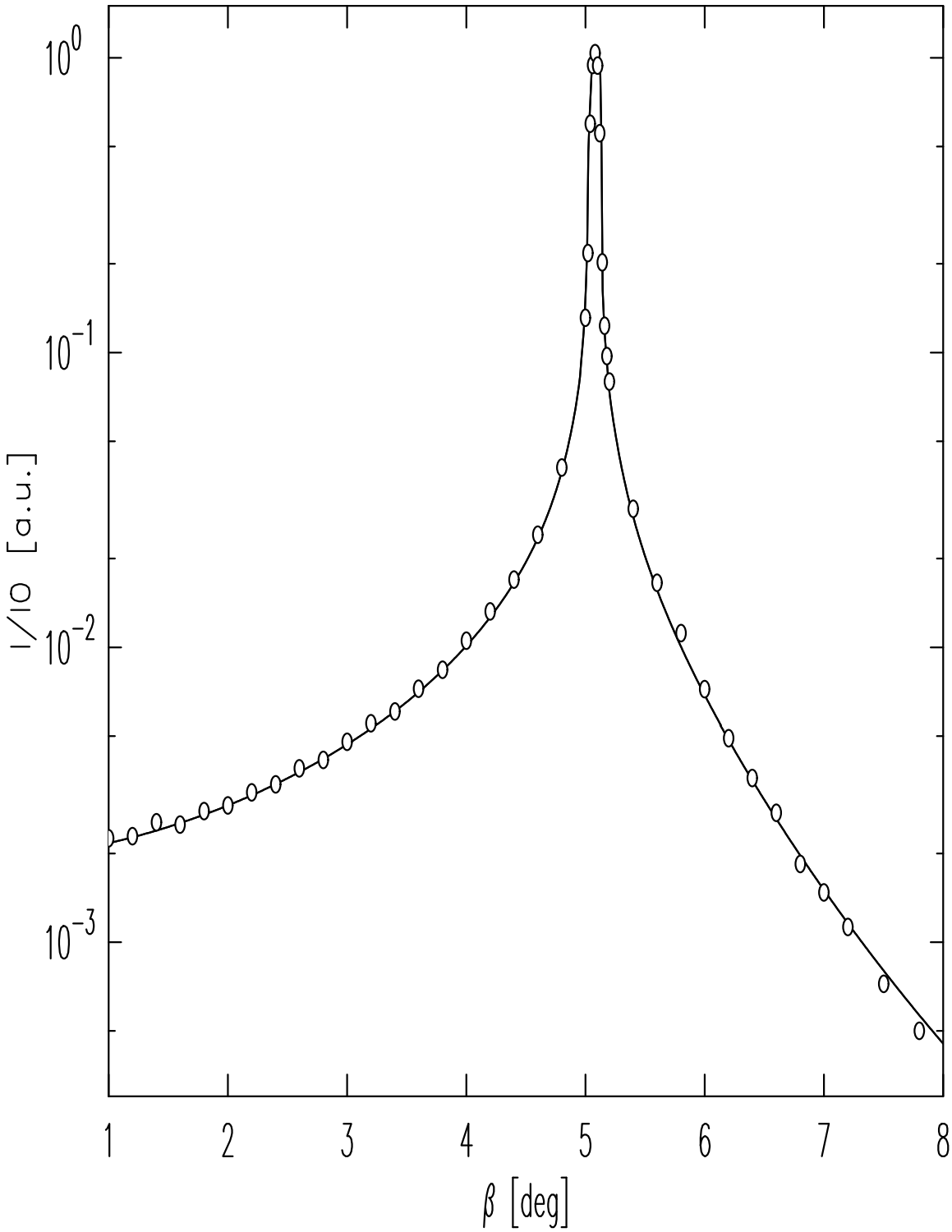



Figure 9.3: Diffuse scattering off the liquid Sn surface measured at a fixed grazing angle of incidence $\alpha = 5.05°$ (open circles). The peak corresponds to the specular condition at $q_z = 0.48$ Å$^{-1}$. The line is the capillary wave theory predictions for surface tension $\gamma = 560$ mN/m.

Fig. 9.3, with the surface tension as the only adjustable parameter. When needed, the cycle can be repeated using now the new surface tension value. In practice, however, a single cycle was enough, since the best fit value for the surface tension, $\gamma = 560$ mN/m, was in good agreement with the published values. Thus, we assert that the form of the diffuse scattering that gives rise to the value of $CW(q_z)$ is fully determined, and the only unknown quantity in Eq. 9.5.2 is the surface structure factor. This quantity is the Fourier transform of the surface-normal derivative of the local electron density, $\rho(z)$, averaged over the surface-parallel directions:[15]

$$\Phi(q_z) = \frac{1}{\rho_\infty} \int dz \frac{\langle d\rho(z) \rangle}{dz} \exp(\imath q_z z) \tag{9.5.2}$$

where $\rho_\infty$ is the electron density of the bulk.

The ratio $R(q_z)/[R_F(q_z)CW(q_z)] = |\Phi(q_z)|^2$ derived from the measured reflectivity, is plotted in Fig. 9.4 (open circles). The dashed line is the theoretical reflectivity calculated using the surface structure factor obtained from the simple atomic layering model that successfully described the intrinsic surface structure factor of the pure liquid Ga and In. As can be seen from the plot, this model does not describe the measured values well. In particular, it does not exhibit any feature corresponding to the weak but distinct peak observed in the measured values at $q_z \approx 0.9$ Å$^{-1}$. As this peak's position is incommensurate with the large layering peak at 2.2 Å$^{-1}$, it must indicate the existence of a second length scale, additional to the periodicity of the surface-induced layering. It is highly unlikely that this second length scale, $2\pi/0.9 = 6.96$ Å, is associated with a *periodic* structure, in the same way that the 2.2 Å$^{-1}$ peak is associated with the surface-induced layering, since such two-periodicity structure would be very difficult to rationalize physically. Similarly, the low-$q_z$ peak can not be assigned to just a single-periodicity layered structure with a

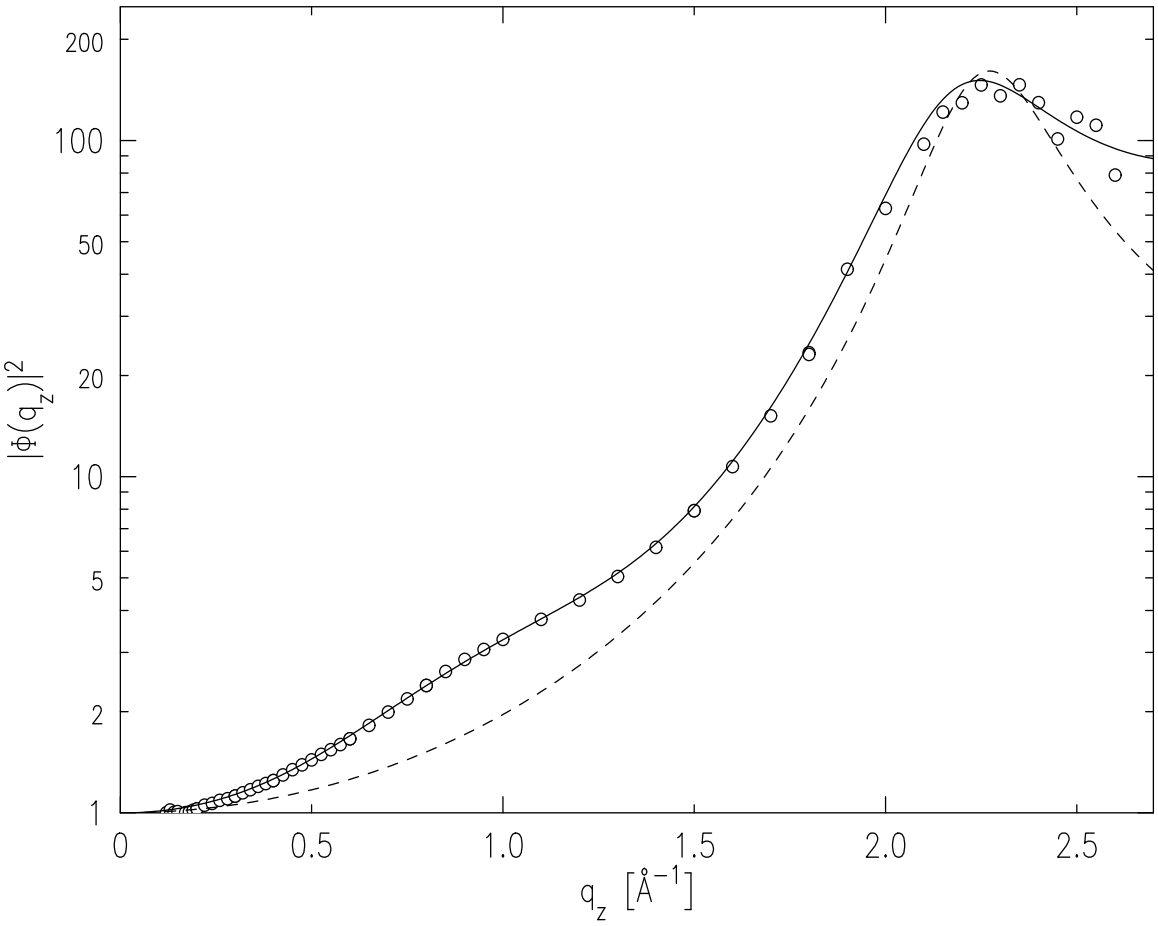



Figure 9.4: The structure factor (squared) of the Sn surface as derived from the measured reflectivity $|\Phi(q_z)|^2 = R(q_z)/[R_F(q_z)CW(q_z)]$ (open circles). The dashed line is the theoretically expected $|\Phi(q_z)|^2$ of a simple layered density profile as found previously for Ga and In. The solid line is a fit to a model, discussed in the text, where the distance between the first and second layers is reduced by 10% relative to that of the subsequent layers.

top layer which is denser than the subsequent layers. While such a structure will yield a subsidiary peak at low $q_z$, this peak would be commensurate with the high-$q_z$ one, i.e. appear at $q_z = 0.5 \times 2.2 \approx 1.1$ Å$^{-1}$ rather than the observed $\sim 0.9$ Å$^{-1}$. Thus, we conclude that an appropriate model needs to include a second, non-commensurate and non-periodic length scale, with a dense top layer. The solid line shown in Fig. 9.4 is a fit of the measured data by a model constructed along these lines. As can be seen, a good agreement is achieved with the measured values. We now proceed to discuss the details of this model.

The simple density model that has been used to represent the reflectivity of Ga[3] and In[4] consists of a convolution of an intrinsic density profile and a Debye-Waller-like factor, which accounts for the smearing of this profile by the thermally-excited capillary waves. The intrinsic profile is modelled by a semi-infinite series of equally-spaced gaussians, each representing a single atomic layer. The gaussians have equal integrated areas (i.e. equal areal electron density) but their widths increase with depth below the surface. This, in turn, results in a gradual decrease with depth of the individual peaks and valleys of the density profile, and an eventual evolution of the density towards the constant average density of the bulk liquid. The decay length of the surface layering is typically of the order of just a few atomic spacings.[3,4] The density profile of this model is shown in a dashed line in Fig. 9.5, and yields the dashed line in Fig. 9.4. The solid line that runs through the measured values in Fig. 9.4 is calculated from a slightly modified model, shown in a solid line in Fig. 9.5. The only difference between this model and the original one is that the distance between the first and second layers, 2.55 Å, is smaller by $\sim 10\%$ than the 2.8 Å spacing of the subsequent layers. The average density over the first two layers is thus larger than

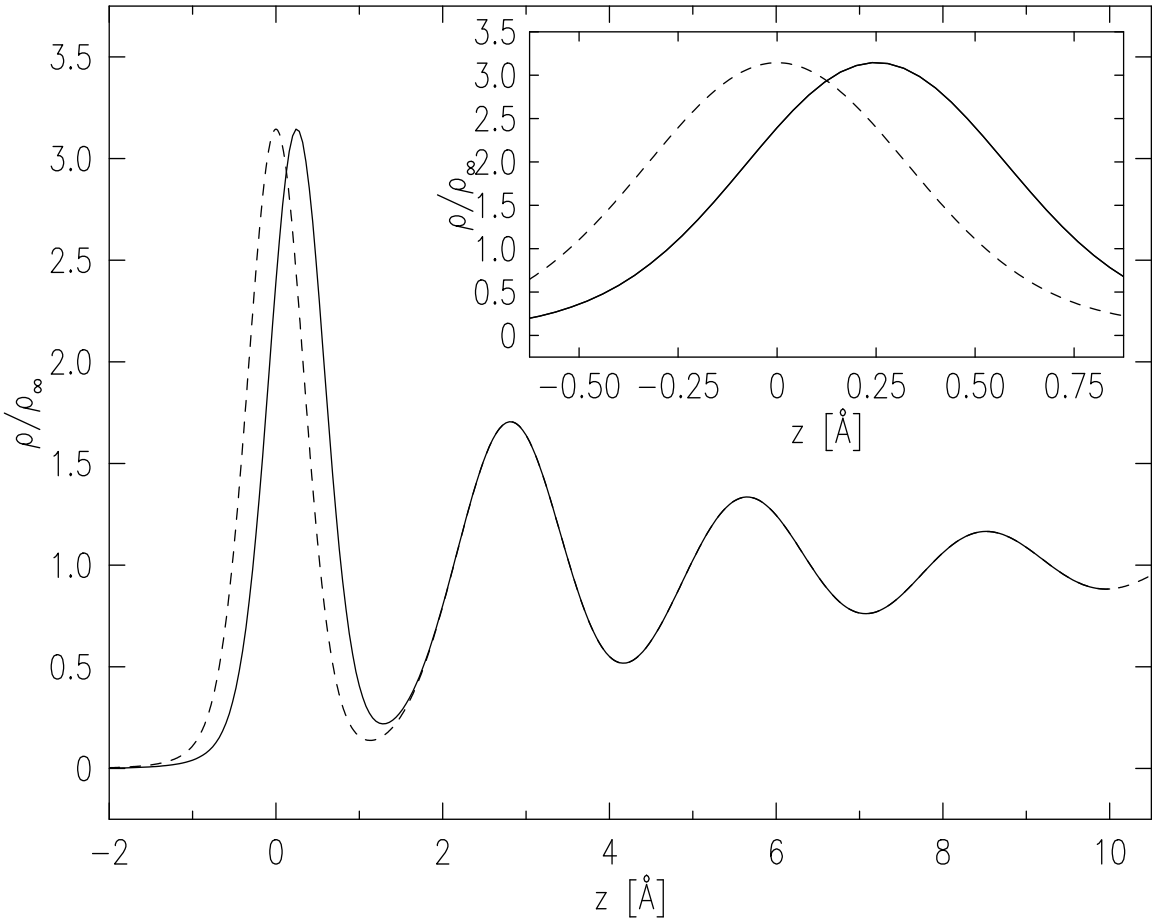



Figure 9.5: Models for the intrinsic surface-normal electron density profiles of Sn for a simple, equally-spaced layering model (dashed line), and for a model including a contraction of the spacing between the first and second layers by 10% (solid line). The models yield the reflectivities shown by the same lines in Fig. 9.2. The inset is a blow up of the peak region.

that of the bulk, and a second, non-periodic, length scale is introduced. The good agreement of this minimally-modified model with the measured data, demonstrated in in Fig. 9.4, strongly supports our interpretation of the surface structure on liquid Sn.

## 9.6 The Case For Exclusion of Surface Impurities

Up to this point we have not considered the possibility that the dense surface layer may be a layer of atoms of a different metal adsorbed onto the Sn surface. This is precisely what happens, for example, in the liquid binary alloys GaBi[13,16] and Ga-Pb,[17] where a (dense) monolayer of the lower-surface-energy species (Bi,Pb) is found to Gibbs-adsorb at the free surface of the alloy. We now show experimental evidence that this is not the case here.

Consideration of the Gibbs rule[18] shows that relatively low concentrations of three metals, Bi ($\gamma$= 378 mN/m, $\rho_e$ = 2.49 e/Å$^3$), Pb ($\gamma$= 458 mN/m, $\rho_e$ = 2.63 e/Å$^3$) and Tl ($\gamma$= 464 mN/m, $\rho_e$ = 2.79 e/Å$^3$) could have produced surface electron densities sufficient to cause the low-$q_z$ peak shown in Fig. 9.4. In order to address this possibility we performed two independent experiments, grazing incidence x-ray fluorescence (GI-XRF) and resonant x-ray reflectivity, both of which are sensitive to the presence of sub-monolayer quantities of impurities at the surface. None of the two measurements found evidence for contamination of the liquid Sn surface by a foreign species. Therefore, this supports the conclusion that the anomalous density feature observed here is in fact an intrinsic property of the liquid Sn surface.

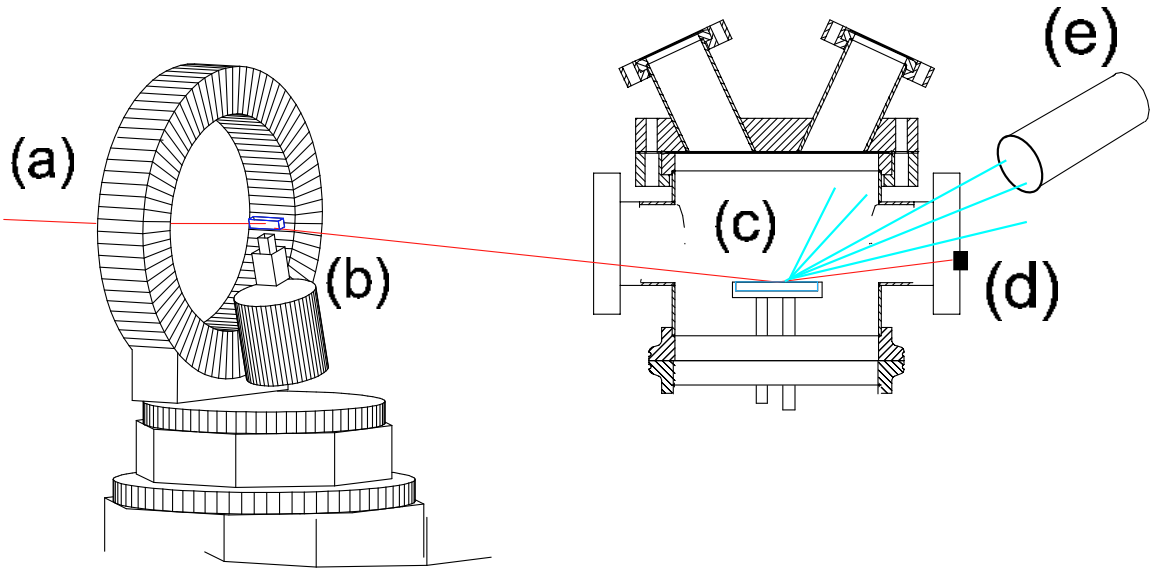



Figure 9.6: Experimental setup used in the GI-XRF measurements: the synchrotron beam (a) is Bragg-reflected from a monochromator (b) which directs it downwards at the liquid Sn sample located inside a UHV chamber (c). The specularly-reflected beam (solid line) is blocked by a beam stop on the exit window (d) to minimize the background. The fluorescence from the sample's surface (dotted lines) is detected off-specularly by an energy-dispersive detector (e) located as close to the chamber as possible to maximize its solid angle of acceptance.

### 9.6.1 Grazing Incidence Fluorescence Scattering

The experimental setup used in these measurements is shown in Fig. 9.6. The sample was illuminated by x-rays of wavelength $\lambda = 0.42$ Å (E=29.5 keV), incident at a grazing angle of $\alpha = 0.03°$. Since this is approximately one third of the critical angle of Sn at this energy, the refracted wave is evanescent. Its penetration depth below the surface is given by[19] $\tau = 1/Im[(4\pi/\lambda)\sqrt{\alpha^2 - \alpha_{crit}^2 - \imath\lambda\mu/2\pi}]$, where the critical angle for Sn is $\alpha_{crit}$ =0.09°, and the linear absorption coefficient is $\mu = 3.26 \times 10^{-6}$ Å$^{-1}$. For these values the incident beam probes only the uppermost $\tau = 30$ Å of the sample. Due to the high surface tension, the surface of the liquid Sn sample is curved, which has to be taken into account as well: for an incident beam height H and a convex

sample with a radius of curvature $r \approx 10$ m the angle of incidence $\alpha$ varies over the illuminated area by $\sim H/(\alpha r)$. In these measurements $H$ was set to 5 $\mu$m, so that for a nominal angle of incidence $\alpha_0 = 0.03°$ the local incidence angle varies by slightly less than $\pm 0.03°$. Over this range, $0° < \alpha < 0.06°$, the penetration length $\tau$ varies from 21 Å to 28 Å. Thus, for our nominal incident angle of $\alpha \approx 0.03°$ any detected fluorescence signal comes mostly from the top 8-10 atomic layers. Depending on the signal-to-noise ratio and other factors, such as the relative fluorescence yield, with this geometry it is possible to detect trace amounts of selected materials to sub-monolayer accuracies, as we show below. Note that at our incident energy, 29.5 keV, which is well above the Sn K edge, the K lines of Sn are all excited. However, the K edges of Bi, Pb and Tl are all $>$ 29.5 keV, so that only the L lines of these elements are excited.

Fluorescent x-ray emission from the illuminated portion of the sample was detected by an energy dispersive intrinsic Ge detector (area $\sim 9$ mm$^2$) that was mounted about 30 cm away from the center of the sample, 15 cm above it, and displaced azimuthally by about 30° from the incidence plane. The experimental setup for this geometry is shown in Fig. 9.6. The signal was recorded using a multichannel analyzer. A lead shield was mounted on the output window as shown in the Fig. 9.6 to eliminate scattering from the specularly reflected beam into the detector by the exit window or outside air. Unfortunately, there was no simple way to shield the detector from scattering or fluorescence originating in the entrance window of the UHV chamber. In order to account for this background scattering, a differential measurement has been performed. The signal detected with the sample displaced 3 millimeters below the incident beam was subtracted from the signal that was measured for the beam

striking the sample. The fluorescence data is shown in Fig. 9.7. The solid line is the as-measured raw fluorescence spectrum. It consists of fluorescence from both the sample and from the entrance window, elastic scattering from the incident beam (the strongest peak at $\sim$ 29.15 keV) and the Sn fluorescence (at 25.2 keV). There are a number of lower-energy peaks originating in the UHV chamber's components. The open circles show the spectrum obtained after subtracting from the raw spectrum the background spectrum recorded when the sample is moved out of the beam. The only remaining prominent peak is the Sn fluorescence observed at 25.2 keV. No other characteristic lines are discernible above the noise level. The ratio of the Sn K-fluorescence to the noise level in the 10-15 keV energy region, where the L-fluorescence lines of the Pb, Bi or Tl are expected, is $\sim$200. Factoring in the ratio of the K-fluorescence yield of Sn (0.84) to the L-fluorescence yields of Pb, Bi or Tl ($\sim$0.4) indicates that the presence of as little as 10% of a full monolayer of these metals (out of the $\sim$10 atomic layers of Sn illuminated by the evanescent wave) should be detectable in this experiment. Since an impurity coverage of the surface required to generate the $\sim$ 0.9 Å$^{-1}$ reflectivity peak is significantly higher than that, the absence of an impurity signal in Fig. 9.7 rules out with a high degree of confidence the possibility that a Gibbs adsorbed layer of impurities is the originator of the 0.9 Å$^{-1}$ peak.

### 9.6.2 Resonant X-ray Reflectivity

The effective electron density of an x-ray-scattering atom is proportional to the scattering form factor $f(q) + f'(q, E)$. Here $f(q) \to Z$ for $q \to 0$ and $Z$ is the atomic number. When the x-ray energy is tuned through an absorption edge of a scattering atom, the magnitude of the real part of $f'$ undergoes a sharp decrease, producing

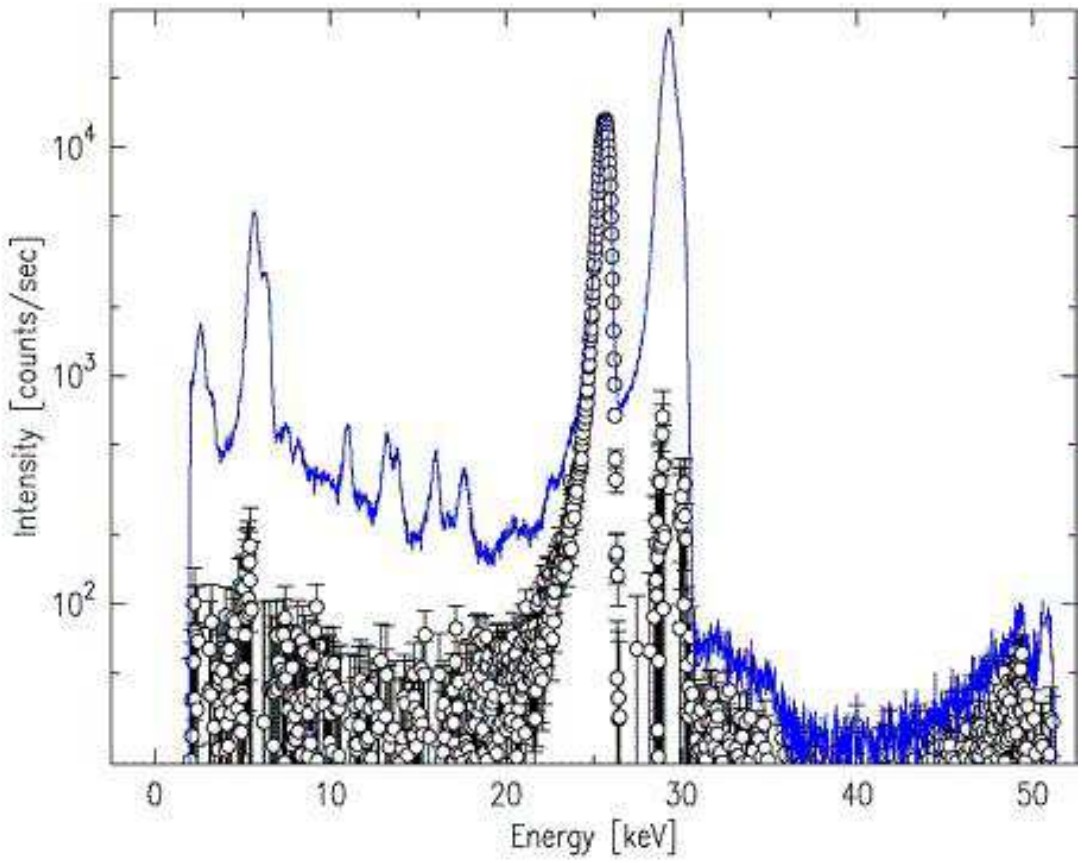



Figure 9.7: Raw (line) and background-subtracted (open circles) measured fluorescence from the surface of liquid Sn. The sharp lines are due to the K emissions lines[20] of Fe (E=6.4 keV), Nb (E=16.6 keV), Mo (E=17.5 keV) and Sn (E=25.2 keV).

a change in the scattering power of that specific atom.[21,22] Thus, by measuring the scattering on- and off-edge it is possible to isolate the scattering due to the specific atom. We have used this method, called resonant (or anomalous) scattering, in the reflectivity mode to probe the liquid surface of Sn for the presence of foreign atoms. This is done by comparing the x-ray reflectivities of the liquid surface measured with the x-ray energy tuned on and off the K edge of Sn (29.20 keV). If the low-$q_z$ feature at $q_z \approx 0.9$ Å$^{-1}$ is due a thin surface layer of foreign atoms, the effective electron density of Sn at the edge will change, while that of the foreign atoms will not. Thus, the density contrast will change, and so will the prominence of the low-$q_z$ peak. If, however, the low-$q_z$ peak is due to an intrinsic Sn structure, the electron density *difference* between high-density surface layer and the bulk will remain unchanged, and so will the low-$q_z$ peak.

The 29.20 keV edge of Sn was identified by a transmission measurement through a Sn foil, shown in Fig. 9.8(b), as well as by the reflectivity from the liquid Sn surface at a fixed $q_z = 0.3$ Å$^{-1}$, shown in Fig. 9.8(a). Since the surface structure factor $\Phi(q_z)$ depends on the electron density contrast between surface and bulk, the only energy dependence of $R(q_z)$ away from both structural peaks ( at $q_z = 0.9$ Å$^{-1}$ and $q_z = 2.3$ Å$^{-1}$) is due to the energy variation of the critical wavevector $q_c$. This leads to a $(Z + f'(E))^2$ energy dependence of the reflectivity at a fixed $q_z$. The minimum value of $f'(E)$, estimated from Fig. 9.8(a), is consistent with the theoretically predicted value calculated by the IFEFFIT[23] program, taking the smearing due to the lifetime widths of the K and L levels into consideration. The observed change in reflectivity at the minimum relative to that 50 eV away is measured to be about 15%, which corresponds, in turn, to a 7% reduction in the effective electron density of Sn.

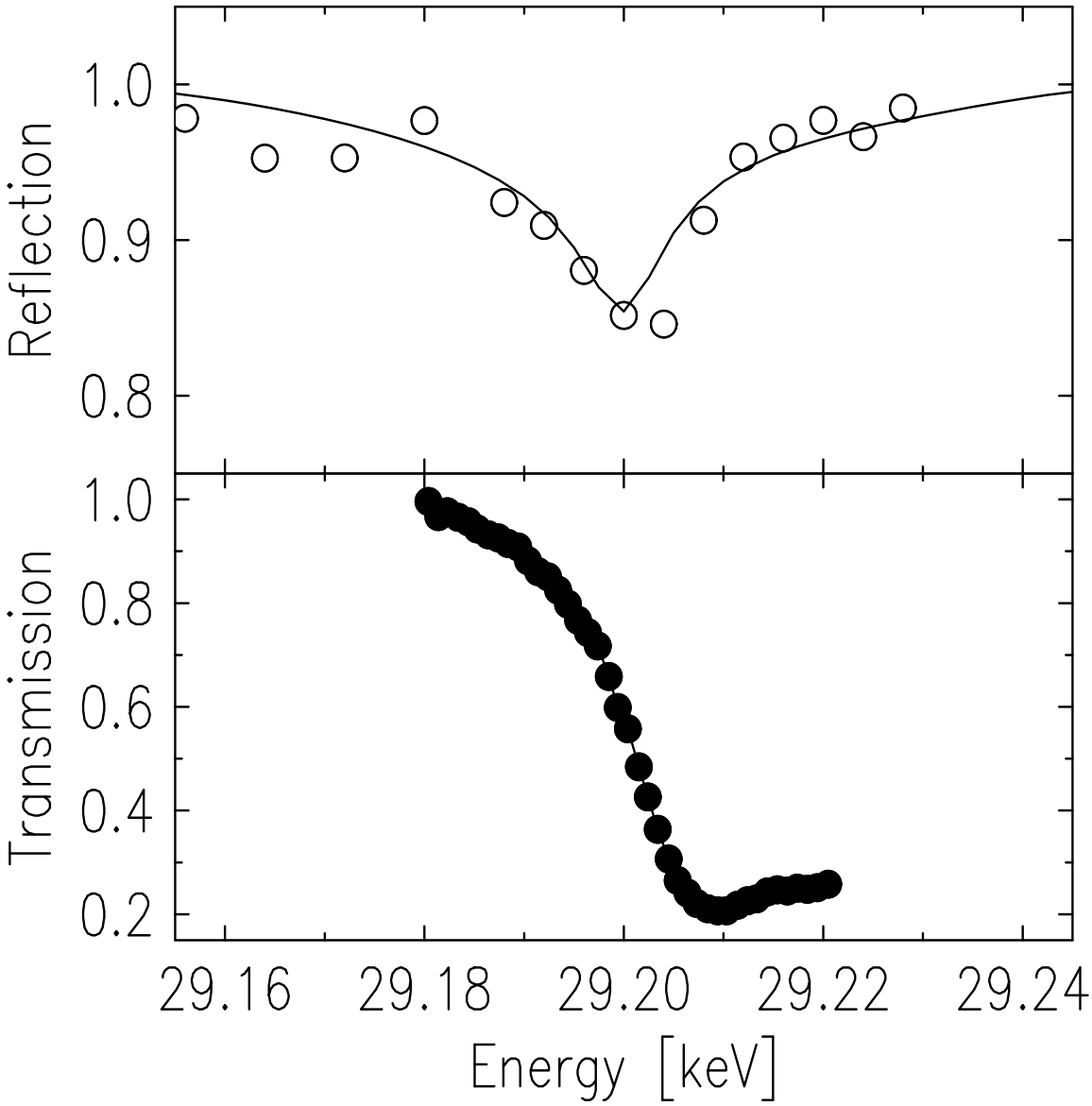



Figure 9.8: (Top) Relative energy variation of the reflectivity off the liquid Sn surface at a fixed $q_z = 0.3$ Å$^{-1}$. The line is the theoretical prediction of the change in the reflectivity due to the variation of the dispersion correction $f'(E)$ of the scattering factor near the edge, as calculated by the IFEFFIT[23] program. The open circles are the measured values. (Bottom) Measured energy variation of the intensity transmitted through an Sn foil (points). The K edge of Sn at E=29.20 keV shows up clearly in both measurements.

In Fig. 9.9 we show the low-$q_z$ normalized reflectivity data, $R(q_z)/[R_F(q_z)CW(q_z)] = |\Phi(q_z)|^2$, measured at the K edge of Sn (29.20 keV), just above the edge (29.22 keV) and far below the edge (17 keV). The fact that the three data sets coincide proves unambiguously that the 0.9 Å$^{-1}$ peak does not arise from contrast between Sn and a different element. A more quantitative analysis can be done in two ways. First, we assume a simple box model for the surface,[19] shown in the inset to Fig. 9.9. In this model, the surface layer's electron density, A, is larger than that of the bulk, B, yielding $|\Phi(q_z)|^2 \approx (2A/B - 1)^2$ at the peak. To obtain the measured peak of $|\Phi(q_z)|^2 = 1.4$, we have to assume $A/B = 1.1$. We note that only a handful of elements would be consistent with a model where this 10% increase in density originates in a surface layer of impurity atoms. Eliminating the elements which have a higher surface tension than that of Sn ($\gamma$=560 mN/m), which will not Gibbs-segregate at the surface, the only reasonably-likely remaining candidates are Bi, Pb and Tl. If we assume that the surface layer is a monolayer of any one of these elements the effect of the resonance is that the effective electron density of the Sn would be reduced by about 7%, as mentioned above. The measured $R(q_z)/[R_F(q_z)CW(q_z)] = |\Phi(q_z)|^2$ would therefore increase at the Sn K-edge to $(2 \times 1.1/0.93 - 1)^2 = 1.86$. The fact that this does not occur proves, again, that the increased density at the surface is an intrinsic surface effect, due entirely to a structure comprising Sn atoms only.

A second quantitative argument is the full modelling of the reflectivity, rather than considering only the maximum of the 0.9 Å$^{-1}$ peak. The solid line in Fig. 9.9 is the same fit shown in Fig. 9.5 to the model where the density of each atomic layer is kept at the Sn density value, while the spacing between the first and the second atomic layer is reduced from the 2.80 Å of subsequent layers to 2.55 Å. The agreement

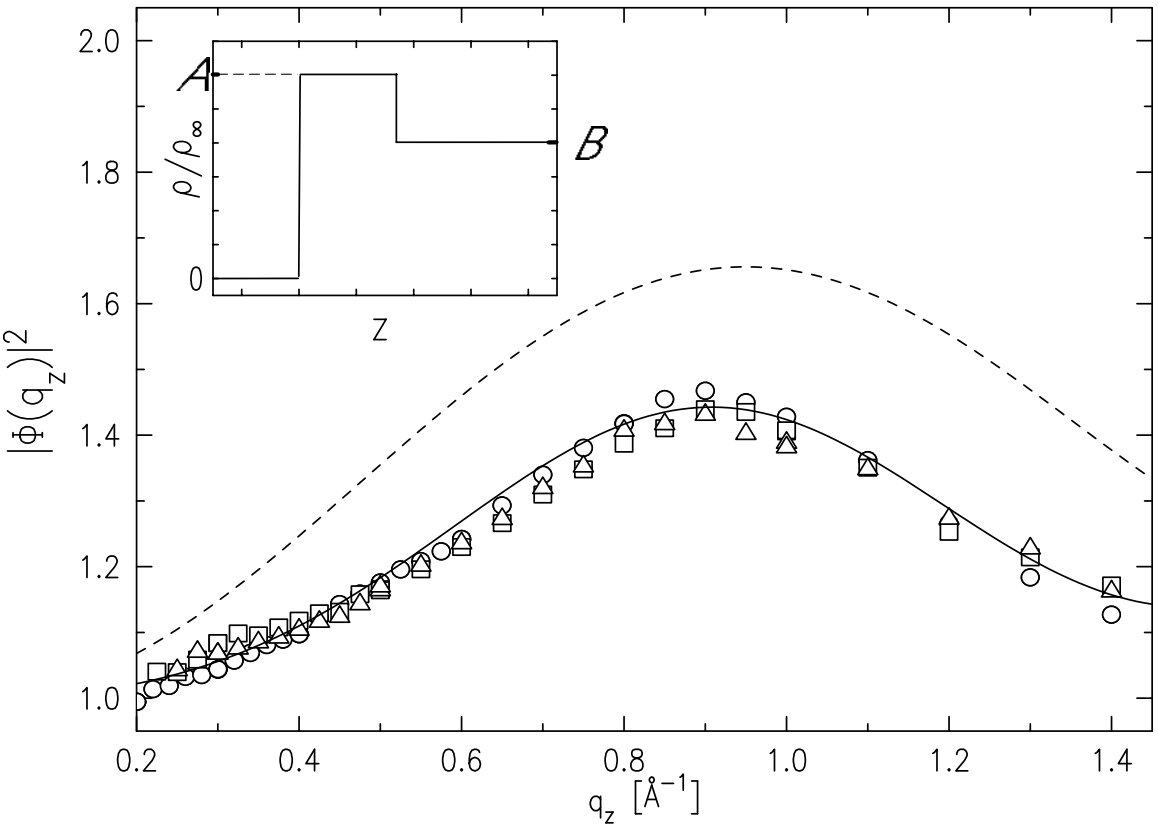



Figure 9.9: The structure factor (squared) of the Sn surface as derived from the measured reflectivity, at (E=29.20 keV, triangles), above ((E=29.22 keV, circles) and below (E=17 keV, squares) the K-edge. The solid line is a fit to the density model featuring reduced interatomic spacing for the top layer by approximately 10 %. The dashed line is calculated for a model with a high-density surface monolayer of an atomic species other than Sn. The inset shows the density profile of such a layer. For a discussion see text.

of all measured reflectivities, in particular that measured at the edge (triangles), with this model is excellent. The dashed line is the reflectivity calculated assuming an additional surface monolayer of a different species having a density higher than that of Sn. As can be seen, for the on-edge measurement, this line is expected to lie considerably higher than off-edge. It clearly does not agree with the on-edge measured data (triangles).

The results of the two measurements presented in this section rule out the possibility that the dense surface layer found in the reflectivity measurements is due to surface segregation of impurity atoms. Thus, they strongly supports our claim that the high-density layer present at the surface is the intrinsic property of the Sn itself.

## 9.7 Conclusion

We have found that the surface of liquid Sn exhibits atomic layering, similar to that found in other metallic systems. However, the surface structure factor exhibits an additional low-$q_z$ peak, which has not been observed for any of the pure metals studied to date. The possibility that this structure is due to a layer of surface-adsorbed contaminants has been addressed by two experiments, both of which confirm that the observed reflectivity feature is an intrinsic property of liquid Sn. The strongest argument comes from the resonant x-ray reflectivity measurement which finds no detectable difference between reflectivities measured on- and off- the Sn K-edge, while model calculations predict a significant change for a layer of foreign surface atoms. Our analysis shows that the anomalous feature at low $q_z$ is consistent with a modified atomic layering density model where the spacing between the first and second atomic layers is reduced by 10% relative to the subsequent ones, thereby increasing the

average density at the surface. The physical reasons for the existence of this denser layer at the surface of liquid Sn are not clear, since the studies of other liquid metals and alloys exhibit no evidence for such a feature. We note, however, that the density of the liquid Sn (6970 kg/m$^3$) is in between the densities of the solid alpha phase Sn (5750 kg/m$^3$), also known as "gray tin" and forming a cubic atomic structure, and the solid beta phase Sn (7310 kg/m$^3$), known as "white tin" and forming a tetragonal atomic structure. It is possible that while the higher-density beta phase is no longer stable in the bulk beyond the melting point, it prevails in some form at the surface, where the packing restrictions are relaxed due to smaller number of nearest neighbors. Another possibility which may be related to the previous argument, is that the Sn-Sn pairing, know to be present in the bulk phase[10,11,12] of liquid Sn, is stronger near the surface than in the bulk, and induces a higher density. Clearly, the origin of this increased surface density in liquid Sn warrants further investigation.

# Bibliography


[1] S.A. Rice, D. Guidotti, and H.L. Lemberg. *Aspects of the study of surfaces*, (Wiley, Chichester, UK, 1974) vol. 27, pp. 543-633

[2] O. M. Magnussen, B. M. Ocko, M. J. Regan, K. Penanen, P. S. Pershan, and M. Deutsch. Phys. Rev. Lett. **74**, 4444 (1995).

[3] M. J. Regan, E. H. Kawamoto, S. Lee, P. S. Pershan, N. Maskil, M. Deutsch, O. M. Magnussen, B. M. Ocko, and L. E. Berman Phys. Rev. Lett. **75**, 2498 (1995).

[4] H. Tostmann, E. DiMasi, P. S. Pershan, B. M. Ocko, O. G. Shpyrko, and M. Deutsch. Phys. Rev. B **59**, 783 (1999).

[5] O. Shpyrko, P. Huber, A. Grigoriev, P. Pershan, B. Ocko, H. Tostmann, and M. Deutsch Phys. Rev. B **67**, 115405 (2003)

[6] E. Dimasi, H. Tostmann, B. M. Ocko, P. S. Pershan and M. Deutsch Phys. Rev. B **58**, 13419 (1998).

[7] A. Di Cicco and A. Filliponi Europhys. Lett. **27**, 407 (1994)

[8] X. S. Gong et al. Europhys. Lett. **21**, 469 (1994)

[9] W. J. Huisman, J. F. Peters, M. J. Zwanenburg, S. A. deVries, T. E. Derry, D. Abernathy, J. F. van der Veen Nature **390**, 379 (1997).

[10] D. Jovic and I. Padureanu. Journal of Physics C **9**, 1135 (1976).

[11] A. DiCicco. Phys. Rev. B **53**, 6174 (1996).

[12] T. Itami, S. Munejiri, T. Masaki, H. Aoki, Y. Ishii, T. Kamiyama, Y. Senda, F. Shimojo, and K. Hoshino. Phys. Rev. B, **67**, 064201 (2003).

[13] P. Huber, O. G. Shpyrko, P. S. Pershan, B. M. Ocko, E. DiMasi, and M. Deutsch Phys. Rev. Lett. **89**, 035502 (2002).

[14] O. G. Shpyrko, M. Fukuto, B. M. Ocko, P. S. Pershan, M. Deutsch, T. Gog and I. Kuzmenko. Phys. Rev. B **69**, 245423 (2004)

[15] A. Braslau, P. S. Pershan, G. Swislow, B. M. Ocko, and J. Als-Nielsen. Phys. Rev. A **38**, 2457 (1988).

[16] H. Tostmann, E. DiMasi, O. G. Shpyrko, P. S. Pershan, B. M. Ocko, and M. Deutsch. Phys. Rev. Lett. **84**, 4385 (2000).

[17] B. Yang, D. Li, Z. Huang, and S. A. Rice Phys. Rev. B **62**, 13111 (2000)

[18] J. W. Gibbs, R. G. Van Name, W. R. Longley, and H. A. Bumstead, *Collected works of J. Willard Gibbs*, (Longmans, Green and Co., New York, 1928).

[19] M. Tolan. *X-Ray Scattering from Soft-Matter Thin Films*, (Springer-Verlag New York, 1999) p. 148.

[20] A. Bearden. Rev. Mod. Phys., 39 (1967).

[21] C. J. Sparks and K. Fischer. *Resonant Anomalous X-ray Scattering: Theory and Applications*, (North-Holland, Amsterdam, 1994).

[22] E. DiMasi, H. Tostmann, O. G. Shpyrko, M. Deutsch, P. S. Pershan, and B. M. Ocko. Journal of Physics: Condensed Matter **12**, 209 (2000).

[23] Matt Newville IFEFFIT: Interactive XAFS Analysis, `http://cars9.uchicago.edu/ifeffit/`, 1997.

# Chapter 10

# Surface Phases in Binary Liquid Metal Alloys

## 10.1 Abstract

Surface sensitive x-ray scattering techniques with atomic scale resolution are employed to investigate the microscopic structure of the surface of three classes of liquid binary alloys: (i) Surface segregation in partly miscible binary alloys as predicted by the Gibbs adsorption rule is investigated for Ga-In. The first layer consists of a supercooled In monolayer and the bulk composition is reached after about two atomic diameters. (ii) The Ga-Bi system displays a wetting transition at a characteristic temperature $T_w \approx 220^o$C. The transition from a Bi monolayer on Ga below $T_w$ to a thick Bi-rich nanoscale wetting film above $T_w$ is studied. (iii) The effect of attractive interactions between the two components of a binary alloy on the surface structure is investigated for two Hg-Au alloys.

## 10.2 Introduction

Theoretical calculations and computer simulations indicate that the microscopic structure of the surface of liquid metals (LM) and alloys is considerably different from the surface structure of dielectric liquids and mixtures[1,2,3]. For liquid metals, the density profile normal to the surface has been predicted theoretically to show oscillations with a period of about one atomic diameter and extending a few atomic diameters into the bulk[2]. This layering normal to the surface has been confirmed experimentally for liquid Hg[4], Ga[5] and, most recently, In[6]. Surface induced layering in LM is is due to the drastic changes in the interactions across the interface from short-ranged screened Coulomb interactions in the liquid phase to long-ranged van der Waals interactions in the gas phase. In dielectric liquids, on the other hand, van der Waals interactions prevail both in the liquid and in the gas phase and theory predicts a monotonic density profile[7].

Compared to elemental LM, binary LM alloys have an additional degree of freedom and it is possible to study the effect of the second component on surface induced layering. Moreover, binary mixtures are expected to exhibit a richer array of surface structures. In partly miscible mixtures for example, the lower surface tension component is expected to segregate at the surface as predicted by the Gibbs adsorption rule of thermodynamics[8]. For binary liquid metal alloys, computer simulations predict that the component that segregates at the liquid-vapor interface forms a nearly pure monolayer[9,10,11]. The adjacent layer on the bulk liquid side is slightly depleted of the surface-active component, and the bulk composition is reached at a distance of about two atomic diameters into the bulk. For simple dielectric mixtures on the other hand, theory predicts that the excess concentration of the segregating component falls

smoothly with distance into the bulk over a range of several atomic diameters[8]. These predictions remain largely untested experimentally.

The bulk phase behavior of demixing leading to a miscibility gap with a critical consolute point induces a new class of surface phase transitions as predicted by Cahn in 1977[12]. Based on scaling law arguments Cahn postulated that a phase transition from nonwetting of the two immiscible phases to complete wetting of one phase by the other necessarily occurs close to the critical consolute point. In this transition, a macroscopically thick wetting phase is formed intruding between the bulk liquid and the vapor phase (or an inert substrate). This is in contrast to the phenomenon of surface segregation that takes place on atomic length scales. Experimental studies of such wetting phase transitions have been restricted mostly to binary dielectric mixtures[13]. Wetting and prewetting phase transitions have been observed only recently in fluid systems governed by screened Coulomb interactions[14], namely K-KCl[15], Ga-Pb[16] and Ga-Bi[17]. These experiments provide no direct microscopic information on the structure of the interface. By contrast, the study presented here probes the structure of the liquid interface with Å resolution using surface x-ray scattering techniques.

A characteristic feature of many well-known and technically important alloys is the formation of intermetallic phases in the solid state[18]. These phases include stoichometric Laves phases, broad Hume-Rothery phases and semiconducting Zintl phases containing polyanions. This phase formation is due to attractive interactions between the two components. An interesting question is whether these attractive interactions affect the surface structure of liquid binary alloys.

In this paper, we will demonstrate how surface x-ray scattering techniques can be used to study LM alloys exhibiting different types of surface structure. In Sections 2

and 3 we review the x-ray scattering techniques and experimental details. In Section 4 we present three different alloy systems with increasing complexity of bulk phase behavior and surface structure: Ga-In, Ga-Bi and Hg-Au.

## 10.3 Surface X-ray Scattering Techniques

X-rays are well suited to study the structure of the surface of liquids with atomic scale resolution. The large dynamic range in intensity required for such studies can be realized to advantage by synchrotron x-ray sources. In this section we describe the surface x-ray scattering techniques used in our studies to determine the structure normal to the surface and within the surface plane.

**2.1. Specular X-ray Reflectivity (XR):** X-ray reflectivity probes the structure normal to the interface. Here, the x-ray intensity is measured at the specular condition where incoming and outgoing angles $\alpha$ and $\beta$ are equal and the azimuthal angle $2\theta$ is zero (see Figure 10.1). In this case, the scattering momentum transfer, $\vec{q} = \vec{k}_{out} - \vec{k}_{in}$, is normal to the surface

$$|\vec{q}| = q_z = \frac{2\pi}{\lambda}(\sin\alpha + \sin\beta) = \frac{4\pi}{\lambda}\sin\alpha \qquad (10.3.1)$$

where $\lambda$ is the x-ray wavelength.

If the liquid surface is ideally flat and abruptly terminated (i.e. has a step function density profile), the reflectivity $R$ is given by the Fresnel reflectivity $R_f$ known from classical optics[19]. The reflectivity of a real surface will deviate from $R_f$. For example, height fluctuations produced by thermally excited capillary waves cause phase shifts in x-rays reflected from different points on the surface. Averaging over these phase variations gives rise to a Debye-Waller type factor, $\exp(-\sigma_{cw}^2 q_z^2)$, characterized by a capillary wave roughness $\sigma_{cw}$[6]. In addition, the density profile normal to the surface

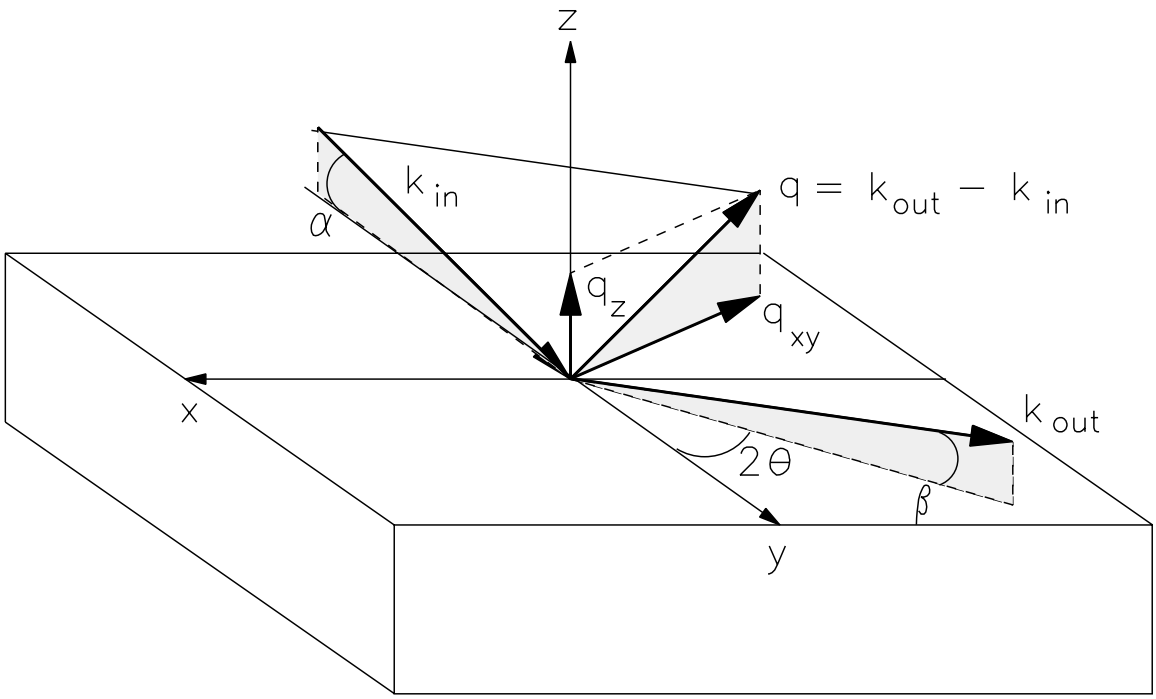



Figure 10.1: Sketch of the geometry of x-ray scattering from the liquid surface with $\alpha$ and $\beta$ denoting incoming and outgoing angle, the incoming and outgoing wavevector $k_{in}$ and $k_{out}$ respectively and the azimuthal angle $2\theta$. The momentum transfer $q$ has an in-plane component $q_{xy}$ and a surface-normal component $q_z$.

deviates from a step function, being oscillatory for elemental LM. For binary alloys displaying phase separation or phase transitions we expect further modification of the surface. Therefore, a surface structure factor $\Phi$ has to be taken into account[20]:

$$\Phi(q_z) = \frac{1}{\rho_\infty} \int_{-\infty}^{+\infty} \frac{d\langle\rho(z)\rangle}{dz} \exp(\imath q_z z) dz \tag{10.3.2}$$

with $\langle\rho(z)\rangle$ denoting the electron density average over a microscopic surface area on the atomic scale and $\rho_\infty$ the bulk electron density. This factor is analogous to the bulk structure factor $S(\vec{q})$ which is the Fourier transform of the bulk electron density. The reflectivity from a real surface is then given by:

$$R(q_z) = R_f \exp(-\sigma_{cw}^2 q_z^2) \left|\Phi(q_z)\right|^2 . \tag{10.3.3}$$

It is not possible to directly invert the measured reflectivity $R(q_z)$ to the density profile normal to the surface due to the loss of phase information. Rather, the common practice is the construction of a physically plausible model for the density profile which is then inserted in Eq. 10.3.2 and fitted to the measured reflectivity[6,21].

**2.2. Grazing Incidence Diffraction (GID):**

GID probes the in-plane structure of the surface. The in-plane momentum transfer $q_{xy}$ is probed by varying the azimuthal angle $2\theta$ (see Figure 10.1). This geometry is surface sensitive if the incident angle $\alpha$ is kept below the critical angle for total external reflection $\alpha_{crit}$ thereby limiting the x-ray penetration depth to $\simeq 50$ $\mathring{A}$ and minimizing the background from bulk scattering[22,23]. The GID surface in-plane structure can be directly compared to the bulk liquid structure by making similar measurements for $\alpha > \alpha_c$.

## 10.4 Experimental

It is essential to establish a clean oxide free liquid alloy surface since even microscopic impurities significantly change the x-ray reflectivity[24]. We use slightly different methods to prepare the three alloys presented in this paper. The eutectic Ga-In alloy is prepared in a High Vacuum chamber using in situ glow-discharge to clean the sample[21]. The sample is transferred into the x-ray UHV chamber, melted and cleaned by Ar ion sputtering.

The Ga-Bi alloy is prepared as follows. Bi is melted under UHV conditions and any residual oxide is evaporated by heating the Bi to about 600° C. After the Bi is transferred into an Ar glove box, liquid Ga is added so that the mole fraction of Bi is $x_{Bi} \approx 0.3$. This value is chosen to correspond to the concentration of the bulk solution at the critical point of 265° C . The sample is then frozen and transferred to the x-ray UHV chamber. The chamber is baked out and the liquid surface sputter cleaned.

The preparation of the Hg-Au alloy is quite different since the high vapor pressure of Hg is not compatible with UHV conditions. Quadruple distilled Hg and Au powder are mixed in a glove box and transferred to a stainless steel reservoir attached to a valve with a filling capillary. This container is attached to a UHV chamber with the valve closed. This chamber is then subjected to a standard UHV bakeout to remove oxygen and water, after which the valve is opened and the Hg-Au alloy is poured into the sample pan. Due to the low oxygen partial pressure in the chamber, residual oxide is instable and disappears from the surface within a couple of hours.

The sample chamber is placed on an active vibration isolation table that effectively quenches all mechanically induced vibrations[6]. The experiments have been

performed at the beamlines X22B and X25 at the National Synchrotron Light Source at Brookhaven National Laboratory. The x-ray energies are 19keV and 10keV at X25 and X22B respectively. A discussion of the liquid surface spectrometer can be found elsewhere[21].

## 10.5 Results and Discussion

### 10.5.1 Surface Segregation in Ga-In

As an example of a simple miscible alloy with a eutectic point we have studied the Ga-In (16.5% In) system[21]. The Fresnel-normalized reflectivity is shown in Figure 10.2 (filled squares). The data have been recorded at room temperature and are compared to the normalized reflectivity from elemental Ga (open squares) at the same temperature. The most pronounced feature of the Ga reflectivity is the quasi-Bragg peak at 2.4 $\mathring{A}^{-1}$ that indicates the presence of surface induced layering[5]. This layering peak is present in the Ga-In alloy as well, although slightly suppressed. The peak position is centered at a smaller value of $q_z$ compared to Ga indicating a larger layer spacing, as expected for a larger In atom. The second pronounced difference between the Ga-In and the Ga reflectivity is the observation that the reflectivity from Ga-In is about 30% higher than the Fresnel reflectivity of an ideal Ga-In surface at intermediate values for $q_z$. This can only be understood if a higher density adlayer exists at the surface. The measured x-ray reflectivity is consistent with the segregation of a 94% In monolayer on top of the Ga-In eutectic. The presence of the In monolayer increases the reflected x-ray intensity at intermediate $q_z$ due to the higher electron density of In but has a less pronounced effect at larger $q_z$ values where the reflectivity is dominated by the Ga layering peak. The density profile that fits the measured XR

can be modeled by a single Gaussian for the In segregation layer plus a semi-infinite sum of Gaussians for the Ga-In eutectic with half widths that increase with distance from the surface, representing the decay of the layering with increasing distance from the surface[21]. The best fit of this model to the data results in a density profile normal to the surface that shows the segregation of an In monolayer with a 2.6 $\mathring{A}$ spacing between the In monolayer and the underlying eutectic layer. This fit is represented by the solid line in Figure 10.2.

These results provide new information about the surface structure of miscible LM alloys. The constituents of this alloy have similar size and the same valency. The Ga-In interactions are comparable to the Ga-Ga and the In-In interactions. As a consequence, Ga-In is close to being an ideal mixture, for which surface segregation of the lower surface tension component is predicted. Our measurements show that this segregation is actually confined to a single monolayer. An arguably more interesting issue is the interplay between surface segregation and surface induced layering. Our measurements show that layering persists, with the In monolayer comprising the outermost layer. Similar conclusions were reached by recent Quantum Molecular Dynamics simulations[25].

### 10.5.2 Wetting phase transition in Ga-Bi

The Ga-Bi system is an example of an alloy with a miscibility gap. Below the monotectic temperature, $T_{mono}$= 222° C, a Ga rich liquid coexists with a solid Bi phase. (see[26] for a full description of the phase diagram). However, due to its lower surface energy a Bi monolayer is expected to segregate at the surface of the Ga rich liquid. The wetting phase transition that is predicted for all binary mixtures with critical demixing[12] occurs at a characteristic wetting temperature $T_w$ below the critical

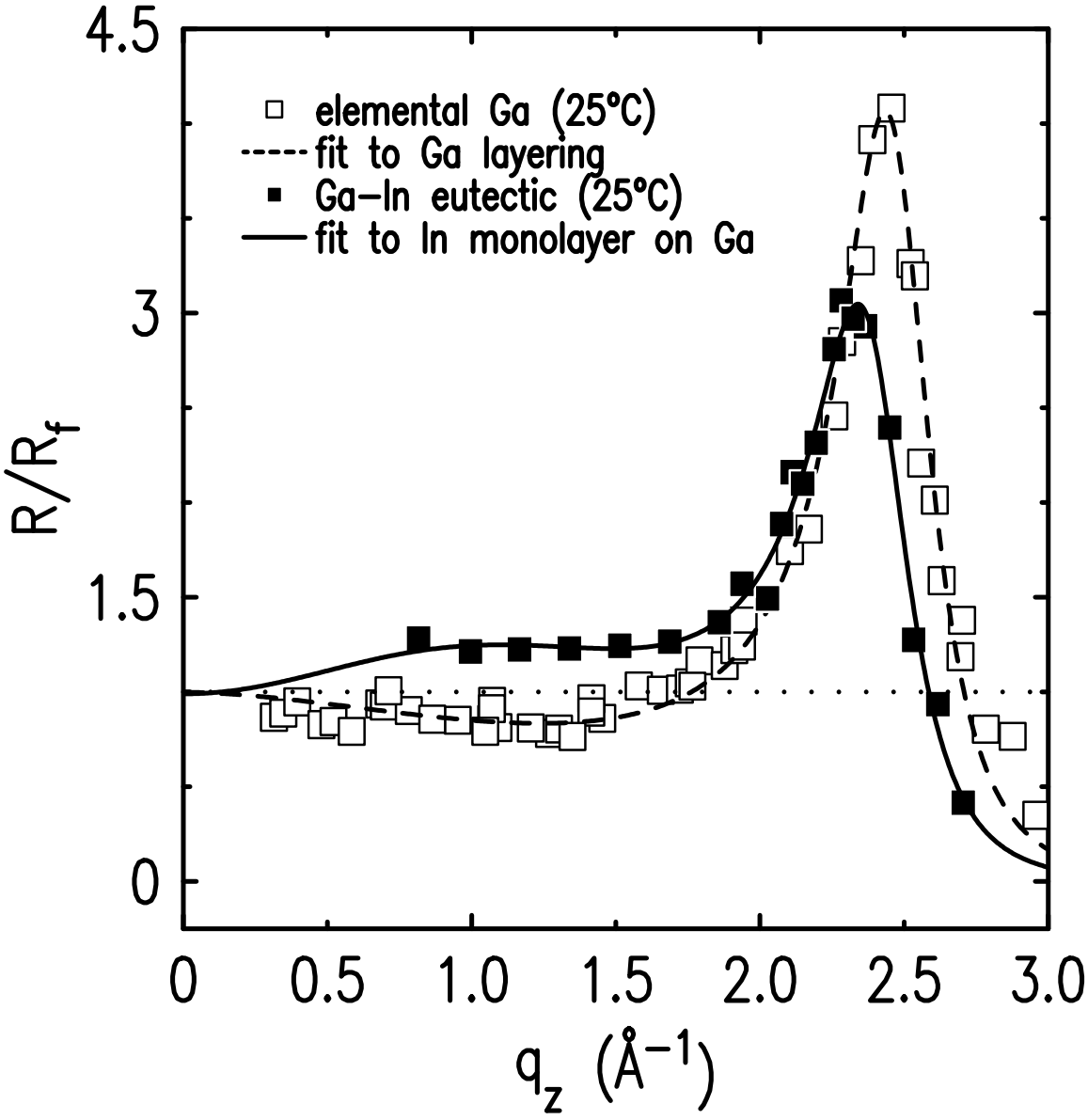



Figure 10.2: X-ray reflectivity from liquid Ga and liquid Ga-In (16.5% In) at 25° C. The broken line represents the fit of the model described in the text to the measured reflectivity from liquid Ga. The solid line represents the fit of the same model with one additional high density adlayer to the measured reflectivity from the liquid Ga-In eutectic.

temperature $T_{crit}$ [27,28]. Optical studies show that $T_w$ coincides with the monotectic temperature for Ga-Bi[14,17]. Above $T_w$, a macroscopically thick Bi rich phase is expected to completely wet the lighter Ga rich phase in defiance of gravity. The Bi concentration in the Ga rich phase increases with increasing temperature as long as the liquid coexists with the solid Bi phase.

The normalized x-ray reflectivity spectra, $R/R_{f,Ga}$, for Ga-Bi at 35° C and 95° C are shown in Figure 10.3 versus $q_z^2$. At the lowest values of $q_z$, the normalized reflectivity approaches the reflectivity of an ideal Ga surface given by the Fresnel Law of Optics. At values of $q_z$ close to the critical q-vector $q_{crit} = 4\pi/\lambda \sin \alpha_{crit}$, the reflectivity is not particularly sensitive to the structure or roughness of the surface (see Eq.(10.3.3)) and is simply related to the electron density within ≈20 $\mathring{A}$ of the surface. The fact that the reflectivity approaches the Fresnel reflectivity given by the Ga electron density implies that the higher density Bi can not be more than a few monolayers thick. With increasing $q_z$, the normalized reflectivity first increases and reaches a maximum at about $q_z \approx 1\ \mathring{A}^{-1}$. The variation of $R/R_{f,Ga}$ with $q_z$, is similar to that observed by Lei et al.[10], corresponding to the thickness of a single atomic layer, again suggesting that only the top layer has a sizeable bismuth concentration. Compared to the Ga-In alloy discussed above, this variation is much more pronounced. This results from the 30% higher electron density of bismuth compared with gallium, and only a 5% higher density for indium. The behavior of the same alloy at 260°C is markedly different. Here, the reflectivity starts out at $R/R_{f,Ga} \approx 2$ and falls off monotonically with $q_z$, a behavior consistent with a thick Bi rich layer terminating the metal/vapor interface above $T_w$.

The reflectivity below $T_w \approx 220$°C has been analyzed in terms of a density profile

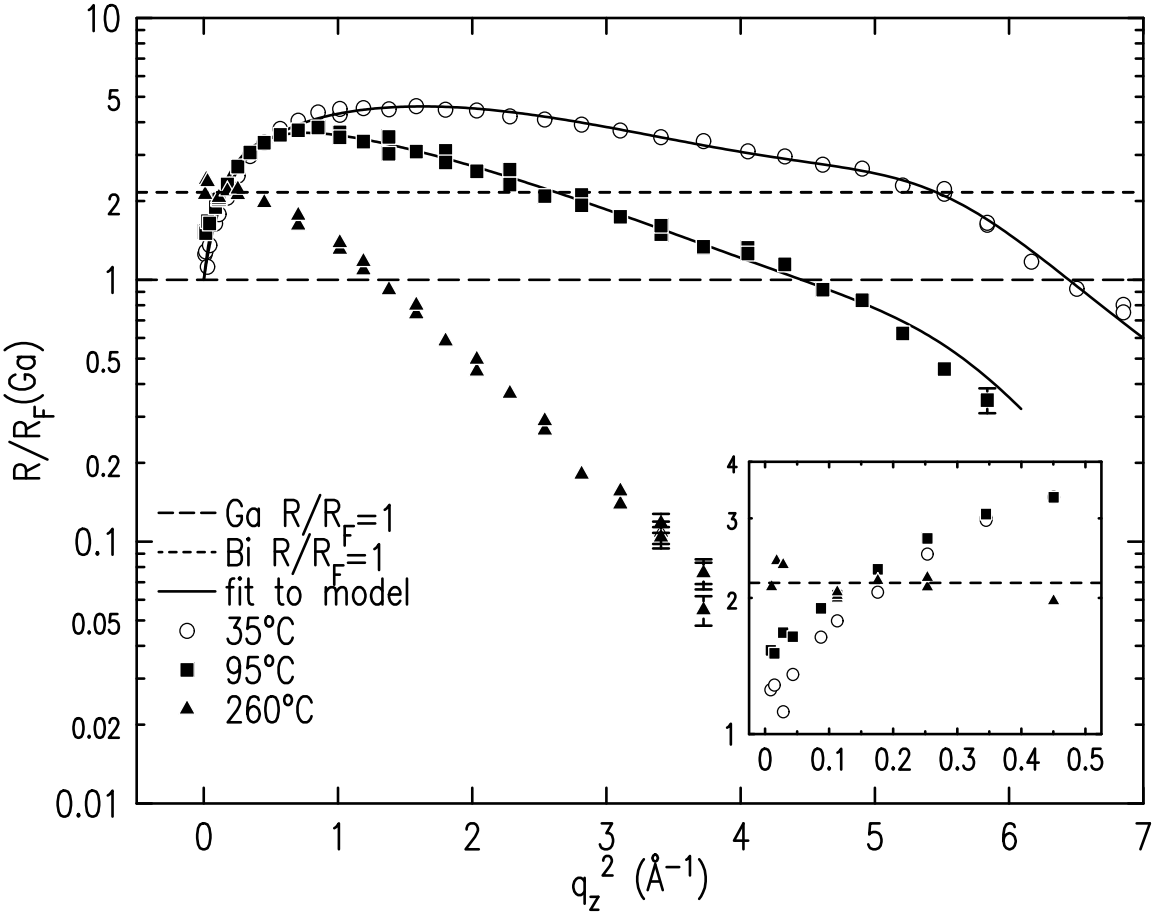



Figure 10.3: X-ray reflectivity from Ga-Bi for three different temperatures. The solid lines show the fit of the data to a simple surface segregation model with one Bi monolayer on top of the Ga rich bulk phase. The difference between the 35° C and the 95° C data is due to the increased roughness at higher temperatures. The 260° C data cannot be fitted by this model. The inset shows the principal difference in surface structure between the 35° C and the 260° C data, indicating a wetting phase transition.

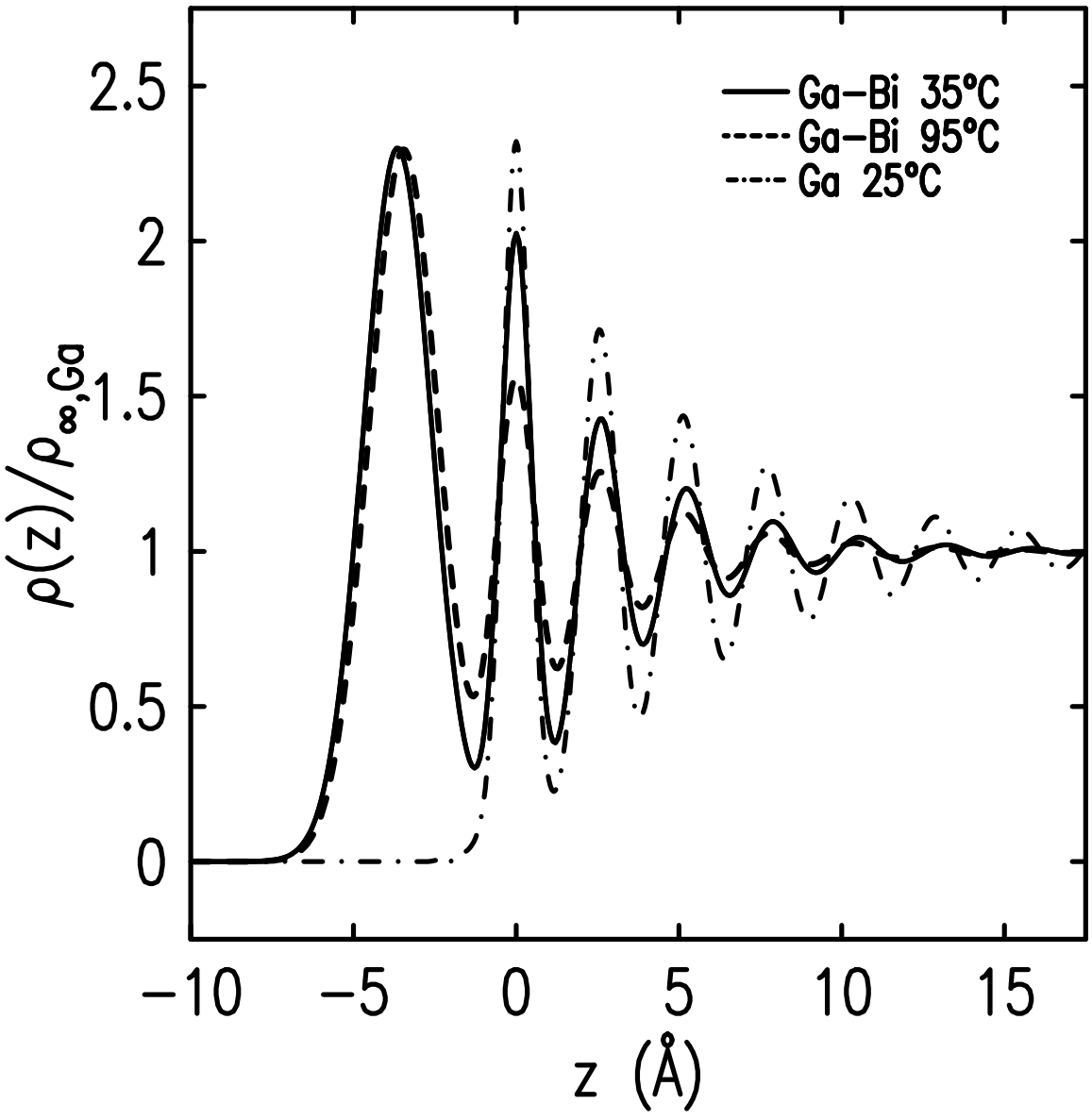



Figure 10.4: Comparison of the intrinsic or local real space density profiles (thermal broadening removed) for Ga-Bi at two different temperatures as well as for elemental Ga. The density is normalized to the bulk density of liquid Ga. The zero position in $z$ is arbitrarily assigned to the center of the first Ga layering peak.

similar to the one which describes the Ga-In data[21]. The best fits, the solid lines in Figure 10.3, provide an excellent description of the data. The corresponding local density profile, shown in Figure 10.4 after removing the temperature dependent capillary wave roughness factor, exhibits a top-layer density which is about 1.5 times higher than the Ga bulk liquid density and is consistent with the formation of a complete Bi monolayer. The 3.6±0.2 $\mathring{A}$ layer spacing between the monolayer and the adjacent Ga layer (obtained from the fits) is much larger than the $2.5 \pm 0.1$ $\mathring{A}$ layer spacing obtained in liquid gallium. This also supports the conclusion of a top layer with a much larger atomic diameter. In addition, the 4.3 Å exponential decay length of the layering amplitude is significantly smaller than the 5.5 Å decay length obtained for pure liquid Ga[5]. The suppression of the layering in the presence of either a bismuth or indium monolayer is much more apparent in the case of bismuth (compare Figure 10.3 to Figure 10.2. A likely explanation is the larger size difference in Ga-Bi (the Bi diameter is 30% larger than that of Ga) compared to Ga-In (In is 15% larger than Ga). As demonstrated by the solid lines, the layering model which describes the 35°C reflectivity profile also agrees closely with the 95°C profile, without a discernible change in the parameters of the density profile, except for the value of $\sigma_{cw}$, which is scaled, using capillary wave theory, to correspond to the higher temperature (see Eq.(10.3.3)).

This picture of a Bi monolayer segregating on top of the Ga rich bulk phase is supported by GID experiments which probe the in-plane structure of the surface (see Figure 10.5). The solid line shows the in-plane liquid structure factor measured for $\alpha > \alpha_{crit}$ where the x-rays penetrate the bulk to a depth > 1000 Å. The broad peak at $q_{xy} \approx 2.5$ $\mathring{A}^{-1}$ and the shoulder on the high-angle side of the peak agree

with bulk liquid Ga structure factor[29]. There is no evidence for a peak or shoulder at the position corresponding to the first peak of the Bi liquid structure factor at $q_{xy} \approx 2.2\ \mathring{A}^{-1}$. The bulk scattering completely masks the weak scattering from the bismuth monolayer due to the large penetration depth of x-rays. The surface sensitivity is drastically enhanced by keeping the incoming angle $\alpha$ below the critical angle for total external reflection (0.14° for Ga). As the x-rays now penetrate only to a depth $< 50$ Å, the first peak of the Bi liquid structure factor is clearly visible at $q_{xy} \approx 2.2\ \mathring{A}^{-1}$ (open triangles in Figure 10.5). Still, since the Bi layer is only a single monolayer thick, the contribution from the underlying Ga is larger then that of the Bi, as seen from the Bi being only a shoulder on the Ga structure factor peak in Figure 10.5.

While the XR results at 35° C and 95° C are consistent with a real space model where the Bi is segregated only in the top atomic layer, at temperatures above 220° C, corresponding to a Bi mole fraction of about 0.08, this model no longer describes the data. The ratio $R/R_{f,Ga}$ for the reflectivity taken at 260° C close to the critical wavevector for Ga is approximately twice as large as the same ratio taken at 35° C and 95° C. The dashed horizontal line, shown in the inset to Figure 10.3, represents the theoretical Fresnel-normalized reflectivity curve for bulk Bi ($R/R_{f,Bi} \approx 2 \times R/R_{f,Ga}$). This curve agrees well with the 260° data at small $q_z$ where the surface roughness contribution is minimal, and clearly supports the conclusion of a thick Bi-rich surface layer. Such a thick wetting layer has been proposed on the basis of previous optical experiments[14,17]. These findings are also supported by GID experiments above 220° C which show a pronounced increase in the intensity of the Bi structure factor relative to the Ga structure factor[30].

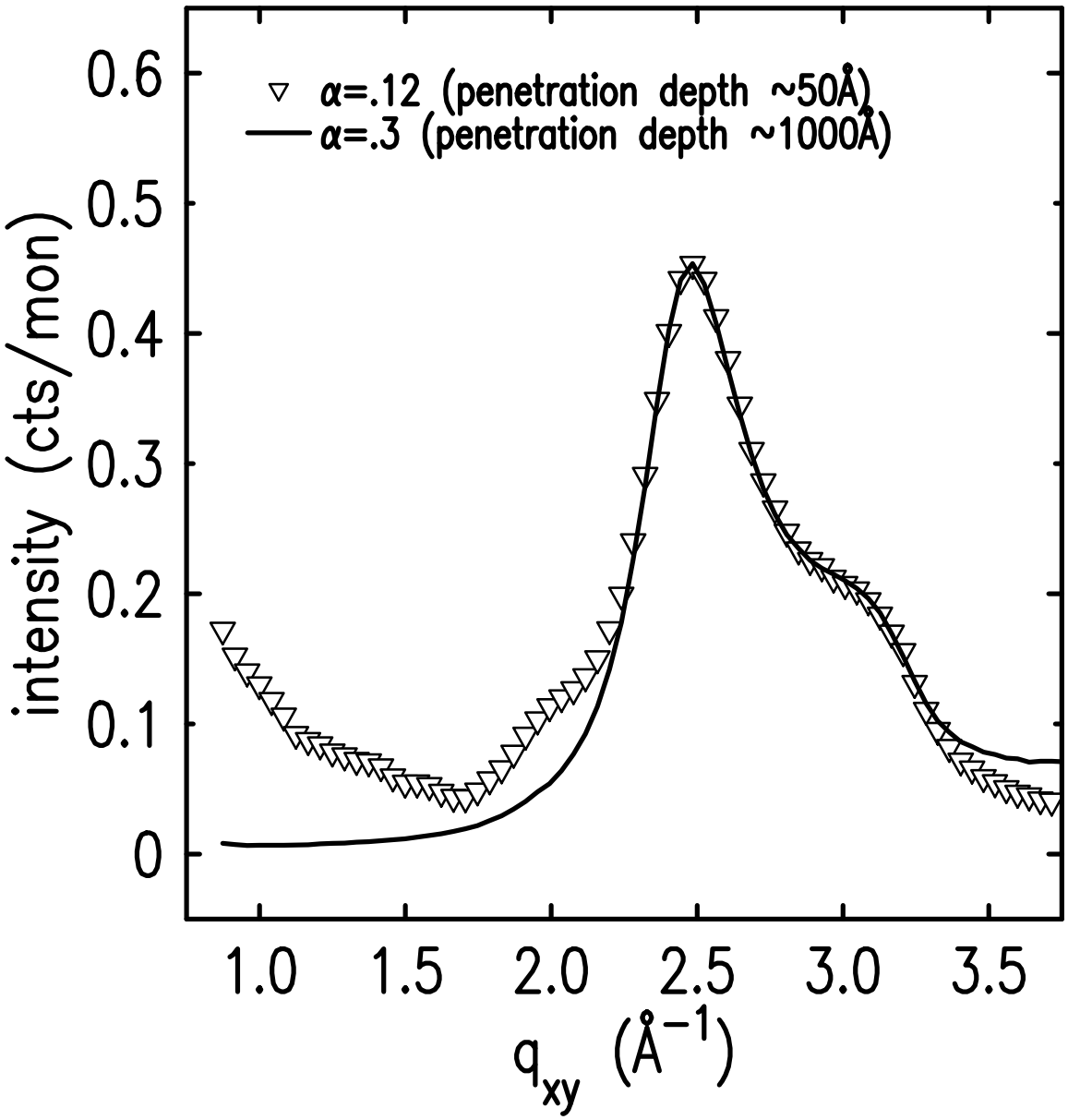



Figure 10.5: Grazing Incidence Diffraction from Ga-Bi at 35° C. The solid line shows the in-plane structure averaged over the penetration depth of x-rays away from the critical angle for total external reflection (about 1000 Å). The open triangles show the diffraction peak obtained for $\alpha < \alpha_{crit}$ ($\alpha_{crit} = 0.14°$ for Ga at $\lambda = 0.653$ $\mathring{A}$) thus probing the surface region evanescently.

### 10.5.3 Pair formation in Hg-Au

Our x-ray reflectivity measurements of dilute liquid Hg-Au alloys demonstrate that dramatic differences in surface structure can be induced by very small changes in concentration. Figure 10.6(a) compares the reflectivity of Hg with that of a solution of 0.06at% Au in Hg. This composition is approximately half of the reported solubility limit for Au in Hg at room temperature[26]. For pure Hg, the surface layering peak at $q_z = 2.2$ $\mathring{A}$ is much more prominent close to its melting point at $-40$°C than at room temperature[31]. This difference arises primarily from increased roughening of the surface due to thermally excited capillary waves with increasing temperatures. The presence of 0.06at% Au sharply suppresses the surface induced layering of Hg, as shown by the substantial attenuation of the layering peak. The temperature dependence in both systems suggests that at this concentration, the suppression of the surface layering by the Au has a small dependence on temperature in comparison to the effect of capillary waves.

Increasing the Au concentration to 0.13at% yields a qualitatively different behavior as shown in Figure 10.6(b). At room temperature, layering is suppressed to a similar extent in both alloys. However, upon lowering the temperature of the 0.13at% solution to $-30$°C, a deep minimum appears at $q_z = 1.4$ Å$^{-1}$. This minimum is produced by destructive interference between x-rays reflecting from layers of different density near the surface, implying that one or more phases have formed that are different from the composition of the bulk. We find significant hysteresis of the reflectivity under temperature cycling. In particular, on returning to room temperature and cooling again, the low temperature minimum is much less deep than that observed previously, and saturates at this higher value even when the sample

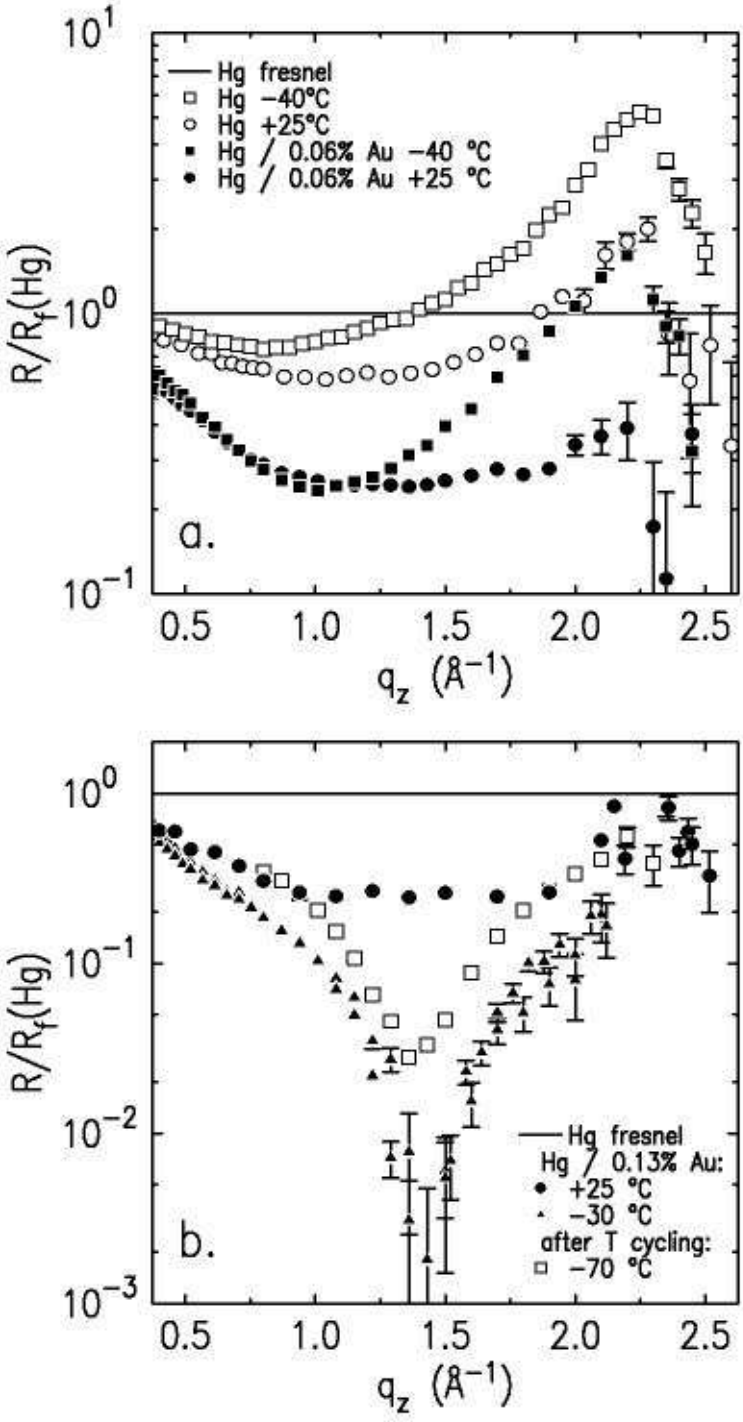



Figure 10.6: (a) X-ray reflectivity of Hg and Hg/0.06at%Au normalized to the Fresnel reflectivity of Hg. (b) Normalized reflectivity of a Hg/0.13% alloy.

is supercooled to about $-70$°C. This pronounced effect has been reproduced and in the absence of detailed modeling we can only speculate about its origin. As opposed to Ga-In and Ga-Bi, the interactions between Hg and Au are attractive leading to intermetallic phase formation in the solid state with $Au_2Hg$ being the best known phase[26]. Several other phases have been reported that are only stable below -39°C[26]. It is known from x-ray studies on FeCo (001)[32] and $Cu_3Au$ (001)[33] surfaces, that this pair formation gives rise to mesoscopic surface segregation profiles in the solid state. As soon as one component segregates at the surface, it is energetically favorable for the next layer to consist entirely of the other component due to the pronounced attractive interactions. It is conceivable that a similar mechanism prevails in liquid Hg-Au. An alternating or more complicated segregation profile would destroy the Hg layering even more effectively than the segregation of a monolayer in Ga-In or Ga-Bi and is consistent with our experimental findings that a small amount of Au completely suppresses the otherwise very pronounced Hg layering peak even at low temperatures.

# Bibliography


[1] M.Iwamatsu and S.K.Lai, J.Phys.:Condens.Matter *4*, 6039 (1992)

[2] J.G.Harris, J.Gryko and S.A.Rice, J.Chem.Phys. *87*, 3069 (1987)

[3] R.Evans and M.Hasegawa, J.Phys.C:Solid State Phys. *14*, 5225 (1981)

[4] O. M. Magnussen, B. M. Ocko, M. J. Regan, K .Penanen, P.S.Pershan and M.Deutsch, Phys.Rev.Lett. *74*, 4444 (1995)

[5] M.J.Regan, E.H.Kawamoto, S.Lee, P.S.Pershan, N.Maskil, M.Deutsch, O.M.Magnussen, B.M.Ocko and L.E.Berman, Phys.Rev.Lett. *75*, 2498 (1995)

[6] H.Tostmann, E.Dimasi, P.S.Pershan, B.M.Ocko, O.G.Shpyrko and M.Deutsch, submitted (1998)

[7] G.A.Chapella et al., J.Soc.FaradayII *73*, 1133 (1977)

[8] J.S.Rowlinson and B.Widom, Molecular Theory of Capillarity, Clarendon, Oxford, 1982

[9] J.G.Harris and S.A.Rice, J.Chem.Phys. *86*, 7531 (1987).

[10] N.Lei, Z.Huang and S.A.Rice, J.Chem.Phys.*104*, 4802 (1996)

[11] S.A.Rice, M.Zhao and D.Chekmarev, submitted (1998)

[12] J.W.Cahn, J.Chem.Phys *66*, 3667 (1977)

[13] M.Schick in: Liquids at Interfaces (Proceedings Les Houches Summer School, Session XL), ed. by J.Charvolin, J.F.Joanny and J.Zinn-Justin, North-Holland, Amsterdam, 1990

[14] W.Freyland and D.Nattland, Ber.Bunsenges.Phys.Chem. *102*, 1 (1998)

[15] H.Tostmann, D.Nattland and W.Freyland, J.Chem.Phys. *104*, 8777 (1996)

[16] D.Chatain and P.Wynblatt, Surf.Sci. *345*, 85 (1996)

[17] D.Nattland, S.C.Müller, P.D.Poh and W.Freyland, J.Non-Cryst. Solids *205–207*, 772 (1996)

[18] W.B.Pearson, The Crystal Chemistry and Physics of Metals and Alloys, Wiley, New York, 1972

[19] J.Als-Nielsen in: Structure and Dynamics of Surfaces, Topics in Current Physics 43, ed. by W.Schommers and P.von Blanckenhagen, Springer, Heidelberg, 1987

[20] P.S.Pershan and J.Als-Nielsen, Phys.Rev.Lett. *52*,759 (1984)

[21] M.J.Regan et al., Phys.Rev.B *55*,15874 (1997)

[22] P.Eisenberger, W.C.Marra, Phys.Rev.Lett. *46*, 1081 (1981)

[23] H.Dosch, Critical Phenomena at Surfaces and Interfaces, Springer Tracts in Modern Physics, Vol. 126, Springer, Heidelberg, 1987

[24] M.J.Regan, H.Tostmann, P.S.Pershan, O.M.Magnussen, E.DiMasi, B.M.Ocko and M.Deutsch, Phys.Rev.B *55*, 10786 (1997)

[25] S.A.Rice and M.Zhao, submitted (1998)

[26] T.B.Massalski et al. (eds.), Binary Alloy Phase Diagrams, ASM International, Materials Park, Ohio, 1990

[27] S.Dietrich, Wetting Phenomena, in: Phase Transitions and Critical Phenomena, Vol. 12, ed. by C.Domb and J.Lebowitz, Academic Press, London, 1986.

[28] S.Dietrich, G.Findenegg and W.Freyland (eds.), Phase Transitions at Interfaces (Proceedings Bunsen Discussion Meeting), Ber.Bunsenges.Phys.Chem. *98* (1994)

[29] A.H.Narten, J.Chem.Phys. *56*, 1185 (1972)

[30] H.Tostmann, E.DiMasi,O.G.Shpyrko, P.S.Pershan, B.M.Ocko, and M.Deutsch, in preparation (1998)

[31] E.DiMasi, H.Tostmann, B.M.Ocko, P.S.Pershan and M.Deutsch, in preparation (1998)

[32] S.Krimmel et al., Phys.Rev.Lett. 78, 3880 (1997)

[33] H.Reichert, P.Eng, H.Dosch and I.K.Robinson, Phys.Rev.Lett. *74*, 2006 (1995)

# Chapter 11

# Surface Induced Order in Liquid Metals and Binary Alloys

## 11.1 Abstract

Surface x-ray scattering measurements from several pure liquid metals (Hg, Ga and In) and from three alloys (Ga-Bi, Bi-In, and K-Na) with different heteroatomic chemical interactions in the bulk phase are reviewed. Surface induced layering is found for each elemental liquid metal. The surface structure of the K-Na alloy resembles that of an elemental liquid metal. Surface segregation and a nanoscale wetting film are found for Ga-Bi. Bi-In displays pair formation at the surface.

## 11.2 Liquid Metals and Surface Induced Order

Liquid metals (LM) are comprised of charged ion cores whose Coulomb interactions are screened by a conduction electron sea. At the liquid-vapor interface, this screened Coulomb potential gives way to the weaker van der Waals interactions that prevail in the vapor. Since the potential changes so substantially across the interface, the potential gradient is high, producing a force that acts on the ions at the liquid surface

as though they were packed against a hard wall. Analytic calculations and molecular dynamics simulations predict that atoms at the LM surface are stratified in layers parallel to the interface[1]. By contrast, a monotonic density profile is predicted for the vapor interface of a nonmetallic liquid.

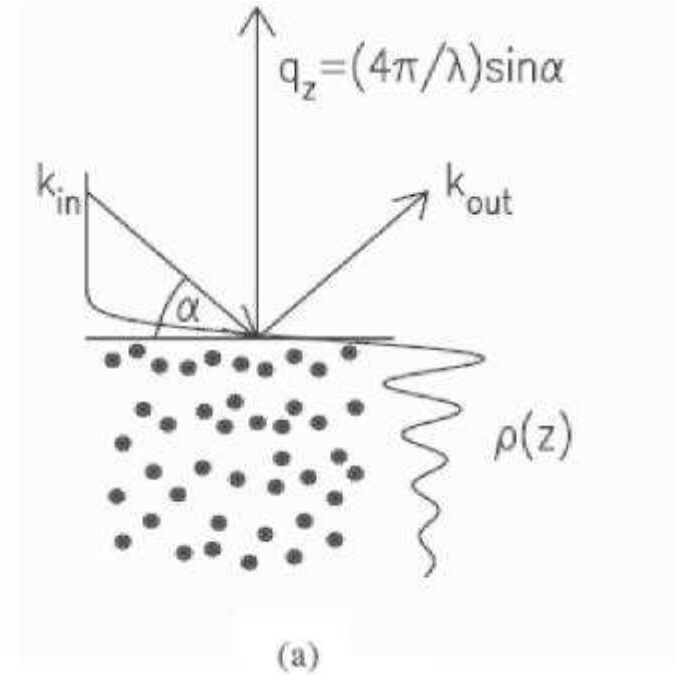
Observation of surface layering in LM requires an experimental technique sensitive to the surface-normal density profile that can resolve length scales of 2–3 Å. Specular X-ray reflectivity provides the most direct probe of the surface normal structure. X-rays incident on the liquid surface at an angle $\alpha$ are scattered at the same angle within the reflection plane defined by the incident beam and the surface normal (Fig. 11.1(a)). The reflected intensity is directly related to the surface normal density profile $\tilde{\rho}(z)$:

$$R(q_z) \propto \left| q_z^{-2} (\partial\tilde{\rho}(z)/\partial z) \exp(iq_z z) dz \right|^2 . \qquad (11.2.1)$$

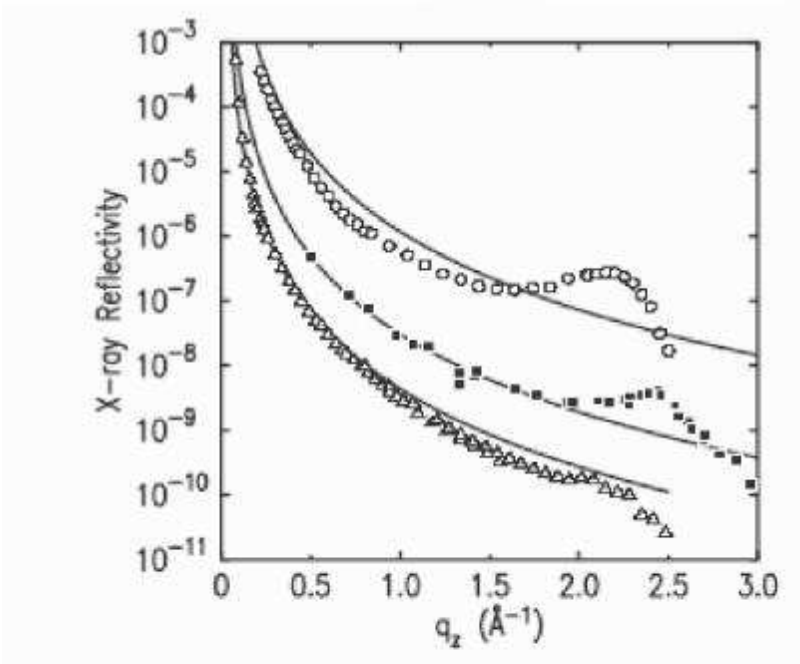
Since $\partial\tilde{\rho}(z)/\partial z$ is nonzero only near the surface, x-ray reflectivity is sensitive to the surface-normal structure and not to the structure of the bulk liquid. For example, surface layering with a spacing $d$ produces a quasi-Bragg peak in the reflectivity, centered at the surface-normal momentum transfer $q_z = (4\pi/\lambda)\sin\alpha \approx 2\pi/d$[2,3,4].

Grazing incidence diffraction (GID) is sensitive to the in-plane structure of the surface. The in-plane momentum transfer $q_\parallel$ is probed by varying the azimuthal angle $2\theta$ at fixed $\alpha$. This geometry is surface sensitive when the incident angle $\alpha$ is kept below the critical angle for total external reflection, $\alpha_c$, thereby limiting the x-ray penetration depth[5].

For these structural studies it is essential to maintain a liquid metal surface that is flat and clean on an atomic scale. The sample is contained either in an ultra high vacuum (UHV) environment, or under a reducing atmosphere such as dry hydrogen




(a)




(b)

Figure 11.1: (a) X-ray reflectivity geometry for the liquid metal, with layering of ions producing an oscillatory density profile $\rho(z)$. (b) X-ray reflectivity for liquid Hg ($-35$°C, $\circ$), Ga ($+25$°C) and In ($+170$°C, $\triangle$). Solid lines: calculated Fresnel reflectivity from a flat surface. Data for Ga and In are shifted for clarity.

gas, to prevent oxidation. For low vapor pressure, UHV-compatible metals such as Ga, Bi, and In, argon ion sputtering is possible, and this is the most reliable way to produce an atomically clean surface [4].

Surface layering in elemental LM was first experimentally confirmed by synchrotron x-ray reflectivity measurements of liquid Hg[3] and Ga[4]. Experiments on In[6] and a number of alloys[7,8,9,10] followed. Fig. 11.1(b) shows experimental reflectivities for three low melting point elemental LM. The principle deviation from the Fresnel reflectivity calculated for a perfectly flat metal surface (solid lines) is in the broad quasi-Bragg peak centered near $q_z = 2.2$ Å$^{-1}$. These reflectivity profiles can be well described by layered density profiles decaying over several layers, shown schematically in Fig. 11.1(a).

## 11.3 Surface Structure of Binary Liquid Alloys

In binary alloys properties such as atomic size, surface tension, and electronic structure can be varied and should affect the details of the surface structure, thus allowing a more systematic understanding of surface layering. Also, since binary alloys form various ordered phases in the bulk, another interesting question arises: How does the alloy's bulk phase behavior manifest itself at the surface, where the electronic structure, atomic coordination and local composition are different? This question has motivated a number of studies on alloys, which have found that in general, surface layering competes with the formation of more complicated surface phases. For example, in miscible alloys the Gibbs adsorption rule predicts that the species having the lower surface energy will segregate at the surface. Observations on Ga-In[9], Ga-Sn[8] and Ga-Bi at low Bi concentrations[7,10] have found that surface segregation

coexists with surface layering. In these alloys the first surface layer is almost entirely composed of the lower surface tension component (In, Sn or Bi). By the second or third atomic layer, the bulk composition has been reached. In the following sections, we describe recent x-ray results from alloy surfaces which demonstrate a range of different surface induced structural effects.

### 11.3.1 K-Na

Alkali metals have a simple electronic structure which can be described by ideal Fermi surfaces, and are soluble in each other with only a weak tendency towards phase formation. Since alkali metals have a very low surface tension, surface fluctuations are enhanced. These properties are expected to make the alkali metals' surface structures different from those of the main group metals studied so far. Ideally alkali metals would be investigated under UHV conditions due to their high reactivity. However, at the melting point their high vapor pressures precludes this. By contrast, the melting point of the eutectic $K_{80}Na_{20}$ alloy is sufficiently low to allow UHV conditions. Due to the almost identical electron densities of the two components, when probed by x-rays this alloy exhibits the structure of a homogeneous liquid metal. Here we present preliminary results for the eutectic $K_{80}Na_{20}$ alloy.

Fig. 11.1(a) shows the x-ray reflectivity from $K_{80}Na_{20}$ along with the predicted reflectivity assuming capillary wave roughness (Gaussian form) of 1.2 and 1.5 Å[11]. At all $q_z$ the reflectivity is bounded by these two curves; at lower $q_z$ it is better described by the 1.5 Å roughness. On length scales $\gtrsim$ 6 Å no obvious structural feature is found beyond the predicted capillary wave roughness. The low surface tension ($\approx 120 dyn/cm$) and the subsequently high roughness, appears to preclude measurements to $q_z$ large enough to directly observe a surface layering peak. This

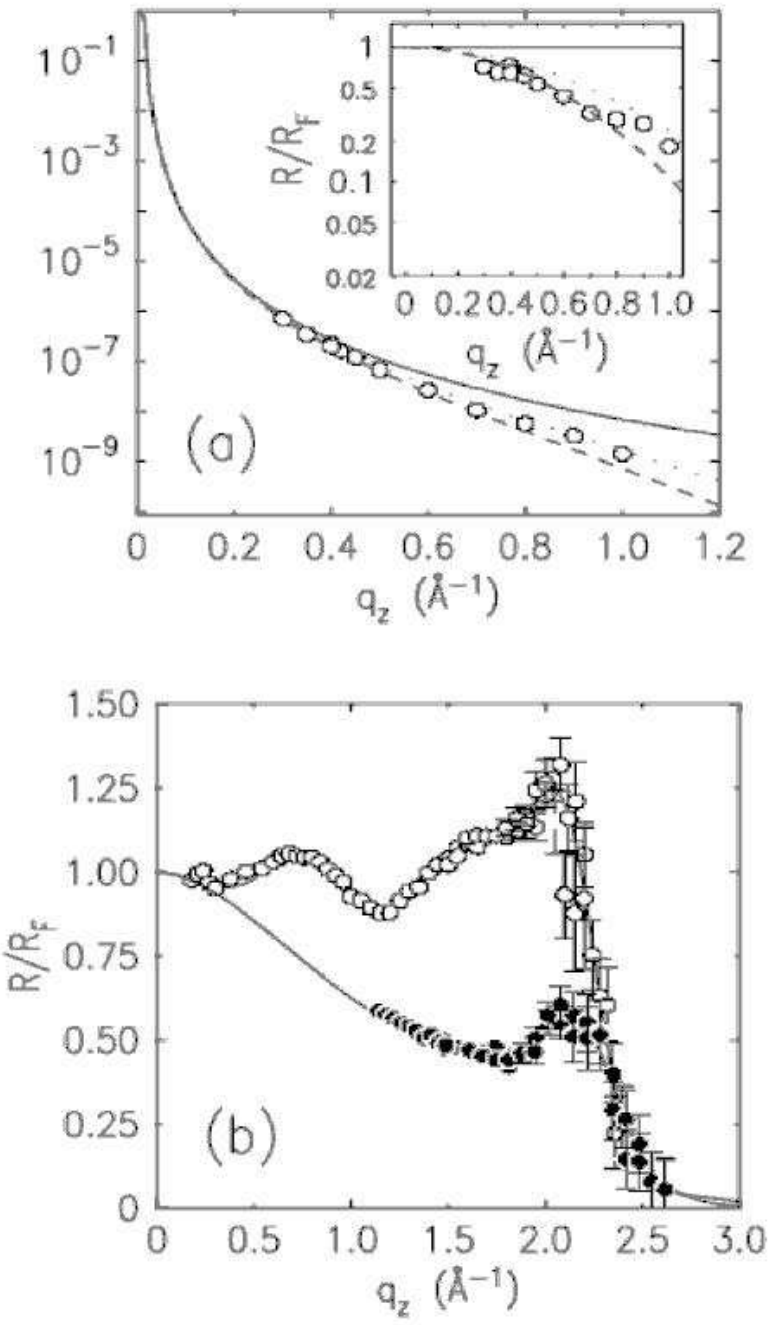



Figure 11.2: (a) X-ray reflectivity from a $K_{80}Na_{20}$ alloy measured by integrating over a large range of $\alpha$ at fixed $\alpha + \beta$. The normalized reflectivity is shown in the inset. The dotted lines show a capillary wave roughness with no layering with $\sigma = 1.2$ $\mathring{A}$ and 1.5 $\mathring{A}$, respectively. (b) Normalized x-ray reflectivity of liquid In (+170°C, closed circles) and In-22at %Bi (80 °C, open circles).

is in contrast to well-defined surface layering peaks observed for Ga, Hg or In (see Fig. 11.1(b))[12].

### 11.3.2 Bi-In

For systems having significant attractive interactions between unlike atoms, the surface structure is more complex. This is especially true of alloys such as Bi-In which form well-ordered intermetallic phases in the bulk solid. In Fig. 11.2(b) we show the normalized reflectivity for the eutectic composition $Bi_{22}In_{78}$, measured at 80°C ($\triangle$) along with the normalized reflectivity for liquid In at +170°C. The alloy exhibits a well defined layering peak centered at 2.0 $Å^{-1}$ which resembles the layering peak found for pure In (**smudges**). In addition, the reflectivity displays a modulation with a period of about 0.9 $Å^{-1}$. This foscillation indicates that ordering over a short region at the surface occurs with a length scale nearly twice that of the longer-range layering. This suggests the presence of Bi-In pairs at the surface. A full report on the phase behavior of three different In-Bi alloys will be given elsewhere[12].

### 11.3.3 Ga-Bi

The Ga-Bi system is an example of an alloy with repulsive heteroatomic interactions leading to a bulk miscibility gap. Below the monotectic temperature, $T_{mono} = 222$°C, a Ga-rich liquid coexists with a solid Bi phase[13]. However, due to its lower surface energy a Bi monolayer is expected to segregate at the surface of the Ga-rich liquid. Above $T_{mono}$, Ga-Bi exhibits a thick wetting film, as predicted for all binary mixtures with critical demixing[14]. This transition occurs at a characteristic wetting temperature $T_w$ below the critical temperature $T_{crit}$[13]. Above $T_w$, a macroscopically

thick Bi-rich phase is expected to completely wet the less dense Ga-rich phase in defiance of gravity. The Bi concentration in the Ga-rich phase increases with increasing temperature as long as the Ga-rich liquid coexists with the solid Bi phase.

The normalized x-ray reflectivity spectra, $R/R_F$, for Ga-Bi at 35°C and 228°C are shown in Fig. 11.3(a) versus $q_z$, along with the profile for pure Ga at room temperature. At 35°C the normalized reflectivity has a broad maximum at $q_z \approx 1$ Å$^{-1}$. As suggested by Lei et al.[7], this is consistent with a density profile with a thin, high density monolayer of Bi.

We have fit the reflectivity profiles to simple density profiles using Eq. (1). The fitted reflectivities are shown in Fig. 11.3(a) (solid lines). At +35°C the local density profile exhibits a top-layer density which is about 1.5 times higher than the Ga bulk liquid density. The $3.4 \pm 0.2$ Å layer spacing between the surface and the adjacent Ga layer obtained from the fits is much larger than the $2.5 \pm 0.1$ Å layer spacing obtained in liquid gallium. The data show that the surface layer has a higher density than in the underlying Ga-rich subphase, confirming the surface segregation of a Bi monolayer.

The behavior of the same alloy at 228°C is markedly different: a sharp peak in $R(q_z)$ has emerged, centered around 0.13 Å$^{-1}$ (Fig. 11.3(a)). The peak at small $q_z$ indicates the presence of a thick surface layer with a density greater than that of the bulk subphase. The absence of additional oscillations following the sharp peak suggests that the boundary between the two regions must either be diffuse or rough. The persistence of the broad maximum at $q_z \approx 0.75$ Å$^{-1}$ indicates that Bi monolayer segregation coexists with the newly formed nanoscale wetting film. Fits to a simple two-box model yield a film thickness of 30 Å consistent with ellipsometry results[13],

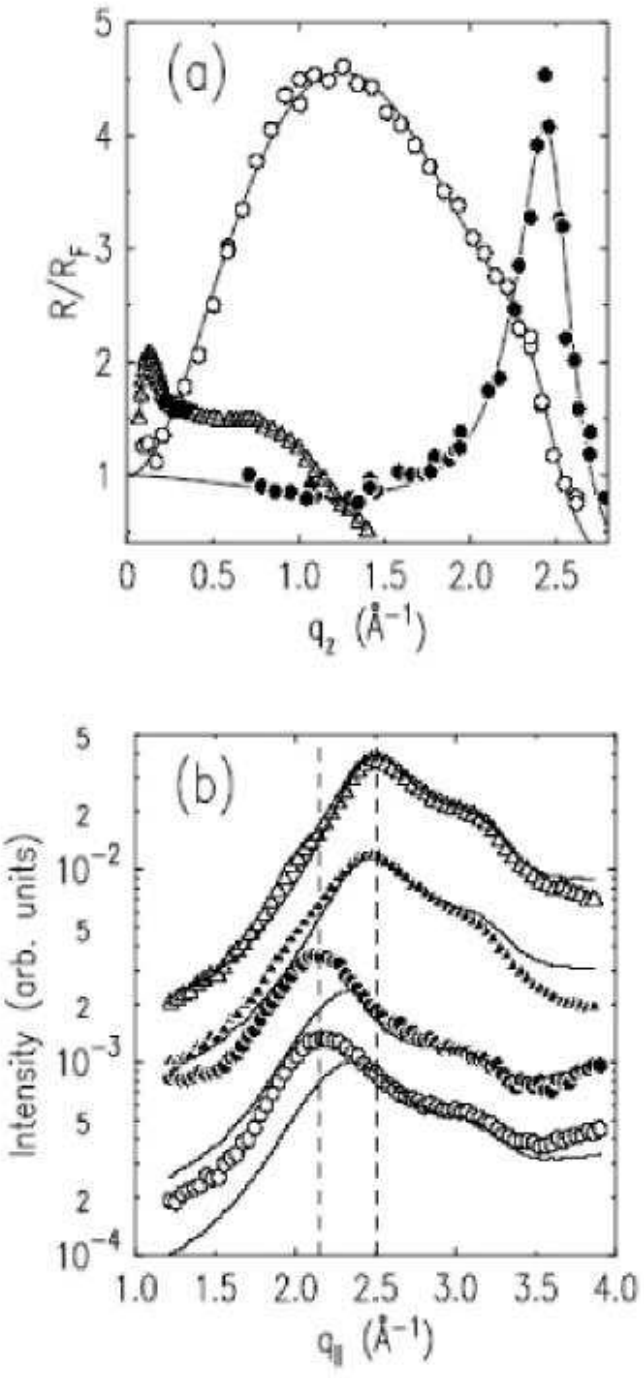



Figure 11.3: (a) Normalized x-ray reflectivity of liquid Ga (+25°C, ∘), and on the Ga-Bi two-phase coexistence curve at 35°C (•) and 228°C. (b)Grazing incidence diffraction from Ga-Bi at 150°C (filled triangles), 205°C (△), 228°C, and 255°C at $\alpha = 0.08°$. The solid line shows corresponding profiles for $\alpha = 0.30°$ where the bulk is predominately sampled. The data was acquired using Soller slits, 0.05 $\AA^{-1}$ FWHM. Still, it was not possible to reliably subtract the background.

and a surface density consistent with the high density liquid phase of the bulk alloy. The temperature dependent reflectivity will be reported elsewhere[12].

In Fig. 11.3(b) GID data are shown from the same Ga-Bi alloy in the temperature range from 150 to 255°C. Data at 35°C was previously reported[10]. In the liquid Ga-rich phase the Bi concentration ranges from 3.3 at% to 17.8at%. At each temperature data was taken above and below $\alpha_{crit} = 0.14°$ at $\alpha = 0.08°$ (symbols) and at $\alpha = 0.30°$(lines). At $\alpha = 0.08°$ the x-ray penetration depth equals 28 $\mathring{A}$ or about 10 atomic layers.

The solid lines in Fig. 11.3(b) at 150 °C show the bulk liquid scattering which is predominately from pure Ga since the Bi concentration is low. The broad peak at $q_{\|} = 2.5$ Å$^{-1}$ and the shoulder on the high-angle side of the peak are in agreement with the bulk liquid Ga structure factor[15]. There is no evidence for a peak or shoulder at the position corresponding to the first peak of the Bi liquid structure factor at $q_{\|} \approx 2.2$ Å$^{-1}$. This is expected since the surface regime is so much smaller than the bulk volume sampled. For $\alpha = 0.08° < \alpha_c$, the x-rays penetrate to a depth of only about 30 Å. Here a shoulder appears on the low-$q$ side of the gallium liquid peak, due to enhanced sensitivity to the Bi surface monolayer. Between 150°C and 205°C (•) there is little change in the GID data, except a slight increase in the shoulder associated with the Bi monolayer.

Above $T_{mono}$ there is a dramatic change in the GID profiles. In Fig. 11.3(b), GID data is shown at 228°C and 255°C. In both cases, for $\alpha > \alpha_c$ the peak has shifted to $q_{\|} \approx 2.3$ Å$^{-1}$ from the 2.5 Å$^{-1}$ peak position found at lower temperatures. This results from the much higher Bi concentration in the bulk at the higher temperatures and the larger atomic size of Bi. Even more dramatic is the shift in the peak position

for $\alpha < \alpha_{crit}$ where the peak is at 2.15 $\text{Å}^{-1}$. Thus, the surface region contains considerably more Bi than the underlying bulk alloy. This finding is consistent with the wetting layer observed in the x-ray reflectivity measurements.

# Bibliography


[1] S. A. Rice, J. Non-Cryst. Solids **205-207** (1996) 755 and references therein.

[2] L. Bosio, R. Cortes, A. Defrain and M. Oumezine, J Non-Cryst. Sol. **61 & 62** (1984) 697.

[3] O. M. Magnussen, B. M. Ocko, M. J. Regan, K. Penanen, P. S. Pershan, and M. Deutsch, Phys. Rev. Lett. **74** (1995) 4444; E. DiMasi, H. Tostmann, B. M. Ocko, P. S. Pershan, and M. Deutsch, Phys. Rev. B **58** (1998) R13419.

[4] M. J. Regan, E. H. Kawamoto, S. Lee, P. S. Pershan, N. Maskil, M. Deutsch, O. M. Magnussen, B. M. Ocko, and L. E. Berman, Phys. Rev. Lett. **75** (1995) 2498; M. J. Regan, P. S. Pershan, O. M. Magnussen, B. M. Ocko, M. Deutsch, and L. E. Berman, Phys. Rev. B **54** (1996) 9730.

[5] P. Eisenberger, W. C. Marra, Phys. Rev. Lett. **46**, 1081 (1981).

[6] H. Tostmann, E. DiMasi, O. G. Shpyrko, P. S. Pershan, M. Deutsch, and B. M. Ocko, Phys. Rev. B **59**, 783 (1999).

[7] N. Lei, Z. Huang, and S. A. Rice, J. Chem. Phys. **104** (1996) 4802.

[8] N. Lei, Z. Huang, and S. A. Rice, J. Chem. Phys. **107** (1997) 4051.

[9] M. J. Regan, P. S. Pershan, O. M. Magnussen, B. M. Ocko, M. Deutsch, and L. E. Berman, Phys. Rev. B **55** (1997) 15874.

[10] H. Tostmann, E. DiMasi, O. G. Shpyrko, P. S. Pershan, B. M. Ocko, and M. Deutsch, Ber. Bunsenges. Phys. Chem. **102** (1998) 1136.

[11] Because the sample surface was curved, these measurements required an integration over a range of $\alpha$ at each $q_z$ point.

[12] E. DiMasi, H. Tostmann *et al*, in preparation.

[13] D.Nattland, S.C.Müller, P.D.Poh and W.Freyland, J.Non-Cryst. Solids **205–207** (1996) 772.

[14] J.W.Cahn, J.Chem.Phys. **66** (1977) 3667.

[15] A. H. Narten, J.Chem.Phys. **56** (1972) 1185.

# Chapter 12

# Surface studies of liquid Hg/Au alloys

## 12.1 Abstract

In this chapter we present temperature dependent x-ray reflectivity measurements of liquid Hg alloyed with 0.06–0.20at% Au. At low Au concentrations, we find temperature dependent surface induced layering similar to that observed in pure Hg, except that the presence of Au reduces the layering amplitude. Upon approaching the solubility limit of Au in Hg, a new surface phase forms which is 1–2 atomic diameters thick and has a density of about half that of bulk Hg. We present a surface phase diagram, summarizing the evolution of this unexpected surface structure through comparatively small changes in temperature and composition. Possible implications for altering the electronic structure for control of catalytic and electrochemical reactions at the liquid metal surface are discussed.

## 12.2 Introduction

Mercury and gold are among the few metals that can be found in their native state in nature, and that were known to early civilizations.[1] The use of Hg to extract Au and Ag from their ores, known as amalgamation, is one of the earliest metallurgical processes known to humanity.[2] It is therefore no surprise that Hg-Au amalgams have captured the interest of alchemists, metallurgists, chemists, physicists, and dentists.[3] Hg and Au are both transition metals having a filled *d*-band, of similar atomic size, and they form a variety of stable intermetallic phases in the solid state.[4] The low cohesive energy of Hg, evident from its low melting point of $-38.9°C$, enables these amalgams to form readily, simply by bringing Au into contact with liquid Hg under ambient conditions.

Despite a prevailing interest in Hg-Au amalgams, not many detailed structural studies of Hg-Au compounds have been performed. It proves very difficult to establish the Hg-Au phase diagram due to the high volatility of Hg, which requires the use of sealed tubes at undetermined pressures for Hg-rich alloys.[4] Much recent work has focussed on surfaces of Hg-Au amalgams. For example, microscopy and spectroscopy studies have addressed the morphology and composition of Hg-Au phases formed by depositing Hg onto Au films.[5,6,7] These studies are complicated by the morphology of the Au substrate, and the coexistence of several Hg-Au phases in the amalgam.[7] Deposition of Hg onto Au electrodes has also been studied through electrochemical techniques.[8] In-situ surface x-ray diffraction measurements of underpotential deposition of Hg onto the crystalline Au(111) electrode have revealed that amalgamation occurs in several steps, characterized by distinct surface phases.[8] Since some of these phases are modified by coadsorbed anions from the electrolyte, and since kinetic

effects produce further complications, it is difficult to obtain basic structural information about the solid Hg-Au amalgam through such studies.

In light of the knowledge about Hg-Au phase formation, it is surprising that Au was once regarded as an "inert" material that could be used as part of a liquid Hg electrode in electrochemical studies.[9] However, it was soon recognized that the potential of the amalgam electrode differed from that of pure Hg. A more interesting observation was that small amounts of Au dissolved into the Hg droplet can strongly affect the electrochemical behavior by forming intermetallic compounds with other dilute metals such as Cd and Zn that are present in the liquid Hg.[9] Dilute metal impurities in liquid Hg have also been observed to affect the activation energies of reactions catalyzed by the liquid metal surface.[10] It is not known whether such effects are due to changes in the electronic properties of liquid Hg, modification of the surface structure, or the formation of intermetallic phases at the surface.

Until very recently, atomic-scale structural measurements on liquid metal surfaces have not been available, leaving such questions unresolved. It is now known that a wide variety of structures form at the surfaces of liquid metals and alloys. Elemental Hg, Ga and In exhibit surface induced layering, in which atoms are stratified parallel to the liquid–vapor interface,[11,12,13,14,15] a result long predicted by theory.[16] This stratification of atoms, with the corresponding oscillatory surface-normal density profile, is shown schematically in Figure 12.1. In liquid metal alloys, surface layering may compete with the formation of surface phases, making the structure more complex. Prominent examples are the monolayer surface segregation observed in Ga-In[17] and Ga-Sn[18], and a concentration dependent wetting transition in Ga-Bi.[19] In all these cases, surface layering persists in the alloys, but is modified to varying extents

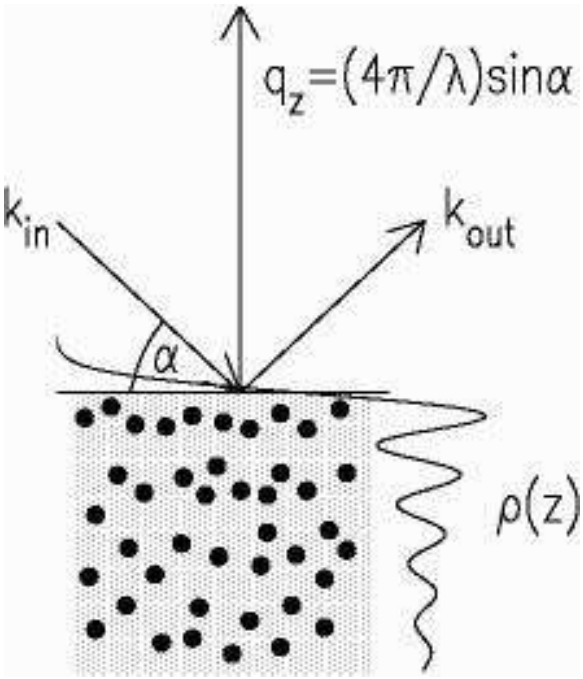



Figure 12.1: Geometry for x-ray reflectivity from a layered liquid metal surface. Maxima in the oscillatory surface-normal density profile $\rho(z)$ correspond to layers of atoms parallel to the liquid–vapor interface.

by the surface phase. Competition between layering and surface phase formation is expected to be particularly important for systems such as Hg-Au, where attractive heteroatomic interactions dictate the formation of intermetallic phases in the bulk solid. Such well ordered phases in the solid typically give way upon melting to homogeneous mixtures in the bulk liquid. However, one may expect that the region close to the liquid–vapor interface, where order is induced in elemental liquid metals, may support the formation of intermetallic phases in the liquid alloy. Structural information for such systems is of fundamental interest, and may well shed light on reactions occuring at liquid alloy surfaces, relevant to catalysis or electrochemistry.

In this paper we report x-ray reflectivity measurements of liquid Hg-Au alloys near the room temperature saturation limit[4,20] of 0.14 atomic(at)% Au in Hg, at

temperatures between +25°C and −39°C. We construct a temperature–concentration surface phase diagram and identify two distinct regions of surface phase behavior. At high $T$ and low Au concentrations, surface layering similar to that of pure Hg is observed. By contrast, at low $T$ and comparatively higher Au concentrations, we find evidence for the formation of a more complicated surface phase, where a new length scale for surface layering emerges along with a low-density layer at the interface.

## 12.3 Experimental Details

X-ray reflectivity measurements were carried out using the Harvard–BNL liquid surface spectrometer at beamline X22B at the National Synchrotron Light Source, with an x-ray wavelength of 1.24 Å and a detector resolution of $\Delta q_z = 0.035$ Å$^{-1}$ within the reflection plane. The background intensity, due mainly to scattering from the bulk liquid, was subtracted from the specular signal by displacing the detector out of the reflection plane. The design of the liquid spectrometer[21] and a review of the measurement technique[22] are given elsewhere.

Samples with nominal concentrations of 0.06, 0.10, 0.13 and 0.20at% Au were produced by adding Au powder (Johnson Matthey, 20 mesh, 99.9995%) to liquid Hg (Bethlehem Apparatus Company, quadruple distilled, 99.9999%), several days or weeks before the x-ray experiments. The main experimental problem in surface measurements of metals is to ensure that a contaminant-free surface is obtained. The most reliable way to produce atomically clean metal surfaces is to keep them under ultra high vacuum (UHV) conditions, and to remove any residual oxide through argon ion sputtering. These UHV techniques, which we found to be very successful for x-ray scattering measurements of Ga, In, and low vapor pressure alloys,[13,15,19] must

be modified in the case of Hg and its alloys due to the high vapor pressure of Hg ($\sim 10^{-2}$ Torr at room temperature). For the measurements presented here, each sample was poured into a stainless steel reservoir within an argon-filled glove box ($< 5$ ppm oxygen, $< 2$ ppm water). The reservoir is connected to a stainless steel valve, filling capillary, and UHV flange and is affixed to a UHV compatible chamber. The empty chamber is evacuated to $10^{-7}$ Torr and baked out, after which the liquid Hg alloy is dropped from the reservoir through the valve and capillary into a ceramic sample pan within the chamber, as was done previously for measurements of pure Hg.[12] Immediately after opening the valve to the reservoir, the Hg vapor pressure determines the total pressure in the chamber, while the partial pressures of possible contaminants such as water and oxygen remain very low. The resulting liquid alloy surfaces were found to be stable for over a week, due to two mechanisms. First, Hg oxide introduced from pouring the sample is unstable and decomposes under these low oxygen partial pressures.[23,24] In addition, slight but continual evaporation constantly refreshes the surface.[25] Preliminary reflectivity measurements utilizing a glass sample chamber evacuated to $10^{-4}$ Torr and backfilled with dry hydrogen gas were qualitatively similar, but not sufficiently reproducible.

The samples were cooled with a liquid nitrogen cold finger beneath the sample pan. Temperatures were monitored at the sample pan and calibrated to that of the liquid surface in separate experiments using thermocouples immersed in the samples. The calibration has an uncertainty of $\pm 1^{\circ}$C.

## 12.4 X-ray Reflectivity and Modelling

X-ray reflectivity is a powerful technique for investigating structure normal to surfaces and interfaces on atomic length scales.[22,26,27,28] In these measurements, the scattered intensity is measured as a function of momentum transfer $q_z = k_{\rm out} - k_{\rm in}$ perpendicular to the surface (Figure 12.1) and normalized to the incident photon intensity.

The simplest interface is a step function describing a sharp truncation of a homogeneous bulk density $\rho_\infty$ (Fig 12.2(a)i, solid line). Scattering from this sharp interface takes the form of the Fresnel reflectivity

$$R(q_z) = \left[ \frac{q_z}{q_c} + \sqrt{\left(\frac{q_z}{q_c}\right)^2 - 1} \right]^{-4} \equiv R_F \, . \tag{12.4.1}$$

In this expression $R_F$ depends on the bulk density through the critical wavevector $q_c = \sqrt{16\pi\rho_\infty r_0}$, where $r_0 = e^2/mc^2 = 2.82 \times 10^{-5}$ Å is the classical electron radius, and absorption has been neglected. Additional structure in the surface-normal density profile $\rho(z)$ modifies the reflectivity from the Fresnel form. When the scattered intensity is much less than the incident intensity (generally the case as long as $q_z \gtrsim 5q_c$), the kinematic approximation is valid and the reflectivity may be written

$$R(q_z) = R_F \left| \frac{1}{\rho_\infty} \int_{-\infty}^{\infty} (\partial\rho/\partial z) \exp(iq_z z) dz \right|^2 \, . \tag{12.4.2}$$

Since the phase information is not accessible to the experimental intensity measurement, Eq. 12.4.2 can not be inverted to determine the density profile directly. For this reason the usual practice is to construct a model density profile and compare its calculated reflectivity to the experiment. Because of this phase problem, distinct structural models can produce essentially identical reflectivity curves, lending some ambiguity to the analysis.

The simplest physically reasonable modification of the step function profile takes surface roughness into account. In a liquid, thermally excited capillary waves produce height variations across the surface, which are averaged in the scattering measurement over length scales determined by the resolution of the spectrometer. These occur in addition to any roughness intrinsic to the local surface-normal profile. Detailed discussions of the effect of capillary waves on the scattering cross section are given elsewhere.[15,21] The capillary wave roughness $\sigma_{cw}$ is a function of the temperature $T$ and the surface tension $\gamma$, and is given by

$$\sigma_{cw}^2 = \frac{k_B T}{2\pi\gamma} \ln\left(\frac{q_{\max}}{q_{\rm res}}\right) . \tag{12.4.3}$$

This expression has been arrived at by integrating over those capillary modes having wavevectors less than $q_{\max} = \pi/a$, where $a$ is the atomic diameter, and greater than $q_{\rm res}$, determined by the instrumental resolution.[29]

We will consider a more general broadening of the density profile, by $\sigma_T^2 = \sigma_{cw}^2 + \sigma_i^2$, to incorporate the capillary wave roughness $\sigma_{cw}$ along with any other roughness $\sigma_i$ intrinsic to the surface. This profile, having

$$\partial\rho/\partial z = \exp(-\sigma_T^2 z^2/2) ,$$

is shown by dashed lines in Figure 12.2(a)i for $\sigma_T = 1.0$ Å. The density profile can be written in terms of the error function:

$$\rho(z) = (\rho_\infty/2)\left[\mathrm{erf}(z/\sigma_T\sqrt{2}) + 1\right] \equiv \rho_{\rm erf}(z) , \tag{12.4.4}$$

yielding for the reflectivity

$$R = R_F \exp(-q_z^2\sigma_T^2) . \tag{12.4.5}$$

The resulting Fresnel-normalized reflectivity is shown in Figure 12.2(b)i, dashed line. The exponential factor in Eq. 12.4.5) is analogous to the Debye-Waller term used

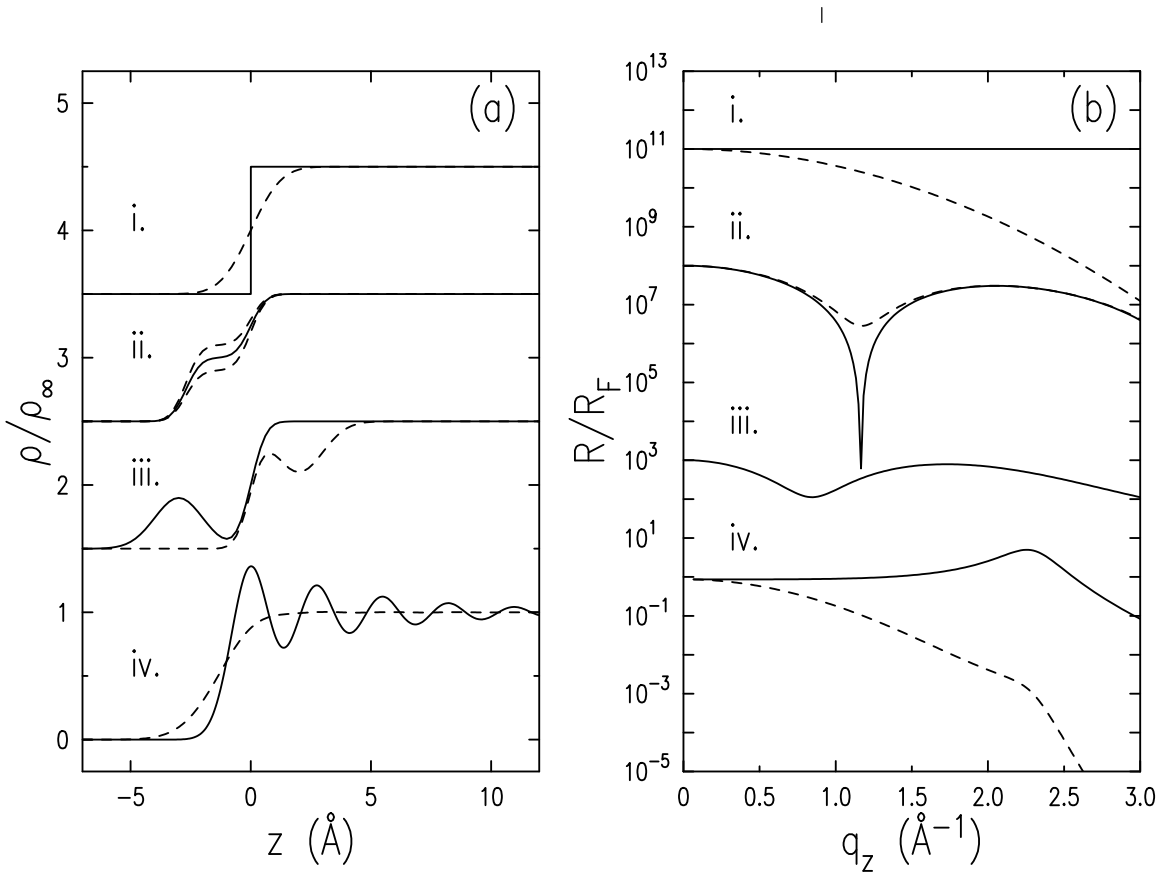



Figure 12.2: (a) Model density profiles and (b) corresponding Fresnel-normalized reflectivities as described in text. Curves i–iii in both panels are shifted for clarity.

to describe the reduction of the diffracted intensity from crystals due to thermal displacements of the atoms from the lattice sites.

When more complicated surface-normal density profiles must be constructed, two straightforward methods are commonly used. Regions of differing electron density can be represented by a combination of error functions, parameterizing the thickness, density, and roughness between each region. A general profile of this type may be written

$$\rho(z) = \sum_{n=0}^{N} \left( \frac{\rho_n - \rho_{n+1}}{2} \right) \left[ \mathrm{erf}\left( \frac{z - z_n}{\sigma_n \sqrt{2}} \right) \right] , \tag{12.4.6}$$

with $\rho_0$ equal to the bulk density $\rho_\infty$, $\rho_{N+1} = 0$ representing the vapor, and $\sigma_n$ describing the broadening between regions $n$ and $n+1$ at position $z_n$. The reflectivity for this model is

$$R/R_F = \left| \sum_{n=0}^{N} \left( \frac{\rho_n - \rho_{n+1}}{\rho_\infty} \right) \left[ \exp(-q_z^2 \sigma_n^2/2 + i q_z z_n) \right] \right|^2 . \tag{12.4.7}$$

Figure 12.2(a)ii shows three such profiles, having one additional slab of density between the vapor and the bulk liquid. Here $\sigma_0 = \sigma_1 = 0.5$ Å and $|z_1| = 2.7$ Å. With the same roughness for both interfaces, the reflectivity at $q_z = \pi/|z_1|$ has an amplitude proportional to $(1 - 2\rho_1/\rho_0)^2$. When $\rho_1/\rho_0 = 1/2$ (Figure 12.2 (a)ii, solid line), the result is total destructive interference at $q_z = \pi/|z_1|$, producing a deep notch in the reflectivity (Figure 12.2(b)ii, solid line). For values of $\rho_1$ symmetrical about 1/2, identical reflectivity curves are obtained. Dashed lines in Figure 12.2(a)ii show profiles having $\rho_1/\rho_0 = 0.4$ and 0.6, which both produce the reflectivity curve shown as a dashed line in Figure 12.2(b)ii. This is an example of the unavoidable ambiguity in interpreting reflectivity measurements even for simple models.

An additional method of constructing a structured surface profile is to define density through Gaussian functions, as shown in Figure 12.2(a)iii. For the example

shown,

$$\rho(z) = \rho_{\rm erf} + \frac{h_g/\sigma_g}{\sqrt{2\pi}} \exp\left[-(z-z_g)^2/2\sigma_g^2\right] \tag{12.4.8}$$

and

$$R/R_F = \left| \left[\exp(-q_z^2\sigma_T^2/2)\right]^2 + \frac{h_g}{\rho_\infty} q \exp(-q_z^2\sigma_g^2/2) \exp\left[i(q_z z_g - \pi/2)\right] \right|^2 . \tag{12.4.9}$$

The Gaussian position $z_g$ and the sign of its amplitude $h_g$ enter only in the cross term of Eq. 12.4.9, which is proportional to $h_g \sin(q_z z_g)$. For this reason, the reflectivity measurement does not distinguish between a positive Gaussian density added to the vapor side at position $z = z_g$ (Figure 12.2(a)iii, solid line) and density subtracted from the liquid side at $z = -z_g$ (Figure 12.2(a)iii, dashed line). These two rather different looking density profiles both produce the reflectivity curve shown in Figure 12.2(b)iii. The effect of this Gaussian term can be similar to that of a shelf of density: both produce a minimum in the reflectivity at low $q_z$, as shown by comparison of Figure 12.2(b)iii and Figure 12.2(b)ii, dashed line.

The models discussed so far describe a liquid–vapor interface having structure near the surface. To describe the surface induced layering of liquid metals, which extends further into the bulk, a damped oscillatory surface-normal density profile must be constructed. A convenient way to do this is to model layers of atoms parallel to the surface by a series of Gaussian terms, representing mean-squared displacements of atoms assigned to each layer at spacing $d$:

$$\rho(z) = \rho_\infty \sum_{n=0}^{\infty} \frac{d/\sigma_n}{\sqrt{2\pi}} \exp\left[-(z-nd)^2/2\sigma_n^2\right] . \tag{12.4.10}$$

With the choice of $\sigma_n^2 = \sigma_T^2 + n\overline{\sigma}^2$, we parameterize two effects in a simple way. First, the surface layers become less well defined with increasing depth into the bulk liquid, at a rate controlled by $\overline{\sigma}$. Second, the effect of increasing $\sigma_T$ is to reduce the

overall layering amplitude, an effect expected both from capillary waves and from any roughness intrinsic to the local surface-normal profile.

The corresponding reflectivity is given by

$$R/R_F = [F_Z(q_z)]^2 \, (q_z d)^2 \exp(-\sigma_T^2 q_z^2) \left[1 - 2\exp(-q_z^2\overline{\sigma}^2/2)\cos(q_z d) + \exp(-q_z^2\overline{\sigma}^2)\right]^{-1} \ . \tag{12.4.11}$$

Since each Gaussian now explicitly represents a collection of scattering atoms, here it is meaningful to incorporate the reduced atomic form factor $F_Z(q_z) = [f_Z(q_z) + f'_Z]/Z$ for atoms having atomic number $Z$.[30] Figure 12.2(a)iv (solid line) illustrates a layered profile with $d = 2.7$ Å, $\sigma_T = 0.8$ Å, and $\overline{\sigma} = 0.45$ Å. The reflectivity (Figure 12.2(b)iv, solid line) shows the broad quasi–Bragg peak produced by the oscillatory density profile. In the limit where $\sigma_T$ is large, the profile approaches the error function form, though with its argument shifted from $z = 0$ to $z = -d/2$ due to the choice of origin in Eq. 12.4.10. A layered profile having $\sigma_T = 1.5$ Å is shown by dashed lines in Figure 12.2(a)iv. Although the intensity falls off quickly for large $q_z$ (Figure 12.2(b)iv, dashed line), constructive interference in the region of the layering peak is still evident.

Finally, this profile can be modified by additional Gaussian terms, and by changing the amplitudes, positions and widths of the terms in Eq. 12.4.10. The most general model that we will present in this study takes the form

$$\rho(z)/\rho_\infty = \left(\frac{w_A d}{\sigma_A\sqrt{2\pi}}\right) \exp\left[-(z - z_A)^2/\sigma_A^2\right] + \sum_{n=0}^{\infty}\left(\frac{w_n d}{\sigma_n\sqrt{2\pi}}\right) \exp\left[-(z - nd)^2/\sigma_n^2\right] \ , \tag{12.4.12}$$

where the Gaussian scaled by $w_A$ is typically much broader than those controlled by $\sigma_n$ in the sum, and $w_n$ may deviate from unity. Since the effect of the extra Gaussian is similar to that of the Gaussian plus error function model described by Eq. 12.4.8, placing this term into the vapor side of the interface has an effect which

can be difficult to distinguish from that of decreasing the weights $w_n$ of the first few terms in the sum.

## 12.5 Experimental Results

Distinctly different reflectivities are obtained depending on whether the Au concentration exceeds the solubility limit. The solubility of Au in Hg is plotted as a function of temperature in Figure 12.3 (open circles; the shaded band is a guide for the eye).[20,31] Normalized reflectivity curves are shown for a selection of temperature and concentration points, identified by small crosses on the graph. All $R/R_F$ curves are shown on a log scale with ranges identical to those shown for 0.13at% Au, $-18$°C. This phase diagram provides an overview of our results, which will be discussed in more detail further below.

At low Au concentrations and high temperatures (upper right region of Figure 12.3), the reflectivity is characterized mainly by the layering peak at $q_z \approx 2.2$ Å$^{-1}$. These reflectivity data are shown in Figure 12.4. Solid lines are fit curves that will be described in the Discussion section. At the lowest Au concentration, 0.06at% Au, the reflectivity is very similar to that of pure Hg. As for Hg, the effect of increased temperature is to monotonically reduce the amplitude of the interference peak, from +25°C down to the lowest temperature measured, $-26$°C. The data are consistent with scattering from a layered liquid metal surface, where thermal excitations partially disrupt the layering. For 0.10at% Au in Hg, comparable behavior is observed at +25°C and +5°C. On cooling further to $-13$°C, however, the amplitude of the layering peak decreases, showing that surface layering is being suppressed at lower temperatures. The reflectivity in the region $q_z \sim 0.3$–$1.0$ Å$^{-1}$ also changes with $T$,

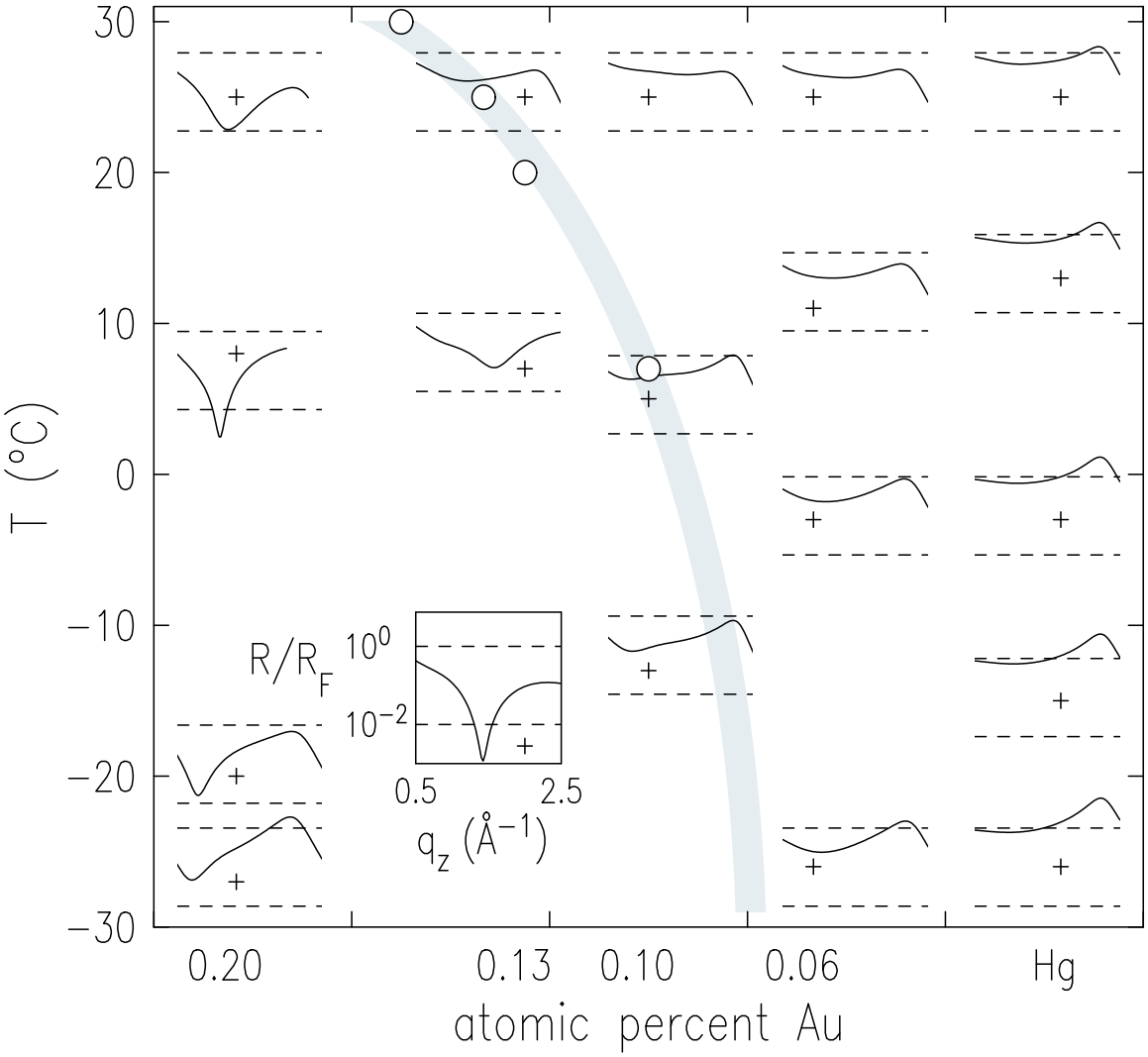



Figure 12.3: Surface phase diagram for liquid Hg-Au alloys, with nominal Au concentrations from 0–0.20% and at temperatures between −28 and +25°C indicated by crosses (+). $R/R_F$ curves are shown on semilog scales, all with identical axes as marked for the 0.13%, −18°C alloy. (∘): Reported solubility limit of Au in Hg. The shaded band is a guide for the eye.

unlike the case of the more dilute alloy. This means that the structure within 2 Å or so of the interface, which for pure Hg and for Hg 0.06at% Au is temperature independent, is being modified by $T$ at the higher concentration of 0.10at% Au. The behavior of the 0.10at% alloy in this temperature range marks the transition between viability of the surface layering, which is enhanced at lower temperatures, and the formation of a competing surface structure. Similarly, the reflectivity from Hg 0.13at% Au can only be described by a simple surface layering model at room temperature, and at lower temperatures is substantially different.

Data from the low temperature, Au-rich phase (bottom left region in Figure 12.3) are qualitatively different. For 0.13at% Au in Hg, below room temperature, the reflectivity exhibits a deep minimum, which shifts with decreasing temperature, from $q_z \approx 1.6$ at $+7°$C to $q_z \approx 1.4$ Å$^{-1}$ at $-67°$C (Figure 12.5). The position and depth of this minimum suggest the formation of a surface region having about half the density of the bulk, which is about one atomic diameter thick and which grows slightly thicker at lower temperatures. This trend with temperature is confirmed more dramatically in reflectivity measurements of 0.20at% Au in Hg, where the Au concentration exceeds the solubility limit at all temperatures. The notch in the reflectivity is present at room temperature, and shifts in $q_z$ from 1.3 Å$^{-1}$ at room temperature to 0.6 Å$^{-1}$ at $-27°$C (Figure 12.5(c)).

Even more interesting, at the lowest temperatures a new layering peak has appeared, at measurably smaller $q_z$ than that of Hg. At these two highest Au concentrations, temperature cycling results in hysteresis and long equilibration times. After cooling the 0.13at% alloy to nearly the melting point, approximately ten hours at room temperature were required to reproduce the reflectivity. With 0.20at% Au, the

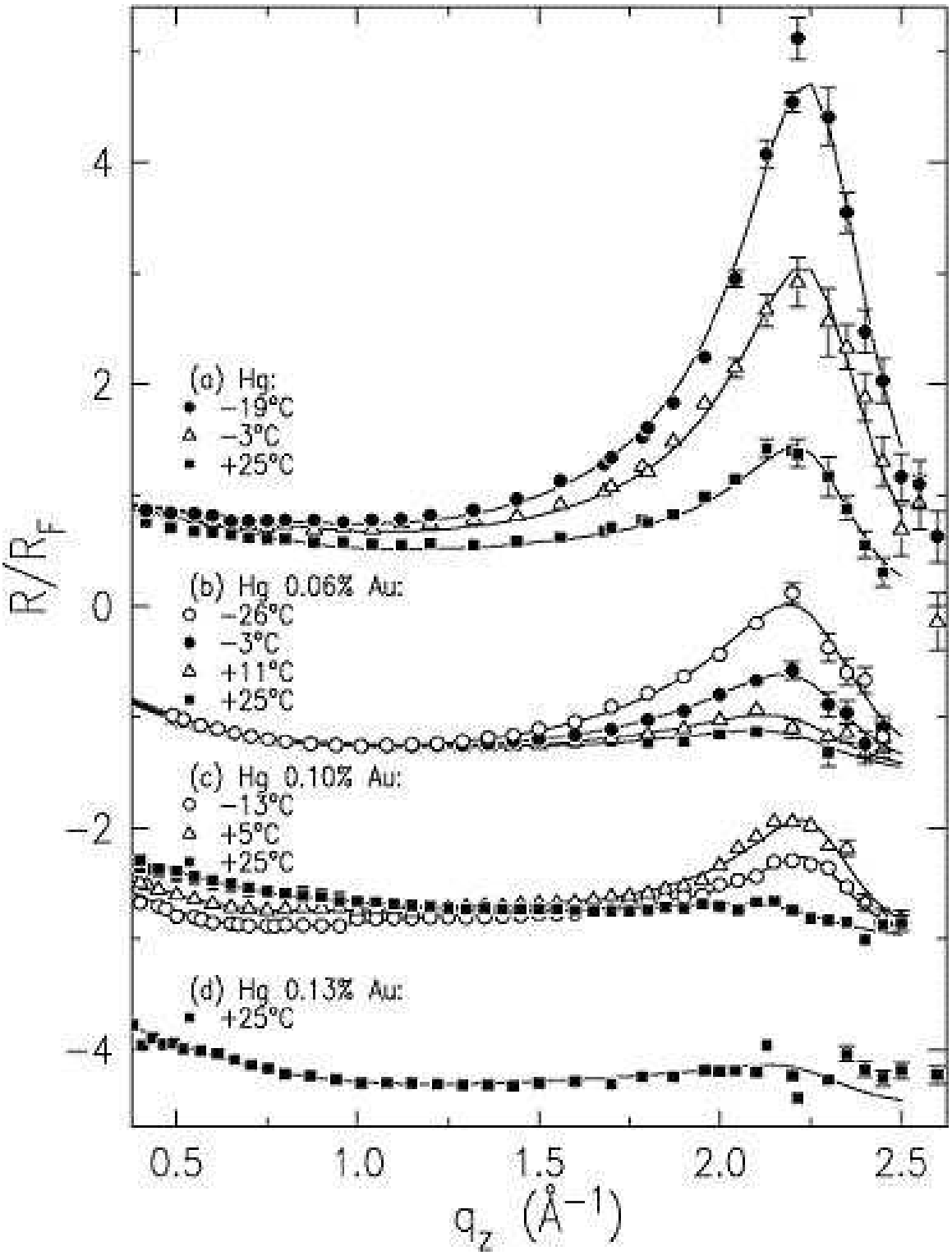



Figure 12.4: Fresnel-normalized reflectivity of (a) Hg 0.06at% Au and (b) Hg 0.10at% Au at all measured temperatures, and (c) Hg 0.13at% Au at room temperature. The curves for 0.10at% and 0.13at% alloys are shifted for clarity. Solid lines are fits as discussed in text.

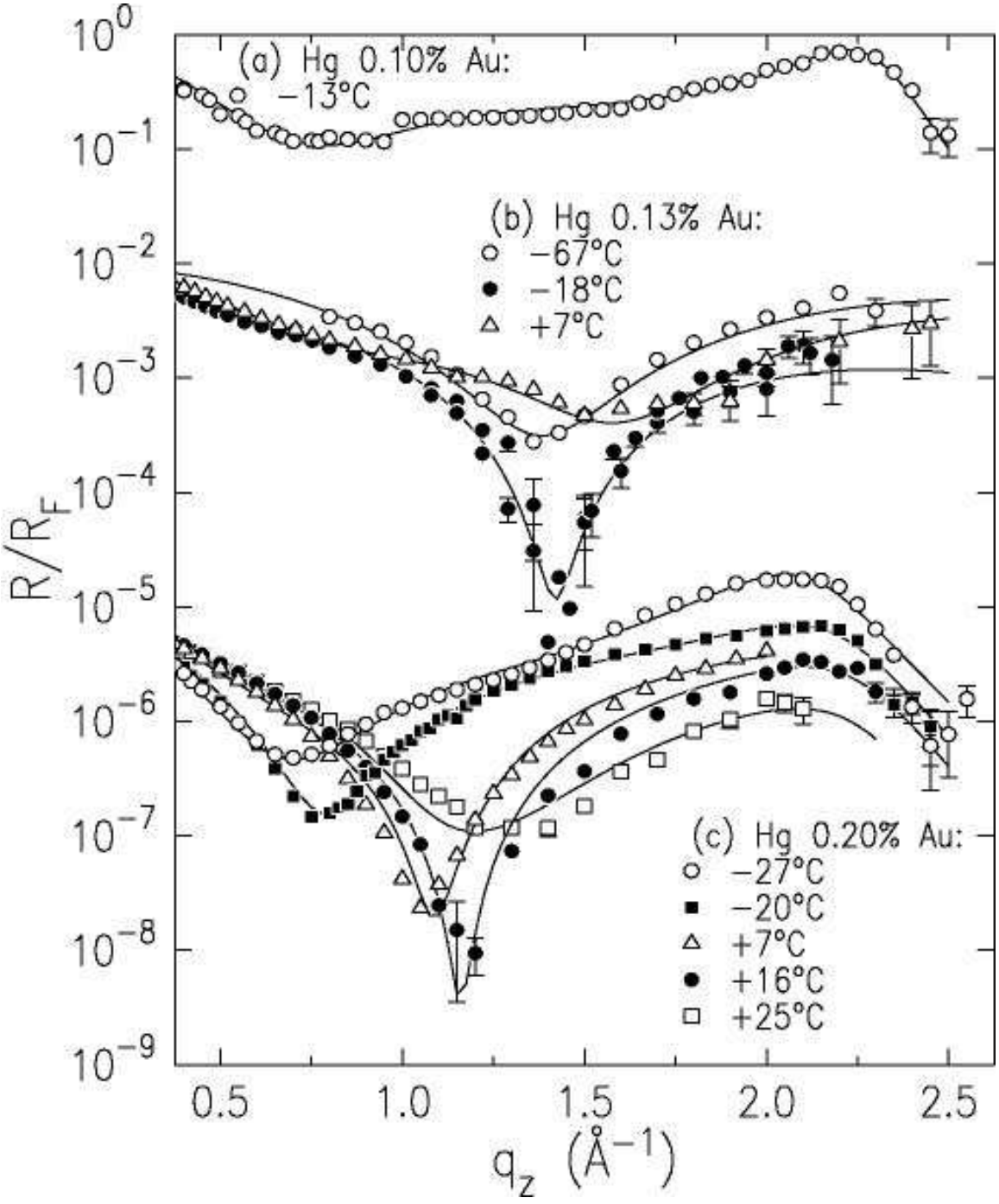



Figure 12.5: Fresnel-normalized reflectivity of (a) Hg 0.10at% Au at −13°C, (b) Hg 0.13at% Au below room temperature, and (c) Hg 0.20at% Au for the first cooldown from room temperature. The curves for 0.13at% and 0.20at% alloys are shifted by factors of $10^{-2}$ and $10^{-5}$ respectively. Solid lines are fits as discussed in text.

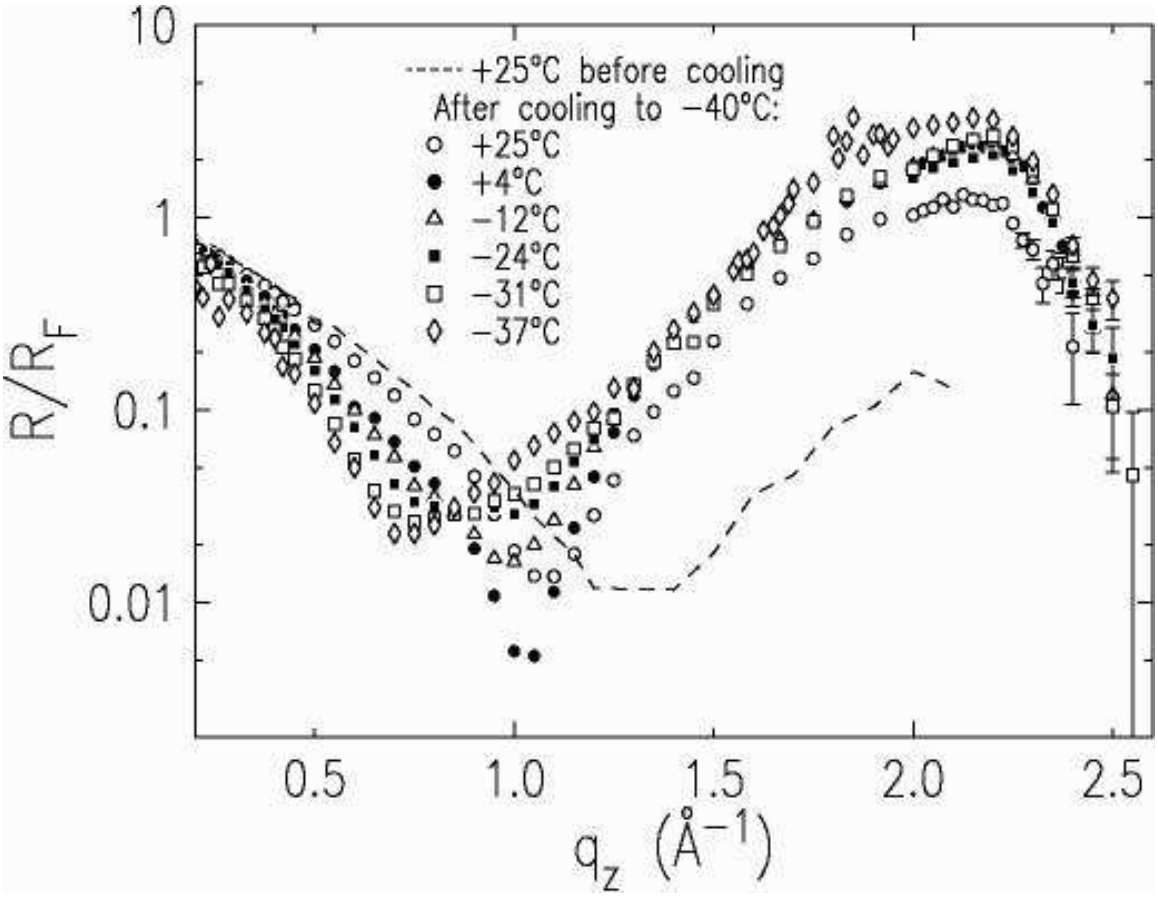



Figure 12.6: Fresnel-normalized reflectivity for Hg 0.20 %Au for the second cooldown from room temperature. +4°C (•), −12°C (△), −24°C (■), −31°C (□), −37°C (⋄), (- - -): +25°C experimental data from first cooldown.

original room temperature reflectivity was never recovered after cooldown, even after fifty hours at +25°C. Reflectivity data for the second cooldown of this alloy are shown in Figure 12.6. The reflectivity curves for the second cooldown all exhibit the notch at lower $q_z$ for each temperature than the first measurements, until the melting point is approached. Au expelled from the bulk, presumably incorporated into the surface structure, apparently can not readily resolubilize at these concentrations.

## 12.6 Analysis and Discussion

To our knowledge, this work is a unique application of surface x-ray scattering to probe the bulk solubility behavior of a liquid alloy. This is of particular importance, since the most reliable methods for determining solubilities in dilute alloys are electroanalytical techniques. These techniques are not applicable to alloys such as Au in Hg, where the solute is more noble than the solvent,[20] unless they are modified by probing the formation of intermetallic compounds with a second added solute such as Zn. For the case of Hg-Au, where formation of a surface phase signals that the solubility limit has been exceeded, atomic-scale surface structural measurements may be of special value.

By fitting reflectivity curves calculated from model surface-normal density profiles to the data, we can obtain more specific information about the surface structure of these alloys. Nearly all of the experimental reflectivity curves exhibit an interference peak along with some additional structure at lower $q_z$. We have fit these measurements to an oscillatory model profile with an additional gaussian term positioned near the liquid–vapor interface, as described by Eq. 12.4.12. Since this is the parameterization used previously in studies of pure liquid Hg, we can compare the pure and alloyed systems quantitatively. The layer spacing $d$, the thermal roughness $\sigma_T$ and the decay parameter $\overline{\sigma}$ are parameters which characterize the layered subsurface structure and are determined well by the fits. Other parameters affect the structure within about 2 Å of the interface, and are somewhat less reliably determined. Some reflectivity data, lacking a prominent layering peak, have been fit with a simpler form consisting of an error function profile along with an extra gaussian term, as in Eq. 12.4.8. Because of the low Au concentrations, the nearly equal scattering factors of Hg and Au, and

| ppm | $T$ (°C) | $\sigma_T$ (Å) | $\overline{\sigma}$ (Å) | $w_1$ | $w_0$ | $w_A$ | $\sigma_A$ (Å) | $z_A$ (Å) |
|---|---|---|---|---|---|---|---|---|
| 0 | +25 | 1.00±0.01 | 0.46±0.05 | 1.0 | 1.0 | 0.2±0.1 | 1.5±0.5 | −2±1 |
| 0 | −3 | 0.87±0.01 | 0.46±0.05 | 1.0 | 1.0 | 0.2±0.1 | 1.5±0.5 | −2±1 |
| 0 | −19 | 0.82±0.01 | 0.46±0.05 | 1.0 | 1.0 | 0.2±0.1 | 1.5±0.5 | −2±1 |
| 0 | −36 | 0.80±0.01 | 0.46±0.05 | 1.0 | 1.0 | 0.2±0.1 | 1.5±0.5 | −2±1 |
| 6 | +25 | 1.04±0.01 | 0.54±0.04 | 0.95 | 0.80 | 0.24±0.10 | 1.6±0.5 | −2±1 |
| 6 | +11 | 1.02±0.01 | 0.53±0.02 | 0.96 | 0.78 | 0.24±0.10 | 1.6±0.5 | −2±1 |
| 6 | −3 | 0.97±0.01 | 0.50±0.02 | 0.97 | 0.78 | 0.24±0.10 | 1.6±0.5 | −2±1 |
| 6 | −26 | 0.91±0.01 | 0.50±0.02 | 0.98 | 0.78 | 0.24±0.10 | 1.6±0.5 | −2±1 |
| 10 | +25 | 1.07±0.02 | 0.52±0.02 | 0.96 | 0.84 | 0.1±0.1 | 2±1 | −2.6±0.5 |
| 10 | +5 | 0.99±0.01 | 0.44±0.02 | 0.96 | 0.84 | 0.4±0.2 | 2±1 | −2.6±0.5 |
| 10 | −13 | 1.02±0.01 | 0.43±0.02 | 0.96 | 0.78 | 0.5±0.2 | 2±1 | −2.6±0.5 |

Table 12.1: Parameters for layered density profiles having the form given in Eq. 12.4.12, where $\sigma_n^2 = n\overline{\sigma}^2 + \sigma_T^2$ and $w_n = 1$ except as indicated in the table. Data for pure Hg, measured in the same UHV chamber, are from Ref. 12. For all fits, $d = 2.72 \pm 0.02$ Å.

the limited $q_z$ range, we will treat our model profiles in this study as though they were entirely composed of Hg. All models incorporate the bulk density and atomic form factor of Hg, and therefore represent an average surface-normal electron density without providing any direct information about the Au composition as a function of depth.

### 12.6.1 Dilute Au limit and Capillary Wave Roughness

At low Au concentrations, the main effect of the Au is to partially disrupt the layered profile near the surface, compared to the structure of Hg. Model Hg profiles, from studies reported previously,[12] are shown in Figure 12.7(a). The oscillatory profile has a layer spacing $d = 2.72$ Å, a decay parameter $\overline{\sigma} = 0.46$ Å, and a temperature dependent roughness $\sigma_T$, given in Table 12.1, that determines the amplitude of the layers in the density profile. The model also incorporates a slight tail of density extending towards the vapor, described by the term proportional to $w_A$ in Eq. 12.4.12.

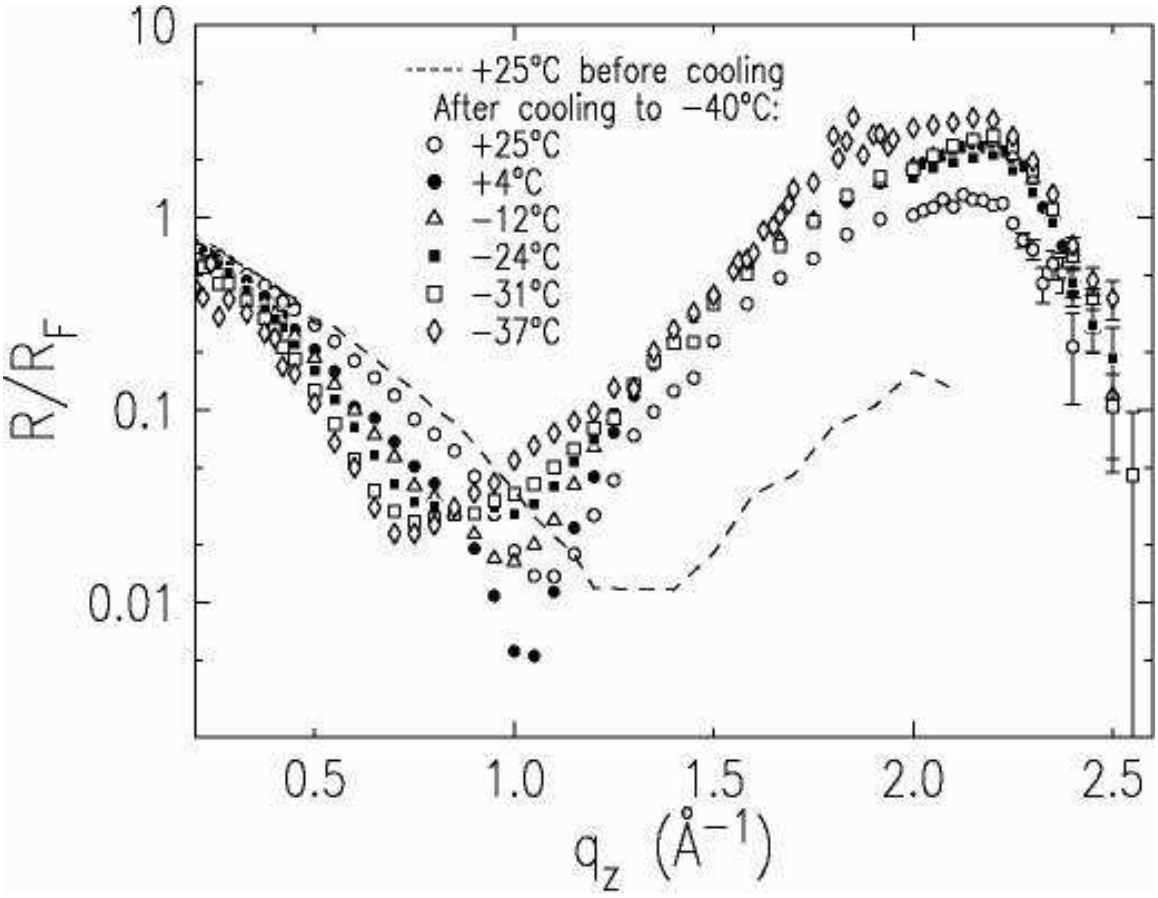



Figure 12.7: Model density profiles calculated from parameters listed in Table 1. Solid lines are from room temperature fits, and shorter dash length corresponds to lower temperatures. (a) Hg (b) Hg 0.06% Au (c) Hg 0.10% Au Inset: temperature dependence of the excess mean-squared surface roughness ($\sigma_T^2 - \sigma_{cw}^2$) for Hg (■), Hg 0.06at% Au (○), and Hg 0.10at% Au (closed triangles).

The surface-normal profile of Hg 0.06at% Au has the same layer spacing of 2.72 Å, but the layering is less well defined (Figure 12.7(b)). For comparable temperatures, the overall roughness $\sigma_T$ is about 0.1 Å greater than that of Hg, and layering decays over a slightly shorter length scale for the alloy. A notable difference between the structures of Hg and Hg 0.06at% Au is that for the alloy, the amplitude of the topmost surface layer is decreased by a factor of $w_0 = 0.8$ compared to pure Hg, where $w_0 = 1$. The reduction of the second layer amplitude by $w_1 \approx 0.95$–$0.98$ has a much smaller effect on the calculated reflectivity. As for Hg, the 0.06at% alloy data are consistent with additional density in the near surface region, described by the Gaussian term proportional to $w_A$. This is in contrast to the sharper surface profiles, such as that illustrated by the solid line in Figure 12.2(a)iv (having $w_A = 0$) that were found to describe liquid Ga and In.

The effect of temperature on the surface structure of Hg 0.06% Au is very similar to that of Hg. While slight variations in several parameters were required to optimize the fits at different $T$ for the 0.06% alloy, it is apparent that the main effect of increased temperature is to reduce the amplitude of the density oscillations. Capillary wave theory, which describes the broadening of the surface profile due to thermally excited surface waves, gives a specific prediction for such a mechanism through the temperature dependent roughness $\sigma_{cw}$ defined in Eq. 12.4.3. Previous studies of the temperature dependent surface roughness of liquid Hg found that thermally excited surface waves were not able to account for all of the temperature dependence observed.[12] This is in contrast with the surface roughnesses of liquid Ga and In, for which capillary wave theory accounted for all measured temperature dependence.[14,15] The temperature dependent reflectivity of Hg 0.06% Au exhibits essentially the same

behavior as that of Hg. In the inset of Figure 12.7 we compare the excess roughness $\sigma_T^2 - \sigma_{\rm cw}^2$ of Hg with that of Hg 0.06at% Au. The 0.06at% alloy has a larger roughness, but the slope of the excess roughness versus $T$ is the same. By alloying Hg with this small amount of Au, it appears that the total surface roughness has increased, without changing its temperature dependence.

The fact that the deviation from capillary wave behavior is the same for elemental Hg as for the 0.06at% alloy, which have distinctly different intrinsic surface-normal structure, suggests that the deviation from capillary wave theory may not arise from a temperature dependence of the local profile. Instead, the apparently anomalous temperature dependence most likely arises from height fluctuations across the surface which are not accounted for properly by the capillary wave model. In our analysis, thermal capillary waves are dependent on a surface tension which is defined as a macroscopic quantity, despite that fact that we integrate over capillary wave modes extending down to atomic length scales. It is very likely that the concept of a constant surface tension is not applicable to these microscopic length scales. The success of capillary wave theory in the description of other liquids may stem from the fact that the modes at atomic length scales make up only a small part of the entire capillary wave spectrum, and hence the contribution of these modes in affecting the overall roughness may differ from system to system. Comparison of diffuse surface scattering from Hg and Hg-Au alloys may provide more information on this question.

The Au concentration of 0.10at% marks the transition between the dilute-Au regime, where a simple layered structure previals, and the Au-rich phase. Here the more pronounced structure at low $q_z$ and the attenuated layering peak complicate the modelling, and the analysis is more ambiguous. For the layered model given,

acceptable parameters lie in the ranges indicated in Table 12.1. The corresponding fit curves are shown in Figure 12.4(b) (solid lines). Relative to Hg, the 0.10at% alloy model density profiles exhibit a reduction in oscillation amplitude and surface layer density very similar to that found in the 0.06at% alloy, as shown in Figure 12.7(c). Unlike the more dilute alloy, however, a more fundamental change in surface structure occurs as temperature is reduced beyond the solubility limit. Upon cooling from room temperature, the surface roughness first decreases, then increases again, so that the layering peak is less pronounced at $-13$°C than it was at $+5$°C. The resulting non-monotonic dependence of $\sigma_T$ on $T$ is shown in the inset of Figure 12.7 (closed triangles).

In addition, as $T$ decreases there is a continuous drop in the reflectivity at low $q_z$. This indicates a further decrease in the surface layer density, an enhanced density bump further towards the vapor region, or a combination of such effects. The density profiles shown in Figure 12.7(c) model this effect as a lump of density extending into the vapor region. The density tail is independent of temperature for Hg and Hg 0.06% Au, but for Hg 0.10% Au climbs steeply as temperature decreases. In this concentration and temperature range, the effect of decreased temperature is not a reduction in surface roughness but the establishment of a low-density surface region that destabilizes surface layering.

### 12.6.2 Au-rich limit and Surface Phase Formation

The 0.13at% Au alloy, near the room temperature saturation limit, could be modelled with a layered density profile only for our measurement at +25°C. Reflectivity data at lower temperatures exhibit a minimum at $q_z \sim 1.4$–$1.6$ Å$^{-1}$, along with a slight dip at $q_z \sim 0.5$ Å$^{-1}$. These features can be fit with very simple shelf-type models,

as shown in Figure 12.8(a). The relatively high reflectivity at the highest $q_z$ requires that these profiles have step edges that, in comparison to roughnesses encountered in other liquid metals and alloys, seem unphysically sharp. While this low surface roughness is a possibility, a much more likely explanation of the reflectivity is that some surface layering prevails in the 0.13at% alloy, too weak to produce a layering peak but substantial enough to produce constructive interference at high $q_z$ and augment the reflectivity which would otherwise be reduced in the washed-out step profile. For this reason, we think that the very simple shelf profiles are likely not the best description of the reflectivity, and models such as those presented below for the 0.20at% alloy may be more realistic. Despite this, attempts to fit the 0.13at% alloy with simple layered models were unsuccessful, resulting in unphysically small layer spacings of $d \approx 2.1$ Å to position the reflectivity minimum properly.

The surface roughness in the step-type profile was especially low for the Hg 0.13at% Au sample supercooled to $-67$°C, the lowest temperature obtainable in our chamber. The 13% Au alloy is the only one for which we observed deep supercooling: all other alloys investigated froze at temperatures close to the melting point of pure Hg, $-38.9$°C. We cannot tell whether the supercooling is particular to the 0.13% Au composition, or is due instead to an especially clean sample environment. It has been suggested before that supercooling at an ordered liquid metal surface may be enhanced due to the reduction of the difference in entropy between the liquid and solid phases relative to a disordered surface.[32] However, without more systematic studies of supercooled samples it is not possible to attach much significance to our observation.

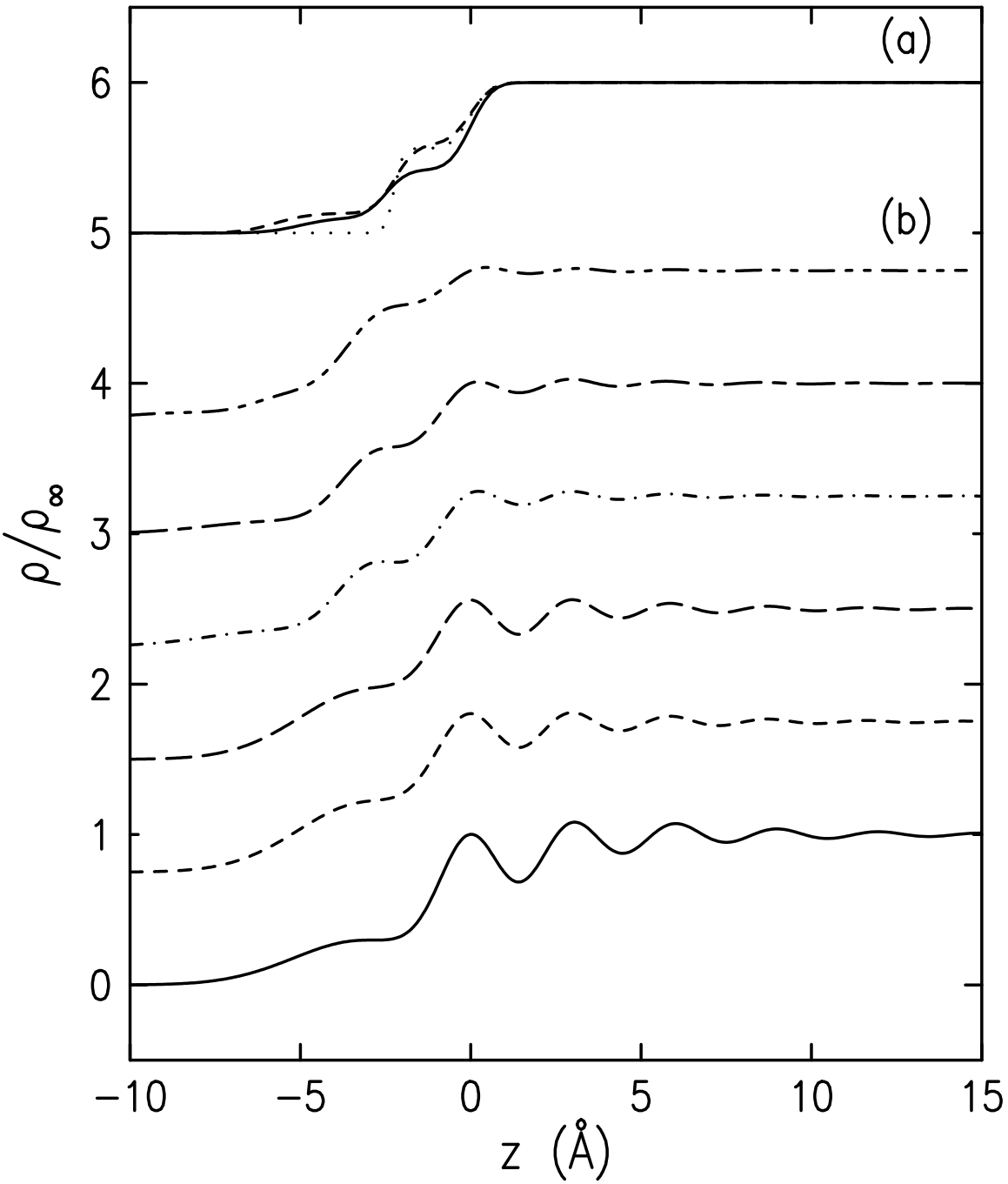



Figure 12.8: Model density profiles. (a) Hg 0.13% Au: +7°C (—), −18°C (- - -), −67°C (· · ·). (b) Hg 0.20% Au: +25°C (— - - —), +16°C (— - —), +8°C (- · - · -), −20°C (— —), −24°C (- - -), −27°C (—).

The concentration of 0.20at% Au in Hg exceeds the solubility limit for all temperatures investigated. Reflectivity data for this alloy exhibit minima at all $T$, along with a layering peak at the lowest $T$. We have fit these data to the simple layered profiles shown in Figure 12.8(b). To keep the number of parameters relatively small, we have used the form of Eq. 12.4.12 and fit the same number of paramters as were used for the dilute alloys. At the lowest temperatures, the surface layer spacing of 2.9 Å for Hg 0.20at% Au is unambiguously distinguished from the 2.72 Å layer spacing obtained for pure Hg and the dilute Hg-Au alloys. Since the atomic radius of Au (2.8 Å) is smaller than that of Hg (3.0 Å),[33] this increase in the layer spacing for the Au-rich alloy indicates that some significant change in packing has occurred in the surface layers. At higher temperatures, evidence for layering lies mainly in the relatively large reflectivity obtained for $q_z \geq 2$ Å$^{-1}$. Here the fits are less satisfactory, and the details of the models show no clear systematic dependence on temperature. It is difficult in this region of the phase diagram to assess the relationship between the details of the surface profile and the underlying layering. While the oscillations in the density profile clearly grow as temperature is reduced, it is not possible to say to what extent this is due to reduction of surface fluctuations rather than to changes in Au content at the surface. Measurement techniques with elemental specificity, such as resonant x-ray scattering or surface x-ray absorption fine structure, will be required to obtain this chemical information. Because of the high vapor pressure of liquid Hg, Auger electron spectroscopy will probably not be possible.

All model profiles for the Au-rich phase incorporate a shelf feature or surface layer that has a density of about half that of the bulk; we were unable to model the notch in the reflectivity without such a feature. Presumably, some fraction of

the Au which is insoluble in the bulk is incorporated into this surface phase, rather than precipitating out of the solution in solid form as might have been expected. It is difficult to explain how a monolayer composed entirely of Hg and/or Au might achieve this low density. All known Hg-Au phases are close-packed, with densities intermediate between those of elemental Au and Hg.[4] A uniform submonolayer of Au with a greatly expanded lateral spacing is one model which could produce the observed density profile. Typically, expanded liquids are created at pressures and temperatures high enough to approach the critical point. In this case, the putative liquid Au monolayer would have to be stabilized at temperatures far below the melting point of bulk Au. Such an expanded Au layer would have a very high surface corrugation, and the tendency of the surface tension to reduce the surface area would be expected to destabilize such a structure. While it may not be clear how to extrapolate quantities such as the surface tension of Au down to these temperatures, the macroscopic contact angles and curvature of our samples certainly suggest that the surface tension is comparable to that of pure Hg. One possibile reason for an expanded spacing is that large changes in the concentration of Au, which has a lower valence than Hg, could reduce the bandfilling in the surface layers. If this serves to greatly reduce the favored atomic coordination, effectively increasing the covalency, the surface atoms might be forced to adopt a more open structure. This picture is also consistent with the expansion of the surface-normal layer spacing in the Au-rich phase. Previous studies of liquid Ga and In surfaces showed that compared to the more covalent Ga, the free-electron-like In had a more compressed surface layer spacing, indicating a structure closer to hard sphere packing.[15]

Another possible explanation is that patches of more closely packed Au-rich monolayers float on the surface, comprising a coverage of about 50%. We believe that several points argue against this model. Liquid Hg has been observed to amalgamate continuously with Au substrates,[8] suggesting that it would be difficult to maintain a laterally inhomogeneous distribution of Au at the surface. Another objection is that if Au were precipitating out of solution and into a separate surface monolayer, we would expect a more monotonic change in coverage with temperature or concentration. Instead, the density seems to drop quickly to 50% of the bulk value and remain at that value. Finally, we find no evidence that the surface layer is solid. The surface profile is not particularly sharp, nor is there any sign of the long-range lateral order that would be expected for a crystalline monolayer.[34]

Studies of underpotential deposition of Hg on Au found that surface amalgams with open packing always incorporated coadsorbed anions from the electrolyte.[35] In the liquid Hg-Au alloys studied here, it is also possible that anions, perhaps formed from impurities dissolved within the Hg, may be incorporated into the outermost atomic layer of the liquid metal, producing the low-density surface region we observe. However, it is important to emphasize that such impurities would also have been present in the pure Hg samples studied previously. While the pure Hg reflectivity provides evidence for a sample-dependent tail of density near the surface, as discussed above, nothing like the shelf feature, or layer having half the bulk density, was ever observed. In the case of the Au-rich liquid alloys presented here, the shelf feature depends entirely on the presence of Au at the surface: only at temperatures and concentrations beyond the solubility limit does this structure appear. In contrast to pure Hg, the Au-rich amalgam surface may be capable of forming a passivated oxide,

even though elemental Au is quite nonreactive, and bulk Hg oxide is unstable under the low oxygen partial pressure. This result may be relevant to reactions catalyzed by liquid metal surfaces. Studies of the rate of formic acid decomposition over liquid Hg having different concentrations of dissolved metals have found that the addition of higher-valence metals decreases the activation energy of the reaction.[10] This was interpreted as indicating that electrons are localized in covalent bonds at the alloy surface, essentially a statement that the primary effect of alloying was electronic. Our observations on the Hg-Au alloys indicate that the formation of intermetallic phases at the surface may be much more important than previously thought, especially since the surface composition can differ so substantially from that of the bulk. At the same time, the surface induced layering intrinsic to all liquid metals may be less important for surface reactions, except for the extent to which the layering competes with the formation of the reactive surface phase.

# Bibliography


[1] L. Aitchison, *A History of Metals*, Interscience, NY, 1960.

[2] F. Habashi, *Principles of Extractive Metallurgy*,

[3] R. Lappalainen and A. Yli-Upro, Scand. J. Dent. Res. **95** (1987) 364; A. Oden and M. Tulberg, Acta Odontol. Scand. **43** (1985) 15.

[4] C. Rolfe and W. Hume-Rothery, J. Less-Common Met. **13** (1967) 1.

[5] X. M. Yang, K. Tonami, L. A. Tagahara, K. Hashimoto, Y. Wei, and A. Fujishima, Surface Science **319** (1994) L17

[6] C. Battistoni, E. Bemporad, A. Galdikas, S. Kačiulis, G. Mattogno, S. Mickevičius, and V. Olevano, Appl. Surf. Science **103** (1996) 107.

[7] R. Nowakowski, T. Kobiela, Z. Wolfram, and R. Duś, Applied Surface Science **115** (1997) 217.

[8] J. Li and H. D. Abruña, J. Phys. Chem. B **101** (1997) 2907.

[9] W. Kemula, Z. Kublick, and Z. Galus, Nature **184** (1959) B.A.56.

[10] G.-M. Schwab, Ber. Bunsenges. **80** (1976) 746.

[11] O. M. Magnussen, B. M. Ocko, M. J. Regan, K. Penanen, P. S. Pershan, and M. Deutsch, Phys. Rev. Lett. **74** (1995) 4444.

[12] E. DiMasi, H. Tostmann, B. M. Ocko, P. S. Pershan, and M. Deutsch, Phys. Rev. B **58** (1998) R13419.

[13] M. J. Regan, E. H. Kawamoto, S. Lee, P. S. Pershan, N. Maskil, M. Deutsch, O. M. Magnussen, B. M. Ocko, and L. E. Berman, Phys. Rev. Lett. **75** (1995) 2498.

[14] M. J. Regan, P. S. Pershan, O. M. Magnussen, B. M. Ocko, M. Deutsch, and L. E. Berman, Phys. Rev. B **54** (1996) 9730.

[15] H. Tostmann, E. DiMasi, P. S. Pershan, B. M. Ocko, O. G. Shpyrko, and M. Deutsch, Phys. Rev. B **59** (1999) 783.

[16] S. A. Rice, J. Non-Cryst. Solids **205–207** (1996) 755, and references therein.

[17] M. J. Regan, P. S. Pershan, O. M. Magnussen, B. M. Ocko, M. Deutsch, and L. E. Berman, Phys. Rev. B **55** (1997) 15874.

[18] N. Lei, Z. Huang, and S. A. Rice, J. Chem. Phys. **107** (1997) 4051.

[19] H. Tostmann, E. DiMasi, O. G. Shpyrko, P. S. Pershan, B. M. Ocko, and M. Deutsch, Ber. Bunsenges. Phys. Chem. **102** (1998) 1136.

[20] C. Guminski, J. Less-Common Metals, **168** (1991) 329.

[21] A. Braslau, P. S. Pershen, G. Swislow, B. M. Ocko, and J. Als-Nielsen, Phys. Rev. A **38** (1988) 2457.

[22] M. Deutsch and B. M. Ocko, Encyclopedia of Applied Physics **23** (1998) 479.

[23] Encyclopedia of Electrochemictry of the Elements, Pourbaix diagram showing potential versus pH for HgO among other things.

[24] B. N. Thomas, S. W. Barton, F. Novak, and S. A. Rice, J. Chem. Phys. **86** (1987) 1036.

[25] B. C. Lu and S. A. Rice, J. Chem. Phys. **68** (1978) 5558.

[26] J. Als-Nielsen, in *Structure and Dynamics of Surfaces II*, W. Schomers and P. von Blanckenhagen, eds., Springer, Heidelberg (1987).

[27] E. Chason and T. M. Mayer, Critical Reviews in Solid State and Material Sciences **22** (1997) 1.

[28] B. A. Bunker, A. J. Kropf, K. M. Kemner, R. A. Mayanovic, and Q. Lu, Nucl. Instrum. Methods Phys. Res. B **133** (1997) 102.

[29] The expression in Eq. (3) is given incorrectly in Eq. (12) of Ref. 15.)

[30] This reduced form factor is given incorrectly in Ref. 12.

[31] A. S. Kertes, Ed. *Solubility Data Series*, Vol. 25 "Metals in Mercury", Pergamon Pres, New York, 1986, p. 378.

[32] D. Turnbull, J. Chem. Phys. **20** (1952) 411.

[33] T. Iida and R. I. L. Guthrie, *The Physical Properties of Liquid Metals*, Clarendon Press, Oxford, 1993, p. 35.

[34] Grazing incidence diffraction measurements, which probe in-plane correlations of the first 50 Å at the surface, were performed for the Hg 0.13% Au alloy at room

temperature and at $-20$°C. No sharp peaks were observed; the data contained only features characteristic of the bulk Hg structure factor.

[35] J. Li, E. Herrero, and H. D. Abruña, Colloids and Surfaces A. **134** (1998) 113.

# Chapter 13

# Resonant x-ray study of liquid Bi-In surface

## 13.1 Abstract

Resonant x-ray reflectivity measurements from the surface of liquid $Bi_{22}In_{78}$ find only a modest surface Bi enhancement, with 35 at% Bi in the first atomic layer. This is in contrast to the Gibbs adsorption in all liquid alloys studied to date, which show surface segregation of a complete monolayer of the low surface tension component. This suggests that surface adsorption in Bi-In is dominated by attractive interactions that increase the number of Bi-In neighbors at the surface. These are the first measurements in which resonant x-ray scattering has been used to quantify compositional changes induced at a liquid alloy surface.

## 13.2 Introduction

Current treatments of the thermodynamics of surface phenomena in solutions rely heavily on the original works by Gibbs in 1878, and one of the most familiar corollaries is the Gibbs adsorption rule. In its simplest invocation, the Gibbs rule states that in a

binary liquid, the species having the lower surface tension will segregate preferentially at the surface. This apparent simplicity is deceptive: a survey of the literature reveals a hundred years' debate over the application of the Gibbs adsorption rule,[1] not to mention its extension to multicomponent systems[2] and crystalline surfaces,[3] and its connection to atomistic models.[4]

Experimental investigations of the validity of the Gibbs rule encompass measurements of adsorption isotherms,[5] surface tension,[6] and surface composition[7] in a variety of systems. Unfortunately, many of the liquids studied are too complicated for the simplest formulations of the Gibbs rule. Liquid metal alloys are in many ways ideal for such studies. Miscible alloys exist which behave as ideal liquids, while in other systems strongly attractive or repulsive heteroatomic interactions can be studied. Perhaps an even more important advantage of liquid metals is that the compositionally inhomogeneous region at the surface is known in some cases to be confined to an atomic layer. This is commonly assumed in calculations of Gibbs adsorption that take a model of a physical surface as their starting point.

For example, x-ray reflectivity, ion scattering, and Auger electron spectroscopy measurements of liquid $Ga_{84}In_{16}$ found a 94% In surface monolayer, as expected given this alloy's positive heat of mixing.[8,9] Subsequent layers have the bulk composition. Similar studies of dilute liquid Bi-Ga ($< 0.2$ at% Bi) likewise found surface segregation of a pure Bi monolayer.[10] Even when the repulsive interactions between Ga and Bi cause more Bi-rich alloys to undergo additional phase separation above 220°C, where a 65 Å thick inhomogeneous Bi-rich region forms, the pure Bi surface monolayer persists.[11,12] In Ga-Bi, then, repulsive heteroatomic interactions substantially change the surface composition profile, but do not defeat the Gibbs adsorption.

The effect of attractive heteroatomic interactions remains an open question. In alloys such as Bi-In, attractive forces between the two species produce a number of compositionally ordered phases in the bulk solid. It is therefore conceivable that Bi-In pairing may exist at the liquid surface, and compete with surface segregation. Our recent temperature dependent x-ray reflectivity measurements of liquid Bi-In alloys having 22, 33, and 50 at% Bi revealed structural features not found in elemental metals or in the Ga alloys discussed above.[13] As we will show, those data were suggestive of Bi-In pair formation along the surface-normal direction. However, since the technique did not measure the Bi surface concentration directly, other interpretations of the data were also possible.

## 13.3 Experimental Setup

A complete characterization of surface composition requires both elemental specificity and Å-scale structural resolution along the surface-normal direction, which is difficult to achieve experimentally. Auger electron spectroscopy, which satisfies the first of these requirements, is hampered by contributions from the bulk liquid.[7] X-ray reflectivity by contrast is a surface-sensitive probe. In the kinematic limit[14] the reflected intensity, measured as a function of momentum transfer $q_z$ normal to the surface, is proportional to the Fresnel reflectivity $R_F$ of a homogeneous surface:[15]

$$R(q_z) = R_F \left| (1/\rho_\infty) \int_{-\infty}^{\infty} (\partial \rho_{\text{eff}}/\partial z) \exp(i q_z z)\, dz \right|^2 . \qquad (13.3.1)$$

Here $\rho_{\text{eff}}$ represents an effective electron scattering amplitude that combines the electron density profile with the scattering form factor, and $\rho_\infty$ is the density of the bulk. The electron density variations that produce modulations in the reflectivity may result from changes in either the composition or the mass density. Thus, inference of

surface composition from the measured reflectivity is sometimes ambiguous.

## 13.4 Resonant X-ray Scattering

This disadvantage can be overcome with the application of resonant x-ray scattering. The effective electron density of a scattering atom depends on the scattering form factor $f(q) + f'(q, E) \approx Z + f'(E)$. When the x-ray energy is tuned to an absorption edge of a scattering atom, the magnitude of $f'$ becomes appreciable, producing changes in contrast between unlike atoms.[16] With one exception,[17] resonant x-ray scattering measurements reported in the past have been confined to studies of solids and bulk liquids, due to the difficulty of the experiment. The present report is the first to find compositional changes induced at a liquid surface.

## 13.5 Sample Preparation

The molten $Bi_{22}In_{78}$ sample was maintained at $T = 101°C$ and $P = 5 \times 10^{-10}$ Torr within an ultra high vacuum chamber, and periodically sputter cleaned with $Ar^+$ ions. Reflectivity measurements were performed at beamline X25 at the National Synchrotron Light Source. The spectrometer has been described previously,[18] except that here a double Si(111) crystal monochromator was used to provide an energy resolution of 9 eV. For the present work, we compare reflectivity measured at 12.5 keV to measurements made at the Bi $L_{III}$ edge at 13.421 keV. The energy was calibrated by transmission through a Bi foil, shown in Figure 13.1(a). At the inflection point indicated by the arrow, $f'_{\mathrm{Bi}}$ has its largest magnitude of $-24.7$ electrons. Uncertainties in $f'_{\mathrm{Bi}}$ may arise from inaccuracies in the calculation, incorrect establishment of the incident energy, and the energy resolution. To account for these possibilities, the

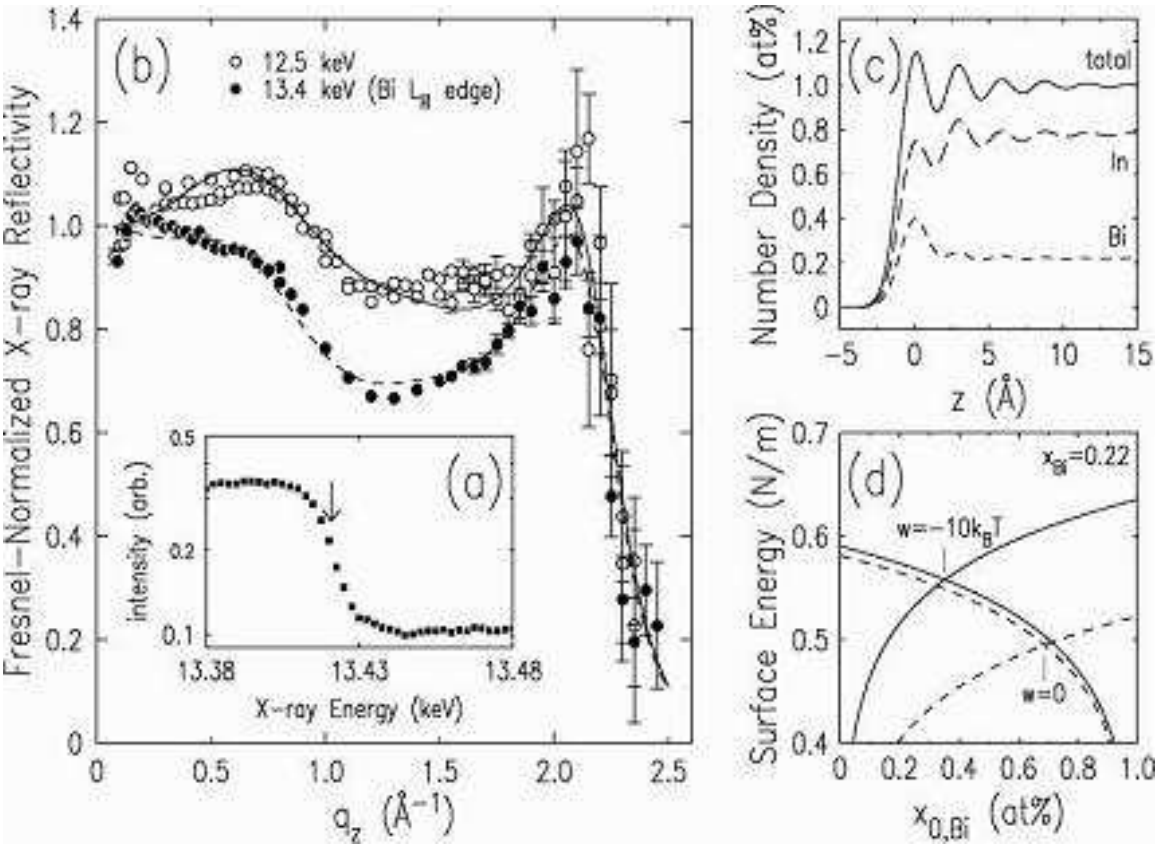



Figure 13.1: (a) Energy scan in transmission through Bi foil. (b) Fresnel-normalized x-ray reflectivity of $Bi_{22}In_{78}$. ○: 12.5 keV (two independent measurements); ●: 13.4 keV; (—): 12.5 keV fit; (- - -) 13.4 keV fit. (c) Best fit real space number density profile relative to bulk atomic percent. (—): Total number density; (– –): In density; (- - -): Bi density. (d) Surface energy as a function of surface Bi concentration $x_{0,\mathrm{Bi}}$ for the bulk concentration $x_{\mathrm{Bi}} = 0.22$, according to Eq. 13.3.1. (- - -): $w = 0$ . (—): $w = -10k_BT$.

analysis was performed for deviations in $f'_{\rm Bi}$ of about 20% (i.e., $f'_{\rm Bi} = -19.7$ and $-29.7$ electrons). The results were incorporated into the error ranges tabulated below.

## 13.6 X-Ray Reflectivity Data

Reflectivity data at both energies are shown in Figure 13.1(b) (symbols). These results were found to be both reproducible in energy and stable over time by measuring two 12 keV data sets, prior to and following the 13.4 keV measurements. The two 12 keV data sets are shown together as open circles in Figure 13.1(b). The interference peak at $q_z = 2.1$ Å$^{-1}$ is due to stratification of the atoms in planes parallel to the surface, a well established feature of liquid metals.[19] For $q_z < 1.8$ Å$^{-1}$, the data exhibit a modulation indicative of a structural periodicity roughly twice that of the surface layering. This feature is consistent with Bi-In dimers oriented along the surface normal, which could also give rise to alternating Bi and In layers (bilayers) at the surface. We also find that the low-$q_z$ reflectivity is strongly decreased when measured at the Bi $L_{III}$ edge. The reflectivity decrease itself varies smoothly with $q_z$ and does not exhibit a bilayer-type modulation, instead suggesting that the surface Bi concentration is larger than that of the bulk.

## 13.7 Electron Density Model

To investigate these possibilities, we calculate the reflectivity of a model density profile according to Eq. 13.3.1, which is refined simultaneously against the data taken at both energies. Resonant effects are included by combining the model structure and the scattering amplitude into an effective electron density profile $\rho_{\rm eff}(z)$. The energy dependence enters the analysis through the Bi concentration defined in $\rho_{\rm eff}(z)$, and

| | E (keV) | $\mu/\rho_m$ [a] ($cm^2/g$) | $\rho_m$ [b] ($g/cm^3$) | $\mu^{-1}$ ($\mu$m) | $f'$ [c] | $Z-f'$ | $\rho_\infty$ ($e^-/Å^3$) | $q_c$ ($Å^{-1}$) |
|---|---|---|---|---|---|---|---|---|
| In: | 12.5 | 74.1 | 7.0 | 19.3 | -0.2 | 48.8 | 1.788 | — |
| | 13.4 | 60.5 | | 23.6 | | | | — |
| Bi: | 12.5 | 75.2 | 10.0 | 13.3 | -7.3 | 75.7 | 2.180 | — |
| | 13.4 | 155.0 | | 6.45 | -24.7 | 58.3 | 1.679 | — |
| $Bi_{22}In_{78}$: | 12.5 | 74.5 | 7.66 | 17.5 | — | — | 1.874 | 0.05154 |
| | 13.4 | 92.6 | | 14.1 | — | — | 1.764 | 0.05000 |

[a]C. H. MacGillavry and G. D. Rieck, eds., *International Tables for X-ray Crystallography* Vol. III, Kynoch Press, Birmingham, England (1962). [b]R. C. Weast, ed., *CRC Handbook of Chemistry and Physics* (see Ref. 20). [c]B. L. Henke, E. M. Gullikson, and J. C. Davis, Atomic Data and Nuclear Tables **54** (1993) 181.

Table 13.1: Parameters used to calculate energy dependent x-ray reflectivity.

also through the Fresnel reflectivity $R_F$, which is a function of the energy dependent mass absorption coefficient $\mu^{-1}$ and the effective bulk electron density $\rho_\infty \propto (Z - f')$ that defines the critical angle $q_c$. Table 13.1 shows the values of these quantities used in our models. Reflectivity data acquired at each energy were normalized to the appropriate energy dependent Fresnel function.

Following past practice,[18] our model incorporates layers of atoms having a Gaussian distribution of displacements from idealized positions $nd$ along the surface normal direction:

$$\rho_{\text{eff}}(z) = \rho_\infty \sum_{n=0}^{\infty} F_n \frac{d}{\sigma_n \sqrt{2\pi}} \exp\left[-(z-nd)^2/\sigma_n^2\right]. \tag{13.7.1}$$

The roughness $\sigma_n$ arises from both static and dynamic contributions:

$$\sigma_n^2 = n\overline{\sigma}^2 + \sigma_0^2 + \frac{k_B T}{2\pi\gamma} \ln\left(\frac{q_{\max}}{q_{\text{res}}}\right). \tag{13.7.2}$$

Here $\overline{\sigma}$ and $\sigma_0$ are related to the surface layering coherence length and the amplitude of density oscillations at the surface. The last term accounts for height fluctuations produced by capillary waves, and depends on the temperature $T = 101°\text{C}$, the surface

tension $\gamma = 0.50$ N/m,[20] and wavevector cutoffs $q_{\max} = 0.99$ Å$^{-1}$ and $q_{\rm res} \sim 0.024$ Å$^{-1}$ (a slowly varying function of $q_z$), as detailed elsewhere.[18]

The scattering amplitude of each layer depends on the form factor and the effective electron density in each layer relative to the bulk, dependent on energy and Bi concentration:

$$F_n = w_n \times \frac{x_{n,\rm Bi}\left[f_{\rm Bi}(q_z) + f'_{\rm Bi}(E)\right] + (1 - x_{n,\rm Bi})\left[f_{\rm In}(q_z) + f'_{\rm In}\right]}{x_{\rm Bi}\left[Z_{\rm Bi} + f'_{\rm Bi}(E)\right] + (1 - x_{\rm Bi})\left[Z_{\rm In} + f'_{\rm In}\right]} \times \frac{x_{n,\rm Bi}\rho_{\infty,\rm Bi} + (1 - x_{n,\rm Bi})\rho_{\infty,\rm In}}{\rho_{\infty,\rm bulk}}. \tag{13.7.3}$$

For the first few layers ($n$=0,1,2), the weight $w_n$ may differ from unity and the Bi fraction $x_{n,\rm Bi}$ can vary from the bulk value $x_{\rm Bi} = 0.22$.

## 13.8 Data Fitting Analysis

We now describe the ingredients that are required to fit the data with this model. The interference peak at $q_z = 2.1$ Å$^{-1}$ can be reproduced by a simple layered profile in which $x_{n,\rm Bi} = x_{\rm Bi}$ for all $n$. The Bi and In number densities for such a model are shown in Figure 13.2(a)i, along with their sum, the total atomic fraction relative to the bulk. The corresponding reflectivity curves calculated for both x-ray energies are compared to the experimental data in Figure 13.2(b)i. Since the Bi concentration is uniform, the energy dependence is so slight that the curves overlap almost completely on the scale of the figure. Turning again to the data, the reduced intensity in the region $q_z < 1.8$ Å$^{-1}$ when measured at the Bi $L_{III}$ edge indicates a reduction in the scattering amplitude at the surface. This implies that the Bi concentration is enhanced there. Increasing the Bi fraction from 22 at% to $\approx 35$ at% in the first layer ($n = 0$) produces an appropriate energy dependence (Figs. 13.2(a)ii and 13.2(b)ii).

Although at this point the frequency of the low-$q_z$ modulation is not well described,

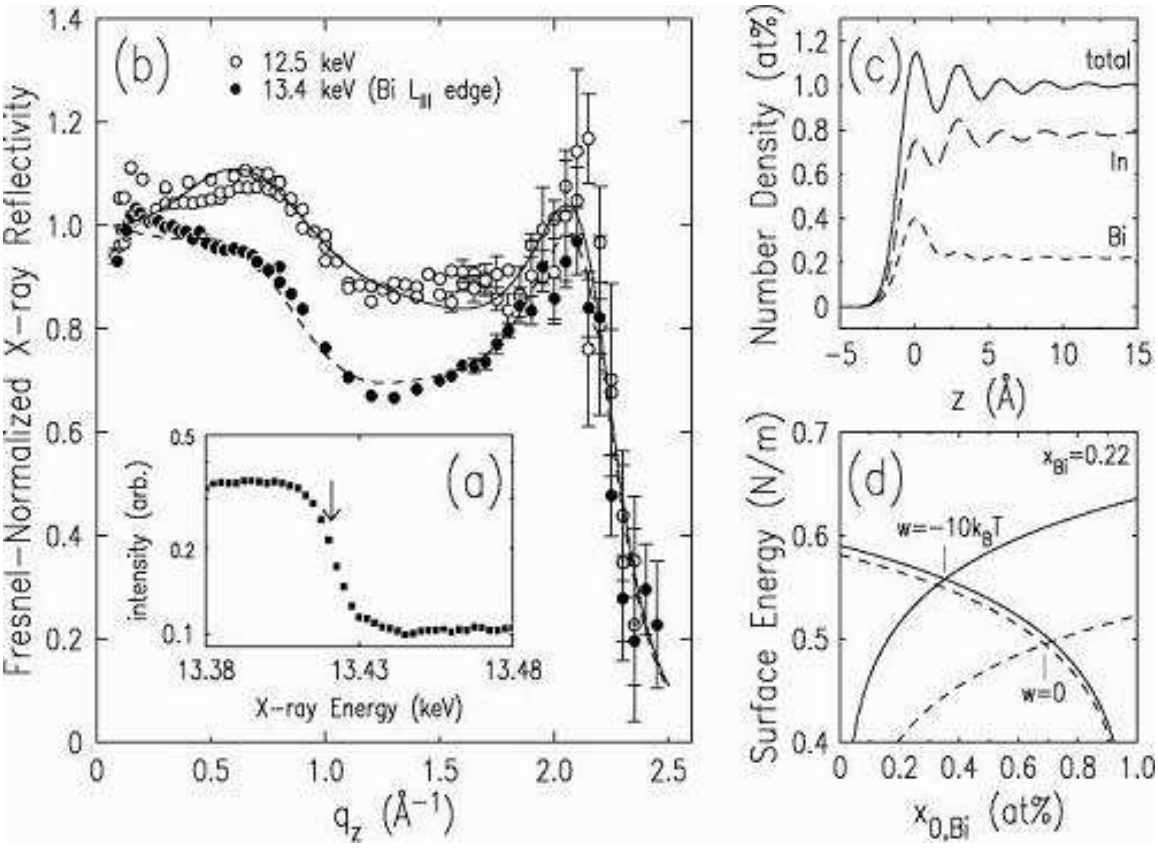



Figure 13.2: (a) Model surface-normal number density profiles, relative to bulk atomic percent. (—): total number density; (– –): In density; (- - -): Bi density. (b) Calculated Fresnel-normalized reflectivity curves. (—): 12.5 keV; (- - -): 13.4 keV. i: Surface layering with uniform composition ($x_{\mathrm{Bi}} = 0.22$). ii: Surface layering, with Bi enhancement in the first atomic layer ($x_{0,\mathrm{Bi}} = 0.35$).

| Figure | $d$ | $\overline{\sigma}$ | $\sigma_0$ | $w_0$ | $x_{0,\mathrm{Bi}}$ | $w_1$ | $x_{1,\mathrm{Bi}}$ | $w_2$ | $x_{2,\mathrm{Bi}}$ |
|---|---|---|---|---|---|---|---|---|---|
| 1 | 2.81 | 0.54 | 0.64 | 0.98 | 0.35 | 1.01 | 0.22 | 0.98 | 0.23 |
| 2i | 2.81 | 0.48 | 0.64 | 1.0 | 0.22 | 1.0 | 0.22 | 1.0 | 0.22 |
| 2ii | 2.81 | 0.54 | 0.64 | 1.0 | 0.35 | 1.0 | 0.22 | 1.0 | 0.22 |

Table 13.2: Fit parameters for model profiles, identified by the figure in which they appear. The length scales $d$, $\overline{\sigma}$, and $\sigma_0$ are in units of Å.

the fit is considerably improved by allowing the Bi fraction and total number densities to vary for the first three surface layers ($n$=0,1,2). We find that the Bi fraction for $n$=1,2 is essentially equal to the bulk value of 22 at%, while the total number densities for $n$=0,1,2 have values of 0.98, 1.01, and 0.98, respectively (Figs. 13.1(b),(c)). Thus, the detailed shape of the low-$q_z$ modulation is modelled by a very slight density wave of about 2% affecting the amplitudes of the first few surface layers. Increasing the number of model parameters to allow for shifts in positions and widths of the surface layers resulted in marginally better fits, but at the expense of high frequency Fourier components appearing as small wiggles in the calculated reflectivity. Variations in these extra fit parameters are extremely slight, and we doubt whether they have any physical basis. Parameters for all models are shown in Table 13.2.

This analysis demonstrates that to model the essential features of our data, there is no need to invoke long-range compositional ordering on a second length scale in the surface-normal direction, which we had suggested based on the previous non-resonant reflectivity measurements.[11,13] Still, we thought it important to investigate additional, specific models based on Bi-In pairs oriented along the surface normal. To test for alternating Bi-rich and In-rich layers, we attempted fits in which we forced the Bi and In compositions to be substantially different from the results shown above. We also described Bi-In pairing by allowing the positions, but not the densities, of the surface layers to vary. None of these profiles successfully described the data.

## 13.9 Summary

Our principal finding is the Bi enrichment of 35 at% in the surface layer, compared to the bulk value of 22 at%. This is considerably less Bi than would be expected in the absence of attractive Bi-In interactions, which can be estimated from the surface free energy requirement:[21]

$$\gamma_{\rm In}+\frac{k_BT}{a}\ln\left(\frac{1-x_{0,\rm Bi}}{1-x_{\rm Bi}}\right)-\frac{1}{4}(x_{\rm Bi})^2\frac{w}{a}=\gamma_{\rm Bi}+\frac{k_BT}{a}\ln\left(\frac{x_{0,\rm Bi}}{x_{\rm Bi}}\right)-\frac{1}{4}(1-x_{\rm Bi})^2\frac{w}{a}. \quad (13.9.1)$$

The quantity $w$ is the excess interaction energy of Bi-In pairs over the average of the Bi-Bi and In-In interaction energies; for an ideal mixture, $w = 0$. This analysis assumes that the inhomogeneous region is confined to a single atomic layer, the atoms are close-packed and take up an area $a$, and $w$ is small. Extrapolating the measured surface tensions to 100°C,[20] $\gamma_{\rm In} = 0.56$ N/m and $\gamma_{\rm Bi} = 0.41$ N/m. Using the Bi atomic size, $a = \pi(3.34/2)^2$ Å$^2$ (for In, the atomic diameter is 3.14 Å),[22] and the bulk composition $x_{\rm Bi} = 0.22$. The equilibrium surface composition $x_{0,\rm Bi}$ is found from the intersection of plots of both sides of Eq. 13.9.1. For $w = 0$, this analysis predicts a surface segregation of 69 at% Bi (Figure 13.2(d), dashed lines). To reproduce our experimental finding that $x_{0,\rm Bi} = 35$ at%, $w$ must be negative, with a magnitude of $\sim 10k_BT$ (Figure 13.2(d), solid lines). Although this large value of $w$ is most likely outside the range of validity of Eq. 13.9.1, the analysis certainly illustrates the qualitative effect of attractive heteroatomic interactions on the surface composition. In this Bi-In alloy, pairing does in fact defeat Gibbs adsorption in the sense that the surface energy is optimized not by segregating a large fraction of Bi, but by forming larger numbers of Bi-In neighbors in the surface layer. Exactly how this balance plays out in Bi-In alloys with the stoichiometric bulk compositions BiIn and $BiIn_2$ remains

to be seen.

# Bibliography


[1] J. W. Cahn and J. E. Hilliard, J. Chem. Phys. **28** (1958) 258; D. W. G. White, Met. Rev. **124** (1968) 73; R. A. Alberty, Langmuir **11** (1995) 3598.

[2] B. Widom, Physica **95A** (1979) 1.

[3] A. I. Rusanov, Surface Science Reports **23** (1996) 173; V. V. Bakovets, Phys. Stat. Sol. (b) **205** (1998) 507.

[4] R. Speiser *et al*, Scripta Metallurgica **21** (1987) 687.

[5] A. W. Adamson, *Physical Chemistry of Surfaces*, Wiley, New York, 1960.

[6] A. B. Bhatia and N. H. March, J. Chem. Phys. **68** (1978) 4651; Y. Oguchi *et al*, Phys. Chem. Liq. **10** (1981) 315.

[7] S. Hardy and J. Fine, in: *Materials Processing in the Reduced Gravity Environment of Space*, G. E. Rindone, Ed. Elsevier, The Netherlands, 1982, p. 503.

[8] M. J. Regan *et al*, Phys. Rev. B **55** (1997) 15874.

[9] M. F. Dumke *et al*, Surf. Sci. **124** (1983) 407.

[10] N. Lei *et al*, J. Phys. Chem. **104** (1996) 4802 and **105** (1996) 9615.

[11] E. DiMasi and H. Tostmann, Synchrotron Radiation News **12** (1999) 41.

[12] H. Tostmann *et al*, Phys. Rev. Lett. **84** (2000) 4385.

[13] E. DiMasi *et al*, J. Phys.: Condens. Matter **12** (2000) A209; E. DiMasi *et al*, to be published.

[14] The kinematic limit, or Born approximation, is valid where $R(q_z) << 1$. In this work, data are fit only for $q_z > 0.2$, where $R(q_z) < 3 \times 10^{-4}$, and the structure is determined principally by data with $q_z > 0.4$, where $R(q_z)$ is in the range $10^{-5}$–$10^{-9}$.

[15] A. Braslau *et al*, Phys. Rev. A **38** (1988) 2457.

[16] G. Materlik, C. J. Sparks, and K. Fischer, eds. *Resonant Anomalous X-ray Scattering: Theory and Applications*, North-Holland, Amsterdam, 1994, p. 47.

[17] E. DiMasi *et al*, MRS Symposium Series **590**, (2000) 183.

[18] H. Tostmann *et al*, Phys. Rev. B **59** (1999) 783.

[19] M. P. D'Evelyn and S. A. Rice, Phys. Rev. Lett. **47** (1981) 1844; S. A. Rice, J. Non-Cryst. Solids **205–207** (1996) 755, and references therein.

[20] This estimate for $\gamma$ is an average of the In and Bi surface tensions extrapolated to 100° (data from the *CRC Handbook of Physics and Chemistry*, R. C. Weast, ed., CRC Press, Boca Raton FL, 1985). Inaccuracies in $\gamma$ are compensated by $\sigma_0$ in Eq. 13.7.2, and do not otherwise affect the results.

[21] E. A. Guggenheim, *Mixtures*, Clarendon Press, London, 1952, Chapter IX.

[22] T. Iida and R. I. L. Guthrie, *The Physical Properties of Liquid Metals*, Clarendon Press, Oxford, 1993, p. 35

# Chapter 14

# Microscopic Structure of the Short-Range Wetting Film at the Surface of Liquid Ga-Bi Alloys

## 14.1 Abstract

X-ray reflectivity measurements of the binary liquid Ga-Bi alloy reveal a dramatically different surface structure above and below the monotectic temperature $T_{mono} = 222^{\circ}$ C. A Gibbs-adsorbed Bi monolayer resides at the surface at both regimes. However, a 30 Å thick, Bi-rich nanometer scale wetting film intrudes between the Bi monolayer and the Ga-rich bulk for $T > T_{mono}$. The internal structure of the wetting film is determined with Å resolution, showing a theoretically unexpected concentration gradient and a highly diffuse interface with the bulk phase.

## 14.2 Introduction

A thick wetting film may be stable at the free surface of a binary immiscible liquid mixture and the temperature dependent formation of this surface film is strongly influenced by the bulk critical demixing of the underlying bulk phase.[1] In contrast to

surface segregation, where a monolayer of the low surface tension component forms at the interface of the binary mixture, wetting is a genuine phase transition occurring at the interface resulting in the formation of a mesoscopically or macroscopically thick film.[2] To date, nearly all studies of wetting phenomena have been carried out with dielectric liquids dominated by long-range van der Waals interactions[3] and the experimental techniques used achieve mesoscopic resolution only. For binary alloys dominated by screened Coulomb interactions, evidence for a wetting transition has so far been obtained only for Ga-Bi[4] and Ga-Pb.[5] In the case of Ga-Bi, the formation of a Bi-rich wetting film has been detected by ellipsometry in the temperature range from 220° C to 228° C.[4] However, since the film thickness is much smaller than the wavelength of visible light, ellipsometry cannot provide Å-resolution structural information. By contrast, x-ray surface scattering techniques allow determination of the structure of the wetting film with atomic resolution and address issues such as the internal structure of the film and its evolution from molecular to mesoscopic thickness, none of which was hitherto addressed by any of the previous measurements.

The wetting phase transition is depicted schematically in Fig. 1. Below the bulk critical point of demixing, $T_{crit}$, the bulk phase separates into two immiscible phases, the high density Bi-rich phase and the low density Ga-rich phase. Below the characteristic wetting temperature $T_w < T_{crit}$, the high density phase is confined to the bottom of the container as expected (see Fig. 14.1(a)). As discussed in more detail below, for Ga-Bi, the high density phase is solid in this case and $T_w$ coincides with the monotectic temperature $T_{mono}$. In contrast, above $T_w$ the high density phase completely wets the free surface by intruding between the low density phase and the gas phase in defiance of gravity (see Fig. 14.1(b)).[2,6]

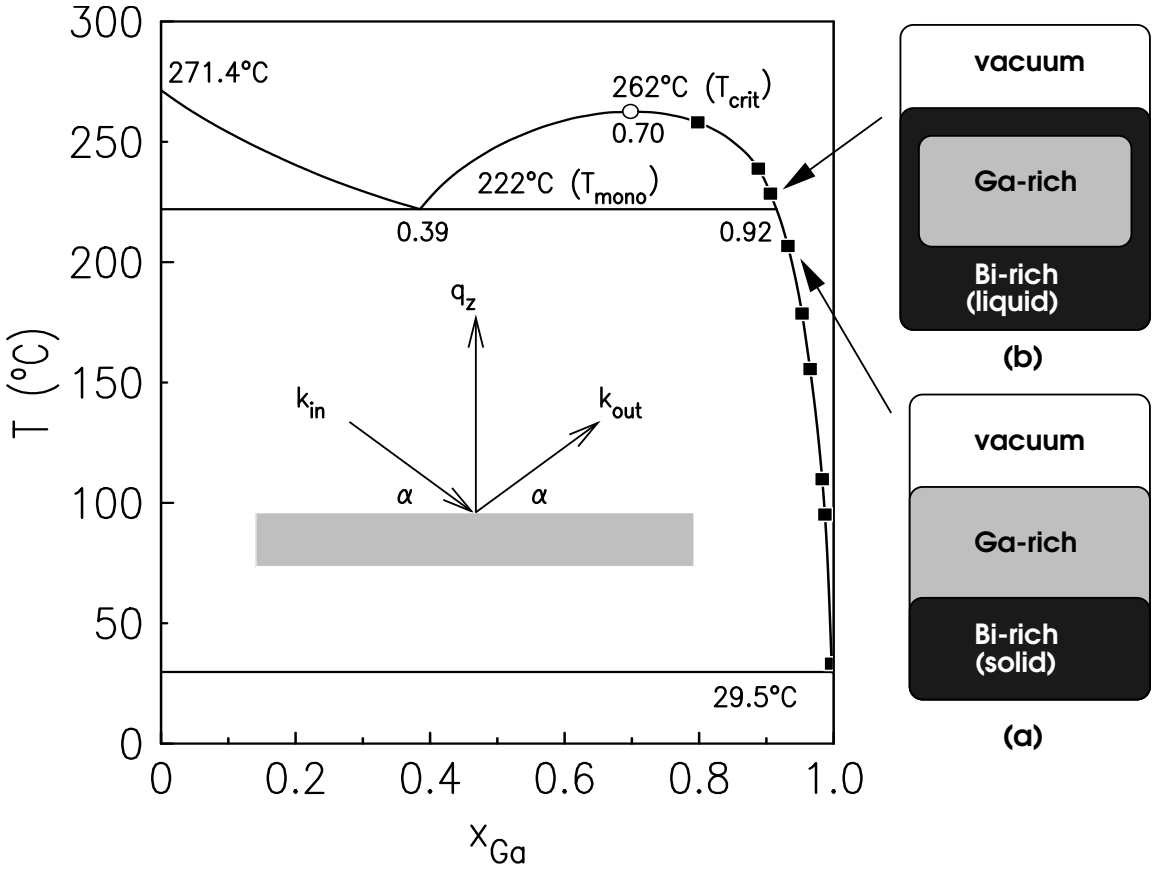



Figure 14.1: Phase diagram of Ga-Bi (Ref. 8). Between 29.5° C and 222° C, solid Bi is in equilibrium with a Ga-rich liquid phase. Between 222° C and 262° C, a liquid Bi-rich phase is in coexistence with a liquid Ga-rich phase. The surface structure of this alloy has been measured between 35° C and 258° C at selected points along the coexistence line (■). For $T$ <222° C partial wetting occurs (a), whereas complete wetting is found for $T$ >222° C (b). The inset depicts the geometry for specular x-ray reflectivity.

## 14.3 Sample Preparation

The Ga-Bi alloy was prepared in a inert-gas box using at least 99.9999% pure metals. A solid Bi ingot was placed in a Mo pan and supercooled liquid Ga was added to cover the Bi ingot. At room temperature, the solubility of Bi in Ga is less than 0.2at%. Increasing the temperature results in continuously dissolving more Bi in the Ga-rich phase with solid Bi remaining at the bottom of the pan up to the monotectic temperature, $T_{mono}$= 222° C. The initial Bi content was chosen to be high enough that the two phase equilibrium along the miscibility gap could be followed up to few degrees below $T_{crit}$ without crossing into the homogeneous phase region (see Fig. 14.1). The temperature on the sample surface was measured with a Mo coated thermocouple. The alloy was contained in an ultra high vacuum chamber and the residual oxide on the sample was removed by sputtering with $Ar^+$ ions.[7] Surface sensitive x-ray reflectivity (XR) experiments were carried out using the liquid surface spectrometer at beamline X22B at the National Synchrotron Light Source with an x-ray wavelength $\lambda$ =1.24 Å and a detector resolution of $\Delta q_z$ =0.03 $\mathring{A}^{-1}$. The background intensity, due mainly to scattering from the bulk liquid, was subtracted from the specular signal by displacing the detector out of the reflection plane.[7]

## 14.4 Experimental Techniques

The intensity reflected from the surface, $R(q_z)$, is measured as a function of the normal component $q_z = (4\pi/\lambda)\sin\alpha$ of the momentum transfer. The XR geometry is depicted schematically in the inset of Fig. 14.1. $R(q_z)$ therefore yields information about the surface-normal structure as given by

$$R(q_z) = R_F(q_z)\,|\Phi(q_z)|^2 \exp[-\sigma_{\rm cw}^2 q_z^2], \qquad (14.4.1)$$

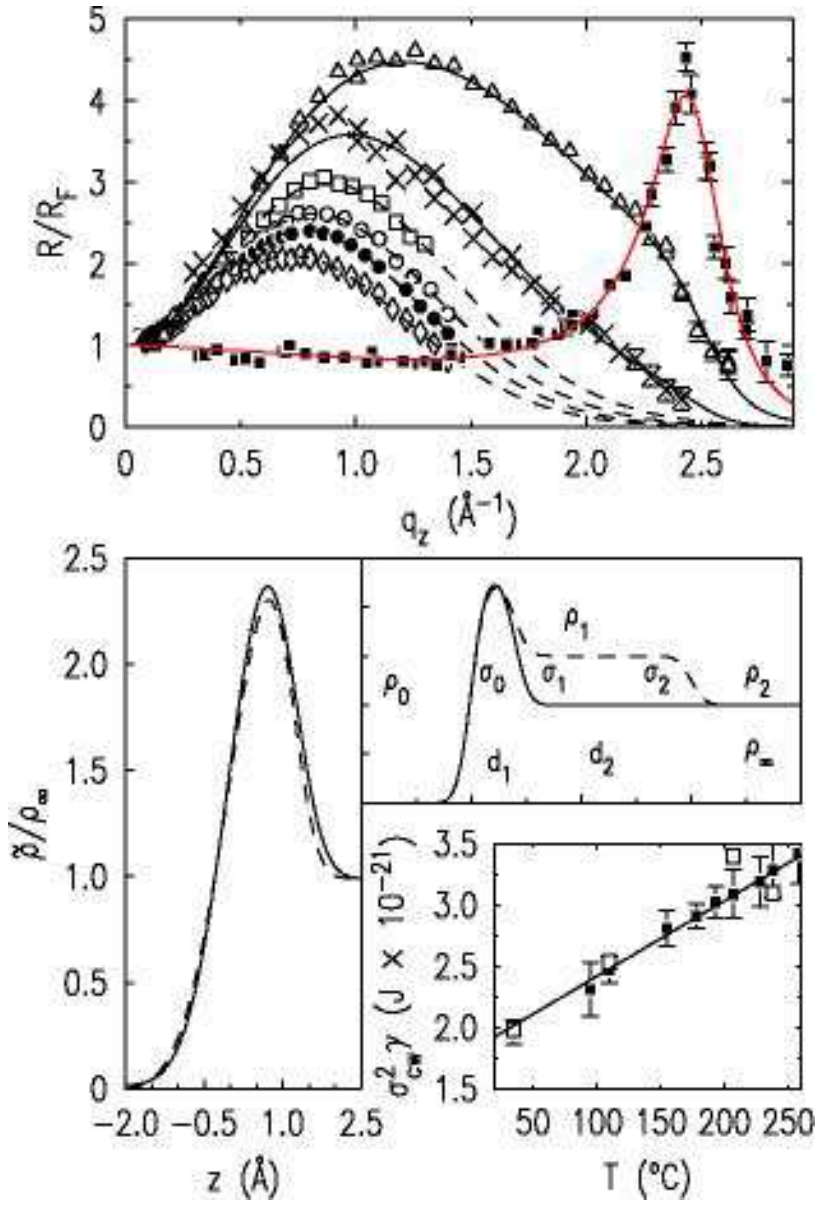



Figure 14.2: (a) Fresnel normalized reflectivity $R/R_F$ from Ga-Bi alloys for $T < T_{mono}$: (■): 100 at% Ga; (△): 99.7 at% Ga (35° C); (×): 98.7% Ga (95° C); (□): 98.4% Ga (110° C ); (○): 96.5% Ga (155° C ); (●): 95.3% Ga (178° C ) and (◇): 93.2% Ga (207° C ). Shaded line: fit to layered density profile of pure Ga (see Ref. 9); solid lines: fit to layered density profile of Ga plus Bi monolayer (see Ref. 10); broken lines: fit to Bi monolayer (this work). (b) Intrinsic density profiles normalized to $\rho_\infty$ for Ga-Bi for 110° C $\leq T \leq$ 207° C using the one-box model described in the text. The profiles essentially fall on top of each other and two representative fits are shown: 110° C (solid line) and 207° C (broken line). (c): Schematic representation of the (two-)box model. (d): CW roughness $\sigma_{cw}$ for Ga-Bi alloys as a function of temperature using $\gamma$ from our fit (■) and from macroscopic surface tension measurements (□, see Ref. 14).

where $R_F(q_z)$ is the Fresnel reflectivity of a flat, infinitely sharp surface and $\Phi(q_z)$ is the Fourier transform of the local surface-normal density profile $\tilde{\rho}(z)$:[7]

$$\Phi(q_z) = \frac{1}{\rho_\infty} \int dz \frac{d\tilde{\rho}(z)}{dz} \exp(\imath q_z z) \tag{14.4.2}$$

with the bulk electron density, $\rho_\infty$. The exponential factor in Eq. 14.4.1 accounts for roughening of the intrinsic density profile $\tilde{\rho}(z)$ by capillary waves (CW):

$$\sigma_{\rm cw}^2 = \frac{k_B T}{2\pi\gamma} \ln\left(\frac{q_{\rm max}}{q_{\rm res}}\right). \tag{14.4.3}$$

The CW spectrum is cut off at small $q_z$ by the detector resolution $q_{res}$ and at large $q_z$ by the atomic size $a$ with $q_{max} \approx \pi/a$.[7] However, $\tilde{\rho}(z)$, can not be obtained directly from Eq. 14.4.2 and we resort to the widely accepted procedure of adopting a physically motivated model for $\tilde{\rho}(z)$ and fitting its Fourier transform to the experimentally determined $R(q_z)$ as will be shown further below.[7]

The reflectivity of pure liquid Ga exhibits a pronounced interference peak indicating surface-induced layering of ions near the surface (see Fig. 14.2(a)).[9] Previous experiments on Ga-Bi at low temperatures[10,11] show that the layering peak is suppressed in the liquid alloy and $R(q_z)$ is dominated by a broad maximum consistent with a single Bi monolayer segregated at the surface as expected since $\gamma$ is considerably lower for Bi than for Ga.[11]

## 14.5 Results

Here, we report x-ray measurements from liquid Ga-Bi for $T$ up to 258° C encompassing the formation of the nanoscale wetting film at $T > T_{mono}$, the lowest temperature at which the liquid Bi-rich phase is stable. The actual wetting transition likely lies below $T_{mono}$ but does not manifest itself since the wetting film is solid for $T < T_{mono}$.

Experimental evidence for this assumption has been found for the similar systems Ga-Pb[12] and K-KCl.[13] The discussion of the data is divided into two parts: (i) $T < T_w \simeq T_{mono}$ (110° C-207° C) and (ii) $T > T_w$ (228° C-258° C). We present the results for $T < T_{mono}$ (scenario (a) in Fig. 14.1) first since this corresponds to the simpler surface structure with monolayer segregation but no wetting film.

**Below $T_{mono}$:** Fig. 14.2(a) shows $R(q_z)$ from liquid Ga-Bi at selected points along the coexistence line between 110° C and 207° C. Since subsurface layering is impossible to resolve at these temperatures, we simply model the near-surface density, which is dominated by the Bi monolayer segregation, by one box of density $\rho_1$ and width $d_1$. The density profiles are shown in Fig. 14.2(b) and the box model is shown schematically in Fig. 14.2(c) (solid line). The best fit to $R(q_z)$ that corresponds to this density profile is represented by the broken lines in Fig. 14.2(a). The mathematical description of the general box model with a maximum number of two boxes is:

$$\tilde{\rho}(z) = \frac{\rho_0}{2}\left\{1 + erf\left(\frac{z}{\sigma_0}\right)\right\} - \sum_{i=1}^{2}\frac{\rho_i}{2}\left\{1 + erf\left(\frac{z-d_i}{\sigma_i}\right)\right\} \qquad (14.5.1)$$

where $\sigma_0$ and $\sigma_i$ are the intrinsic roughnesses of each of the three interfaces. The total roughness, $\sigma$, of the interface between the vapor and the outermost surface layer is given by $\sigma^2 = \sigma_0^2 + \sigma_{cw}^2$ with $\sigma_0 = 0.78 \pm 0.15$ Å for $T < T_{mono}$. As predicted by capillary wave theory, the product $\sigma_{cw}^2\gamma$ (with $\gamma$ from our fits) depends linearly on $T$ (see Eq. 14.4.3 and (■) in Fig. 14.2(d)) over the entire temperature range. This variation is essentially the same if $\gamma$ is not taken from our fits but from macroscopic surface tension measurements (□).[14] Apart from the increasing surface roughness, the structure of the surface does not change over the entire temperature range from 110° C to 207° C, as witnessed by the intrinsic density profiles that fall right on top of each other once the theoretically predicted temperature dependence of the CW roughness has been corrected for (Fig. 14.2(b)). Between 212° C and 224° C, we observed rapid and random changes in the scattered intensity over the entire $q_z$ range. This unstable behavior of the surface is most likely due to the coexistence of patches of different

film thickness induced by the temperature gradient of about 6K normal to the the sample pan.

**Above $T_{mono}$:** The surface stabilized above $T_{mono}$ at about 228° C and and a sharper peak in $R(q_z)$ appeared centered around 0.13 $\mathring{A}^{-1}$ (see Fig. 14.3), indicating a thick film of high density forming near the surface. The persistence of the broad maximum centered around $q_z \approx 0.75$ Å$^{-1}$ indicates that Bi monolayer segregation is still present along with the newly formed thick wetting film. Several models were used to fit $R\,(q_z)$ but they all result in essentially the same density profiles. Here, we use the simple two-box model (see broken line in Fig. 14.2(c) and Eq. 14.5.1). As can be seen in Fig. 14.3, this simple model gives an excellent description of the experimentally obtained reflectivity. The pertinent density profiles describing the surface-normal structure of Ga-Bi alloys for $T > T_{mono}$ are shown in the inset of Fig. 14.3 and have the following features that can be compared to present predictions of wetting theory: (i) density, (ii) thickness and (iii) roughness of the wetting film.

(i) The concentration profile is highly inhomogeneous with a high density region at the outermost surface layer.[15] The integrated density of this adlayer is consistent with a monolayer of the same density as the monolayer found for $T < T_{mono}$. However, the Bi monolayer segregated on top of the wetting film is rougher and broader than the Bi monolayer segregated on top of the Ga-rich bulk phase for $T < T_{mono}$. This change in surface structure corresponds to a change in the intrinsic roughness of the interface liquid/vacuum, $\sigma_0$, from 0.78±0.15 Å below $T_{mono}$ to 1.7±0.3 Å above $T_{mono}$. However, the CW roughness still follows the predicted T-dependence of Eq. 3 (see Fig. 14.2(d)).

This change of $\sigma_0$ upon crossing $T_{mono}$ is possibly related to the fact that for

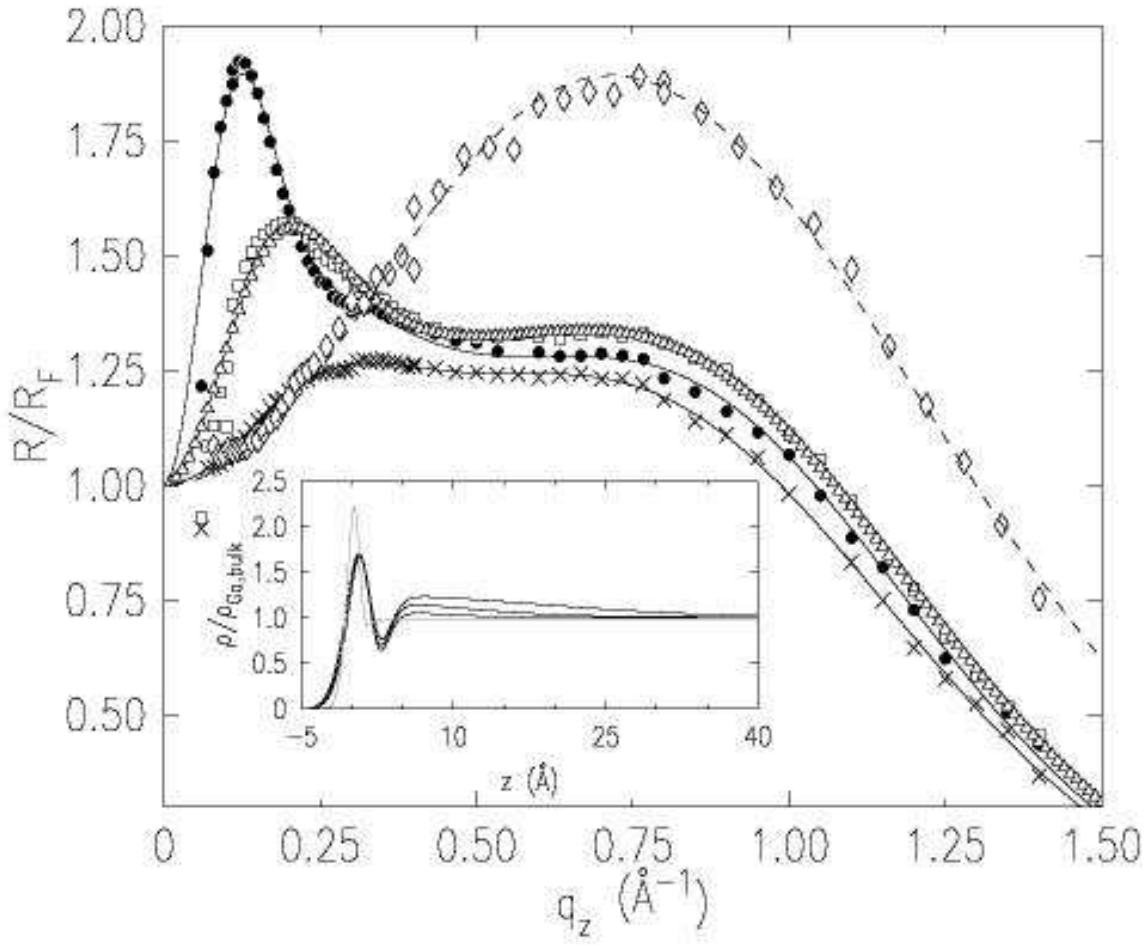



Figure 14.3: $R/R_F$ from Ga-Bi alloys for $T > T_w$: (•): 90.6 at% Ga (228° C); (□): 88.8% Ga (238° C); (△): ditto, but after heating to 258 ° C and cooling down; (×): 79.1% Ga (258° C); (for comparison, see:(⋄), 207° C). Solid lines fit to two-box model; broken line: fit to one-box model. Inset: intrinsic density profiles, $\tilde{\rho}(z)$, for Ga-Bi alloys normalized to the bulk density, $\rho_{Ga,bulk} = \rho_\infty$, at $T > T_w$: solid lines ordered in decreasing wetting film density: 228° C, 238° C and 258° C. Compare to the one-box density profile of Ga-Bi at 207° C (shaded line).

$T > T_{mono}$, the pure Bi monolayer segregates against a Bi-rich wetting film made out of atoms of different size and with repulsive heteroatomic interactions. By contrast, for $T < T_{mono}$, this segregation takes place against almost pure Ga. The fact that the Bi monolayer segregation persists from partial wetting to complete wetting means that the nano wetting film does not intrude between the Ga-rich bulk phase and vacuum, as assumed by wetting theory, but between the Bi monolayer already segregated at the surface and the Ga-rich bulk phase. This should have a pronounced influence on the energy balance at the surface which ultimately governs the wetting phase transition. Even though the possibility of an unspecified concentration gradient is included in Cahn's general theory[1], to our knowledge, an inhomogeneous density profile is neither treated explicitly in theoretical calculations (see the homogeneous profiles displayed in [16,17]) nor found experimentally. At 228° C the density of the thick wetting film is $\rho_2 = (1.25 \pm 0.03)\rho_\infty$ where $\rho_\infty$ is the density of the Ga-rich bulk phase. This agrees very well with the ratio of the densities of the coexisting Bi-rich and Ga-rich phases in the bulk, calculated from the phase diagram to be 1.23. The density of the wetting film reaches $\rho_\infty$ with increasing T ($\rho_2/\rho_\infty = 1.18 \pm 0.03$ at 238° C and 1.08±0.02 at 258° C) as the densities of the two bulk phases converge upon approaching $T_{crit}$ (their density ratio is 1.20 at 238° C and 1.08 at 258° C). This strongly supports the conclusion that the thick wetting film is the Bi-rich bulk phase as predicted by wetting theory.

(ii) The thickness of the wetting film, $d_2$, at 228° C is determined from the density profile to be ∼30 Å, consistent with a model-dependent estimate from ellipsometry results.[4] In addition, the thickness of the wetting film is corroborated by independent grazing incidence diffraction experiments resolving the in-plane structure which will

be reported elsewhere.[18] The wetting film in this Coulomb liquid with short-range interactions is considerably thinner than wetting films that have been observed in dielectric liquids with long-range interactions.[3,19] An important question concerning the thickness of a wetting film is whether the wetting film has been investigated in equilibrium. The fact that identical reflectivities were measured at 238° C taken 24 hours apart (Fig. 14.3), is strong evidence that the film thickness is in equilibrium in our study.[19]

(iii) The roughness between the Bi-rich wetting film and the Ga-rich bulk film is much higher that the roughness of the free interface LM/vacuum. This is be expected since the interfacial tension between two similar liquids is generally much lower than the liquid/gas surface tension.[20] On the other hand, it is not clear how sharp a concentration gradient should be expected between the Ga-rich and the Bi-rich phase and the interface may be essentially diffuse, independent of CW roughness. With increasing temperature, the wetting film becomes less well defined and it is not obvious whether this is due to the fact that the film is becoming slightly thinner, or if only the interface between two converging phases gets more diffuse. At any rate, we are far enough away from $T_{crit}$ that the predicted thickening of the wetting film due to the increasing correlation length of the concentration fluctuations should not play a role. Once the thick wetting film has formed, it is not possible to cool the sample below $T_{mono}$ since the Bi-rich wetting film remains at the surface and freezes.

## 14.6 Summary

In summary, we investigated the structural changes occurring on atomic length scales at the surface of liquid Ga-Bi during the wetting transition. In the case of partial

wetting ($T < T_{mono}$), a Bi monolayer segregates at the surface to lower the surface energy. Above the monotectic temperature complete wetting is found and a 30 Å thick wetting film intrudes between this monolayer and the Ga-rich bulk phase. This is the first time that the microscopic structure of a wetting film has been studied and that the concentration profile of the wetting film has been shown to vary on a level of several atomic diameters.

# Bibliography


[1] J. W. Cahn, J. Chem. Phys. **66**, 3667 (1977).

[2] S. Dietrich, Physica A **168**, 160 (1990).

[3] S. Dietrich in: C. Domb and J. L. Lebowitz, *Phase Transitions and Critical Phenomena*, Vol. 12, Academic Press, 1988.

[4] D. Nattland, P. D. Poh, S. C. Müller and W. Freyland, J. Non-Cryst. Solids **205-207**, 772 (1996).

[5] D. Chatain and P. Wynblatt, Surf. Sci. **345**, 85 (1996).

[6] J. S. Rowlinson and B. Widom, *Molecular Theory of Capillarity*, Clarendon Press, 1982.

[7] H. Tostmann, E. DiMasi, P. S. Pershan, B. M. Ocko, O. G. Shpyrko, and M. Deutsch, Phys. Rev. B **59**, 783 (1999).

[8] T. B. Massalski et al., *Binary Alloy Phase Diagrams*, ASM International, 1990.

[9] M. J. Regan et al., Phys. Rev. Lett. **75**, 2498 (1995).

[10] H. Tostmann et al., Ber. Bunsenges. Phys. Chem. **102**, 1136 (1998).

[11] N. Lei, Z. Huang and S. A. Rice, J. Chem. Phys. **104**, 4802, 1996.

[12] P. Wynblatt and D. Chatain, Ber. Bunsenges. Phys. Chem. **102**, 1142 (1998).

[13] H. Tostmann, D. Nattland and W. Freyland, J. Chem. Phys. **104**, 8777 (1996).

[14] K. B. Khokonov et al., Elektrokhimiya **10**, 911 (1974); H. U. Tschirner et al., Wissenschaftliche Zeitschrift der Technischen Hochschule Karl Marx Stadt **26**, 640 (1984).

[15] The dip in density between the outermost Bi adlayer and the thick wetting layer can be modeled with an atomic model similar to the one used for Bi segregated on top of Ga with subsurface layering (see Ref. 10). Including subsurface layering provides a slightly improved fit but does not substantially alter the parameters of the wetting layer.

[16] for example, see p. 218 in Ref. 3 or p. 75 in Ref. 4.

[17] D. Beysens and M. Robert, J. Chem. Phys. **87**, 3056 (1987).

[18] E. DiMasi et al., J. Phys: Condensed Matter, submitted (2000).

[19] R. F. Kayser, M. R. Moldover and J. W. Schmidt, J. Chem. Soc. Faraday Trans. II **82**, 1701 (1986).

[20] J. Israelachvili, *Intermolecular & Surface Forces*, Academic Press, 1992.

# Chapter 15

# Wetting film at GaBi surface

## 15.1 Abstract

Here we present x-ray reflectivity measurements from the free surface of a liquid gallium-bismuth alloy (Ga-Bi) in the temperature range close to the bulk monotectic temperature $T_{mono} = 222°C$. Our measurements indicate a continuous formation of a thick wetting film at the free surface of the binary system driven by the first order transition in the bulk at the monotectic point. We show that the behavior observed is that of a complete wetting at a tetra point of solid-liquid-liquid-vapor coexistence.

## 15.2 Introduction

Interfacial phenomena at the surface of critical systems, particularly at the surfaces of critical binary liquid mixtures, have attracted interest ever since the seminal paper by J.W. Cahn[1] demonstrating the existence of a wetting line, starting at the wetting temperature, $T_W$, below the critical point of demixing, $T_{crit}$. Initially, experimental efforts were mainly focused on systems dominated by long-range van-der-Waals interactions like methanol-cyclohexane and other organic materials.[2][3] Only recently have experiments probed the wetting behavior in binary metallic systems, most prominently

in gallium-lead (Ga-Pb)[4], gallium-thallium (Ga-Tl)[5], and gallium-bismuth (Ga-Bi)[6]. Those systems allow the study of the influence of interactions characteristic of metallic systems on the wetting behavior. By the same token, they allow one to obtain information on the dominant interactions in metallic systems by measurements of the thermodynamics and structure of the wetting films.

This paper reports measurements of the wetting behavior of Ga-Bi close to its monotectic temperature $T_{mono} = 222°C$. We first present the bulk phase diagram of Ga-Bi and relate it to the structures at the free surface (liquid-vapor interface) known from optical ellipsometry[6] and recent x-ray reflectivity measurements.[7,8] The experimental setup is then described, along with some basic principles of the x-ray reflectivity experiment and the data analysis. Finally, our results and the conclusions emerging therefrom are discussed.

## 15.3 Bulk and Surface Structure

The bulk phase diagram of Ga-Bi has been measured by Predel using calorimetric methods[9], and is shown in Fig. 15.1. Assuming an overall concentration of 70% Ga, the following behavior is found: Below $T_{mono}$ (regime I) and at temperatures higher than the melting point of Ga $T_m(Ga) = 29.5°C$, solid Bi coexists with a Ga-rich liquid phase. In this regime, previous x-ray measurements have shown that a Gibbs-adsorbed Bi monolayer resides at the free surface.[7,8] For $T_{mono} < T < T_{crit}$ (regime II), the bulk phase separates into two immiscible phases, a high density Bi-rich phase and a low density Ga-rich phase. The heavier Bi-rich phase is macroscopically separated from the lighter Ga-rich phase and sinks to the bottom of the sample pan. In temperature regime II, the high density, Bi-rich phase wets the free surface

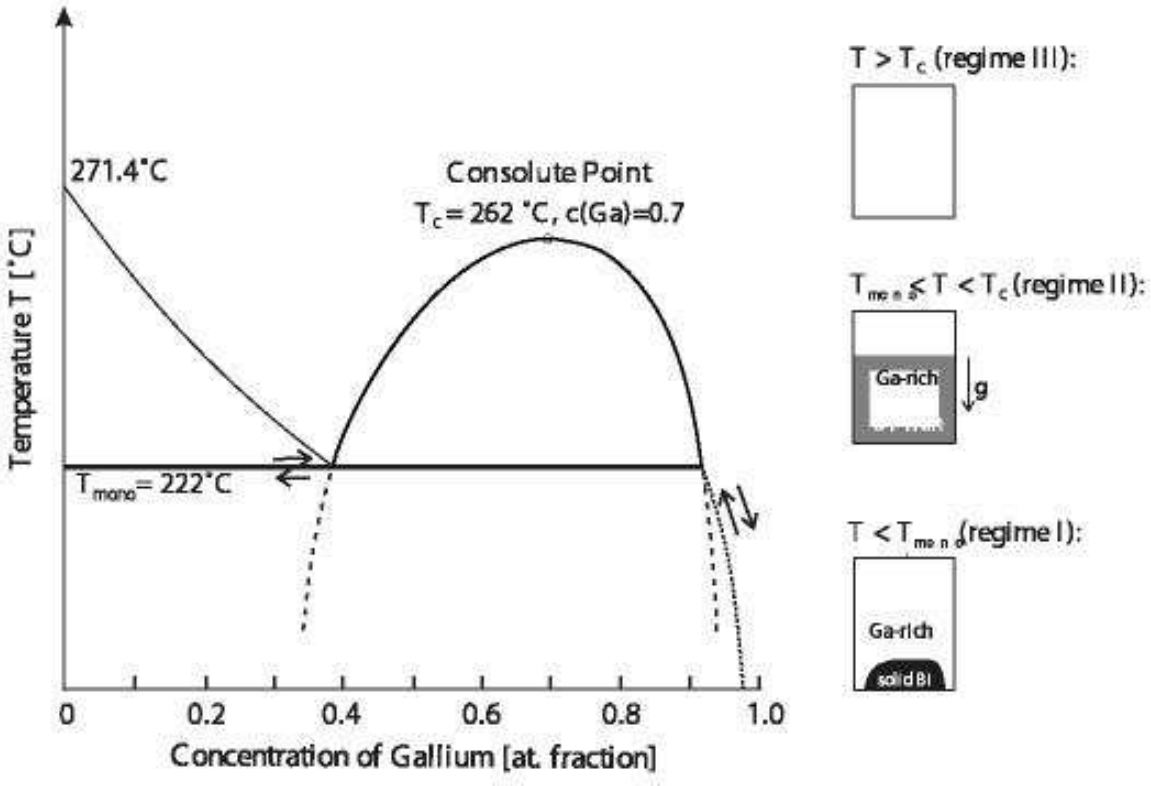



Figure 15.1: Bulk Phase diagram of Ga-Bi (Ref.[9]). Bold solid line: liquid-liquid coexistence, dashed line: liquid-liquid coexistence metastable, dotted line: liquid-solid coexistence. On the right: Schematic bulk behavior in the different temperature regimes.

by intruding between the low density phase and the Bi monolayer, in defiance of gravity.[8] Considering that pure Bi has a significantly lower surface tension than pure Ga, the segregation of the Bi-rich phase at the surface is not too surprising. In fact, the thickness of the wetting layer in such a geometry is believed to be limited only by the extra gravitational potential energy paid for having the heavier phase at the top[10]. In regime III, above the consolute point, the bulk is in the homogeneous phase and only a Gibbs-adsorbed Bi monolayer has been found at the free surface.[14]

Despite extensive experimental efforts to relate the bulk phases to the corresponding surface phases, two important question remain unanswered: What kind of transitions take place at the free surface between regime I and regime II and between regime II and regime III. Here, we focus on the transition between regime I and regime II. Note that these temperature regimes are separated by $T_{mono}$, a temperature characterized by the coexistence of the solid Bi, the Bi-rich liquid, the Ga-rich liquid and the vapor. $T_{mono}$ is therefore a solid-liquid-liquid-vapor tetra point, at which the solidification of pure bulk Bi takes place. The question is, then, how is this first order bulk transition related to the changes at the surface?

## 15.4 Experimental Techniques

The Ga-Bi alloy was prepared in an inert-gas box using metals with purities greater than 99.9999%. A solid Bi ingot was placed in a Mo pan and oxide formed at the surface was scraped away. Liquid Ga was then added to completely cover the Bi ingot. The sample with an overall Ga amount of 70 at% was transferred through air into an ultrahigh vacuum chamber. After a one day of bake-out, a pressure of $10^{-10}$torr was achieved and the residual oxide on the liquid sample was removed by sputtering with $Ar^+$ ions, at a sputter current of a 25 microamps and a sputter voltage of 2 kV.

To avoid temperature gradients between the bulk and the surface induced by thermal radiation, a temperature-controlled radiation shield was installed above the sample. The temperature was measured with thermocouples mounted in the bottom of the sample pan and on the radiation shield. The sample pan and the radiation shield temperature were controlled by Eurotherm temperature controllers yielding a temperature stability of $\pm 0.05°C$.

Surface-specific x-ray reflectivity measurements were carried out using the liquid surface reflectometer at beamline X22B at National Synchrotron Light Source with an x-ray wavelength $\lambda = 1.54\mathring{A}$. Background and bulk scattering were subtracted from the specular signal by displacing the detector out of the reflection plane. The intensity $R(q_z)$, reflected from the surface, is measured as a function of the normal component $q_z$ of the momentum transfer and yields information about the surface-normal structure of the electron density as given by

$$R(q_z) = R_F(q_z) \mid \Phi(q_z) \mid^2 \exp[-\sigma_{cw}^2 q_z^2 \tag{15.4.1}$$

where $R_F(q_z)$ is the Fresnel reflectivity from a flat, infinitely sharp surface, and $\Phi(q_z)$ is the Fourier transform of the local surface-normal density profile $< \widetilde{\rho}(z) >$[11]:

$$\Phi(q_z) = \frac{1}{\rho_\infty} \int dz \frac{d < \widetilde{\rho}(z) >}{dz} \exp(iq_z z) \quad (2), \tag{15.4.2}$$

with the bulk electron density $\rho_\infty$ and the critical wave vector $q_{crit}$. The exponential factor in Eq. 15.4.2 accounts for roughening of the intrinsic density profile $< \widetilde{\rho}(z) >$ by capillary waves:

$$\sigma_{cw}^2 = \frac{k_B T}{2\pi\gamma} \ln(\frac{q_{\max}}{q_{res}}) \quad (3),$$

where $\gamma$ is the macroscopic surface tension of the free surface, and $\sigma_{cw}$ is the roughness due to thermally excited capillary waves (CW) . The CW spectrum is cut off at small $q_z$ by the detector resolution $q_{res} = 0.03\text{Å}^{-1}$ and at large $q_z$ by the inverse atomic size $a$ , $q_{max} \approx \pi/a$.[13].

In Expression (1) the validity of the Born approximation is tacitly assumed. Since the features in $R/R_F$ characteristic of the thick wetting film appear close to the critical wavevector $q_c = 0.049\text{Å}^{-1}$ of the Ga-rich subphase, where the Born approximation is no longer valid, we had to resort to Parratt's dynamical formalism[12] for $q_z$ less than $0.25\text{Å}^{-1}$. Details of this analysis will be reported elsewhere.[14]

## 15.5 Results

Fig. 15.2(a) shows the reflectivity at three temperatures: well below $T_{mono}$ at $T = 205°C$ (regime I), well above $T_{mono}$ at $T = 222.5°C$ (regime II) and at an intermediate temperature $T = 220°C$. Due to the loss of phase information (Eq. 15.4.1) the interesting electron density profiles cannot be obtained directly from the measured reflectivity. One has to resort to the widely accepted procedure of adapting a physically motivated model for the electron density profile and fitting its Fourier transform to the experimentally determined $R/R_F$. The resulting density profiles for the different temperatures are depicted in Fig. 15.2(b) and the corresponding fits to $R/R_F$ can be found as solid lines in Fig. 15.2(a).

At $T = 205°C$ $R/R_F$ (Fig. 15.2(a), diamonds) shows a pronounced maximum centered around $q_z = 0.8\mathring{A}^{-1}$. This maximum is indicative of a high electron density at the surface of the alloy and a previous analysis shows that it is compatible with the segregation of a monolayer of pure Bi at the liquid-vapor interface of the bulk alloy.[8]

The normalized reflectivity at $T = 222.5°C$ (Fig. 15.2(a), solid circles) shows two peaks (Kiessig fringes) at low $q_z$ characteristic of a Bi-rich wetting film $\approx 50\mathring{A}$ thick. This thickness is in good agreement with ellipsometric measurements on Ga-Bi alloy

surfaces in the same temperature regime.[6] The interfacial roughness between the Bi-rich and the Bi-poor phase, indicated by the decay of the Kiessig fringes, is $\approx 12\mathring{A}$. Additionally, $R/R_F$ continues to exhibit an increased intensity around $q_z = 0.8\mathring{A}^{-1}$: The monolayer of pure Bi is still present at the surface in regime II, while the Bi-rich wetting film has intruded between it and the Ga-rich subphase.

The reflectivity at the intermediate temperature $T = 220.0°C$ (Fig. 15.2(a), open circles) still exhibits a peak at low $q_z$. However, compared to the peak at $T = 222.5°C$, it is now shifted to higher $q_z$. The corresponding electron density profile, depicted in Fig. 15.2(b) as the dashed curve, indicates a highly diffuse, thin film of a Bi enriched phase between the monolayer and the Ga-rich subphase.

To obtain further information about the temperature dependent transition between the different surface regimes, we performed temperature-dependent x-ray reflectivity measurements at a fixed $q_z$ in a temperature range close to $T_{mono}$. These measurements are referred to in the following as T-scans. As can be seen in Fig. 15.2(a) the reflectivities in the two regimes differ most distinctly in the low $q_z$ part, and somewhat less, but still significantly in the higher $q_z$-part. Due to the high sensitivity of the reflectivity to temperature dependent sample height changes at low $q_z$, we carried out measurements at a relatively high $q_z = 0.8\mathring{A}^{-1}$.

A T-scan while cooling (heating) with a cooling (heating) rate of $1°C$/hour between $226°C$ and $210°C$ is shown in Fig. 15.3. For temperatures higher than $T_{mono}$ the reflectivity stays constant. Upon $T$ reaching $T_{mono}$ the intensity starts rising continuously. When reaching $210°C$ the x-ray reflectivity has increased by about 30% as compared to its value above $T_{mono}$ - as one would expect from Fig. 15.2(a) for the change from regime I to regime II at that $q_z$-position. While heating, we observed

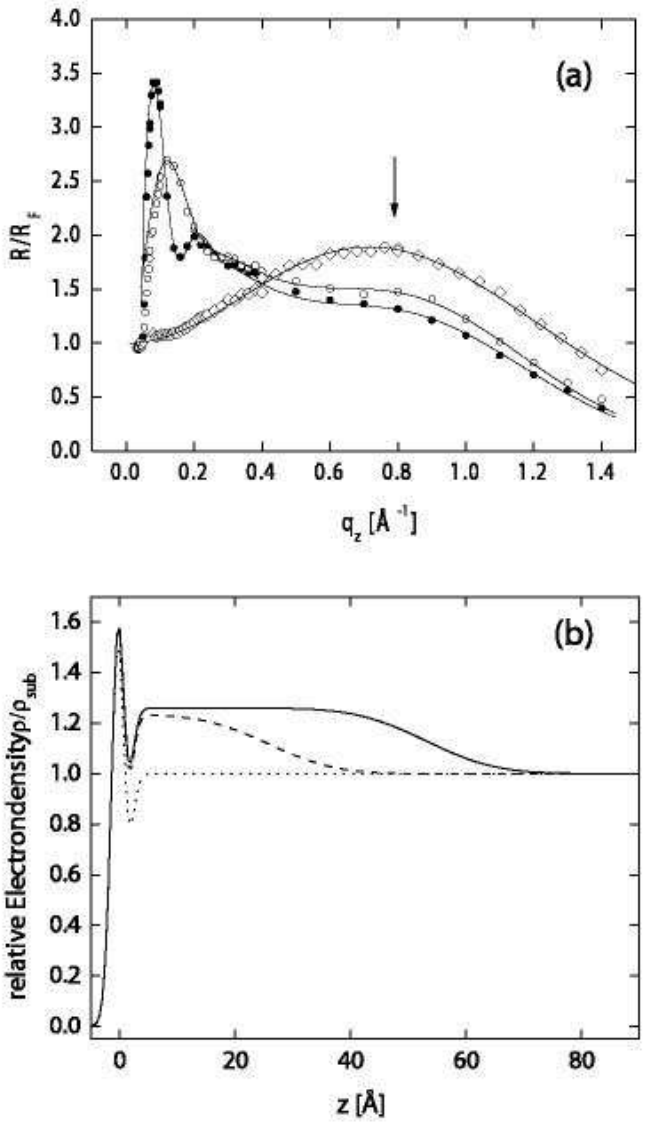



Figure 15.2: (a) Fresnel normalized x-ray reflectivity $R/R_F$ from the surface of Ga-Bi: (diamonds) $T = 205°C$, (open circles) $T = 220°C$, (solid circles) $T = 222.5°C$. solid lines: fit to $R/R_F$ with density profiles depicted in Fig. 15.2(b). The arrow indicates the $q_z$-position for the temperature-dependent reflectivity measurements at fixed $q_z = 0.8\mathring{A}^{-1}$ (T-scan) shown in Fig. 15.3; (b): Electron density profiles for $T = 205°C$ (dotted line), $T = 220°C$ (dashed line) and $T = 222.5°C$ (solid line), normalized to the bulk electron density of the Ga-rich subphase.

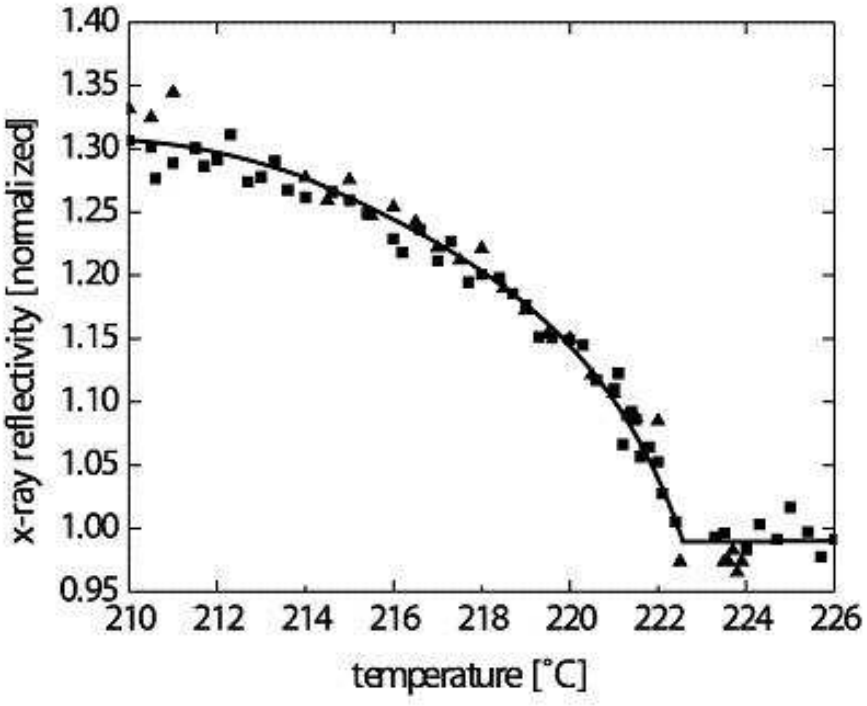



Figure 15.3: temperature-dependent x-ray reflectivity at $q_z = 0.8\mathring{A}^{-1}$ normalized to $R/R_F$ at $T = 222.5°C$. (squares) decreasing temperature, (triangles) increasing temperature. line: guide for the eye.

the inverse behavior, the intensity decreases until it reaches its lowest value at $T_{mono}$. No hysteresis was observed between cooling and heating for cooling (heating) rates smaller than $2°C$ per hour. We also carried out one temperature scan with a cooling rate of 10°C per hour. This showed a hysteresis of $4°C$ and also the formation of a solid film at the surface. We attribute this to the expected diffusion-limited growth and the corresponding long equilibration times in such wetting geometries[15] and to a temperature gradient between bulk and surface rather than to an intrinsic feature of the transition.

## 15.6 Conclusions

The behavior of the reflectivity in the T-scan shows that the Bi-rich wetting film forms while approaching $T_{mono}$ from below and vanishes in the same way on cooling, i.e. without hysteresis. Hence, the surface sensitive x-ray reflectivity measurements suggest that the first order bulk transition at the monotectic point drives a continuous structural transition at the surface. A similar behavior has been reported for Ga-Pb, a system with an analogous phase diagram (monotectic point + consolute point ), by Wynblatt and Chatain[4]. The topology of the phase diagram of Ga-Bi forces the approach of the liquid-liquid coexistence line at $T_{mono}$ from off coexistence while heating. Conversely, it enforces a path leading off coexistence while cooling below $T_{mono}$- see arrows in Fig. 15.1. Therefore, as Dietrich and Schick[18] have pointed out, one measures along a path that probes a complete wetting scenario (according to the wetting nomenclature). Since the path ends in the monotectic point with its four phase coexistence, the phenomenon is readily described as a complete wetting at a tetra point of four-phase coexistence. It should, however, be noted that $T_{mono}$ is not the wetting temperature, $T_w$ of the liquid-liquid system. $T_w$ is defined as the temperature where the formation of the wetting film can be observed on coexistence between the two liquids. This temperature has to be below $T_{mono}$, but it would be experimentally accessible only if the pure Bi can be supercooled sufficiently to reach the liquid-liquid coexistence, albeit in a metastable condition.

The observed transition at the surface is closely related to triple point wetting phenomena[16] which have been extensively studied for one component systems like Krypton on graphite[17]. There, one observes that the liquid wets the interface between

substrate and vapor, while the solid does not. Hence, there is a wetting transition pinned at the bulk triple point $T_3$. In the triple point wetting scenario one walks off the liquid-vapor coexistence line following the solid-vapor sublimation line.

Another aspect of the wetting behavior close to the monotectic point is the possible nucleation of solid Bi at the surface while cooling below $T_{mono}$. Systematic studies on that aspect were reported only recently for different Ga-Bi alloys, concluding that Ga-Bi shows a phenomenon that can be described as surface freezing. The free surface acts as substrate for wetting of the liquid by the forming solid Bi[19 20]. We did also observe the formation of solid Bi at the surface while cooling below $200°C$, but we could not study this effect in detail, since the forming solid film destroyed the flat surface of the liquid sample hampering further reflectivity measurements.

A more detailed experimental study of the wetting transition at $T_{mono}$ has already been performed[14]. It has revealed the evolution of the thick film via intermediate film structures dominated by strong concentration gradients - as reported here for $T = 220°C$. This behavior is in agreement with density functional calculations for wetting transitions of binary systems at hard walls[21], which also reveal concentration gradients. Conversely, the study shows that the liquid vapor interface of a metal system acts not only as a hard wall for one component systems[22] forcing the ions into ordered layers parallel to that surface[23],[24], but also affects other structure and thermodynamic phenomena at the surface, e.g. the wetting behavior in a binary liquid metal system discussed here.

# Bibliography


[1] J.W. Cahn, J. Chem. Phys. 66 (1977) 3667

[2] S. Dietrich, in C. Domb and J.L. Lebowitz (Eds.), Phase Transitions and Critical Phenomena, Vol. 12, Academic Press, NY, 1988

[3] B.M. Law, Progress in Surface Science 66 (2001) 159

[4] D. Chatain, P. Wynblatt, Surface Science 345 (1996) 85

[5] H. Shim, P. Wynblatt, D. Chatain, Surface Science 476 (2001) L273

[6] D. Nattland, S.C. Müller, P.D. Poh, W. Freyland, J. Non-Crystalline Solids 207 (1996) 772

[7] N. Lei, Z.Q. Huang, S.A. Rice, J. Chem. Phys. 104 (1996) 4802

[8] H. Tostmann, E. DiMasi, O.G. Shpyrko, P.S. Pershan, B.M. Ocko, M. Deutsch, Phys. Rev. Lett. 84 (2000) 4385

[9] P. Predel, Z. f. Phys. Chem. Neue Folge 24 (1960) 206

[10] P.G. De Gennes, Rev. Mod. Phys. 57 (1985) 827

[11] P. S. Pershan and J. Als-Nielsen, Phys. Rev. Lett. 52 (1984) 759

[12] L. G. Parratt, Physical Review 95 (1954) 359

[13] B.M. Ocko, X.Z. Wu, E.B. Sirota, S.K. Sinha, M. Deutsch, Phys. Rev. Lett. 72 (1994) 242

[14] P. Huber, O.G. Shpyrko, P.S. Pershan, H. Tostmann, E. DiMasi, B.M. Ocko, M. Deutsch, in preparation

[15] R. Lipowsky and D. A. Huse, Phys. Rev. Lett. 57 (1986) 353

[16] R. Pandit and M. E. Fisher, Phys. Rev. Lett. 51 (1983) 1772

[17] G. Zimmerli, M.H.W. Chan, Phys. Rev. Lett. 45 (1992) 9347

[18] S. Dietrich and M. Schick, Surface Science 382 (1997) 178

[19] C. Wang, D. Nattland, W. Freyland, J. Phys.-Condensed Matter 12 (2000) 6121

[20] A. Turchanin, D. Nattland, W. Freyland, Chem. Phys. Lett. 337 (2001) 5

[21] H.T. Davis, Statistical Mechanics of Phases, Interfaces and Thin Films, Wiley-VCH, NY (1996)

[22] J. G. Harris, J. Gryko, and S. A. Rice, Journal of Chemical Physics 87 (1987) 3069

[23] O. M. Magnussen, B. M. Ocko, M. J. Regan, K. Penanen, P.S. Pershan, M. Deutsch, Phys. Rev. Lett. 74 (1995) 4444

[24] M. J. Regan, E. H. Kawamoto, S. Lee, P.S. Pershan, N. Maskil, M. Deutsch, O.M. Magnussen, B. M. Ocko, L.E. Berman, Phys. Rev. Lett. 75 (1995) 2498

# Chapter 16

# Short-Range Wetting at Alloy Surfaces: Square Gradient Theory

## 16.1 Abstract

In this chapter of the thesis we present an x-ray reflectivity study of wetting at the free surface of the binary liquid metal gallium-bismuth (Ga-Bi) in the region where the bulk phase separates into Bi-rich and Ga-rich liquid phases. The measurements reveal the evolution of the microscopic structure of nanometer-scale wetting films of the Bi-rich, low-surface-tension phase along different paths in the bulk phase diagram. A balance between the surface potential preferring the Bi-rich phase and the gravitational potential which favors the Ga-rich phase at the surface pins the interface of the two demixed liquid metallic phases close to the free surface. This enables us to resolve it on an Ångström level and to apply a mean-field, square gradient model extended by thermally activated capillary waves as dominant thermal fluctuations. The sole free parameter of the gradient model, i.e. the so-called influence parameter, $\kappa$, is determined from our measurements. Relying on a calculation of the liquid/liquid interfacial tension that makes it possible to distinguish between intrinsic and capillary wave contributions to the interfacial structure we estimate that fluctuations affect the

observed short-range, *complete* wetting phenomena only marginally. A *critical* wetting transition that should be sensitive to thermal fluctuations seems to be absent in this binary metallic alloy.

## 16.2 Introduction

The concept of a wetting transition that was introduced independently by Cahn[2] and Ebner and Saam[3] in 1977, has stimulated a substantial amount of theoretical and experimental work[4,5,6,7,8]. Due to its critical character it is not only important for a huge variety of technological processes ranging from alloying to the flow of liquids, but has the character of an extraordinarily versatile and universal physical concept, which can be used to probe fundamental predictions of statistical physics. For example, as shall be depicted in more detail later on, it can be employed in the case of wetting dominated by short-range interactions (SRW) in order to test the predictions for the break-down of mean-field behavior and the necessary "transition" to a renormalization group regime, where this surface phenomenon is significantly affected by thermal fluctuations.

A wetting transition occurs for two fluid phases in or near equilibrium in contact with a third inert phase, e.g., the container wall or the liquid-vapor interface. On approaching the coexistence critical point the fluid phase that is energetically favored at the interface forms a nano scale wetting film that intrudes between the inert phase and the other fluid phase. In general, this surface phenomenon is a delicate function of both the macroscopic thermodynamics of the bulk phases and the microscopic interactions.

Whereas one of the seminal theoretical works[3] on the wetting transition gave a

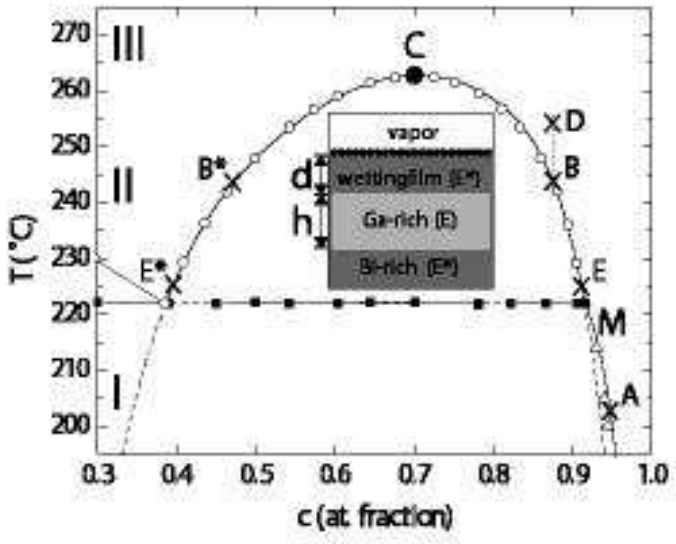



Figure 16.1: The atomic fraction ($c$)-temperature($T$) bulk phase diagram of Ga-Bi. The symbols indicate coexistence lines of Predel's phase diagram. The lines show the phase boundaries calculated from thermodynamic data. The dashed lines represent the metastable extension of the (l/l) coexistence line below $T_M$. The points are: C-bulk critical point, M-monotectic point, A,B,D,E-points on the experimental path. The insets illustrate the surface and bulk phases. In region II the wetting film is 50 $\mathring{A}$ thick and the Ga-rich fluid is 5 mm thick. The bold circles in the insets symbolize the Bi-monolayer.

microscopic view on this phenomenon, experimental results at this same level of detail were only recently obtained through application of X-ray and neutron reflection and diffraction techniques[9,10,11]. Moreover, almost all of these experimental studies dealt with systems, like methanol-cyclohexane and other organic materials, that are dominated by long-range van-der-Waals interactions[8]. The principal exceptions to this are the studies of the binary metallic systems gallium-lead (Ga-Pb)[12], gallium-thallium (Ga-Tl)[13], and gallium-bismuth (Ga-Bi)[1], for which the dominant interactions are short-range.

Here, we will present an x-ray reflectivity study of wetting phenomena that occur

at the free surface in the binary metallic liquid Ga-Bi when the bulk demixes in two liquid phases, i.e. a Bi-rich and a Ga-rich liquid phase. The fact that the wetting geometry pins the liquid/liquid (l/l) interface that divides the two liquids to the surface allows measurements that show the compositional profile of the nanoscale wetting film at the Ångström level. We will show results for the structure of the film as it evolves towards the gravity-thinned film. Through a combination of this structural information and the bulk thermodynamics of the system, it was possible to extract detailed information on the dominant interaction parameters governing the surface phenomenology. We will show that a square gradient theory that is combined with the effects of thermally excited capillary waves provides a reasonable description of that interface. In fact, we will be able to extract the sole free parameter of that model, i.e. the influence parameter $\kappa$. This, in turn, will allow us to distinguish between intrinsic (mean-field) and fluctuation (capillary waves) contributions to the interfacial structure. On the basis of this distinction we will estimate the influence of fluctuations on the observed SRW at the free surface.

Moreover, the knowledge of the energetics of the (l/l) interface will allow us to discuss from a more general perspective the rich wetting phenomenology which has been reported here and in former works on this system, ranging from surface freezing to tetra point wetting.

This paper is structured as follows: In the first section, we introduce the bulk phase diagram of Ga-Bi and relate its topology to the wetting transitions observable at the free surface of this binary alloy. X-ray reflectivity measurements on the wetting films along different paths in the bulk phase diagram will be discussed in the second section. The third section will focus on the thermodynamics and structure of the liquid-liquid

interface. In this section we will develop a square gradient theory in order to model the concentration profile at the liquid/liquid interface. Finally, in the last section we will provide a more general discussion of the rich wetting phenomenology at the free surface of this binary liquid metal.

## 16.3 Bulk & Surface Thermodynamics

The bulk phase diagram of Ga-Bi, cp. Figure 16.1, was measured by Predel with differential thermal analysis[14]. It is dominated by a miscibility gap with consolute point C (critical temperature $T_C = 262.8°C$, critical atomic fraction of Ga, $c_{crit} = 0.7$) and a monotectic temperature, $T_M = 222°C$. In the part of region I with $T < T_M$, solid Bi coexists with a Ga-rich liquid. At $T_M$, the boundary between region I and region II, a first order transition takes place in the bulk due to the liquidisation of pure Bi. For $T_M < T < T_C$ (region II), the bulk separates into two immiscible phases, a high density Bi-rich liquid and a low density Ga-rich liquid. The heavier Bi-rich phase is macroscopically separated from the lighter Ga-rich phase due to gravity. In region III, beyond the miscibility gap, a homogeneous liquid is found.

Additionally, the plot depicts the extension of the l/l coexistence line for $T < T_M$. This illustrates Dietrich and Schick's observation that the path leading to coexistence on heating from A to M is dictated by the topology of the phase diagram and corresponds to a path which probes "complete wetting". Moreover, Fig incorporates the thermodynamic path towards D the costarting at the critical point C running to the monotectic point M.

Following the observation of Perepezko[15] that on cooling fine Ga-rich droplets are coated by a Bi-rich solid phase, Nattland et. al. studied the liquid-vapor interface in

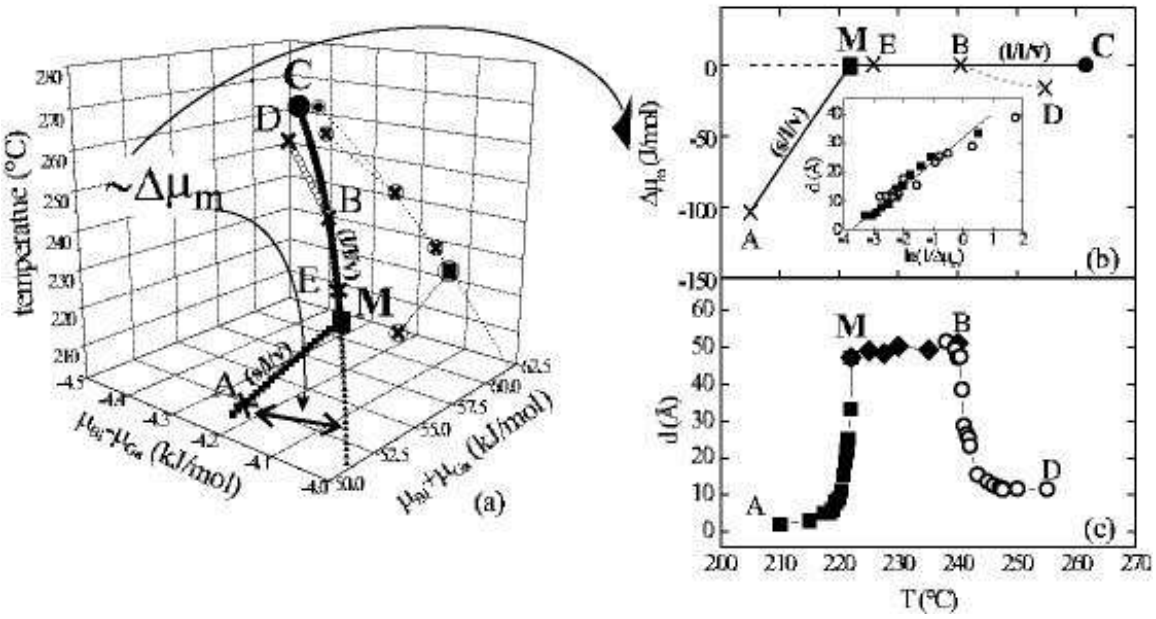



Figure 16.2: **(a)** The chemical potential ($\mu$)-temperature ($T$) bulk phase diagram of Ga-Bi. The axes are temperature, $T$, the difference $(\mu_{Bi} - \mu_{Ga})$ of the chemical potentials of the single species, and their sum $(\mu_{Bi} + \mu_{Ga})$. The solid symbols indicate the following coexistence lines: (solid circles) liquid/liquid/vapor (l/l/v) triple line, (solid squares) solid/liquid/vapor (s/l/v) triple line, (small triangles) metastable extension of the liquid/liquid/vapor (l/l/v) triple line below $T_M$, (open circles) experimental path B-D probing complete wetting. The points are: C-bulk critical point, M-monotectic point, A,B,D,E-points on the experimental path. To illustrate the 3-dimensional structure of the phase diagram, a projection of the phase boundary lines on the $(\mu_{Bi} - \mu_{Ga}, T)$ plane is drawn in the plot. The symbols surrounded by a circle show where the aforementioned characteristic points fall on this projection. **(b)**$(\Delta\mu_m, T)$ phase diagram: (A-M) is the (s/l/v), and (M-C) is the (l/l/v) coexistence line. The path B-D is in the single phase region, and M and C are the monotectic and critical points. Inset: effective wetting layer thickness $d$ on A$\rightarrow$M (squares) and B$\rightarrow$D (open circles). The solid line is a fit to the A$\rightarrow$M $d$-values. **(c)** The measured $d$ along the experimental path.

region II using ellipsometry. They found that a thin Bi-rich film intrudes between the vapor and the Ga-rich subphase in defiance of gravity[1], as implied by the illustration in Figure 16.1. This was a clear example of the critical point wetting in binary systems that was described by Cahn[2]. On approaching to point C, the Bi-rich phase necessarily becomes energetically favored at the free surface and as a result it forms the wetting film that intrudes between the Ga-rich subphase and the surface. In fact the situation is slightly more complicated since x-ray studies indicate that throughout region III the free surface is coated by a monolayer of pure Bi[16]. More recently we showed that on heating the binary liquid a thicker wetting layer of Bi rich liquid forms between the Bi monolayer and the bulk Ga rich liquid. This appears to be an unusual example of complete wetting that is pinned to the monotectic temperature $T_M$. This phenomenon was first discussed by Dietrich and Schick in order to explain an analogous finding in the binary metallic alloy Ga-Pb[12,17]. The nature of this apparent coincidence of a surface transition with the first order transition in the bulk at $T_M$ can most easily be illustrated by a transformation of the $(c, T)$-diagram to the appropriate chemical potential-temperature ($\mu$, $T$)-diagram that is depicted in Figure 16.2(a) for Ga-Bi. The axis are temperature, $T$, the difference $(\mu_{Bi} - \mu_{Ga})$ of the chemical potentials of the single species, and their sum $(\mu_{Bi} + \mu_{Ga})$. In this plot, the (l/l)-miscibility gap of Figure 16.1, which strictly spoken is a liquid/liquid/vapor (l/l/v) coexistence boundary, transforms into a (l/l/v)-triple line extending from $M$ to $C$ (solid circles). At M this triple line intersects with another triple line, i.e. the solid/liquid/vapor (s/l/v)-coexistence line (solid squares), rendering M a *tetra point* of four phase coexistence[1]. At M a solid Bi, a Ga-rich , a Ga-poor phase, and the

[1]Additionally, the (s/l/v) triple line due to the coexistence of a Bi-rich liquid, a pure Bi solid, and the vapor phase - cp. the left side of the ($c$,$T$) phase diagram (Figure 16.1) starts at M. Since it

vapor coexist.

The thermodynamics by which the surface transition at M is pinned by the bulk phase transition is obvious if one considers the topology of the ($\mu$,T)-plot in the proximity of M. The wetting of the free surface by the Bi-rich phase as well as the bulk transition are driven by the excess free energy, $\Delta\mu_m$, of the Bi-rich phase over that of the Ga-rich liquid phase[6]. This quantity is proportional to the distance between the (l/l/v)-triple line and any other line leading off (l/l/v)-coexistence, e.g. the (s/l/v)-triple line (A→M) or the line B→D in Figure 16.2(a). The wetting thermodynamics is displayed in a slightly simpler way by the plot $\Delta\mu_m$ vs. $T$ in Figure 16.2(b). In this figure for $T > T_M$, the (l/l/v) coexistence line transforms into a horizontal straight line that extends from M to C. For $T < T_M$ the horizontal dashed line indicates the metastable (l/l/v) extension of the coexistence and that is above the solid-Bi/Ga-rich/vapor (s/l/v) coexistence line that goes from M to A. This illustrates the observation by Dietrich and Schick[17] that the path A→ M leads to coexistence, and thus complete wetting is dictated by the topology of the phase diagram.

A more quantitative understanding of the surface wetting phenomena can be developed by analyzing the grand canonical potential, $\Omega_S$ per unit area A of the surface[6]: $\Omega_S/A = d\,\Delta\mu + \gamma_0\, e^{-d/\xi}$. Here, $d$ is the wetting film thickness, $\xi$ is the decay length of a short-range, exponential decaying potential, $\gamma_0$ its amplitude and $A$ an arbitrary surface area. The quantity $\Delta\mu$ comprises all energies that are responsible for a shift off true bulk (l/l/v) coexistence, i.e. the aforementioned quantity $\Delta\mu_m$. The formation of the heavier Bi-rich wetting layer at some height, $h$, above its bulk reservoir

is not relevant for the considerations of the wetting thermodynamics at the surface, it is not shown in Figure 16.2(a),(b) for the sake of simplicity.

costs an extra gravitational energy $\Delta\mu_g{=}g\Delta\rho_m h$ where $\Delta\rho_m$ is the mass density difference between the two phases. Minimization of $\Omega_S$ in respect to $d$ then yields the equilibrium wetting film thickness of the Bi-rich phase $d = \xi \ln(\gamma_0/\Delta\mu)$. In fact the gravitational energy is only significant in comparison with the other terms for very small values $\Delta\mu_m$ and for most of the data shown in Figure 16.2 the gravitational term can be neglected, allowing of $\Delta\mu = \Delta\mu_m$. Thus, one expects a logarithmic increase of the wetting film thickness upon approaching M from A that is given by $d = \xi \ln(\gamma_0/\Delta\mu_m)$, in agreement with the experimental finding that was presented in our recent Physical Review Letter on this phenomenon - cp. inset in Figure 16.2(b)[18]. The slight deviations for small values of $\Delta\mu_m$, as well as the finite value of $d \sim 50$ $\mathring{A}$ along the coexistence line M→B are due to the gravitational term. Since this approach of the (l/l/v)-coexistence line ends in M with its four phase coexistence, the phenomenon is properly described as *tetra point wetting*. As demonstrated here, the occurrence of this complete wetting phenomenon at the surface is an intrinsic feature of the bulk phase diagram.

In this paper we shall present additional x-ray reflectivity measurements that show the evolution of the wetting film on approaching coexistence from point D in regime III, and hence along a path probing complete wetting that is not dictated by the topology intrinsic to the bulk phase diagram, but rather by the experimentator's choice of the overall atomic fraction of Ga in the sample $c_{nom}$, i.e. the path B→D in Figure 16.1 and Figure 16.2(a,b). Furthermore, we will probe the wetting film structure along an on-(l/l/v) coexistence path B→ E.

## 16.4 X-ray reflectivity measurements

### 16.4.1 Experiment

#### Sample Preparation & Sample Environment

The Ga-Bi alloy was prepared in an inert-gas box using $> 99.9999\%$ pure metals. A solid Bi pellet was covered by an amount of liquid Ga required for a nominal concentration $c_{nom} = 88$ at% Ga. It was then transferred in air into an ultrahigh vacuum chamber. A 24-hour period of bake-out yielded a pressure of $10^{-10}$ torr. The residual surface oxide on the liquid's surface was removed by sputtering with $Ar^+$ ions. Using thermocouple sensors and an active temperature control on both sample pan and its adjacent thermal shield a temperature stability and uniformity of $\pm 0.05°C$ was achieved. A sketch of the experimental setup, sample environment resp. can be found in Figure 16.3(b).

A challenge in all x-ray reflectivity measurements of liquid metals is the high surface tension of these systems, e.g. pure Ga has a surface tension of ≈700mN/m. It often prevents liquid metal from wetting non-reactive container walls or substrates. This also leads to large curvatures of the liquid surface hampering x-ray reflectivity measurements[19]. Remnant oxide layers that exists at the liquid/container, liquid/substrate interface resp. even enhance this non-wetting effect; therefore, we removed these oxide layers from the Mo sample pan by sputtering with $Ar^+$ ions, at a sputter current of 25mA and a sputter voltage of 2kV, and could reach wetting of the Mo crucible by the liquid metal. This resulted in small curvatures of the free surface as was judged by eye and later on by x-ray reflectivity measurements. The resulting flat surfaces facilitated the accumulation of reliable x-ray reflectivity data sets,

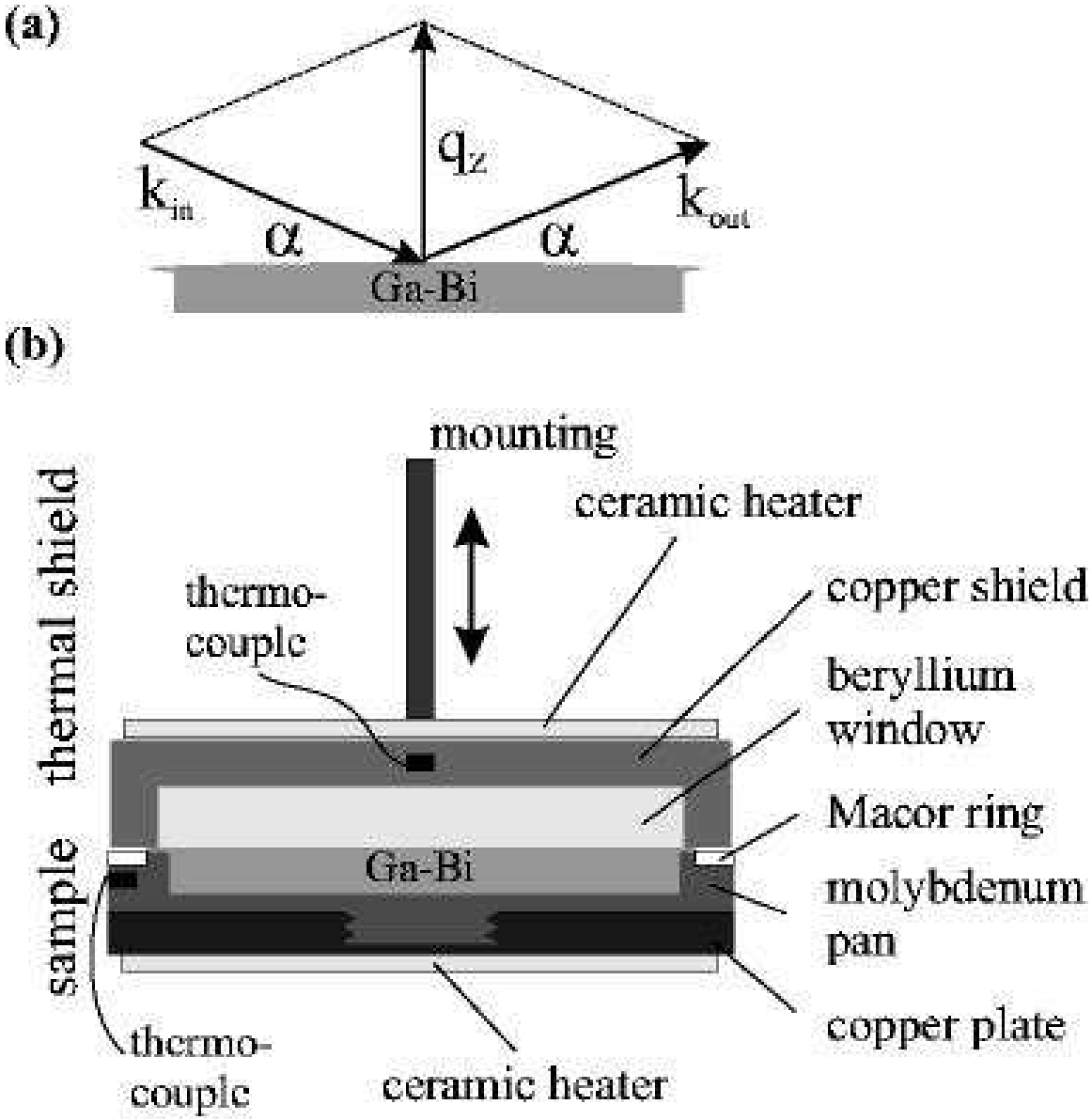



Figure 16.3: (a) scattering geometry (b) Sketch of the experimental setup. The arrow close to the mounting indicates the variable position of the thermal shield in respect to the sample surface.

particularly for small incident angles, $\alpha$. On the other hand, the wetting of the container wall by the liquid alloy promoted some spilling of the liquid during the sample movements that were necessary to track the sample position during the reflectivity scan. We circumvented this problem by installing a ceramic ring that surrounded the sample pan. The ceramics is not wetted by the liquid metal and, therefore, inhibits any liquid flow at the outermost circumference of the sample pan.

Another experimental challenge is related to x-ray reflectivity measurements from liquids in general. The surface of a liquid is sensitive to any kind of vibrations or acoustic noise. In order to obtain a stable reflected signal from the liquid surface, we mounted our UHV chamber on an active vibration isolation[19].

### X-Ray Reflectivity

X-ray reflectivity measurements were carried out using the liquid surface reflectometer at beamline X22B at National Synchrotron Light Source with an x-ray wavelength $\lambda = 1.54$ Å. Background and bulk scattering were subtracted from the specular signal by displacing the detector out of the reflection plane by 0.3°. The scattering geometry can be found as inset in Figure 16.3. The intensity $R(q_z)$, reflected from the surface, is measured as a function of the normal component $q_z = 4\pi/\lambda \sin(\alpha)$ of the momentum transfer and yields information on the surface-normal structure of the electron density $\rho(z)$ as described by the so-called master formula[20]. This formula relates the Fourier-transformed electron density gradient with the experimentally obtained $R/R_F$. The symbol $R_F$ denotes the Fresnel reflectivity that is expected from an ideally flat and sharp surface having the electron density of the Ga-rich liquid. The standard procedure for determining the electron density profile $\rho(z)$ from the measured reflectivity $R(q_z)$ is to construct a simple and physically meaningful density model and to fit

its Fourier transform to experimentally obtained data sets of $R/R_F$[21]. We employ a three-box model[10], where the upper box represents the Gibbs-adsorbed Bi monolayer the second represents the Bi-rich wetting film and the lower box represents the bulk liquid. The relative electron densities of these boxes correspond to pure Bi (top box) and to the electron density of the Bi-rich wetting film, $\rho$. The quantity $\rho_{sub}$ denotes the electron density of the Ga-rich subphase. In the simplest approximation the electron density profiles of the interfaces between the different phases can be described analytically by error-functions. The relevant model for this problem includes three error-functions (erf)-diffusenesses for the following interfaces: vapor/Bi monolayer, Bi monolayer/Bi rich film, Bi rich film/Ga rich bulk phase. The first two interfaces describing the monolayer feature were remained unchanged in the presence of the Bi-rich film, while only the diffuseness of the Bi rich film/Ga rich bulk phase interface, $\sigma_{obs}$, was a variable parameter as a function of $T$. The model also included size parameters that describe the thickness of the two upper boxes. The box that describes the bulk sub-phase extends to infinity. During the fitting the thickness of the monolayer box was kept constant while the thickness of the Bi-rich film was allowed to vary.

The use of the master formula tacitly assumes the validity of the Born approximation. This assumption holds true for wave vectors, $q_z$, much larger than the value of the critical wavevector $q_c$ of the Ga-rich subphase, where multi-scattering effects can be neglected[22]. Here, however, we will be interested in features corresponding to 30-60 $\mathring{A}$ thick wetting films, which when translated to momentum-space corresponds to features in $q_z$ around 0.05-0.1 $\mathring{A}^{-1}$ that are comparable to the value of the critical wavevector $q_c \approx 0.05$ $\mathring{A}^{-1}$ (The $q_c$-values change only slightly depending on $T$, cp.

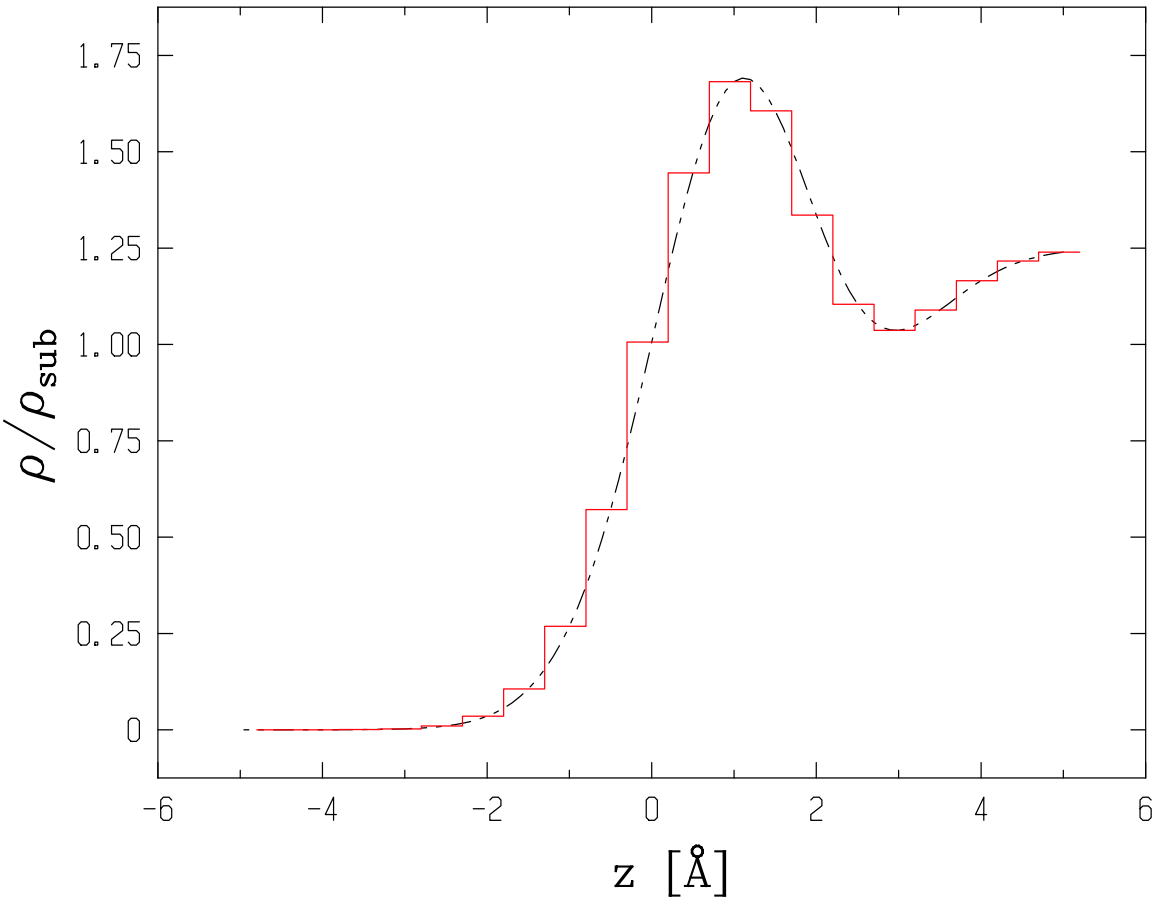



Figure 16.4: Illustration of the approximation of the analytic electron density profile (dashed line) by thin slabs in order to apply the Parratt formalism. Here, only the region close to the monolayer feature is depicted.

Table 16.1). In order to deal with this we resort to the recursive Parratt formalism[23] for $q_z$-values close to $q_c$. In this formalism one develops a 2x2 matrix that relates the amplitudes and phases for the incoming and outgoing waves on both sides of a slab of arbitrary dielectric constant. For the present problem we approximate the above mentioned three-box profile by a large number of thinner slabs whose amplitudes are chosen to follow the envelope of the analytic profile - cp. Figure 16.4. Typically the number of slabs was of the order of 300.

### 16.4.2 Wetting film structures approaching (l/l/v)-coexistence

Here we will present x-ray reflectivity measurements from the free surface of Ga-Bi along a path approaching (l/l/v) coexistence from the homogeneous part of the bulk phase diagram (regime III), i.e. the path D→B . This path, particularly the position of its characteristic point B, is solely determined by the overall atomic fraction of Ga in the sample pan, $c_{nom}$. While cooling this path intersects the (l/l/v) triple line (cp. Figure 16.2) at the point B, corresponding to temperature $T_B$ of the miscibility boundary (cp. Figure 16.1). For $T < T_B$ the heretofore homogeneous bulk liquid phase separates into the heavier Bi rich liquid that settles towards the bottom of the pan and the lighter Ga rich liquid on top. The actual position in the ($c$,$T$)-plane was chosen from consideration of the vanishing electron density contrast between Ga-rich and Bi-rich phase upon approaching C on the one hand or the (l/l/v) triple line (cp. Figure 16.2(a)) enforcing the spinodal demixing of the afore homogeneous bulk liquid. In our case, its position in the ($c$,$T$)-plane was chosen after a consideration of the vanishing electron density contrast between Ga-rich and Bi-rich phase upon approaching C, on the one hand, and a reasonably "long path" on (l/l/v) coexistence on the other hand. The compromise was a value of about 12% for $c_{nom}$, which corresponds to $T_B = 240.4°C$.

X-ray reflectivity $R(q_z)$ was measured at selected temperatures on path D→B. In order to avoid artifacts associated with the fact that the evolution of the wetting film is governed by slow diffusion processes[24,25,26] equilibration was monitored by continuous taking repeated reflectivity scans following increments of small temperature steps of $0.5°C$. Typically the measured reflectivity fluctuated wildly for a couple of hours, after which it slowly evolved to a stable equilibrium. The fits (lines)

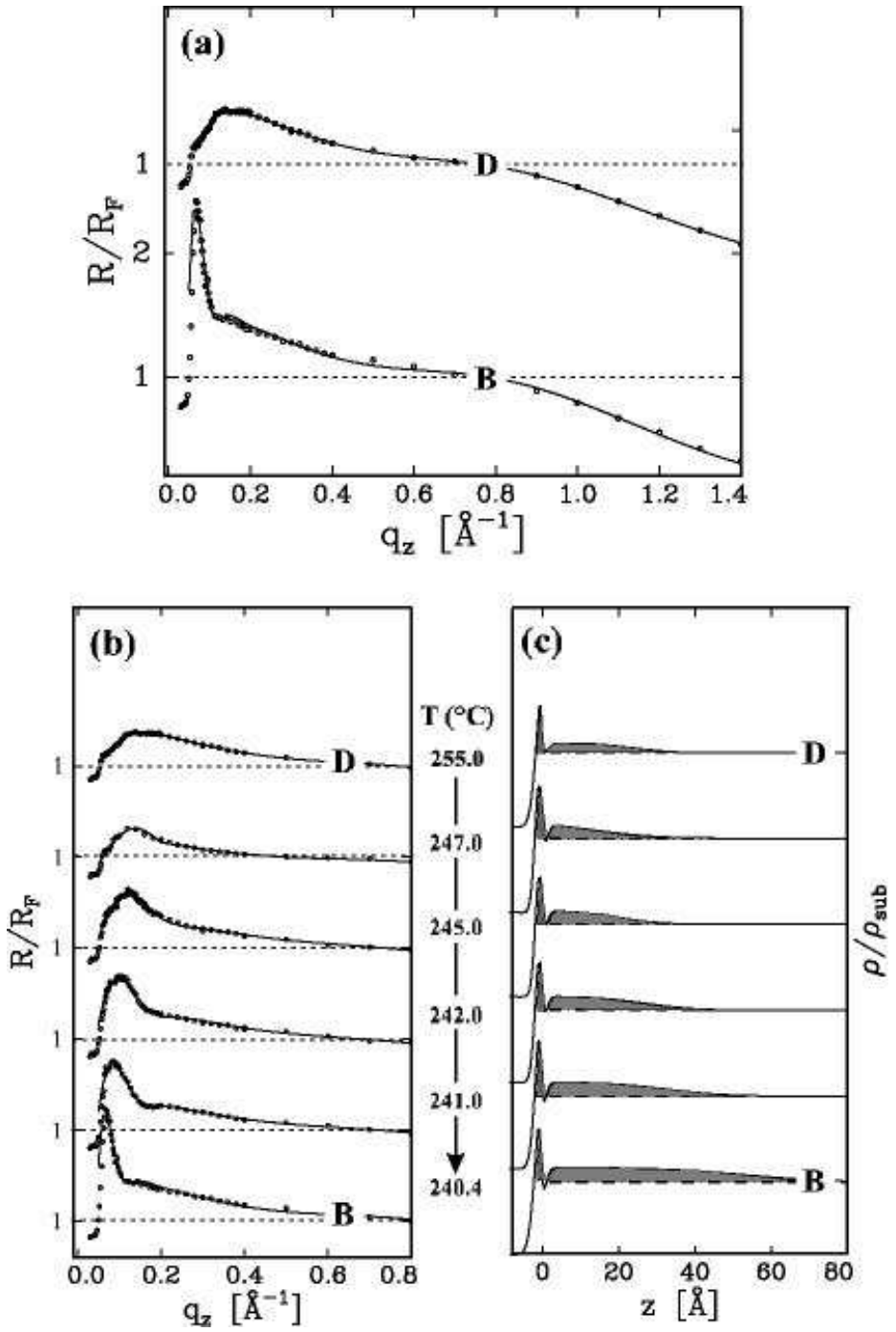



Figure 16.5: **(a)** Normalized reflectivities $R/R_F$ for selected points D and B corresponding to $T_D$=255.0°C, $T_B$ = 240.4°C. Dashed lines indicate $R/R_F = 1$. **(b)** $T$-dependent normalized reflectivities $R/R_F$ while approaching coexistence on path D →B along with fits. Dashed lines indicate $R/R_F = 1$.**(c)** Electron density profiles $\rho/\rho_{sub}$. All regions with $\rho/\rho_{sub} > 1$ indicating Bi-enrichment as compared with the Ga-rich subphase are gray shaded.

to these "equilibrium" $R/R_F$ (points) are shown in Figure 16.5(a,b), and the corresponding $\rho(z)$ profiles - in Figure 16.5(c). At point D [$T_D = 255°C$], typical of region III, $R/R_F$ exhibits a broad peak at low $q_z$ as well as an increased intensity around $q_z = 0.8\ \mathring{A}^{-1}$. The corresponding electron density profile $\rho(z)$ obtained from the fit indicates a thin, inhomogeneous film of increased electron density (as compared with $\rho_{sub}$) close to the surface along with a peak right at the surface. It is consistent with a segregated monolayer of pure Bi along with a thin layer of a Bi-enriched phase. As the temperature is decreased towards B, the peak is gradually shifting to lower $q_z$ and its width decreases. This behavior manifests the continuous growth in thickness of the wetting layer upon approaching $T_B$ and is in agreement with the thermodynamic path probing complete wetting: $\Delta\mu_m \to 0$ on path D→B.

Our experimental data clearly indicate film structures dominated by sizeable gradients in the electron density, which contrasts with frequently used "homogeneous slab" models, but is in agreement with theoretical calculations. These range from density functional calculations via square gradient approximations to Monte Carlo simulations for wetting transitions at hard walls[3,27,28]. Inhomogeneous profiles have also been observed experimentally in microscopically resolved wetting transitions for systems dominated by long-range van-der-Waals interactions[9,29]. Clearly detailed interpretation of the inhomogeneity for the GaBi nano-scale wetting films will require either a density functional analysis, or some other equivalent approach. Nevertheless, even a simple model approximating the wetting layer by a slab of thickness $d$ allows a reliable determination of the surface potential governing this complete wetting transition. In order to do so, effective film thicknesses $d$ have been extracted form the $\rho(z)$ profiles. In Figure 16.2(c) we show plots of these $d$-values versus both $T$ and $\Delta\mu_m$.

The last plot shows the expected logarithmic behavior and allows determination of the values for the parameters of the short-range potential, i.e. $\gamma_0 = 400mN/m$ and $\xi = 5.4\ \mathring{A}$[18]. Moreover, agreement between the new ($d$,$\mu_m$)-behavior along $D \rightarrow B$ and the data for the path A$\rightarrow$M provides an experimental prove that both paths have the same thermodynamic character, i.e. they probe complete wetting: $\Delta\mu_m \rightarrow 0$ on path A$\rightarrow$M and D$\rightarrow$B.

### 16.4.3 Wetting film structures: On (l/l/v)-coexistence

As discussed before, on cooling from the one phase region (III) we reach the (l/l/v)-coexistence at B. The data for the measured dependence of $R/R_F$ on $q_z$ along coexistence between points B and M are shown in Figure 16.4.3(a). The existence of two peaks at low $q_z$ indicates the presence of a fully formed thick film ($\sim 50\ \mathring{A}$). The solid lines indicate the best fit results corresponding to the real space profiles that are shown in Figure 16.4.3(b). The best fit value for maximum density of the thick film $\rho/\rho_{sub} = 1.20$ agrees reasonably well with the value of 1.21 that is calculated form the phase diagram at point B.

These results are also reasonably consistent with what is expected for a gravity limited slab of uniform density. Using $\xi = 5.4\ \mathring{A}$, $\sigma_0 = 400mN/M$ and the known material constants that make up $\mu_m$ (see table 16.1 below) the calculated value for $d = d_g = \xi \ln(\sigma_0/\Delta\mu_g) = 15.6\xi = 85\ \mathring{A}$. In view of the fact that this estimate does not take into account the excess energy associated with associated with concentration gradients across the interfaces some overestimation of $d_g$ is not too surprising. Nevertheless, this rough calculation does show that the wetting film thickness is expected to be on a mesoscopic rather than on the macroscopic length scale that has been observed for similar wetting geometries in systems governed by long-range, dispersion forces[7].

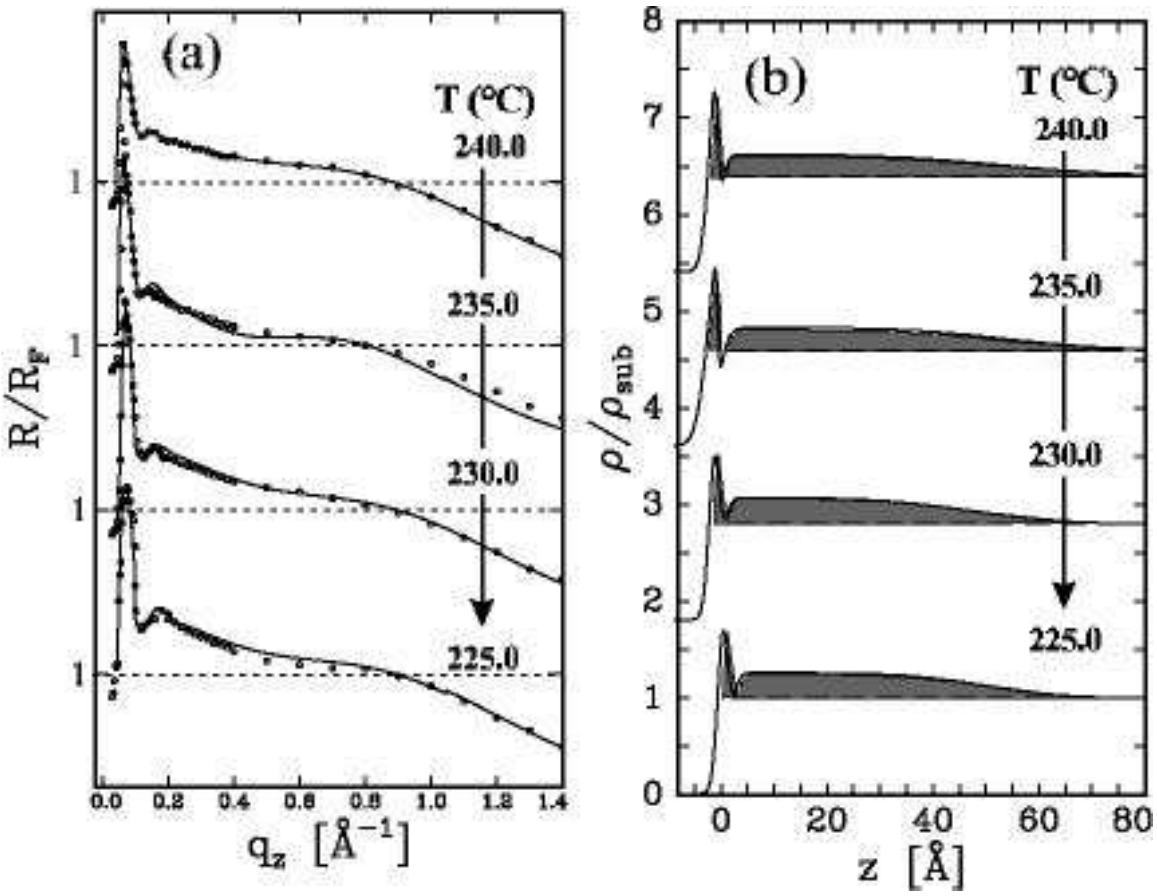



Figure 16.6: **(a)** T-dependent normalized reflectivities $\mathrm{R/R}_F$ while leaving coexistence on path B $\rightarrow$D along with fits. Dashed lines indicate $R/R_F = 1$. With increasing $T$, each $R/R_F$ is shifted by 1.2. **(b)** Electron density profiles $\rho/\rho_{sub}$. All regions with $\rho/\rho_{sub} > 1$ indicating Bi-enrichment as compared with the Ga-rich subphase are gray shaded.

Upon cooling from point B to M, the intensity of the first peak of $R/R_F$ increases as expected due to the gradual increase of the electron density contrast $\rho/\rho_{sub}$ that follows from the increase in the Bi concentration of the bulk phase. Similarly, there is a small shift in the position of the peak indicating that the thickness varies slightly from 53 $\mathring{A}$ near B to 50 $\mathring{A}$ near E that follows from the $T$-dependence of the density contrast $\Delta\rho_m(T)$ as estimated from the bulk phase $\Delta\rho_m(T)$ - cp. Table 16.1. The on-coexistence path B→E is too far away from C to expect more pronounced effects on the wetting layer thickness due to a vanishing density contrast or the increase of the influence of the criticality on the interaction potentials[6,8,30].

Moreover the gravitational thinning of the on-coexistence wetting film thickness to a length scale comparable to the range of the exponentially decaying short-range interactions prevents testing the influence of long-range, van-der-Waals like atomic interactions on the wetting behavior that is present regardless of whether the system is insulating or metallic[31,32].

Finally, we would like to highlight the unique wetting geometry encountered here: The subtle balance between the surface potential that favors the Bi-rich liquid phase at the surface and the gravitational potential that favors the Ga-rich liquid phase above the denser Bi-rich phase, pins the (l/l) interface between the two coexisting phases close to the free surface. It is this property that makes it possible to study the structure of these wetting films. For example, the width of the interface between that film and bulk, $\sigma_{obs}$, is the case of the decay of the Kiessig fringes at low $q_z$. This will be discussed further in the following section.

| $T(^\circ C)$ | $c^I$ | $c^{II}$ | $\Delta\rho_{\ m}$ | $\rho/\rho_{sub}$ calc | $\rho/\rho_{sub}$ observ | $q_c$ | $d_g$ | $d$ | $\sigma_{obs}$ | $\sigma_{calc}$ |
|---|---|---|---|---|---|---|---|---|---|---|
| 225.0 | 0.39 | 0.91 | 2.30 | 1.24 | 1.25 | 0.0498 | 84.7 | 50 | 11.78 | 12.0 |
| 230.0 | 0.41 | 0.90 | 2.20 | 1.24 | 1.25 | 0.0499 | 84.9 | 51 | 14.2 | 13.3 |
| 235.0 | 0.43 | 0.89 | 2.09 | 1.22 | 1.22 | 0.0500 | 85.2 | 52 | 15.0 | 14.9 |
| 240.0 | 0.45 | 0.88 | 1.95 | 1.21 | 1.21 | 0.0502 | 85.5 | 53 | 17.5 | 17.25 |

Table 16.1: Material parameters of the coexisting liquid phases as calculated from the bulk phase diagram as well as electron density profiles as obtained from our fits to $R/R_F$ for selected temperatures $T$ along the on-coexistence path B→E. The atomic fraction of Ga in the coexisting Ga-rich, Bi-rich liquid phase are $c^I$, $c^I$ resp. The symbols $\rho/\rho_{sub}(calc)$, $\rho/\rho_{sub}(obs)$ denote the calculated, observed electron density ratios resp.

## 16.5 Liquid/Liquid Interface

In this section, we will discuss the microscopic structure of the (l/l)-interface separating the gravitationally thinned film of the Bi-rich phase from the Ga-rich subphase along the on-coexistence path B→E. We shall first describe a simple square gradient theory for this interface and then extend it by the consideration of thermally excited capillary waves. We will use this theory in order to extract the (l/l)-interfacial profile and the (l/l)-interfacial tension from our measurements of the average surface structure.

### 16.5.1 Square Gradient Theory

At the (l/l)-interface between the two phases, the concentration varies continuously from the bulk concentration of the homogeneous Bi-rich phase, $c^I$, to the bulk concentration of the homogeneous Ga-rich phase, $c^{II}$. Assuming that the variation in concentration within the interface is gradual in comparison with the intermolecular distance, the excess free energy for the inhomogeneous region can be expanded in terms of local variables $c(\overrightarrow{r})$ and $\bigtriangledown c(\overrightarrow{r})$[27]. The Gibbs free energy density cost

within the interface can then be expressed in terms of a combination of a local function $g(c(\overrightarrow{r}, T)$ and a power series in $\bigtriangledown c(\overrightarrow{r})$[27,33,34,35]:

$$\widetilde{G} = N \int_V \left[ g(c(\overrightarrow{r}), T) + \frac{1}{2}\kappa \left(\nabla c(\overrightarrow{r})\right)^2 + ... \right] dV \tag{16.5.1}$$

where $N$ is the number of molecules per unit volume. The function $g(c(\overrightarrow{r}, T)$ is the Gibbs free energy density that a volume would have in a homogeneous solution. The next term is the leading term in the power series expansion. The coefficient $\kappa$ referred to as the influence parameter characterizes the effect of concentration gradients on the free energy. From first principles, it is related to the second moment of the Ornstein-Zernike direct correlation function and can be replaced by the pair potential weighted mean square range of intermolecular interactions of the system[27]. Equation (16.5.1) can be considered the Landau-Ginzburg functional for this problem.

Applying (16.5.1) to the one-dimensional composition change $c(z)$ across the interface and neglecting terms in derivatives higher than the second gives for the total Gibbs free Energy $\widetilde{G}$ of the system:

$$\widetilde{G} = NA_0 \int_{-\infty}^{+\infty} \left[ g(c(z)) + \frac{1}{2}\kappa \left( \frac{dc(z)}{dz} \right)^2 \right] dz \tag{16.5.2}$$

The variable $z$ represents the direction perpendicular to the interface. The symbol $A_0$ denotes an arbitrary surface area. The interfacial tension $\gamma_{ll}$ is defined as the excess energy of this inhomogeneous configuration in respect to the Gibbs free energy $G$ of the homogeneous liquid of one of the coexisting phases. The reference system we have chosen is the homogeneous Bi-rich liquid with concentration $c^I$:

$$\gamma_{ll} = \frac{1}{A_0} \left[ \widetilde{G}(c(z) - G(c^I) \right] \tag{16.5.3}$$

Combining the gradient approximation (16.5.2) with the thermodynamic definition

of the interfacial tension (16.5.3) yields:

$$\gamma_{ll} = N \int_{-\infty}^{+\infty} \left[ \Delta g(c(z)) + \frac{1}{2}\kappa \left( \frac{dc(z)}{dz} \right)^2 \right] dz \tag{16.5.4}$$

where the grand thermodynamic potential $\Delta g(c)$ is given by

$$\Delta g(c(z)) = g(c(z)) - g(c^I) \tag{16.5.5}$$

It follows then from (16.5.3) that the interfacial tension is a functional of the concentration profile $c(z)$ at the interface. The equilibrium surface tension is obtained by minimizing this functional leading to the following Euler-Lagrange equation:

$$\Delta g(c) = \kappa \, \frac{d^2 c(z)}{dz^2} \tag{16.5.6}$$

This differential equation along with the boundary conditions that the concentration has to vary from $c^I$ on the one side of the interface to $c^{II}$ on the other side determines $c(z)$ unambiguously. In fact, the simplicity of (16.5.6) allows its direct integration, yielding an expression for $z(c)$:

$$z(c) = z_0 + \int_{c^I}^{c^{II}} \sqrt{\frac{\kappa}{\Delta g(c)}} \, dc \tag{16.5.7}$$

where $z_0$ and $c_0$ represent an arbitrary chosen origin and composition. It should be noted, that from a renormalization of the integrand of equation (16.5.7), one can conclude that any characteristic length scale, such as the intrinsic width of the interfacial profile, $\sigma_{intr}$, has to scale as $\sqrt{\kappa}$.

An attractive feature of this gradient theory is that it relates the profile to $\kappa$ and $g(c(\overrightarrow{r}, T)$ without regard for the theoretical basis by which $g(c(\overrightarrow{r}, T)$ is derived. In this paper we will use the extended regular solution model that will be presented in the appendix to model the homogeneous Free Energy of the binary liquid metal,

particularly the one used to model its miscibility gap. The sole quantity required then in order to calculate the (l/l) interfacial profile and tension is an expression for the influence parameter $\kappa$, that precedes the square gradient[36]. It follows that the influence parameter can be extracted from the measurement of the microscopic structure of the interface. For example, from an appropriate choice for $\kappa$, solving of (16.5.6) or (16.5.7) will yield a profile characterized by the intrinsic width $\sigma_{intr}$ that can be compared with $\sigma_{obs}$.

### 16.5.2 Capillary Wave Excitations on the (l/l) Interface

The formalism presented so far relies on a simple mean-field picture that neglects any thermal fluctuations on the (l/l) interface. By contrast, the real experiment is sensitive to not only the mean-field diffuseness of the interface, but is also sensitive to the fact that thermal fluctuations contribute additional broadening to the fluid interface. An intuitive, semiphenomenological approach to handle the interplay of these two quantities was initiated by Buff, Lovett, and Stillinger[37,38]. Essentially, they imagined the interface as if it were a membrane in a state of tension characterized by the bare interfacial energy $\gamma_{ll}$, as calculated in the former paragraph; it sustains a spectrum of thermally activated capillary waves modes whose average energy is determined by equipartition theorem to be $k_BT/2$. By integration over the spectrum of capillary waves, one finds the average mean square displacement of the interface, $\sigma_{cap}$, as

$$\sigma_{cap}^2 = \frac{k_BT}{4\pi\gamma_{ll}(\kappa)} \ln \frac{q_{min}}{q_{max}} \tag{16.5.8}$$

Here $q_{max}$ is the largest capillary wave vector that can be sustained by the interface. For bulk liquids this is typically of the order of $\pi$/molecular diameter; however, it

does not seem realistic to describe excitations with wavelengths that are smaller than the intrinsic interfacial width as surface capillary waves[39,40]. Thus $\sigma_{intr}$ describes the intrinsic interfacial width $q_{max} = \pi/\sigma_{intr}$. The value of the quantity $q_{min}$ is slightly more complicated since it depends on whether the resolution is high enough to detect the long wavelength limit at which an external potential $v(z)$, such as either gravity or the van der Waals interaction with the substrate, quenches the capillary wave spectrum. If the resolution is sufficiently high then $q_{min} = \pi/L_v$ where $L_v^2 = \gamma_{ll}^{-1}\frac{\partial^2 v(z)}{\partial z^2}$. If it is not then the value of $\sigma_{cap}^2$ is limited by the resolution limited average length scale $L_{res}$ over which the observed fluctuations can be resolved. In this case $q_{min} = \Delta q_{res} = \pi/L_{res}$ where $\Delta q_{res}$ is the projection of the detector resolution on the plane of the interface. In our case $q_{res}$ is significantly larger than $q_v$ therefore, $q_{min} = q_{res} = 0.04\ \mathring{A}^{-1}$.

Using the fact that capillary waves obey a gaussian statistics which manifests itself as an erf-function type profile for the average interfacial roughness[41] together with the observation that the intrinsic profiles $c(z)$ are also well described by erf-function profiles, the two contributions to the interfacial width can be added in gaussian quadrature[41]. Thus we write the total observed interfacial width, $\sigma_{calc}$, as

$$\sigma_{calc}^2 = \sigma_{intr}(\kappa)^2 + \sigma_{cap}(\gamma_{ll}(\kappa))^2 \tag{16.5.9}$$

Comparison of (16.5.8) and (16.5.6) reveals that both, $\sigma_{intr}$ and $\sigma_{cap}$ depend on $\kappa$. Thus, the determination of $\kappa$ leads to the problem of finding the self-consistent value that yields a value for $\sigma_{calc}$ that agrees with the experimentally determined roughness $\sigma_{obs}$.

### 16.5.3 Intrinsic Profile and (l/l) interfacial tension of Ga-Bi

We performed a self consistent calculation of $\kappa$ for the observed (l/l) interface at point E, where $\sigma_{obs}(E) \approx 12\ \mathring{A}$. In order to do so, we solved the Euler-Lagrange Equation (16.5.6)[2] which yields the intrinsic $c(z)$ profile as depicted and compared with an erf-profile in Figure 16.7(a). From that we calculated the corresponding erf-diffuseness $\sigma_{intr}(E)$ and via numerical integration of (16.5.3) the corresponding interfacial tension $\gamma(E)$ as well as the resultant capillary induced roughness and the overall average diffuseness, $\sigma_{cap}$ and $\sigma_{intr}$ resp. After starting with a reasonable value of $\kappa$, as judged by a scaling analysis of (16.5.6), this procedure was iterated until $\sigma_{calc}(E) = \sigma_{obs}(E)$. The value we obtained was $\kappa_{opt} = 5.02 \cdot 10^{-13} Nm^3/mol$. The other quantities of interest at E are: $\sigma_{cap}(E) = 10.32\ \mathring{A}$ , $\sigma_{intr}(E) = 6.35\ \mathring{A}$ and $\gamma_{ll}(E) = 3.3\ mN/m$.

It is interesting to observe that (16.5.6) implies $\sigma_{intr} \propto \frac{1}{\kappa}$, whereas from (16.5.8) one obtains $\sigma_{cap} \propto \sqrt{\kappa}$. Hence, the function of $\sigma_{calc}(\kappa)$ exhibits a minimum for $\sigma_{calc}$ at a characteristic value, $\kappa_{min}$. It is interesting to note, that the $\kappa_{opt}$, determined from our measurements, corresponds to this peculiar value $\kappa_{min}$ meaning that the system selects from all possible $\sigma_{intr}$, $\sigma_{cap}$ combinations, the one with the minimum overall width for the (l/l)-interface.

Assuming a $T$-independent influence parameter along with the available thermochemical data sets that are available over a wide range of the phase diagram allows calculation of the $T$-dependent interfacial profiles and (l/l) interfacial tension from very low up to very high $T$, close to $T_C$. In Figure 16.7(b) the intrinsic (l/l) interfacial

[2]We used the standard procedures for solving differential equations included in the *Maple 7* software package (Waterloo Maple Inc.) as well as the *"Shooting Technique for the solution of two-point boundary value problems"* as implemented for this software package by D.B. Maede[42].

profiles are plotted for selected $T$'s versus the reduced temperature, $t = |T - T_C|/T_C$ (Here $T$ denotes the absolute temperature in Kelvin units). The increasing width of the interface while approaching $T_C$ ($t \to 0$) is well-demonstrated. In Figure 16.9 the $t$-dependent interfacial tension, $\gamma_{ll}(T)$, is depicted. As expected, it vanishes as $t \to 0$.

Comparison of $\gamma_{ll}(T)$ with other measurements would be a useful test of our measurements and interpretation. Unfortunately, measurements are rather difficult and we are not aware of any such measurements for Ga-Bi. Fortunately, it is still possible to estimate $\gamma_{ll}(T)$ using other available experimental data sets on this alloy. For example, Predel[14] noted that in the vicinity of C the (l/l)-coexistence curve of Ga-Bi can be represented by a function of the form $|\phi_c - \phi| = K(T_c - T)^\beta$ with $\beta \cong 0.33$, where $\phi$ is the volume fraction of Ga, Bi resp. and $K$ a constant[14]. This behavior suggests that the demixing transition in Ga-Bi belongs to the same universality class as binary nonmetallic liquid mixtures, i.e. Ising lattice model with dimensionality D=3. Moreover, it allows for an estimation of the interfacial tension based on a scaling relation for these quantities, i.e. the hypothesis of two-scale-factor universality (TSFU)[43] should apply. Using this concept along with available $T$-dependent measurements of the specific heat, Kreuser and Woermann extracted an expression for the $T$-dependent interfacial tension in Ga-Bi[44], $\gamma_{ts} = \gamma_{ts0}\, t^\mu$, where $\mu$ is a critical exponent with universal character for a bulk demixing transition, $\mu \cong 1.26$ and $\gamma_{ts0} = 66 \pm 15 mN/m$. The corresponding $t$-dependent $\gamma_{ts}$ $(-)$ is plotted in Figure 16.9. A good agreement with the $t$-dependence of $\gamma_{ll}$ calculated by our square gradient theory is found, e.g. at $t_E = 0.07, T_E = 225°C$: $\gamma(E) = 3.31 mN/m$, $\gamma_{ts}(E) = 5.7 mN/m$ [3]

[3]In the strict sense, the TSFU hypothesis is only valid in a $T$-range, where mapping of the

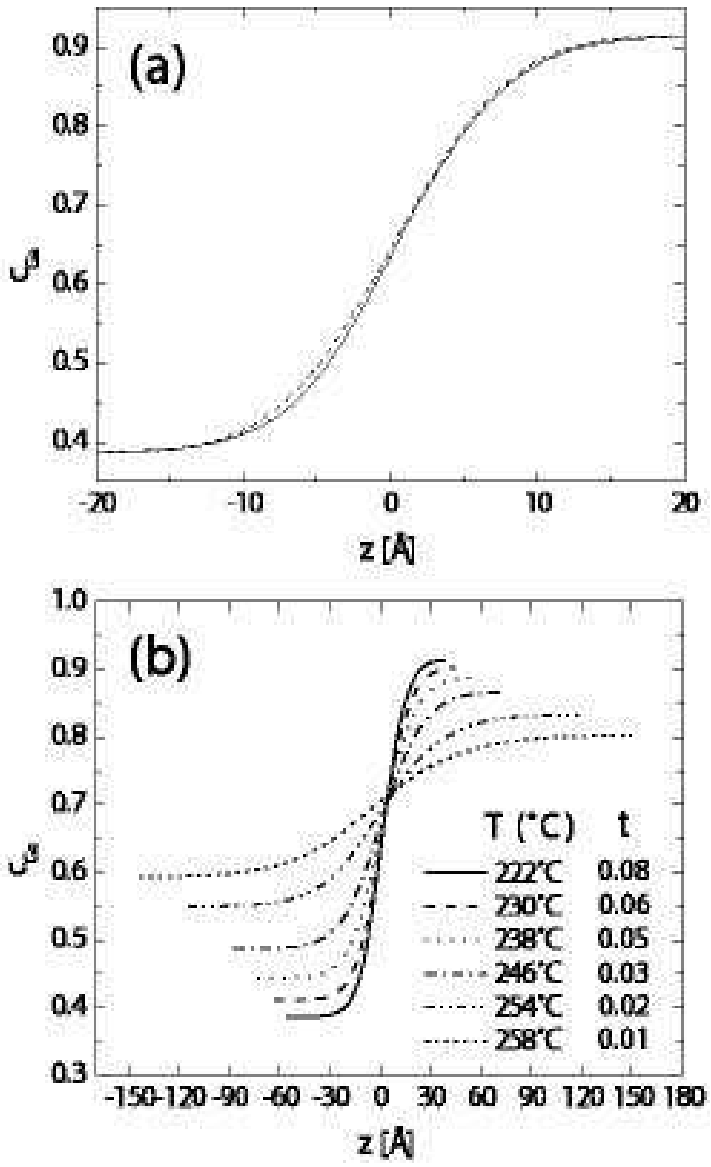



Figure 16.7: **(a)** Calculated intrinsic profile $c(z)$ $(-)$ for $T = T_E = 225°C$, $t = 0.07$ in comparison with the erf-function profile (dashed line): $c(z) = \frac{c^I + c^{II}}{2} + \frac{(c^{II} - c^I)}{2}$ erf $\left(\frac{z}{\sqrt{2}\sigma_{intr}(E)}\right)$ with $\sigma_{intr}(E) = 6.35$ $\mathring{A}$. **(b)** Calculated intrinsic concentration profiles $c(z)$ for selected temperatures $T$, reduced temperatures $t$ resp. as indicated in the figure.

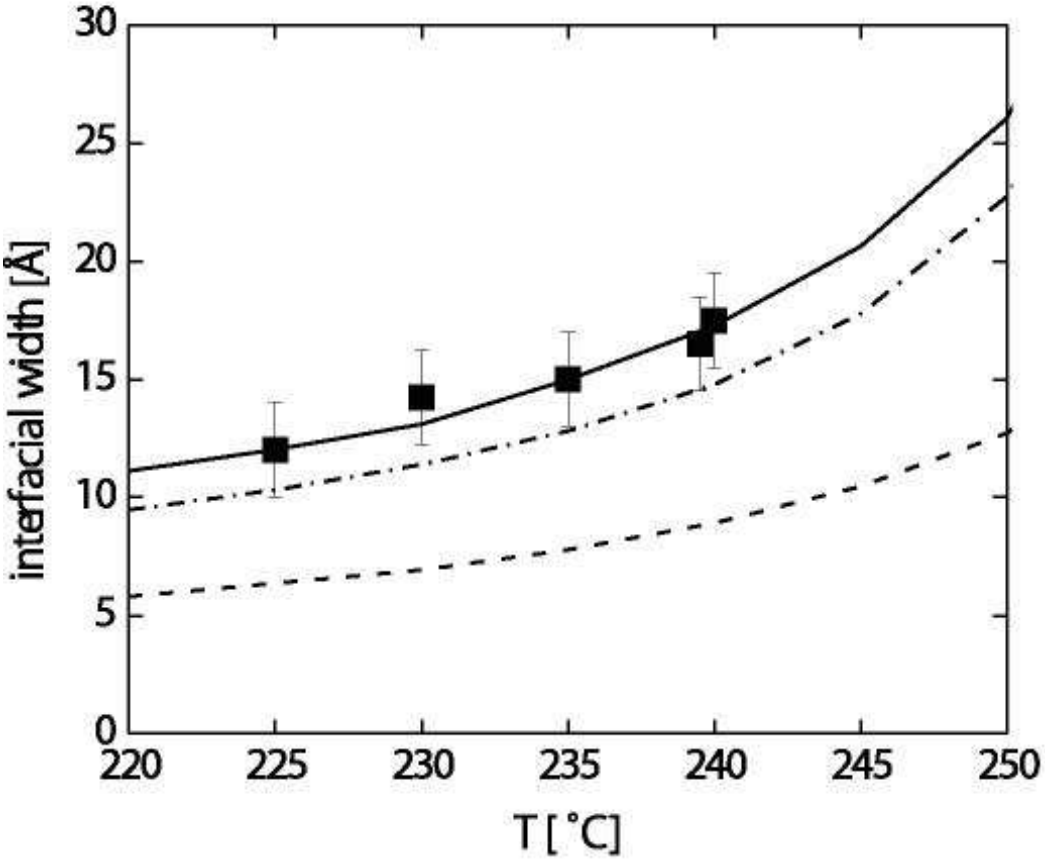



Figure 16.8: Comparison of temperature dependent, measured interfacial width $\sigma$ (■) with calculated interfacial widths (lines): $\sigma_{calc} = \sqrt{\sigma_{intr}^2 + \sigma_{cap}^2}$ $(-)$ , intrinsic width $\sigma_{intr}$ $(\cdot-)$, and capillary width $\sigma_{cap}$ $(--)$.

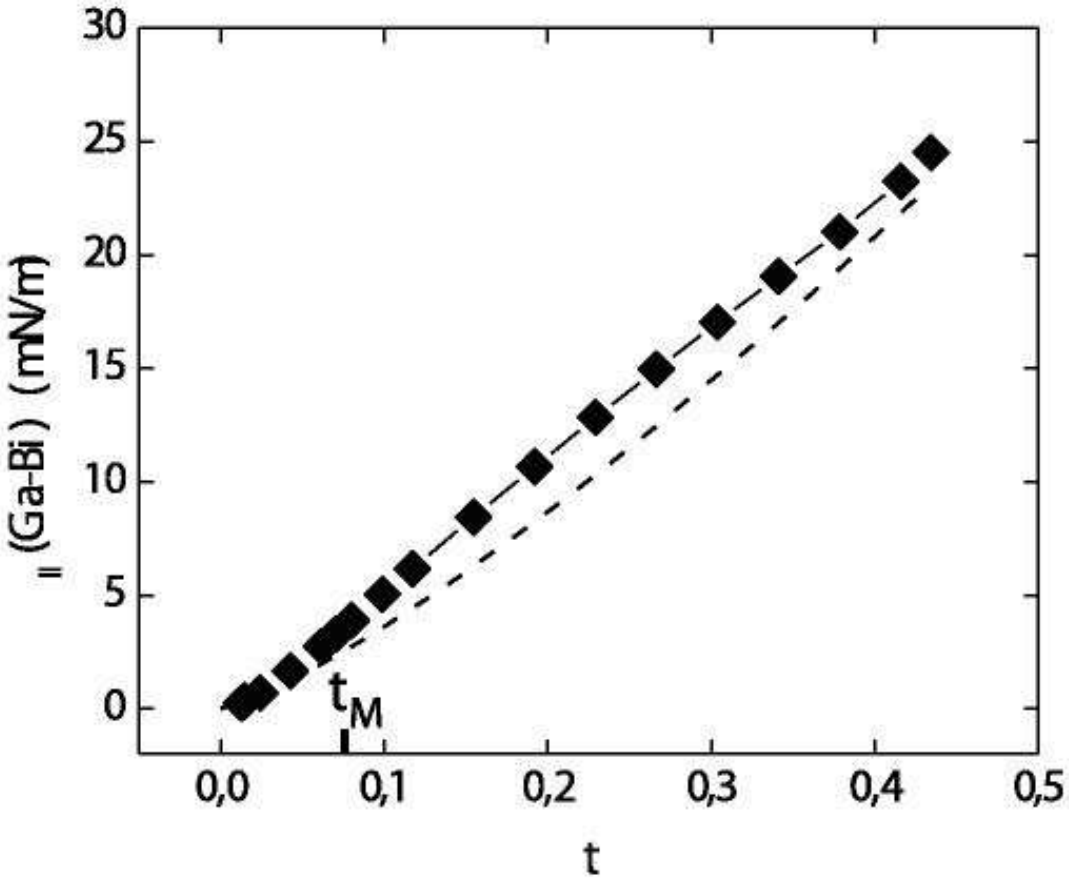



Figure 16.9: Calculated (l/l) interfacial tension $\gamma_{ll}$ of Ga-Bi as a function of the reduced temperature $t$. The dashed line represents the TSFU prediction for Ga-Bi. The symbol $t_M$ indicates the monotectic temperature at $t_M$(Ga-Bi)= 0.08.

### 16.5.4 (l/l) interfacial tension of Ga-Pb

Aside from the Ga-Bi system the only other metallic system for which detailed temperature dependent measurements[45] and estimations[46] of the (l/l) interface are reported, is Ga-Pb . Given the close relationship between Ga-Bi and Ga-Pb (similar constituents, identical phase diagram topology with consolute point C and monotectic point M), we felt encouraged to also apply our gradient theory to this binary system. Moreover, we assumed that the influence parameter, $\kappa$, as determined by the measurements on Ga-Bi, also provides a reasonable value for this metallic system. Available thermochemical data sets for the miscibility gap of Ga-Pb[47] allowed us to calculate the $t$-dependent (l/l) interfacial tension. As can be seen in Figure 16.10, where our calculated values for $\gamma_{ll}$ are shown in comparison with the experimental values, an excellent agreement is found.

Overall, our results suggest that our model of an intrinsic, mean-field interface broadened by capillary waves describes the (l/l) interface reasonably well. One must, however, bear in mind the approximation implicit in the presented analysis. For instance, we have assumed that the free surface of the liquid alloy behaves like a rigid wall, whereas it will have its own spectrum of capillary waves that could be coupled to the waves at the interface. However, since the interfacial tension of the free surface is about two orders of magnitude larger than the (l/l) interfacial energy in this metallic system, we believe that the rigid wall assumption is a reasonable starting point. Furthermore, the calculation presented above has the shortcoming of a $T$-independent influence parameter $\kappa$. It should be mentioned, though, that theory

demixing process on a second order phase transition is justified, which is typically the case for reduced temperatures, $t < 10^{-1}$. Despite of this restriction, it often fits well experimental results[45] and obviously also our results of the gradient theory in a much wider temperature range.

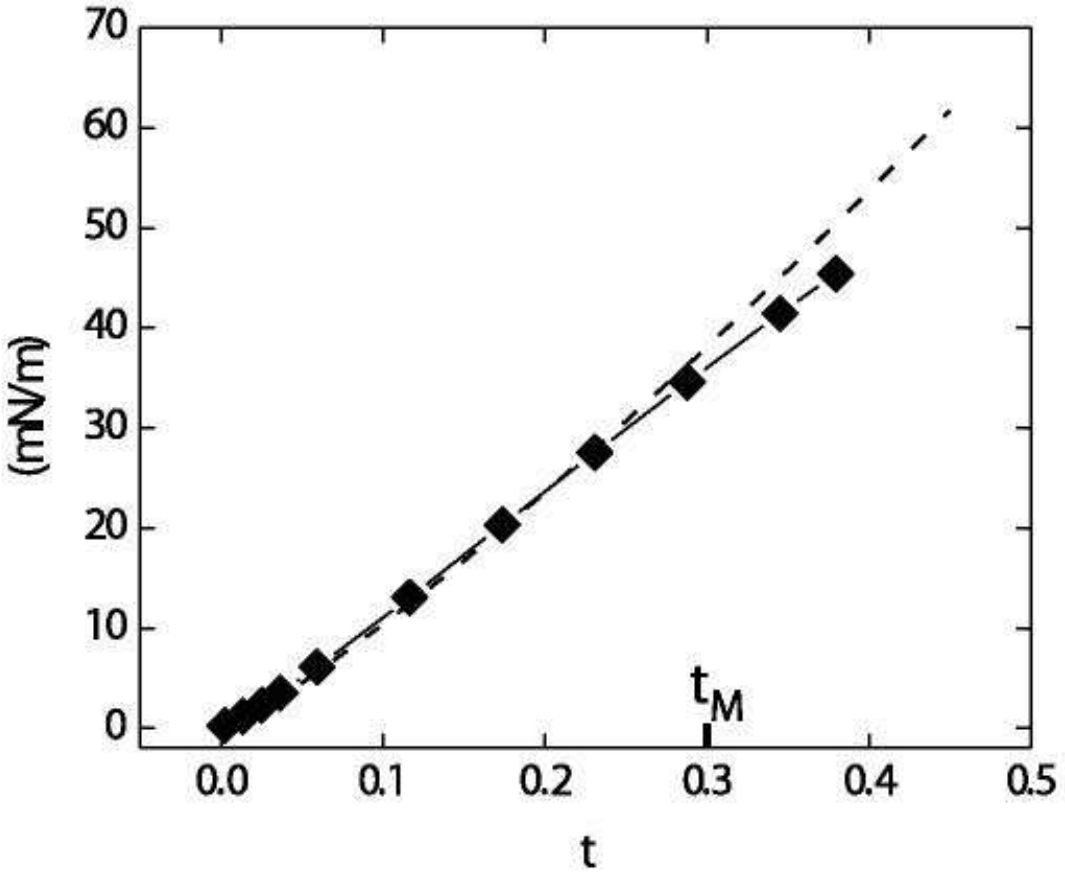



Figure 16.10: Calculated (l/l) interfacial tension $\gamma_{ll}$ of Ga-Pb as a function of the reduced temperature $t$. The solid points are our calculated values. The dashed line represents a fit to the measurements by Merkwitz et. al.. The symbol $t_M$ indicates the monotectic temperature at $t_M$(Ga-Pb)= 0.3.

predicts a divergence of $\kappa$ close to $T_C$ for real fluids, $\kappa \approx (T - T_C)^{-0.02}$ for $T \to T_C$. In fact, it can even be shown that this divergence is necessary to obtain the correct scaling behavior of $\gamma_{ll}(T)$ near C[48,49,50].

## 16.6 Wetting Phenomenology at the Free Surface

### Effects of Fluctuations on Short-Range Wetting

Our analysis in section 1 of the complete wetting transition at B was based on a mean-field (MF) model for a SRW transition. Such a model accurately predicts the critical behavior (i.e. the critical exponents) of systems close to a phase transition, provided fluctuations can be neglected. For SRW transitions, however, it can be shown that the upper critical dimensionality $D_u = 3$[51]. The value $D_u$ is the dimension beyond which MF theory can be applied successfully. If the dimension is smaller than $D_u$ fluctuations are important and one has to resort to renormalization group (RG) methods to describe the critical behavior of a phase transition. Because its upper critical dimensionality is exactly equal to 3, the SRW transition has received a great deal of theoretical attention, since it allows one to explore the regime where the MF behavior breaks down due to fluctuations, and the RG approach becomes applicable. This break-down depends on the so-called fluctuation parameter, $\omega = k_B \cdot T/(4\pi\gamma_{ll}\xi_b^2)$ (where $\xi_b$ is the bulk correlation length, and $\gamma_{ll}$ is the (l/l) interfacial tension) which measures the magnitude of the dominant thermal fluctuations, the thermally induced capillary waves at the fluid, unbinding interface, in our case at the (l/l) interface of the coexisting Bi- and Ga-rich liquids.

For a complete wetting transition RG analysis of the divergence of the wetting film thickness yields a changed prefactor of the logarithmic divergence, $d_{RG} \sim$

$\xi_{RG}\,(1+\omega/2)\,\ln\,(1/\Delta\mu)$ [6,52,53]. An estimation of $\omega$ using the bulk correlation length, $\xi_b$, estimated from the aforementioned TSFU prediction, yields for the wetting transitions at M, $\omega_M = 0.3 \pm 0.2$ and for the observed wetting complete wetting transition at B, $\omega_B = 0.4 \pm 0.2$. Thus, the prefactors of the logarithmic increase of the wetting film thickness with $\Delta\mu$ is changed by only $\approx 10\%$, 20% resp. in comparison with the mean-field prediction. This is well within our experimental error of about 30% for the determination of $\xi$. (The large error bar on $\xi$ is due to its extraction from a slab thickness analysis whereas the measured wetting films have significant inhomogeneous structures). A clear distinction between RG and MF behavior cannot be drawn in our case.

A *critical* wetting transition characterized by the wetting film formation on-(l/l/v)-coexistence, while changing $T$, with a similar value of $\omega$ should show more pronounced deviations from MF behavior. Thus, we shall estimate the characteristic temperature $T_W$ of that transition in the following.

**The Critical Wetting Transition in Ga-Bi**

It follows from our measurements that the critical wetting transition has to be hidden in the metastable range of the (l/l/v) coexistence line somewhere below $T_M$. An estimation of $T_W$ is possible by a consideration of the Free energy at the surface for the wet (Bi-rich wetting at surface) and non-wet (Ga-rich phase at the surface) situation. In order to do so, we introduce the spreading energy, $\Theta(T)$. It estimates the preference of the Bi-rich phase in respect to the Ga-rich phase at the free surface at any temperature and is given by the following energetic contributions. In the wet-situation, the energy is given by the sum of the free surface tension of the Bi-rich phase and the tension of the (l/l) interface between the Bi-rich phase and the Ga-rich

subphase. The non-wet situation is characterized by the surface energy of the bare Ga-rich liquid phase, $\gamma(Ga-rich)_{lv}$. We define $\Theta(T)$ therefore in the following way:

$$\begin{aligned}\Theta(T) &= \gamma(Ga-rich)_{lv}(T) - \\ &\quad (\gamma(Bi-rich)_{lv}(T)+\gamma_{ll}(T)) \\ &= (\gamma(Ga-rich)_{lv}(T)-\gamma(Bi-rich)_{lv}(T)) \\ &\quad -\gamma_{ll}(T) \\ &= \Gamma(T)-\gamma_{ll}(T) \qquad (16.6.1)\end{aligned}$$

In equation (16.6.1) the quantity $\Gamma(T)$ denotes the difference in the bare liquid-vapor surface tensions of the coexisting phases.

From the definition of $\Theta(T)$ it follows that establishment of the wetting film is energetically preferred if $\Theta > 0$ (wet-situation), whereas for $\Theta < 0$ it is unfavorable (non-wet situation). The condition $\Theta(T) = 0$ marks, therefore, the transition temperature $T_W$, where the system switches on-coexistence from a non-wet to a wet-situation or vice versa.

In order to estimate $\Theta(T)$, in addition to $\gamma_{ll}(T)$, as extracted in the previous section we need measurements or estimations of $\gamma(Ga-rich)_{lv}(T)$ and $\gamma(Bi-rich)_{lv}(T)$. Measurements of these quantities are reported in the literature[54,55,56], the one by Ayyad and Freyland that employed the noninvasive method of capillary wave spectroscopy is the most recent one. From these measurements, we get a conservative $T$-independent estimate for $\Gamma$ of the order of 100mN/m. Our calculation of $\gamma_{ll}(T)$, particularly its extrapolation towards very low temperature $t \to 1$ which yields $\gamma_{ll}(0K) = 75mN/m$, indicates that it is always significant smaller than $\Gamma$. Our analysis suggests, therefore, that $\Theta(T) > 0$ for all $T$ meaning that *no* critical wetting

transition occurs on the metastable extension of the (l/l/v) coexistence line.

This remarkable conclusion is, on the one hand, in contrast to the findings for the few examples of binary metallic wetting systems studied so far: In Ga-Pb and Ga-Tl, Wynblatt and Chatain et al. estimated a value for $T_W$ significantly below the corresponding monotectic temperatures $T_M$, but still at final values of the order of $0.3 \cdot T_C(K)$, $0.2 \cdot T_C(K)$ for Ga-Pb, Ga-Tl resp. ($T_C(K)$ denotes the critical temperature of bulk demixing on the Kelvin temperature scale.) On the other hand, it reflects the general finding that in binary metallic systems with short-range interactions the critical wetting transition occurs at significantly lower temperatures than this is the case in organic liquid systems, where $T_W$ is found to lie above $0.5 \cdot T_C(K)$. This tendency seems to be driven to its extreme in the case of Ga-Bi: $T_W = 0 \cdot T_C(K) = 0K$.

A semiquantitative argument for the absence of a critical wetting transition in Ga-Bi as compared to the two other metallic systems investigated so far might relate to the fact that in comparison with the others the liquid/liquid coexistence region for GaBi system is significantly shifted towards the Ga-rich, high surface tension phase and, in addition the miscibility gab is much narrower. As a result the change in concentration across the l/l interface is smaller for the GaBi system than for the others. In view of the fact that one can express

$$\gamma_{ll} = \kappa \int dz \frac{dc(z)}{dz}^2 \approx \sqrt{\kappa} \, (\Delta c)^2 \tag{16.6.2}$$

this suggests that $\gamma_{ll}$ could be expected to be smaller for GaBi than for the others. If this effect is important, and if it is not compensated by an accompanying reduction in the value of $\Gamma$, then it is possible that $\Theta(T) = \Gamma - \gamma_{ll} > 0$ for all temperatures, thereby precluding a wetting transition.

### Tetra Point Wetting ⇔ Surface Freezing

Finally, we would like to comment on the fact that the observed wetting by the Bi rich liquid at the GaBi monotectic point is not necessarily the only phenomena that can occur. In principle one expects at this tetra point a similar or even more diverse wetting phenomenology as has been predicted[57] and found[58] in the proximity of a triple point for one component systems. For example, another possibility is that the free surface could be wet by solid Bi. In the bulk both solid Bi and the Bi rich liquid are stable for $T > T_M$; however, for $T < T_M$ the free energy of the Bi rich liquid is larger than that of solid Bi. Consequently, if the solid Bi surface phase had a favorable spreading energy it would certainly wet the free surface for $T < T_M$. In fact, on the basis of optical and surface energy measurements Turchanin et al.[59,60] proposed a surface phase diagram for which a surface frozen" phase of solid Bi forms at the free surface of the GaBi liquid for temperatures below $T_M$. Unfortunately, we have a problem with this. The first may be purely semantic, but the idea of a "surface frozen phase" originates in the experiments by Earnshaw et al. and Deutsch, Gang, Ocko et al[61,62] on the appearance of solid surface phases at temperatures above that of bulk freezing for alkanes and related compounds. For the GaBi system the crystalline phase of bulk Bi is stable at temperatures well above those of at which Turchanin et al made their observations. We believe that if their observations do correspond to thermal equilibrium phenomena, the effect would be more appropriately described as wetting of the free surface by solid Bi. Unfortunately, the second problem we have is that we do not believe that surface wetting by solid Bi is favored by the spreading energy. If wetting by solid Bi were favored, as implied by Turchanin et al, then the wetting layers of Bi rich liquid that are the subject of this paper would have

to be metastable, existing only because of a kinetic barrier to the nucleation of the solid wetting film. In fact we have regularly observed that on cooling below $T_M$ the original fluid, smooth, highly reflecting surfaces became both rough and rigid. The effect is exacerbated by the presence of temperature gradients and by rapid cooling. We interpreted this as the formation of bulk solid Bi, rather than wetting, since we never saw any direct evidence for the formation of films, rather than bulk Bi. We argued that if there not enough time for the excess Bi in the bulk liquid phase below the surface to diffuse, and precipitate as bulk solid Bi at the bottom of the liquid pan, the bulk liquid would simply undergo bulk spinodal phase separation. This is consistent with our observations. Unfortunately it is very difficult to absolutely prove that our films are stable and this issue can't be resolved from the existing evidence. Nevertheless we find it difficult to understand why solid Bi would wet the surface for $T < T_M$ and not wet the surface as $T$ approaches $T_M$ from above.

## 16.7 Summary

In this paper we reported x-ray reflectivity measurements of the temperature dependence of wetting phenomena that occur at the free surface of the binary metallic alloy Ga-Bi when the bulk demixes into two liquid phases, i.e. a Bi-rich and a Ga-rich liquid phase. We characterized the temperature dependence of the thickness and interfacial profile, with Ångström resolution, of the Bi-rich wetting films that form at the free surface of the liquid on approaching the (l/l/v) coexistence triple line, i.e. along a path of complete wetting . The results, which are characterized by large concentration gradients, agree with density functional calculations for such transitions at hard walls. On the basis of this it was possible to determine the short-range surface

potential that favors the Bi-rich phase at the free surface and hence is governing the wetting phenomenology. The short-range *complete wetting* transition turns out to be only marginally affected by thermal fluctuations. According to renormalization group analysis the *critical wetting* transition should be more sensitive to critical fluctuations; however, according to our analysis the wetting layer of Bi rich liquid should be present for all temperatures. This is in contrast to the results for the other binary liquid metal systems for which the wetting transitions exists but since the metastable l/l/v line it falls below the liquidus line it is hidden.

The largest thickness of the gravitationally limited Bi rich wetting layers that formed at the free surface at (l/l/v)-coexistence were typically of the order of $\approx 50$ $\mathring{A}$. As a result of the fortuitous balance between the surface potential that favors the Bi-rich Phase and the gravitational potential which favors the lighter Ga-rich phase the interface dividing the two coexisting phases is sufficiently close to the free surface that x-ray reflectivity was sensitive to its microscopic structure. We interpreted these measurements in terms a Landau type of square gradient phenomenological theory from which it was possible to extract the sole free parameter of that model, i.e. the influence parameter $\kappa$. To the best of our knowledge this is the first time that such a parameter has been directly determined from measurement. Furthermore, it was possible to make a distinction between the intrinsic width of the interface and the additional contributions to the width from thermal capillary wave features fluctuations. On making using of available bulk thermodynamic data, along with the extracted influence parameter, we were able to calculate the experimentally difficult to get (l/l) interfacial tension for a wide temperature range. As a test of our methods we performed the same calculation of the (l/l) interfacial tension for Ga-Pb with its

analogous miscibility. We assumed that the influence parameter, $\kappa$, as determined from our measurements on the (l/l) interfacial structure in Ga-Bi, was also applicable to Ga-Pb and, using the thermochemical data sets available for Ga-Pb, we obtained good agreement between our calculated values and macroscopic measurements of the (l/l) interfacial tension. This suggests that the value of the influence parameter extracted in this study might provide a reasonable value for the larger class binary metallic alloys. If this proves to be true, then the value determined here can be used, along with the surface potential, to predict wetting properties of this larger class of systems.

## 16.8 Appendix: Bulk thermodynamics

Here[4], we focus on the part of the phase diagram dominated by the miscibility gap and the monotectic point M. In a liquid-liquid (l/l) equilibrium of binary systems, consisting of two components (Ga and Bi resp.), at atmospheric pressure p, temperature T, the compositions $c_I$, $c_{II}$ of two coexisting bulk phases (I and II) are given by the thermodynamic conditions:

$$\mu^I_{Ga}(T) = \mu^{II}_{Ga}(T) \qquad \mu^I_{Bi}(T) = \mu^{II}_{Bi}(T) \tag{16.8.1}$$

where $\mu$ is the chemical potential. The experimental conditions of the experiments that we are going to present are constant temperature, pressure and a fixed number of moles of each component, therefore we have to resort to the Gibbs free energy $G$

[4]Note unless it is is explicitly indicated otherwise, in this paper "$T$" denotes the absolute temperature in Kelvin units.

in order to describe the thermodynamic equilibrium:

$$G = U - TS + PV \tag{16.8.2}$$

$$G = n\, g = n_{Ga}\, \mu_{Ga} + n_{Bi}\, \mu_{Bi} \tag{16.8.3}$$

Since the total number of particles in mol $n = n_{Ga} + n_{Bi}$ is constant and only two components have to be considered, the system can be described with a molar Gibbs Free Energy g(c,T) that depends on only on the molar fraction of one component:

$$G = n\,(c\,\mu_{Ga} + (1-c)\,\mu_{Bi}\,) \tag{16.8.4}$$

$$\Rightarrow g(c,T) = c\,\mu_{Ga} + (1-c)\,\mu_{Bi} \tag{16.8.5}$$

With this notation the phase equilibrium conditions (equation (16.8.1) transform into the following two equations:

$$\frac{\partial g}{\partial c}|c^I = \frac{\partial g}{\partial c}|c^{II} \tag{16.8.6}$$

$$\frac{\partial g}{\partial c}|c^I = \frac{g(c^I) - g(c^{II})}{c^I - c^{II}} \tag{16.8.7}$$

Having a model for the free energy of a binary system, it is possible, then, to calculate $c_I$ and $c_{II}$ of the coexisting phases by solving of equation (16.8.7). The standard approach to describe a miscibility gap in a binary demixing system is the regular solution model for the Gibbs free energy[63]. The resulting miscibility gap has a symmetric shape and is centered around the consolute point $c_{crit} = 0.5$ in the ($c$,$T$)-plane, quite in contrast to the miscibility gap of Ga-Bi with its asymmetric shape, centered around $c_{crit}$=0.7 in the ($c$,$T$)-plane. Therefore, it is necessary to resort to an *extended* regular solution model. Relying on data sets for Ga-Bi from the Calphad initiative[64], we use such a model based on Redlich-Kister polynoms $L_\nu(T)$[65,66] and express $g(c,T)$ in the following way:

| $\nu$ | Redlich-Kister polynomial $L_\nu(T)$ |
|---|---|
| 0 | 80000-3389+T |
| 1 | -4868-2.4342·$T$ |
| 2 | -10375-14.127·$T$ |
| 3 | -4339.3 |
| 4 | 2653-9.41·T |
| 5 | -2364 |

Table 16.2: Redlich-Kister polynomials used to model the (l/l) miscibility gap of Ga-Bi.

$$\begin{aligned} g(c,T) &= c \cdot g_0(Ga)(c,T) + (1-c) \cdot g_0(Bi) \\ &\quad + R \cdot T\,[\,c\,ln(c) \;+\; (1-c)\,ln(1-c)] \\ &\quad + \Delta g_{mix}(c,T) \\ \Delta g_{mix}(c,T) &= c(c-1)\;\sum_{\nu=1}^{5} L_\nu(T)(1-2c)^\nu \end{aligned} \tag{16.8.8}$$

The first two terms correspond to the Gibbs energy of a mechanical mixture of the constituents; the second term corresponds to the entropy of mixing for an ideal solution, and the third term, $\Delta g_{xs}$ is the so-called excess term. Here, it is represented by an extension of the usual regular solution expression, i.e. a sum of Redlich-Kister polynomials, $L_\nu(T)$, as listed in Table 16.2.

By solving the nonlinear equations (16.8.7) applied on $g(c,T)$ for the temperature range $T_M < T < 262°C$ we could calculate the binodal coexistence line as plotted in Figure 16.1. The agreement of the calculated phase boundaries with Predel's measured phase boundaries is excellent. Particularly, the measured consolute point C ($T_C = 262°C$, $c_{crit} = 0.7$ is nicely reproduced by the calculated critical values $T_C = 262.8C$ and $c = 0.701$. Furthermore, the knowledge of $g(c,T)$ allows us to extrapolate the binodal lines below $T_M$ into the region of metastable (l/l) coexistence,

and, hence, to get information on the energetics of the metastable Ga-rich, Bi-rich phase resp. Similar to the procedure presented above, we also calculated the phase boundaries below $T_M$. Here, we used data sets for the Gibbs free energy of pure solid Bi, which coexists for $T < T_M$ with a Ga-rich liquid.

# Bibliography


[1] D. Nattland, P. D. Poh, S. C. Muller, and W. Freyland. *J. Phys. C*, 7(L457), 1995.

[2] J. W. Cahn. Critical-point wetting. *Journal of Chemical Physics*, 66(8):3667–3672, 1977.

[3] C. Ebner and W. F. Saam. New phase-transition phenomena in thin argon films. *Phys. Rev. Lett.*, 38(25):1486–1489, 1977.

[4] P. G. Degennes. Wetting - statics and dynamics. *Rev. Mod. Phys.*, 57(3):827–863, 1985.

[5] D. E. Sullivan and M. M. T. da Gama. Wetting transitions and multilayer adsorption at fluid interfaces. Fluid Interfacial Phenomena, edited by C.A. Croxton:45–143, 1986.

[6] S. Dietrich. *Phase Trans. and Crit. Phen.*, volume 12. Acad. Press, NY, 1988.

[7] B. M. Law. Wetting, adsorption and surface critical phenomena. *Prog. Surf. Sci.*, 66(6-8):159–216, 2001.

[8] D. Bonn and D. Ross. Wetting transitions. *Rep. Prog. Phys.*, 64(9):1085–1163, 2001.

[9] A. Plech, U. Klemradt, M. Huber, and J. Peisl. Wetting transition of a binary liquid mixture at a solid boundary. *Europhys. Lett.*, 49(5):583–589, 2000.

[10] H. Tostmann, E. DiMasi, P.S. Pershan, B.M. Ocko, O.G. Shpyrko, and M. Deutsch. Microscopic surface structure of liquid alkali metals. *Physical Review B (Condensed Matter)*, 61(11):7284–7, 2000.

[11] M.L. Schlossman. *Curr. Opinion Coll. & Interf. Sc.*, 7(235), 2002.

[12] D. Chatain and P. Wynblatt. Experimental evidence for a wetting transition in liquid ga-pb alloys. *Surf. Sci.*, 345(1-2):85–90, 1996.

[13] H. Shim, P. Wynblatt, and D. Chatain. Wetting-related adsorption transitions in liquid ga-tl alloys. *Surf. Sci.*, 476(3):L273–L277, 2001.

[14] P. Predel. Die zustandsbilder gallium-wismut und gallium-quecksilber, vergleich der koexistenzkurven mit den theorien der entmischung. *Zeitschrift fr Physikalische Chemie Neue Folge*, 24:206–216, 1960.

[15] J. H. Perepezko, C. Galang, and K. P. Cooper. Materials processing in the reduced gravity environment of space. page 491. Elsevier, Amsterdam, 1982.

[16] N. Lei, Z. Q. Huang, and S. A. Rice. Surface segregation and layering in the liquid-vapor interface of a dilute bismuth:gallium alloy. *Journal of Chemical Physics*, 104(12):4802–4805, 1996.

[17] S. Dietrich and M. Schick. Wetting at a solid-liquid-liquid-vapor tetra point. *Surf. Sci.*, 382(1-3):178–181, 1997.

[18] P. Huber, O.G. Shpyrko, P.S. Pershan, B.M. Ocko, E. DiMasi, and M. Deutsch. Tetra point wetting at the free surface of liquid Ga-Bi. *Phys. Rev. Lett.*, 89(3):035502/1–4, 2002.

[19] M.J. Regan, P.S. Pershan, O.M. Magnussen, B.M. Ocko, M. Deutsch, and L.E. Berman. X-ray reflectivity studies of liquid metal and alloy surfaces. *Physical Review B (Condensed Matter)*, 55(23):15874–84, 1997.

[20] P.S. Pershan and J. Als-Nielsen. X-ray reflectivity from the surface of a liquid crystal: surface structure and absolute value of critical fluctuations. *Phys. Rev. Lett.*, 52(9):759–62, 1984.

[21] P.S. Pershan. X-ray or neutron reflectivity: limitations in the determination of interfacial profiles. *Physical Review E (Statistical Physics, Plasmas, Fluids, and Related Interdisciplinary Topics)*, 50(3):2369–72, 1994.

[22] M. Tolan. X-ray scattering from soft-matter thin films - materials science and basic research - introduction. *X-Ray Scattering from Soft-Matter Thin Films*, 148:1–+, 1999.

[23] L. G. Parratt. Surface studies of solids by total reflection of x-rays. *Physical Review*, 95(2):359–369, 1954.

[24] R. Lipowsky and D. A. Huse. Diffusion-limited growth of wetting layers. *Phys. Rev. Lett.*, 57(3):353–356, 1986.

[25] X. L. Wu, M. Schlossman, and C. Franck. Wetting of a glass substrate by a binary-liquid mixture. *Phys. Rev. B-Condens Matter*, 33(1):402–412, 1986.

[26] D. Fenistein, D. Bonn, S. Rafai, G. H. Wegdam, J. Meunier, A. O. Parry, and M. M. T. da Gama. What controls the thickness of wetting layers near bulk criticality. *Phys. Rev. Lett.*, 89(9):art. no.–096101, 2002.

[27] H. T. Davis. *Statistical Mechanics of Phases, Interfaces, and Thin Films*. Wiley-VCH, New York, 1996.

[28] F. Schmid and N. B. Wilding. Wetting of a symmetrical binary fluid mixture on a wall - art. no. 031201. *Phys. Rev. E*, 6303(3):1201–+, 2001.

[29] A. Plech, U. Klemradt, and J. Peisl. Wetting transition and pretransitional thin films in binary liquids: alcohol/perfluoromethylcyclohexane mixtures studied by x-ray reflectivity. *J. Phys.-Condes. Matter*, 13(24):5563–5576, 2001.

[30] D. Bonn, E. Bertrand, J. Meunier, and R. Blossey. Dynamics of wetting layer formation. *Phys. Rev. Lett.*, 84(20):4661–4664, 2000.

[31] N. W. Ashcroft. Electronic fluctuation and the vanderwaals metal. *Philos. Trans. R. Soc. Lond. Ser. A-Math. Phys. Eng. Sci.*, 334(1635):407–423, 1991.

[32] B. Pluis, T. N. Taylor, D. Frenkel, and J. F. Vanderveen. Role of long-range interactions in the melting of a metallic surface. *Phys. Rev. B-Condens Matter*, 40(2):1353–1356, 1989.

[33] J. D. van der Waals. *Z. Phys. Chem.*, 13, 1894.

[34] J. W. Cahn and J. E. Hilliard. Free energy of a nonuniform system .1. interfacial free energy. *J. Chem. Phys.*, 28(2):258–267, 1958.

[35] S. A. Safran, editor. *Statistical Thermodynamics of Surfaces, Interfaces, and Membranes*. Frontiers in Physics. Westview Press, 1994.

[36] S. Enders and K. Quitzsch. Calculation of interfacial properties of demixed fluids using density gradient theory. *Langmuir*, 14(16):4606–4614, 1998.

[37] F. P. Buff, R. A. Lovett, and Stilling.Fh. Interfacial density profile for fluids in critical region. *Phys. Rev. Lett.*, 15(15):621, 1965.

[38] J. S. Rowlinson and B. Widom. *Molecular Theory of Capillarity*, volume 8 of *International Series of Monographs on Chemistry*. Oxford University Press, 1982.

[39] T. Wadewitz and J. Winkelmann. Density functional theory: X-ray reflectivity studies of pure fluid liquid/vapour interfaces. *Phys. Chem. Chem. Phys.*, 1(14):3335–3343, 1999.

[40] R. Evans and M. Hasegawa. *J. Phys. C: Solid State Phys.*, 14(5225), 1981.

[41] J. Daillant and A. Gibaud. *X-Ray and Neutron Reflectivity: Principles and Applications*. Lecture Notes in Physics. Springer-Verlag, Berlin Heidelberg, 1999.

[42] D. Maede, B. S. Haran, and R. E. White. *Mapletech*, 3(85), 1996.

[43] D. Stauffer, M. Wortis, and M. Ferer. Universality of second-order phase-transitions - scale factor for correlation length. *Phys. Rev. Lett.*, 29(6):345, 1972.

[44] H. Kreuser and D. Woermann. Estimation of liquid-liquid interfacial-tensions of metallic mixtures using 2-scale-factor universality. *Journal of Chemical Physics*, 98(9):7655–7656, 1993.

[45] M. Merkwitz, J. Weise, K. Thriemer, and W. Hoyer. Liquid-liquid interfacial tension in the demixing metal systems Ga-Hg and ga-pb. *Z. Metallk.*, 89(4):247–255, 1998.

[46] P. Wynblatt and D. Chatain. Wetting and prewetting transitions in ga-pb alloys. *Ber. Bunsen-Ges. Phys. Chem. Chem. Phys.*, 102(9):1142–1150, 1998.

[47] I. Ansara and F. Ajersch. The ga-pb (gallium-lead) system. *Journal of Phase Equilibria*, 12(1):73–77, 1991.

[48] P. M. W. Cornelisse, C. J. Peters, and J. D. Arons. On the fundamentals of the gradient theory of van der waals. *Journal of Chemical Physics*, 106(23):9820–9834, 1997.

[49] S. Fisk and B. Widom. Structure and free energy of interface between fluid phases in equilibrium near critical point. *Journal of Chemical Physics*, 50(8):3219, 1969.

[50] J. V. Sengers and J. M. J. Vanleeuwen. Capillary waves of a vapor-liquid interface near the critical- temperature. *Phys. Rev. A*, 39(12):6346–6355, 1989.

[51] M. Schick. Liquids at interfaces. In J. Charvolin, J. F. Joanny, and J. Zinn-Justin, editors, *Les Houches Summer School Lectures*, volume XLVIII, pages 415–498. North Holland, Amsterdam, 1990.

[52] E. Brezin, B. I. Halperin, and S. Leibler. Critical wetting in 3 dimensions. *Phys. Rev. Lett.*, 50(18):1387–1390, 1983.

[53] D. M. Kroll, R. Lipowsky, and R. K. P. Zia. Universality classes for critical wetting. *Phys. Rev. B-Condens Matter*, 32(3):1862–1865, 1985.

[54] K. B. Khokonov and S. N. Zadumkin. *Sov. Electrochem.*, 10(865), 1974.

[55] A. H. Ayyad, I. Mechdiev, and W. Freyland. Light scattering study of surface freezing and surface viscoelasticity in a eutectic liquid Ga-Bi alloy. *Chem. Phys. Lett.*, 359(3-4):326–330, 2002.

[56] A. H. Ayyad and W. Freyland. Wetting transition in liquid Ga-Bi alloys: light scattering study of surface energy and entropy. *Surf. Sci.*, 506(1-2):1–11, 2002.

[57] R. Pandit and M. E. Fisher. Wetting transitions near bulk triple points. *Phys. Rev. Lett.*, 51(19):1772–1775, 1983.

[58] G. Zimmerli and M. H. W. Chan. Triple-point wetting of multilayer films physisorbed on graphite. *Phys. Rev. B-Condens Matter*, 45(16):9347–9356, 1992.

[59] A. Turchanin, D. Nattland, and W. Freyland. Surface freezing in a liquid eutectic Ga-Bi alloy. *Chem. Phys. Lett.*, 337(1-3):5–10, 2001.

[60] A. Turchanin, W. Freyland, and D. Nattland. Surface freezing in liquid Ga-Bi alloys: optical second harmonic and plasma generation study. *Phys. Chem. Chem. Phys.*, 4(4):647–654, 2002.

[61] J. C. Earnshaw and C. J. Hughes. *Phys. Rev. A*, 46(R4494), 1992.

[62] X. Z. Wu, R. Sikorski, S. K. Sinha, B. M. Ocko, and M. Deutsch. *Phys. Rev. Lett.*, 70(958), 1993.

[63] P. W. Atkins, editor. *Physical Chemistry*. 2001.

[64] The calculations of the phase boundaries rely on data sets for Ga-Bi from the Calphad initiative (Larry Kaufman (MIT)), which have been refined in order to more accurately reproduce predels phase diagram.

[65] U. R. Kattner. The thermodynamic modeling of multicomponent phase equilibria. *Journal of the Minerals Metals & Materials Society*, 49(12):14–19, 1997.

[66] H. L. Lukas, J. Weiss, and E.-Th. Henig. Strategies for the calculation of phase diagrams. *Calphad-Comput. Coupling Ph. Diagrams Thermochem.*, 6:229–251, 1982.

# Index


accelerometer, 52

alkali metals, 3, 39, 73, 106, 107, 134, 136, 151, 152, 247

alkanes, 122, 176, 367

Alvine, Kyle, xxx

amalgam, 58, 257, 258

Argonne, xxx, 154, 180, 198

Auger electron spectroscopy, 282, 291, 292

bakeout, 55, 56, 93, 97, 109, 153, 197, 227

Boralectric resistive heater, 59, 197

Born approximation, 26, 180, 323, 343

box model, 31

Bragg reflection, 31, 50, 169

Brookhaven, xxx, 92, 108, 228, 322

C-PLOT, 79

Cahn, John, 223, 313, 332, 337

Calphad, 371

Chacón, Enrique, 151, 170, 177

Chatain, Dominique, 327, 366

chemical potential, 336, 337, 370

correlation length, 33, 35, 314, 363, 364

critical

- angle, 23, 36, 113, 116, 155, 182, 208, 226, 235, 236, 244, 296
- wavevector, 26, 48, 73, 79, 212, 235, 262, 322, 323, 343

curvature, 283, 340

- local, 60, 64
- macroscopic, 60
- radius, 209

Daillant, Jean, 36, 184, 185

Debye-Waller, 3, 40, 48, 74, 156, 157, 159, 164, 167, 170, 205, 224, 263

demixing transition, 223, 229, 304, 357, 361

Deutsch, Moshe, xxx, 367

dielectric contstant, 22

Dietrich, Siegfried, 34, 327, 335, 337, 338

differential cross section, 33, 34, 37, 111, 112, 114, 150, 156, 185
DiMasi, Elaine, xxx
dispersion, 26, 185, 213, 350
distorted crystal model, 76, 77, 79

Einstein, Albert, 21
electron density model, 77
ellipsometry, 1, 250, 305, 313, 319, 337
EPICS, 52
erf-function, 355, 358
error function, 28, 76
eutectic, 134, 136, 227, 228, 230, 247, 249
external reflection, 21, 110, 113, 155, 182, 226, 235, 236

Fermi
  gas, 135, 151, 177
  surface, 135, 247
fitting
  function, 77, 79, 297, 309, 343
  parameters, 77, 184, 234, 299, 331
form factor, 22, 29, 76, 96, 116, 167, 210, 267, 292, 297
Fourier transform, 27, 76
Fresnel reflectivity, 24, 26, 32, 38, 48, 73, 74, 80, 83, 179, 224, 231, 309
Freyland, Werner, 365
Fukuto, Masafumi, xxx

Gang, Oleg, xxx, 367
gaussian, 28, 76, 205, 274, 355
Gebhardt, Jeffrey, xxx
Gibbs
  adsorption, iv, 5, 197, 207, 214, 221, 222, 246, 290, 300, 304, 319, 320, 343
  free energy, 351, 352, 370–372
Gog, Thomas, xxx
Graber, Timothy, xxx
Grigoriev, Alexei, xxx

Halcyonics GmbH, 52
hard wall, 3, 135, 150, 151, 244, 328
Heilmann, Ralf, xxx
Huber, Patrick, xxx
Hume-Rothery phases, 223

IFEFFIT, 212, 213
immiscible phase, 223, 305, 319, 335
in-plane ordering, 110, 226, 234, 244, 313

index of refraction, 22

interactions

Coulomb, 6, 105, 135, 151, 222, 223, 243, 305

heteroatomic, 243, 249, 259, 291, 300, 313

Van der Waals, 5, 105, 177, 189, 222, 243, 305, 318, 333, 347, 350, 355

interfacial energy, 6, 354, 361

Ising model, 357

Landau, Lev, 369

Landau-Ginzburg functional, 352

lattice spacing, 29

Laue, 21

Lin, Binhua, xxx

linear transfer mechanism, 58

liquid

crystals, 2, 72, 177, 189

dielectric, iii, 2, 70, 90, 105, 134, 151, 175, 222, 305, 314

metallic, iii, 2, 6, 53, 60, 175, 177

structure factor, 106, 107, 134, 226, 234, 235

liquid-vapor interface, iii, 70

local electron density, 70, 104, 203

Maple, 356

Master formula, 27

mean-field square gradient model, 6, 331, 332, 354, 361, 363

Meron, Mati, xxx

miscibility gap, 223, 249, 307, 335, 337, 354, 361, 370

model independent methods, 74

molecular Dynamics simulations, 105, 126, 229, 244

molybdenum, 58

monotectic point, 6, 229, 231, 249, 304, 305, 307, 315, 318, 319, 327, 328, 333, 335, 360, 366, 370

nanoscale, 1, 11, 67, 221, 243, 250, 304, 309, 313, 331, 334

Nattland, Detlef, 335

nearly free electron, 3, 104, 106, 151, 152, 334

neutron scattering, 124, 333

nonwetting, 223

Ocko, Benjamin, xxx, 367

Ornstein-Zernike function, 352

Parratt formalism, 27, 323, 343, 344
Penanen, Konstantin, xxx
Pershan, Peter, xxx, 74
phase diagram, 5, 131, 229, 256, 268, 282, 306, 313, 319, 320, 327, 331, 333–337, 339, 348, 356, 367, 370
phase separation, 226, 291, 305, 319, 331, 345, 368
polyanions, 223
prewetting, 223
pump
  ion, 55, 110, 154
  turbo, 55, 154

quasi-Bragg peak, 31, 91, 94, 159, 175, 196, 200, 228, 244, 267

reciprocal lattice vector, 50
Redlich-Kister, 371, 372
Regan, Michael, 196
renormalization group, 332, 363, 369
residual gas analyzer, 55
resolution function, 38, 39, 46, 85, 119, 156, 185
Rice, Stuart, 176, 188, 195
Roentgen, Wilhelm Conrad, 21
Rozenwayn, Alexey, xxx

Schick, Michael, 327, 335, 337, 338
Schlossman, Mark, 169
self-assembled monolayers, 4
short-range interactions, 6
Sinha, Sunil, 37, 113
solubility limit, 5, 237, 256, 269, 270, 274, 279, 282, 284
spectrometer, 79, 92, 108, 139, 198, 228, 260, 293, 307
spectrometer resolution, 33
specular
  plane, 24
  reflection, 24
spinodal demixing, 345, 368
square gradient theory, 335, 361, 369
Steimer, Christoph, xxx
step function, 28
sterring crystal, 50
superfluid helium, 2
surface
  freezing, 328, 334, 367

layering, 70, 73, 74, 176, 188, 237, 295
premelting, 126
structure factor, 27, 36, 38, 40, 73, 74, 77, 84, 85, 104, 134, 169, 179, 180, 188, 226, 235
synchrotron
radiation, 2, 48, 49
source, iii, 4, 50, 55, 92, 108, 139, 143, 159, 224, 228, 260, 293, 307, 322, 342

thermal radiation shield, 53, 56, 321
Tostmann, Holger, xxx
tracking parameters, 52
Turchanin, Andrei, 367
two-scale-factor universality, 357

UHV
chamber, 51, 53, 54, 92, 97, 227, 261, 342
conditions, 73, 107, 127, 227
methods, 190
ultrasonic bath, 54

Velasco, Enrique, 70
vibration isolation, 51, 52, 94, 110, 227, 342
viewport, 57

walking scan, 61
wavevector transfer, 25
wetting
complete, 223, 306, 313, 315, 318, 327, 335, 336, 338, 347, 363, 368
critical, 2, 364, 365, 369
film, 221, 243, 249, 250, 304, 305, 309, 311, 313, 314, 331–334, 337, 339, 343, 347, 348, 350, 363, 364
short-range, 331, 363
tetra-point, iv, 5, 6, 26, 318, 321, 327, 334, 337, 339, 367
transition, iv, 5, 221, 305, 369
triple point, 327, 328, 367
Wynblatt, Paul, 327, 366

x-ray
absorption, 22, 262
absorption edge, 23, 210, 293
absorption fine structure, 282
absorption length, 22, 31, 208
anomalous scattering, 22, 212

diffuse scattering, 4, 23, 33, 85, 91, 101, 104, 119, 126, 134, 139, 150, 156, 175, 179, 183, 184, 201
fluorescence, 4, 23, 195, 207
footprint, 60, 140
grazing incidence diffraction, 21, 23, 110, 184, 207, 226, 244, 313
monochromatic beam, 24, 48
polarization, 25
resonant scattering, 5, 195, 207, 212, 216, 282, 290, 293, 295
spectrum, 21, 210
specular reflectivity, 4, 23
windows, 53, 55, 182

Yano, Yohko, xxx

Zintl phases, 223